Cu2ZnSnS4 Nanocrystal Ink Absorber Layers for Thin Film Solar Cells

STROH, KAREN,PATRIZIA

Durham University

Department of Physics
Centre for Materials Physics

Cu_2ZnSnS_4 Nanocrystal Ink Absorber Layers for Thin Film Solar Cells

Thesis submitted by

Karen P. Stroh

in candidature for the degree of
Master of Science by Research

in January 2019

Abstract

A promising approach to low-cost photovoltaic devices is to fabricate thin film solar cells using solution-processable nanocrystal inks. This is applicable to the material class of kesterites having favourable opto-electronic properties and the potential for high efficiencies. This study looks at the chalcogenide compound Cu_2ZnSnS_4 (CZTS) in particular which consists of earth-abundant elements and therefore provides means for truly sustainable energy generation. Re-dispersed in an organic solvent, the nanoparticles can easily be deposited in thin films on top of glass substrates. Subsequent annealing is used to promote grain growth for a dense, polycrystalline absorber layer. The resulting films (or as-synthesised particles) are analysed with respect to their crystal structure, phase purity, morphology, chemical composition, and opto-electronic properties. Combining a variety of methods helps to disentangle the complex material characteristics of the quaternary compound.

The reproducibility of CZTS nanocrystal synthesis by the hot-injection method is briefly discussed. The focus of this thesis is on the influence of the annealing temperature held at a constant value in a range between 400 °C and 600 °C for 1 h on the film development. This is supplemented by an investigation of the influence of different annealing times between 0.5 h and 3.0 h at a moderate temperature of 500 °C and by an exemplary analysis of cross-sections through samples of a CZTS absorber on a molybdenum rear contact layer. The experiments suggest that temperatures around 600 °C are preferable in order to enhance the quality of the crystal structure and to obtain large-grained films which is seen as a major area of improvement in this field of research. Increasing the annealing time, in contrast, does induce hardly any changes in the material and is therefore less effective in achieving high-quality absorber layers. The final state of the films is reached after only about 1 h of annealing.

Declaration

Herewith I declare that I wrote the thesis at hand on my own, based on my own work unless otherwise indicated. In particular:

- ICP-MS has been carried out by Dr Chris Ottley (Department of Earth Sciences, Durham University). The results are mainly used in Section 6.1.
- The cross-sectional images from the FIB presented in Section 6.4 have been done by Mr Leon Bowen (Department of Physics, Durham University).

All material taken or adapted from published work is explicitly referenced and identified as such. Moreover, I affirm that I did not submit this thesis, neither in its entirety nor in excerpts, for a degree at this or any other institution.

Durham, 14th January 2019

Karen P. Stroh

Acknowledgements

First of all, I would like to give a big thank to my supervisor Dr Douglas P. Halliday who provided great support in various ways throughout the whole project. Also my co-supervisor Dr Marek Szablewski always had an open ear and helped especially with all chemistry-related issues. I deeply appreciate that I had such an excellent supervisory team that spent advise, was always available for inspiring discussions, and gave me the opportunity to do this master's project in the first place. I also value all the support from the other members of the Inorganic Opto-Electroactive Materials research group, especially from PhD candidate Yasir Altowairqi and fellow master's student I. Gerardo Pérez Marín. I enjoyed the interesting discussions and I am very grateful for the shared lab expertise.

Many other people helped with the sample preparation and measurement facilities as well and I very much appreciate these various contributions. I would like to thank Dr Christopher J. Bosson for the introduction to annealing in the tube furnace and Mr David Pattinson for maintenance of the same, Dr Aidan Hindmarch for the training in molybdenum sputtering and provision of the facility, Mr Gary Oswald for the instruction to the laboratory XRD setup, and Prof Andrew Beeby for help and guidance with his Raman microscope. Furthermore, I appreciate support by Mr Leon Bowen, who not only organised the training on the SEM and had an open ear for questions but also did cross-sectional imaging of some samples with the FIB microscope, as well as by Dr Chris Ottley who performed the ICP-MS analysis for my samples. Summer student Alexandre M. A. Richard kindly gave a helping hand with some temperature-dependent PL measurements.

I would like to extend my cordial thanks to all the other people who made the time of my master's such a rewarding experience, whether we met in the department, St Chad's College or in another context. Last but not least I would like to express my sincere gratitude for my family's support throughout my entire studies which has been a great privilege. A special thanks is due to my father for his personal commitment to proof-reading. In the hope not to have missed anybody: Thank you, Dziękuję bardzo, شكرا, Gracias, Merci, Danke schön! – I will not forget the lovely time I had in Durham.

Contents

Part II. Experimental

Appendix

List of Abbreviations

As-syn/dep	As-synthesised (nanoparticles)/as-deposited (films)
BSE	Backscattered electrons (in the SEM)
CB	Conduction band
CI(G)S	Copper indium (gallium) sulphide or selenide
CL	Cathodoluminescence
CZTS	Copper zinc tin sulphide, i.e. Cu_2ZnSnS_4
CZTSe	Copper zinc tin selenide, i.e. $Cu_2ZnSnSe_4$
CZTSSe	Selenised copper zinc tin sulphide, i.e. $Cu_2ZnSn(S_x,Se_{1-x})_4$
EBIC	Electron-beam-induced current (SEM-based technique)
EDX	Energy-dispersive X-ray spectroscopy (elsewhere also EDS)
FF	Fill factor
FIB	Focused ion beam microscope
FWHM	Full width at half maximum
ICP-MS	Inductively coupled plasma mass spectroscopy
ITO	Indium tin oxide, i.e. $InSnO_2$
NC	Nanocrystal
NIR	Near-infrared (radiation/spectral region)
OAm	Oleylamine, i.e. $C_{18}H_{35}NH_2$
PL	Photoluminescence
PVD	Physical vapour deposition
SE	Secondary electrons (in the SEM)
SEM	Scanning electron microscopy or microscope
SLG	Soda lime glass
TCO	Transparent conductive oxide
TEM	Transmission electron microscopy or microscope
UV-vis	Ultraviolet-visible (spectral region)
VB	Valence band
XRD	X-ray diffraction

1. Introduction

One of the key challenges for us today is to satisfy an increasing energy demand while fighting against global warming at the same time. The global electricity consumption has been growing with a rate of 3.3 % on average since 1974 and is at a level of 25 082 TWh at present times, as recorded in 2016 [1]. Climate change simultaneously became an integral part of the public dialogue and renewable energies are therefore rather unsurprisingly regarded as a universal remedy. Among the other options, photovoltaic devices have an extraordinary potential, as the amount of solar radiation reaching Earth per hour could principally cover the worldwide energy consumption of about a year [2]. In order to make the most of these capabilities, however, much work still needs to be done. Globally, only 218 TWh electricity were produced by photovoltaics in 2016, but the average annual growth rate of 43.3 % since 1990 is higher than for any other source of green electricity [3]. Solar power is hence capable of producing electricity on a terawatt scale and promises a great development towards the provision of a substantial part of the required energy in an environment-friendly manner.

A number of factors have to be considered in order to determine the optimal approach to solar energy conversion. First of all, the elemental constituents should be Earth-abundant to assure sustainability and long-term cost efficiency [4]. Non-toxic materials are, as a matter of course, preferable to health-damaging and environmentally harmful substances. Furthermore, the material should have suitable opto-electronic properties such as a band gap in the optimal energy range and a direct one at best [5–7]. This is related to a high optical absorption, so that thin films of only a few microns are sufficient to serve as absorber layer in a solar cell, lowering the amount of material needed as well as limiting the costs. In contrast, devices made from the indirect band gap material silicon would require up to hundreds of microns of thickness [5]. Thin films also have the advantage of better defect tolerance which relieves the pressure on the required purity of the materials and allows for a simple thermal treatment [6]. Energy consumption and other cost-driving aspects also have to be taken into consideration when choosing the processing technique [8]. Last but not least, the resulting device efficiency is an important aspect as well since it will enter all economic comparisons as universal factor [4]. From all this it is easy to see that only a combination of a high-performance material and an easy fabrication process can both satisfy ecological aspects and meet the market challenges.

The first practical photovoltaic device was presented in 1954 [9]. However, even six decades later, further technological progress regarding efficiency and costs is still essential to allow for a breakthrough of photovoltaic power generation and the ultimate energy turnaround towards renewables [10]. Traditional photovoltaic devices such as silicon-based solar cells have several drawbacks such as relatively high costs and energy requirements of the fabrication process [8]. However, also more advanced ones including commercial thin film technologies based on cadmium telluride (CdTe) and copper indium sulphide ($CuInS_2$/CIS) do not meet all above-mentioned requirements of a truly future-proof technology [8, 11]. This also applies to related compounds such as the gallium-doped CIGS and the corresponding selenide variant CIGSe. Admittedly, devices made of these materials have reasonable efficiencies – the best-reported single-junction cells (until May 2018) achieved $(21.0 \pm 0.4)\,\%$ for CdTe and $(22.9 \pm 0.5)\,\%$ for CIGS respectively [12] – but these alloys contain relatively rare elements, namely tellurium, indium, and selenium. Additionally, tellurium, indium, and gallium are quite expensive and cadmium as well as selenium are toxic [11]. As a consequence, not only ways of optimising existing approaches are being explored but also alternative materials and technologies for solar cells are an active field of research [10].

Proceeding from the CIS family as one of the current mainstream solar cell material groups, another chalcogenide compound with improved characteristics can be derived by isoelectronic substitution of the scarce element indium with the far more abundant elements zinc and tin [7, 13, 14]. The resulting quaternary compound is the kesterite-structured copper zinc tin sulphide (CZTS) with the chemical formula Cu_2ZnSnS_4. It preserves favourable characteristics of its predecessor material such as high absorption and stability [15], but it does not have any of the other issues discussed before. Related materials are $Cu_2ZnSn(S_x,Se_{1-x})_4$ (CZTSSe) and $Cu_2ZnSnSe_4$ (CZTSe) have shown some beneficial traits, but it is important to notice that they contain the toxic element selenium [16]. This study consequently focusses on the pure sulphide compound. Based on the advantages mentioned above, it is evident that CZTS is a promising candidate as a material for future photovoltaics, composed of Earth-abundant, non-toxic elements and offering favourable opto-electronic properties [5].

Katagiri et al. [17] were the first to build a CZTS-based solar cell, reaching a power conversion efficiency of 0.66 % by a vacuum deposition approach in 1997 [7]. By now, Wang et al. [18] managed to produce a CZTSSe-based device by a hydrazine pure-solution approach with an efficiency of 12.6 % on a laboratory

scale. However, this is still far away from the theoretical limit and a lot of potential remains. – According to the detailed balance limit originally introduced by Shockley and Queisser [19], the maximum efficiency for selenised CZTS is about 31 % [7]. The first commercially available sulphide-based solar cells were the CIS thin film modules sold by the company Sulfurcell (later Soltecture) from 2005 onwards [5, 20]. This demonstrates that the route chosen is generally promising. Until CZTS devices will have become economically competitive as well, their efficiency still needs to be improved significantly but there is also plenty of room for development and the corresponding need for further studies [7, 21].

As mentioned earlier, the focus of investigations will not only have to be on the material itself but also on the fabrication process. To this end, CZTS offers different options including convenient and profitable solution-based processing techniques [8]. It is often argued that vacuum deposition results in better performance; however, it has been pointed out that a predominant part of the champion cells was fabricated via solution processing since 2009 [7]. Among the benefits are the low costs and a high throughput; even a fully printable solar cell is conceivable [8]. One approach, which is also applicable to some other semiconductor materials [6], is using a dispersion or 'ink' of nanoparticles to deposit the absorber layer. It is advantageous that this way, the chemical composition and the crystal structure of the absorber can be controlled prior to film deposition, reducing the proportion of secondary phases and the number of defects in the final films [21]. Also, this method potentially allows for lower processing temperatures and hence for better energy efficiency [6, 21]. Altogether, considering the fundamental characteristics of the material as well as its fabrication, CZTS thin film solar cells made of nanocrystal inks have good prospects for becoming economically competitive compared against more progressed technologies as they are sustainable, low-cost, and show promise of reaching high efficiencies [21].

The nanocrystal approach for the absorber layer formation of photovoltaic devices is encouraging indeed but nevertheless, it is still in its development process. Advances in nanocrystal synthesis for a higher level of control, e.g. regarding the level of being monodispersed, could make uniform film deposition easier [15], but many of the current issues also concern subsequent film treatment by annealing. Due to the fact that the quaternary alloy is relatively complex and that the constituent elements have significantly different vapour pressures, several dependencies between the material properties and processing parameters are observed [21]. In this study, a sulphurisation approach is addressed, which means

annealing in a sulphur-rich atmosphere. The resulting films often suffer from insufficient uniformity in regard of composition, phase, and structure. Ensuing key challenges for the devices as a whole are a loss in open circuit voltage and in short circuit current, a relatively high series resistance, and a low fill factor. Optimising the heat-treatment could provide a remedy [7, 21].

During the annealing process, the nanocrystal film undergoes several changes. Recrystallisation of the material helps to reduce point defects as the temperature rises. Additionally, the particles start to grow so that their surface-to-volume ratio decreases and voids in the absorber layer start to disappear. The final film is ideally composed of densely packed, large grains with a minimal grain boundary area to limit carrier scattering and recombination losses for an improved device efficiency [21]. However, depending on the annealing conditions, secondary phases can appear and layer formation is observed [5]. Specifically, large CZTS grains often grow on top of the film surface, also referred to as abnormal grains. Beneath, there is a fine-grained or even nanocrystalline 'floor layer' which undergoes a uniform, but very modest size development [22]. Not only layers of grains with different sizes are observed but also with differing carbon content [5]. The effects of these carbon residues from the organic solvents used for particle synthesis and ink fabrication have been controversially discussed and are not yet fully understood. Another commonly observed phenomenon is the formation of a MoS_2 interlayer between the CZTS absorber and the molybdenum rear contact layer on the substrate [7]. All of these observations make clear that further understanding of the growth mechanisms and the effects of these features on the device performance is necessary in order to optimise the fabrication process.

In this study, the focus is on the effect of different annealing parameters on the film properties, specifically regarding the temperature and the duration of this processing step. The nanocrystals used to fabricate the inks are synthesised by a solution-based hot-injection method, according to the process described by Guo et al. [23, 24]. Thin film deposition from the resulting nanocrystal inks is mainly done by spin coating on top of glass substrates and annealing is performed in a sulphur-rich atmosphere. The as-synthesised nanoparticles, the as-deposited, and the annealed films are analysed with respect to their opto-electronic properties, crystal structure, phase purity, composition, and morphology. For this purpose, a combination of various measurement techniques is used. These are X-ray diffraction (XRD), Raman spectroscopy, scanning electron microscopy (SEM) with energy dispersive X-ray analysis (EDX), inductively coupled plasma

mass spectroscopy (ICP-MS), UV-visible absorption spectroscopy (UV-vis), and photoluminescence spectroscopy (PL). This way, various changes in the material characteristics can be monitored.

In order to place this work into an appropriate context, Chapter 2 summarises the most important properties of the material CZTS, supplemented by Chapter 3, where the material's application in nanocrystal-based thin films for photovoltaic devices is discussed. The latter also includes a literature review in Section 3.3, highlighting some open questions and challenges relevant to this thesis. Details about the experimental methods used for the sample preparation as well as some background information are provided in Chapter 4. Subsequently, in Chapter 5, an overview of the measurement techniques used is given. The discussion of the experimental results in Chapter 6 is divided into five parts, each of which contains a conclusion of the respective findings. Section 6.1 compares the characteristics of nanoparticles from different synthesis batches in order to analyse the procedure's reproducibility. The main results are discussed in Sections 6.2 and 6.3 which deal with varying annealing temperatures and times of the annealing process respectively. Subsequently, a cross-sectional analysis in Section 6.4 compares the previous results with exemplary samples of CZTS on a molybdenum rear contact layer, mimicking a part of the device structure of a solar cell. Section 6.5 finally elaborates on sources of error within the experiments presented beforehand. A brief summary and an outlook are given in Chapter 7. Supplemental tables and figures are provided in the appendix.

2. Copper Zinc Tin Sulphide – CZTS

The material of interest, Cu_2ZnSnS_4 (CZTS), is a quaternary compound and hence relatively complex in its structure and its properties. This chapter intends to give a brief overview of these in order to provide background information for the research described in this thesis. Many of the material characteristics are interrelated which will be pointed out in the following.

2.1. Crystal Lattice

2.1.1. Kesterite and Stannite Structure

CZTS belongs to the adamantine compound family for which Pamplin [25] developed some empirical rules. Crystallographically, 'Adamantines' are derived from the diamond-type and the lonsdaleite-type structure, both of which are modifications of carbon having tetrahedral bonding to the four closest neighbours [5]. Elemental constituents common in this family such as Cu and Zn energetically favour tetrahedral coordination and tend to form sp^3 bonding [5]. They can not only occur in binary and ternary but also in quaternary materials. The latter include $A^{I}_2B^{II}C^{IV}X^{VI}_4$ compounds adopting kesterite- and stannite-type structure (both tetragonal crystal system, parent structure diamond) or wurtz-kesterite- and wurtz-stannite-type structure (monoclinic and orthorhombic superstructures of wurtzite respectively, parent structure lonsdaleite) [5]. CZTS in particular can occur in eskebornite, primitive mixed CuAu-like (PMCA), and sphalerite structure under certain conditions as well [26]; however, kesterite, stannite, and wurtzite are the most common forms. The latter is less stable in the bulk than in nanostructured material [15]. The names of the different structure types mentioned go back to naturally occurring minerals [26].

In terms of application in photovoltaics, kesterite is most favourable due to the optimum value of the band gap energy [21, 26]. Fortunately, first-principle calculations using the density functional formalism show that CZTS is most stable in the kesterite structure since it has a formation enthalpy of $\Delta H = -361.9\,\mathrm{kJ/mol}$ being slightly smaller than that of the stannite variant and significantly smaller than that of the wurtzite variant [27]. This is why the wurtzite variant is not considered in detail here. However, it is interesting to note that CZTS thin films made of wurtzite-structured nanoparticles can adopt kesterite structure upon annealing [28]. The different structures are distinct from one another by the cation

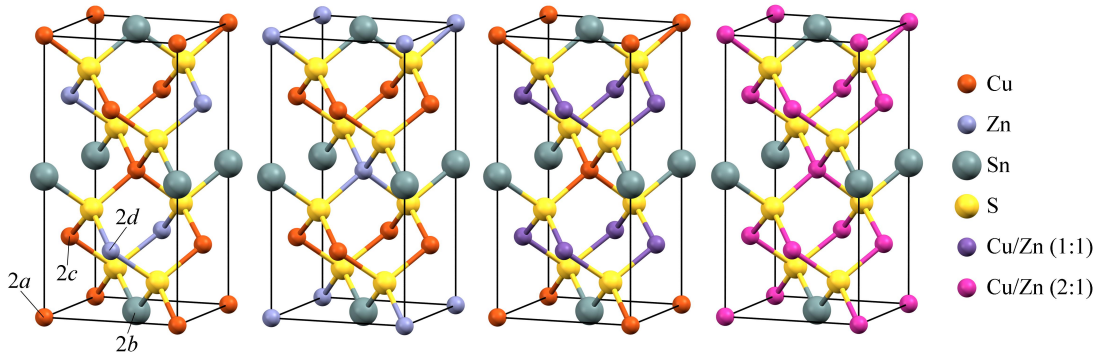

Fig. 2.1: Kesterite, stannite, half-disordered kesterite, and fully disordered kesterite crystal structure of CZTS. The Wyckoff positions in kesterite are 2a $(0, 0, 0)$, 2b $(1/2, 1/2, 0)$, 2c $(0, 1/2, 1/4)$, and 2d $(0, 1/2, 3/4)$. Adapted from [26].

positions (kesterite vs. stannite) and by the anion positions (kesterite/stannite vs. wurtzite) [15]. Concerning the two most relevant structures, cation layers of CuSn and CuZn alternate in the kesterite CZTS variant, whereas ZnSn and Cu_2 layers are stacked in the stannite variant. Sn is found at the same positions in both cases [5]. The S anions are located on the same lattice sites as well but only in the stannite structure they lie on a mirror plane. The two structure types therefore have different space groups: Kesterite belongs to $I\bar{4}$ and stannite to $I\bar{4}2m$ [5]. The lattice parameters of CZTS in the tetragonal crystal system are $a = 5.427\,\text{Å}$ and $c = 10.871\,\text{Å}$ so that the c/a ratio is close to two [5, 29].

The most important structure types of CZTS absorbers are shown in Figure 2.1, namely kesterite and stannite as well as two variations of disordered kesterite. The latter refers to ill-defined lattice occupancy by randomly mixed Cu and Zn cations amongst their respective positions in the crystal structure. This can occur at various degrees. High levels of disorder are assumed to be present in most samples of CZTS used for experimental studies reported in the literature [30]. Among others, cation disorder or Cu-Zn disorder influences the phase transition mechanism and is related to the chemical composition, including its variation on a nanoscale, as well as to the presence of defects and defect complexes [11, 16, 31].

2.1.2. Point Defects

Antisites, vacancies, and interstitials are point defects all of which can occur in CZTS but not with the same probabilities. This is strongly dependent on the chemical composition which determines the chemical potential and thereby the formation energies of the different defects [26]. As discussed further below, off-stoichiometric Cu-poor/Zn-rich CZTS was found to be beneficial to device

performance – even though this is commonly supposed to increase the probability of defects and secondary phase formation [5] where either of these is not usually desired. This is because defects can result in trap-assisted recombination, an important loss mechanism in photovoltaic devices [32]. The role of secondary phases is discussed in a subsequent section. For understanding why higher device efficiencies can be reached despite defect formation, it is relevant that two defects of opposite charge may form a defect complex if they are located close to each other. As compared to the isolated defects, lattice strain is relieved and the energy level is lowered since the charges compensate each other. This way passivated, the defects have a less detrimental effect on material performance since recombination is reduced [26, 33].

In stoichiometric CZTS, the dominant intrinsic defect is the Cu_{Zn} antisite (as the most stable defect in the entire stability range of CZTS [34]) and the most prevalent self-compensated donor-acceptor defect complex is $[{Cu_{Zn}}^{-} + {Zn_{Cu}}^{+}]^{0}$ as concluded from thermodynamic considerations [35]. The latter combination of defects is related to the most common type of disorder which in turn is seen as a decisive factor for device performance [26, 36, 37]. Under Cu-poor/Zn-rich conditions, the copper vacancy V_{Cu} is becoming more common whereas Cu_{Zn} is being suppressed. Nevertheless, related defect pairs are still prevalent, including those involving the antisite Zn_{Cu} particularly easily formed under these conditions, too [5, 33, 35]. In addition, Sn_{Zn} antisites are also suppressed which is beneficial since it is a deep-level donor defect that could act as recombination centre otherwise [7]. V_{Cu}, in contrast, is not very detrimental in terms of device performance since it has the shallowest defect level of all acceptors [26]. Under converse Cu-rich/Zn-poor conditions, Cu_{Zn} is dominant to V_{Cu} which reduces photovoltaic efficiency since the former is a deep acceptor level [35]. In addition, the formation of the Cu_{Sn} antisite is promoted which is considered harmful and is a probable reason for dissatisfying device performance in this region of the phase diagram [26]. This is due to potential Fermi-level pinning of this acceptor having a relatively large binding energy [7].

The considerations presented support the choice of a Cu-poor/Zn-rich composition as the optimum for application in solar cells as discussed further within the next section. Details on the above-mentioned and other defects in CZTS can, for instance, be found in the following references [7, 26, 34]. Further effects of point defects on the material properties are mentioned in the subsequent sections.

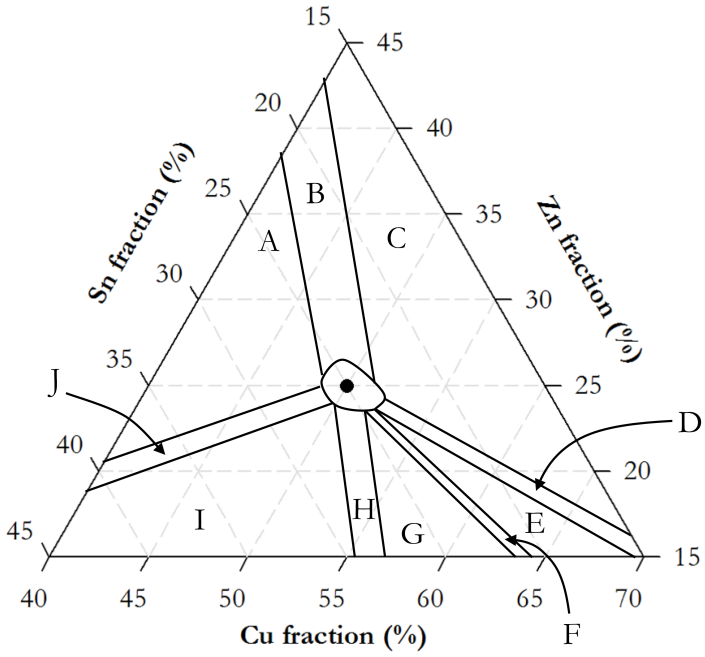

Phase regions:

A: $ZnS + Cu_2ZnSn_3S_8$

B: ZnS

C: $ZnS + Cu_2S$

D: Cu_2S

E: $Cu_2S + Cu_4SnS_4$

F: Cu_4SnS_4

G: $Cu_4SnS_4 + Cu_2SnS_3$

H: Cu_2SnS_3

I: $Cu_2ZnSn_3S_8 + Cu_2SnS_3$

J: $Cu_2ZnSn_3S_8$

(Cu_2ZnSnS_4 is expected in all)

Fig. 2.2: Quasi-ternary phase diagram of CZTS including secondary phases that are stable in the region in question alongside with CZTS. The dot in the centre indicates pure stoichiometric Cu_2ZnSnS_4 which is hardly achievable in sample preparation due to the narrow stability region. The sulphur amount is considered to be constant at the desired value. Other elemental concentrations are given in atomic percent. Illustration from [26].

2.2. Chemical Composition

2.2.1. Phase Diagram and Secondary Phases

The stability region of CZTS is restricted to a relatively narrow range of compositions. This can be seen from theoretical considerations of phase equilibria in the quasi-ternary system $Cu_2S - ZnS - SnS_2$ [38]. Even slight deviations from the stoichiometric composition with atomic ratios of $2:1:1:4$ ($Cu:Zn:Sn:S$) are expected to lead to defect formation being related to disorder phenomena as discussed before and to partial decomposition of CZTS into secondary phases which adopt different crystal structures [39]. The latter is also visible in the XRD spectra in Figure 5.3 (p. 48) discussed later. Notwithstanding those tendencies, optimum performance of the resulting solar cells was found for off-stoichiometric CZTS with a Cu-poor/Zn-rich composition [7, 35, 40], having cation ratios of $Cu/(Zn+Sn) \approx 0.85$ and $Zn/Sn = 1.1 - 1.3$ at best [41]. Different ways of representing the composition (cation ratios, empirical formulas, and amount of the elements in atomic as well as in weight percent) are compared for stoichiometric and Cu-poor/Zn-rich CZTS by way of example in Table A.1 (p. 148).

Secondary phases may be other binary or ternary compounds consisting of Cu, Zn, Sn, and S, but different from Cu_2ZnSnS_4, especially various sulphur compounds such as copper or zinc sulphides. Within an absorber layer, adjacent grains may have a different phase so that composition measurements will usually only provide an average value [26]. In general, non-uniformities in phase and secondary phases are considered detrimental to device performance, for example because recombination centres can be formed or the open-circuit voltage may be lowered due to a lower band gap energy of the secondary phase in question [26]. Nevertheless, some authors considered that the latter effect can sometimes be beneficial as in the case of Cu_2S [42]. Also, secondary phases with a similar structure to CZTS segregating at grain boundaries, for instance ZnS, can form heterointerfaces due to small lattice misfits and passivate the grain boundaries by lowering the recombination rate this way which can improve device efficiency [43].

Figure 2.2 provides a quasi-ternary phase diagram illustrating regions where specific secondary phases are stable beside CZTS which itself is expected in the entire compositional range shown. Good summaries of various characteristics of common secondary phases can for example be found in [26, p. 59] or [39, p. 54] and some of their most relevant effects are discussed further in subsequent sections. Under Cu-poor/Zn-rich conditions, ZnS is the most probable secondary phase to be formed [34]. It has been reported that ZnS can suppress other secondary phases and also detrimental defects [44]. It is important to note that annealing can induce significant changes in composition and secondary phases. Thermal processing itself will be discussed in more detail in Section 3.3.

2.2.2. Sodium Impurities

Aside from secondary phases, annealing may cause introduction of sodium (Na) impurities to the material by diffusion from the glass substrate into the absorber as also discussed in Section 3.3.5. This is similarly true for some other elements contained in soda lime glass such as potassium but their effect is less significant [26]. Sodium incorporation is generally deemed as beneficial [45–50]. For example, an improvement of several electronic properties is observed including an increase of the effective hole concentration and an enhanced hole mobility [46, 47].

Na atoms are incorporated into the crystal lattice by substituting the cations Cu, Zn, and Sn and thereby forming antisite defects. These are Na_{Cu}, Na_{Zn}, and Na_{Sn} being an isovalent dopant without specific effects, a shallow acceptor beneficially

contributing to conductivity, and a deep defect level able to act as a detrimental hole trap respectively [51]. The substitution of some cations by larger Na atoms may become apparent in an increasing average unit cell size [47]. Furthermore, related defect complexes including [Na_{Zn} + Zn_{Cu}] can form [51]. The impurities are suspected to accumulate particularly at surfaces and grain boundaries which are thereby passivated so that less non-radiative recombination occurs at the interfaces improving material performance [48, 52]. Finally, Na enhances desired grain growth during annealing [49, 53]. This is possibly related to its prevalence at grain boundaries.

Above a certain threshold, however, Na has some negative effects such as trapping of minority carriers being detrimental to device performance [54]. This has to be seen in relation to modified abundance of the above-mentioned defect types. In conclusion, there is a tradeoff between improvements of the crystallisation process and changes in the opto-electronic-properties [50]. The desired Na/(Cu+Zn+Sn) ratio is reported to be up to 1 % for an improved crystallinity, higher electrical conductivity, and the enhancement of grain growth [55]. Other than sodium diffusion, external doping with Na has been successfully performed as well [53].

2.3. Opto-electronic Properties

2.3.1. Band Structure

The band gap energy of kesterite CZTS as estimated by theoretical methods is $E_g = 1.56\,\text{eV}$ (relatively similar to 1.42 eV for stannite CZTS), being in agreement with experimental results lying in a range of $1.4 - 1.6\,\text{eV}$ for kesterite CZTS [29]. These values are sufficiently close to the optimum band gap of 1.35 eV for harnessing the light irradiation of an average solar spectrum [56]. The band gap energy of CZTS varies with composition and is thereby tuneable [21]. For example, it decreases steeply with decreasing Sn/Cu ratio which is possibly related to changes in defect density [57]. In addition, a decreasing level of cation order in the kesterite structure results in a decrease of the band gap energy as well [58]. Another aspect to be kept in mind concerns secondary phases many of which have another band gap energy than CZTS and can hence distort the average value obtained by common methods. E_g values of some relevant compounds are included in Table 5.2 (p. 72).

As it can be seen from the band structure plot in Figure 2.3, CZTS has a direct band gap which is preferable for application in photovoltaics. Absorption does

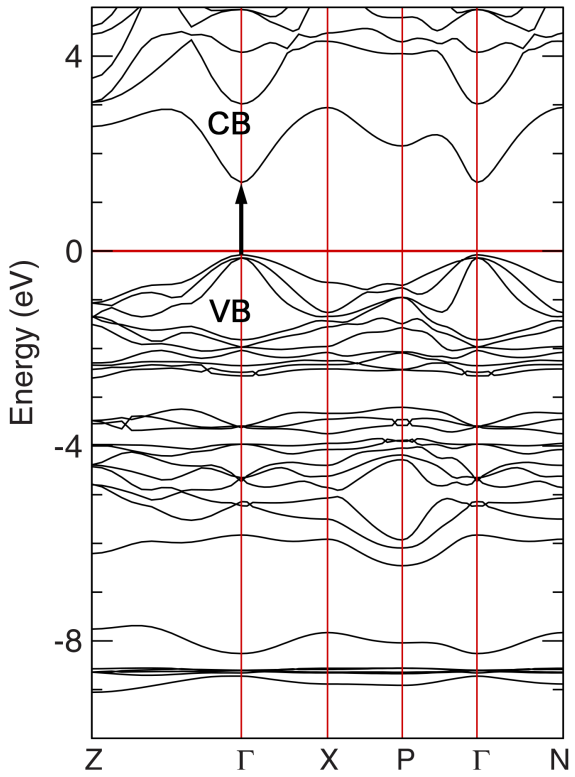

Fig. 2.3: The band structure of the direct band gap semiconductor CZTS in its kesterite structure is shown as predicted by density functional theory. The x-axis shows the symmetry points in k-space. The corresponding energy values are relative to the valence band maximum. The arrow in the Brillouin zone centre indicates a direct transition as induced by light absorption. Adapted from [59].

not require the involvement of phonons in this configuration which makes the material a strong absorber suitable for thin film devices [56]. The dispersion of the lowest conduction band (CB) and the uppermost valence bands (VB) in CZTS is relatively flat so that direct gaps at points away from Γ in reciprocal space are similar to that described before [29]. Further details on the general electronic structure can, for instance, be found in the following references [29, 59].

It should be mentioned that intrinsic defects can lead to potential fluctuations in the band structure [60, 61]. The associated band tailing may lead to band gap decrease [7]. However, band tailing in CZTS is controversially discussed. Some authors hold the view that electrostatic potential fluctuations rather than band gap fluctuations are responsible for tail states [62, 63], whereas others assume band gap fluctuations originating from nanoscale variations in chemical composition to account for them [64]. The relation of band tails to cation disorder (and the related defects) is seen critical [64, 65]. Nevertheless, disorder is also interrelated with nanoscale compositional inhomogeneities [31] so that open questions remain.

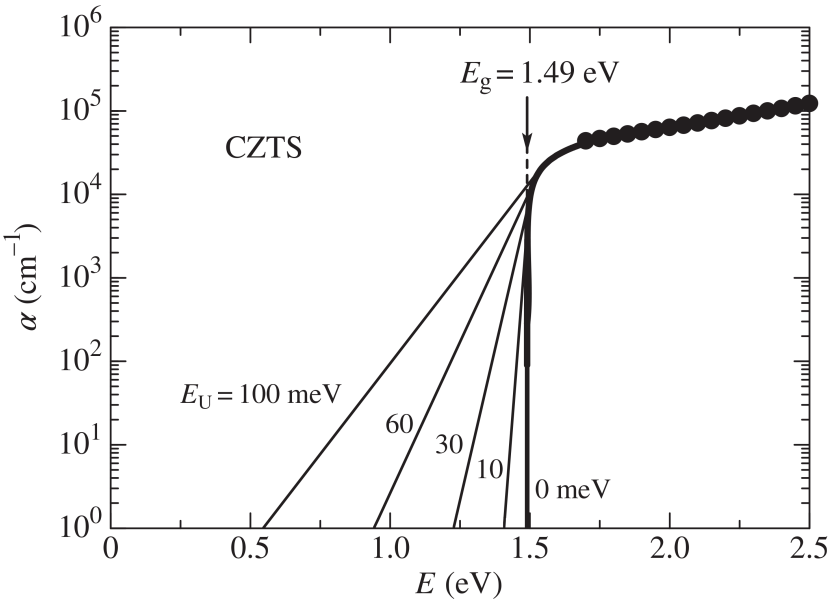

Fig. 2.4: Semilogarithmic plot of the optical absorption spectrum of CZTS showing the absorption edge at E_g. The continuous lines stand for the calculated behaviour, whereas experimental data is shown as dots. $E_U = 0$ represents the ideal case of a sharp absorption edge in the absence of band tailing, where no absorption is expected below E_g. This is different to the case of present tail states spread over certain energy ranges as specified by higher values of the Urbach parameter. Illustration from [66].

2.3.2. Absorption Characteristics

Without going into details of its derivation from the electronic band structure, the absorption spectrum of the absorption coefficient α versus the photon energy E_{Ph} is now briefly considered. It represents the linear optical response of CZTS through transitions from the VBs to the lowest CBs upon phonon absorption [29]. In the form of a semilogarithmic plot, the absorption edge at the band gap energy can be clearly seen as demonstrated in Figure 2.4. It is apparent that the absorption edge's steepness depends on the width of the absorption tail which can be described by the Urbach parameter E_U [66]. In a general sense, tail states in the band gap result from impurities, not only by forming bands of intermediate energy levels if they are present at high concentration but also by perturbation of the VB and CB edges via Coulomb interaction and the deformation potential [67]: Ionised donors attract conduction band electrons and repulse holes of the valence band (or the other way round for ionised acceptors) via Coulomb interaction. The deformation potential originates from the size difference between the original atom and the impurity atom and the resulting strain of compression or dilation in the lattice. Aspects of band tailing specific to CZTS were covered above already.

CZTS is a particularly good absorber in the spectral region of interest with an absorption coefficient α larger than $10^4\,\mathrm{cm}^{-1}$ as predicted theoretically and confirmed experimentally [29]. This fact makes it a suitable material for the application in solar cells, in the form of thin films in particular. The magnitude of the band gap, below which no absorption is expected in the absence of tail states, was discussed above already and it lies in the optimum range for photovoltaics, too. More detailed information on the optical properties including relevant electronic transitions can be found elsewhere [29, 59].

2.3.3. Carrier Transport

CZTS is a p-type semiconductor with an inherent acceptor density/carrier concentration of $p = 3.2 \times 10^{15}\,\mathrm{cm}^{-3} - 1 \times 10^{20}\,\mathrm{cm}^{-3}$ at room temperature, a minority carrier diffusion length of $L = 170\,\mathrm{nm} - 519\,\mathrm{nm}$, a minority carrier lifetime of $\tau = 1.7\,\mathrm{ns}$, and a minority carrier mobility of $\mu = 0.09\ ^{\mathrm{cm}^2}/_{\mathrm{Vs}} - 57.6\ ^{\mathrm{cm}^2}/_{\mathrm{Vs}}$ as cited in [26]. As discussed in Section 2.1.2, $Cu_{Zn}^{\ -}$ antisites (and $V_{Cu}^{\ -}$ under Cu-poor/Zn-rich conditions) are the dominant acceptor defects in CZTS. These are assumed to be responsible for the p-type conductivity in both, stoichiometric and Cu-poor/Zn-rich CZTS [33, 34, 68].

As it will be explained in Section 3.2.1, the operation of a solar cell is crucially dependent on effective charge separation of free carriers generated by the incident light. Interestingly, studies indicate that grain boundaries, which are otherwise often seen as detrimental recombination centres, actually provide a current pathway and enhance charge separation in their vicinity, leading to an improved collection of minority carriers (here electrons) [7, 69, 70]: Majority carriers (here holes) are trapped by defects or impurities at grain boundaries, causing an electric field to develop and the formation of a depletion region which in turn acts as an electrostatic potential barrier attractive to electrons and repulsive to holes [69]. This is related to the observation that in high-efficiency devices, downward band-bending at grain boundaries dominates, with the opposite behaviour in low-efficiency devices [70]. Altogether, these effects are suspected to contribute to the high efficiencies of kesterite-based solar cells [7, 69]. Still, some grain boundaries may have deep level traps impeding carrier transport so that grain boundaries remain a controversial topic in the context of polycrystalline kesterite solar cells [70]. This issue is further addressed in Section 3.3.1 dealing with thermal annealing and its purpose of grain growth enhancement where other aspects like electrical contact between individual nanoparticles play a role as well.

3. Photovoltaics with CZTS Nanocrystal Inks

The previous chapter gave a general overview of the material CZTS, the next one shifts the focus towards its application in photovoltaics. As the compound is used in the form of nanoparticles in the framework of this project, Section 3.1 covers some characteristics specific to these small crystals. Section 3.2 introduces the general idea of building a solar cell as well as the specific case of CZTS-based devices. A more detailed literature review of current challenges in solar cells made of CZTS nanocrystal inks is contained in Section 3.3. The chapter concludes with Section 3.4 briefly defining the aim of this study.

3.1. Nanocrystal Properties

Even though quantum confinement effects only occur for nanocrystals with diameters smaller than 3 nm in case of CZTS [71], small particles will always exhibit some distinct properties as compared to bulk material. These are addressed in the following. Quantum properties are not taken into consideration, as the particle sizes used in this project do not fall into the appropriate range.

3.1.1. Interparticle Heterogeneity

A certain distribution of sizes rather than a single one is usually expected to be obtained in the synthesis of nanocrystals. The particles may also cover a more or less narrow range of compositions and could have slight deviations in crystallinity. Some of these properties are related to each other, there is for instance a dependency between size and composition [72]. The reason for such observations could be a S rich particle surface among others [71]. For reproducible results and uniform films, monodisperse particles are generally more desirable; however, previous studies indicate that heterogeneities in size or composition may even have beneficial side effects [72]. It is in any case relevant for the interpretation of the measurements to keep in mind that distributions rather than singular values are present in reality. Most methods provide an average value of a certain characteristic property. This is a potential source for errors in the analysis.

3.1.2. Ligand Capping

Solution-based fabrication methods for nanocrystals mostly involve organic solvents in which molecular and elemental reactants are dissolved and brought to reaction

[73]. The capping ligands introduced into the reaction mixture help to control the growth process and influence size as well as shape of the resulting particles [6, 74]. On the one hand, the so synthesised particles covered with organic ligands or surfactants on their surface can easily be dispersed in other solvents to obtain a so-called 'ink', basically a colloidal suspension, which in turn can easily be deposited to thin films by a variety of methods. On the other hand, as discussed in more detail in Section 3.3.4, the residual carbon originating from these organics may also hamper charge transport through the films due to the insulating behaviour of the capping layer on the particles [6, 75]. A graphical representation of a ligand-capped particle is shown in Figure 3.1.

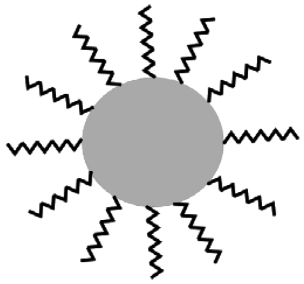

Fig. 3.1: 2D representation of a ligand-capped particle. Adapted from [6].

The specific effects depend on the particular type of ligands that vary with the synthesis protocol. Usually, long-chain organic ligands are used for the stabilisation. For CZTS in particular, the corresponding coordinating solvents are often oleic acid (OA), tri-n-octylphosphine (TOP), or oleylamine (OAm) [75]. The procedure followed in this study involving OAm is described in Section 4.1. In terms of ligand engineering, there is the possibility of performing a ligand exchange, where the organic ligands remaining from the synthesis procedure are replaced by shorter organic ligands or by inorganic ligands [6, 73]. Relatively easy is the replacement of amines with thiols [74], as it is done is this study as well. Also, annealing can lead to decomposition of the ligands [73]. The complete removal of the ligands, however, can potentially introduce surface defects on the particles being detrimental to the device performance [6]. Annealing involves similar risks of leaving behind uncontrolled charges, defects, and an unpassivated surface due to dangling bonds that might result in carrier traps [73]. The latter is due to the fact that unpassivated surfaces contain unsatisfied chemical bonds leading to defect levels, possibly deep in the band gap [74]. Nevertheless, careful annealing treatment that transforms the nanocrystalline films into densely packed, large-grained bulk material improves the conductivity and the tunneling rate between the crystallites [73], as also explained in Section 3.3.1.

Due to the large number of synthesis protocols available, results presented in academic literature can be difficult to be compared as the approach to sample preparation and the resulting ligands can heavily affect the properties investigated.

For instance, some of the issues observed in CZTS nanoparticle thin films concerning undesired layer formation occur in layers based on OAm capped particles, but do not seem to occur in those based on formamide capped particles [76]. Even though parameters such as the binding energies between the ligands and the (metal) atoms are not yet fully understood, it is known that, for example, very strong bonds are very effective in surface passivation, however, they might impair particle growth. Very weak bonds, in contrast, lead to uncontrolled growth kinetics and might cause worse solubility of the nanocrystals in the desired solvent [74]. Both head and tail of a surfactant molecule are essential for a good control of the interaction between the particle and the surrounding liquid, so that the nanocrystals do not aggregate but form a stable colloidal suspension [74]. Bulky ligands with longer tails might be less effective as compared to those with shorter ones because they cannot bind to the particle surfaces very densely [74]. Simplified models are often used in the description of capping agents. As an example, there are indications that the binding energies even depend on the specific facet of a nanoparticle, not only on the sort of atoms and molecules involved [74]. In order to properly understand all the relevant details and to govern the processes in a targeted way, nanoscale surface science needs to progress further, especially in case of curved or faceted particles [73].

3.2. CZTS-based Thin Film Solar Cells

In 1954, Chapin, Fuller, and Pearson developed the first solar cell which used a single bandgap silicon p-n junction [77]. A wide range of different materials and technologies is successfully applied in photovoltaics today, but these approaches still rely on the same principles. The following section gives a very brief, qualitative summary of the underlying physics.

3.2.1. Basic Principles of Photovoltaics

Fundamental for a conventional photovoltaic device are the properties of a p-n junction, i.e. the interface between a p-type and an n-type semiconductor [67], which has firstly been described by Shockley in 1949 [81]. Due to the initial difference in electrochemical potential or Fermi level E_F between these two regions, charge carriers are redistributed. Namely, electrons diffuse into the p-type side and holes into the n-type side, where they recombine [67]. Due to these so-called diffusion or recombination currents I^rec, a transition zone called depletion layer or space-charge region is formed and the Fermi levels are aligned. As a consequence,

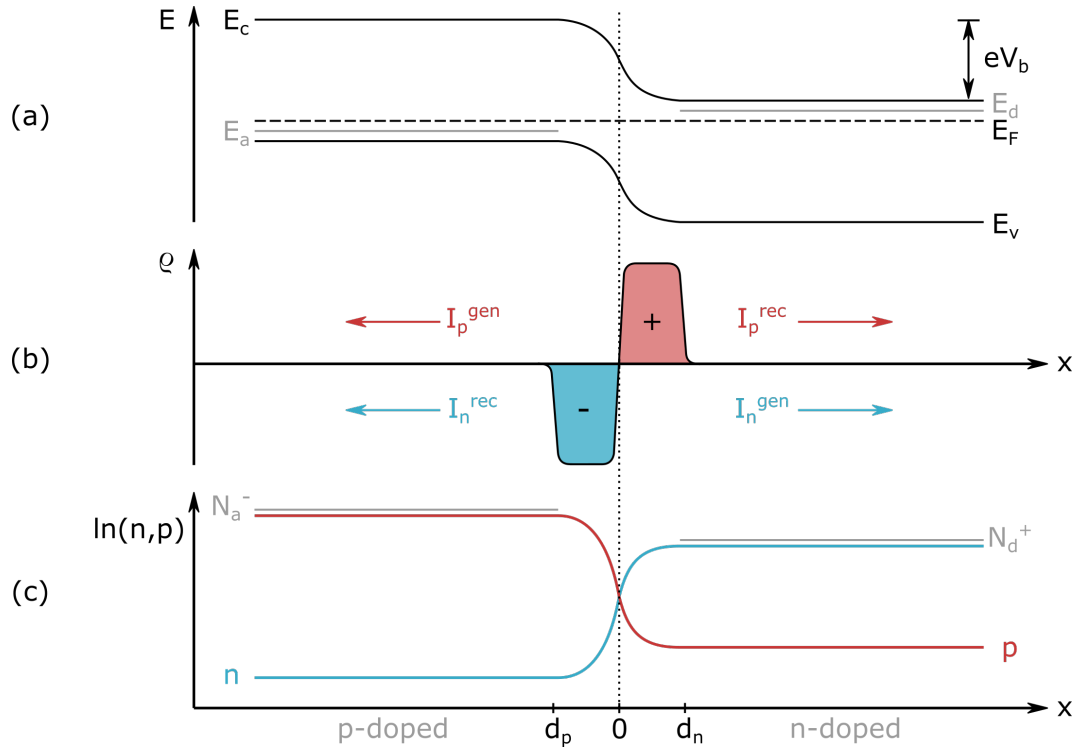

Fig. 3.2: Part (a) shows band bending of valence and conduction band at the interface between a p-type and an n-type semiconductor in equilibrium, where no external voltage is applied. E_a and E_d are the energy levels of acceptors and donors respectively, E_v is the valence band's top edge and E_c is the conduction band's bottom edge. The space charge ϱ as well as the flow of charge carriers from one side to the other are shown in (b). The related charge carrier densities of electrons (n) and holes (p) are plotted in part (c). N_a^- and N_d^+ symbolise the ionised acceptor and donor atoms. The boundaries of the depletion area are indicated by d_n and d_p. Figure initially used in [78], adapted from [79, 80].

the valence and conduction bands are bent. Furthermore, a potential difference known as the built-in voltage V_b emerges between the two junction sides due to the ionisation of donor and acceptor atoms. Another current arises as a result, the drift or generation current I^gen, which opposes the recombination current. These processes are illustrated in Figure 3.2 for the equilibrium case of compensated currents in the absence of a bias voltage.

The magnitude of the potential barrier as well as the width of the depletion area or junction thickness depend on the respective doping densities of the p-type and n-type regions. With the aid of the approximations of the Schottky model, which involves the assumption of completely ionised donors and acceptors as well as a sharp transition between the differently doped junction sides, the according equations connecting the space-charge density with the electric potential as a function of the distance x from the p-n interface can be solved. If an external

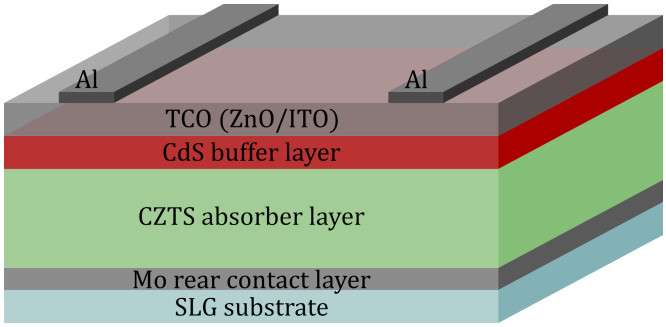

Fig. 3.3: Basic device structure of a CZTS-based solar cell, layer thicknesses not to scale. Based on illustrations from [8, 21].

voltage is applied, i.e. if the junction is not in equilibrium anymore, the potential difference across the junction as well as the transition area are altered. The charge stored in the depletion region is related to a differential capacitance, the so-called depletion capacitance. More details can be found, for example, in reference [67].

A solar cell has the purpose of absorbing photons and converting the corresponding energy into an electric current. Light incident on a material can excite electrons into higher energy levels if there are photons with an energy larger than the band gap energy of the semiconductor. Left behind are holes, so to say positive charge carriers. This process is known as the inner photoelectric effect. In order to generate a current, the electron-hole pairs have to be separated, which is possible by means of an interface such as a p-n junction. The built-in electric field discussed above accelerates the positive and negative carriers into opposite directions. As a consequence, a voltage known as the photovoltage can be measured across the junction [67]. This is the photovoltaic effect. A suitably designed device collects the carriers as efficiently as possible and thereby produces 'green' electrical energy.

3.2.2. Device Structure

As explained in the introduction, the material CZTS followed historically on CIS and likewise, the device structure of CZTS-based solar cells is the same as the one of CIS-based solar cells [21]. The basic layout is shown in Figure 3.3. A rear contact layer, usually made of molybdenum, is placed on top of a glass substrate. On top of it, the absorber layer of the inherently p-type CZTS is placed followed by a buffer/emitter layer of n-type cadmium sulphide (CdS) forming the p-n junction [8, 21, 26]. The former layer has thickness of around one micron suitable for efficient light absorption. The latter needs to be sufficiently thin so that the junction that separates electrons and holes is not more than one diffusion

length away from the surface where the incident photons with $h\nu \gg E_g$ generate the free carriers [67]. The use of two materials with different band gap energies extends the spectral regime exploited. For this purpose, the incident light enters the material of such a heterojunction with the larger E_g first [67]. The device is completed by a layer of a resistive/conductive transparent oxide which lets the incident light transmit, commonly aluminium doped zinc oxide (ZnO) or indium tin oxide (ITO), and aluminium grid contacts on top [8, 21, 26]. The top contacts serve to collect the charge carriers generated. In addition, a passivation layer between rear contact and absorber, a window layer between buffer and transparent conductive oxide (TCO), and an anti-reflection coating on the surface may be added. Also, alternative materials for parts of the cells have been studied in the academic literature but since no complete devices are analysed in this thesis, this brief overview is restricted to the standard device structure just presented. More information can, for example, be found in reference [26].

Current-voltage (I-V) curves are a very useful tool for studying the electrical response of a solar cell. In the absence of irradiation, it follows the ideal diode equation [19, 67]

$$I = I_s \left[\exp\left(\frac{eV}{k_B T}\right) - 1\right] . \tag{3.1}$$

The injection current I characterises the current flowing through the junction under forward bias V with a maximum of I_s, the saturation current. Under illumination, this equation requires some modifications and the I-V curve is shifted as described by the open circuit voltage V_{OC} and the short circuit current I_{SC}. The evaluation of device performance by these parameters as well as by the fill factor FF and by conversion efficiencies are for example described in [67, 77].

3.3. Absorber Layer Made of Ink

Guo et al. [23] were the first to report the synthesis of CZTS nanocrystals in 2009 and they concurrently demonstrated their use in nanocrystal inks for the deposition of solar cell absorber layers. Since then, much research has been published investigating the formation of the final films. It is worth mentioning that firstly, other semiconductor materials could principally be used in this nanocrystal approach for solar cells as well and secondly, two fundamentally different techniques of device fabrication can be chosen one of which uses the as-deposited nanocrystal films and another one where the thin film deposition is followed by high temperature annealing [6]. Arguments for CZTS as the material

of choice have been summarised in Chapter 1 already and have been discussed further in the subsequent sections. The following section not only illustrates why an annealing treatment is reasonable but also elaborates on the accompanying formation process of the final absorber layer as the corresponding changes in the material and film properties are a key subject of the thesis at hand.

To begin with, Section 3.3.1 introduces the procedure of thermal annealing with a focus on the atmosphere in the furnace. Corresponding literature is then reviewed specifically in the areas of grain growth mechanisms, resulting film morphology, and their dependence on the chosen annealing parameters in Section 3.3.2, together with considerations of the role of grain boundaries. Further parameters concerning the nanocrystals themselves and the ink, as well as residual carbon left over from the solvents used during nanoparticle synthesis and ink fabrication are discussed in Section 3.3.3 and 3.3.4 respectively. The relevance of the substrate material and potential layer formation at the interface between rear contact and CZTS absorber layer are covered in Section 3.3.5. Finally, Section 3.3.6 elaborates on the modification of the opto-electronic properties induced by the annealing process. In this way, the experiments performed within this study are put into the context of the current state of research in the field of CZTS nanocrystal thin films, allowing for later comment, comparison, and discussion of the results. In addition, a reasoning is provided for the choice of parameters to be investigated as well as for the method of sample preparation chosen including the type of substrate and the use of a sulphur-rich annealing atmosphere. The open challenges put forward in the literature and pointed out in this section finally lead to the aims and objectives of the research project presented in this thesis which are outlined in Section 3.4.

3.3.1. Thermal Annealing and Sulphurisation

The most successful application of CZTS in solar cell absorbers heretofore involved a fabrication step at elevated temperatures [6, 21]. This is due to the fact that carriers tend to recombine and scatter at the nanocrystal surfaces. Thermal annealing allows the nanocrystals to grow and to form large grains that significantly lower the surface-to-volume ratio. By reducing the amount of potential scattering and recombination centres, i.e. the total grain boundary area, the resulting short circuit current and especially the open circuit voltage can be enhanced which is seen as a major area for improvement of current CZTS solar cell efficiencies [5, 21, 82]. It cannot be denied, however, that other studies came to the contrary conclusion that grain boundaries would rather provide a flow channel for the

electrons and they could enhance charge separation [7, 69]. Nevertheless, voids between the nanocrystals are closed due to sintering and grain growth, leading to a polycrystalline film with improved electric conductivity. Large-grained films also exhibit a higher photocurrent as compared to fine-grained films [83]. These facts are supported by previous research on the already more advanced CIGS-based solar cells suggesting to take the annealing route instead of using the as-deposited nanocrystal thin films, since large grains in the micrometre range were found to be essential in order to produce highly efficient devices [21]. The work on CZTS presented in this thesis therefore specifically focuses on this high-temperature fabrication step that promotes grain growth.

The first important decision to make is the atmosphere to use during the annealing process. Leaving the furnace filled with air does not lead to satisfying results due to oxidisation of the film surface [84]. Other options can be categorised into the two groups of inert and reducing atmospheres respectively [84]. Nitrogen is a frequently used inert gas to prevent any reactions, sometimes also argon, whereas reducing atmospheres are obtained by adding sulphur. Annealing with a selenium-rich gas mixture is another alternative. However, commonly reported problems due to annealing are Sn loss and the occurrence of unwanted secondary phases [14]. It is known that CZTS starts to decompose at temperatures above 500 °C, but depending on the chosen gas environment, the detrimental effects can be limited [5]. In order to find the most appropriate gas environment, insights into the decomposition mechanism of CZTS are therefore essential.

Scragg et al. [13] presented a detailed study on the underlying process leading to decomposition and Sn loss, combining the proposition of two theoretical models and their subsequent validation by means of experiments. It should be mentioned that their samples had been prepared by co-sputtering of Cu : Sn and ZnS precursors. This is different to the nanocrystal ink approach followed in this work. Nevertheless, the processes studied by Scragg et al. should be transferable to a good extent as they are material-related. It becomes apparent that a two-stage decomposition model is more appropriate to explain the changes in phase and composition than a one-stage model would be, although it is still conceivable that even more steps are involved. The process is divided into the decomposition of CZTS into secondary phases followed by the evaporation of SnS. Another group showed that SnS losses in CZTS thin films can be reversed if S as well as SnS vapour is provided [85]. However, SnS annealing is not commonly done [13]. From their study, Scragg et al. concluded that S as well as SnS vapour would be necessary

to completely prevent the CZTS absorber from decomposing, but that also S vapour alone can slow down the decomposition process. Other experimental studies on solution-processed CZTS confirm that sulphur provided in form of a mixed N_2/H_2S atmosphere is able to prevent secondary phase formation effectively [86, 87]. Taken together, these findings strongly support the application of a so-called sulphurisation, sometimes also referred to as sulphidation [88], instead of annealing in a simple inert atmosphere.

As alternative to sulphurisation, also selenisation is commonly applied in annealing of CZTS films. The addition of selenium to the absorber slightly decreases the band gap [5]. Moreover, the grain size which is achievable by selenisation is significantly higher than that obtained from sulphurisation [21]. At this stage of research, the resulting performance of selenised films is hence superior to that of sulphurised films [21]. Two significant drawbacks, however, are the toxicity and relative scarcity of selenium in the Earth's crust, which is why it would be highly desirable to avoid its usage [16]. Due to these arguments, this study leaves aside selenisation and explores the absorber layer formation during sulphurisation instead.

Sulphurisation can be realised in different ways. In practical terms, either some solid sulphur can be placed inside the furnace tube which will then evaporate and saturate the gas inside, or a mixture of hydrogen sulphide (H_2S) and nitrogen or argon gas is used. For the experiments described here, the furnace is filled with a $H_2S : N_2$ atmosphere. Given that, the sulphur pressure is still a variable, although not investigated here, which can strongly influence the film development. Due to complex dependencies between this and other parameters including the target temperature and the time of the sulphurisation treatment, their effects on grain growth and the growth mechanisms are jointly discussed within the following section.

3.3.2. Grain Growth under Different Annealing Conditions

Initially neglecting the possibilities of a multiple-step heat treatment or varying ramp rates during the heating-up stage is likely to facilitate the understanding of fundamental processes. This lays the foundation of more complex annealing procedures for optimised device properties to be developed in future. The target temperature and the duration of the isothermal step are very important annealing parameters and, in the case of sulphurisation, the sulphur pressure is significant

as well. Several groups reported huge differences of the resulting grain sizes and growth mechanisms depending on the chosen annealing conditions as discussed in the following section. This is investigated further by the experiments presented in this work. The focus is thereby on the temperature and time dependency, whereas the sulphur supply in the annealing atmosphere is kept constant.

Grain growth or crystal growth means that the nanocrystals become larger in size and ideally form micron-sized grains and form a continuous polycrystalline layer. However, it has been frequently reported that the final films exhibit a bimodal size distribution with a fine-grained bottom layer and large grains of CZTS on top instead of being uniform throughout the entire absorber layer [22, 84, 88]. According to a terminology established by Chernomordik et al., the uniformly growing nanoparticles at the bottom undergo normal grain growth and form a 'floor layer', whereas the fast-growing and unusually large grains on the film surface are called abnormal grains [22, 88]. These terms are adopted here.

The above-mentioned study published by Chernomordik et al. [22] investigated the impact of varying temperature, time, and sulphur pressure during the annealing of CZTS nanocrystal films on their microstructure. Similar to the approach used in this work, that group used a hot-injection route for the nanocrystal synthesis. Although the nanocrystal ink was produced using another solvent, namely toluene, and the sulphurisation was realised by use of solid sulphur in the furnace instead of a H_2S gas mixture, the findings are transferable for the most part since the nanocrystal approach itself as well as the subsequent sulphurisation annealing are very similar. Two fundamental mechanisms, normal and abnormal grain growth were found to compete against each other, where the normal grains reach sizes of several hundred nanometres and abnormal CZTS grains up to ten microns [22]. Although large grains are generally desirable as pointed out before, abnormal grain growth can produce detrimental voids in the absorber layer that potentially short-circuit the electrical contacts. The occurrence of these voids was traced back to the fact that the material incorporated into the abnormal grains appears to diffuse along the grain boundaries and nanocrystal surfaces from the nanocrystal floor layer on top of which they grow [22]. Other studies on this and related chalcogenide systems reported cation diffusion to the film surface indeed [89]. Vapour transport was mentioned by Chernomordik et al. as another possible explanation for the migration of some of the elemental species and in particular, this mechanism could apply to tin in the form of SnS vapour [22]. This would be consistent with the study of Scragg et al. [13] discussed in the previous section.

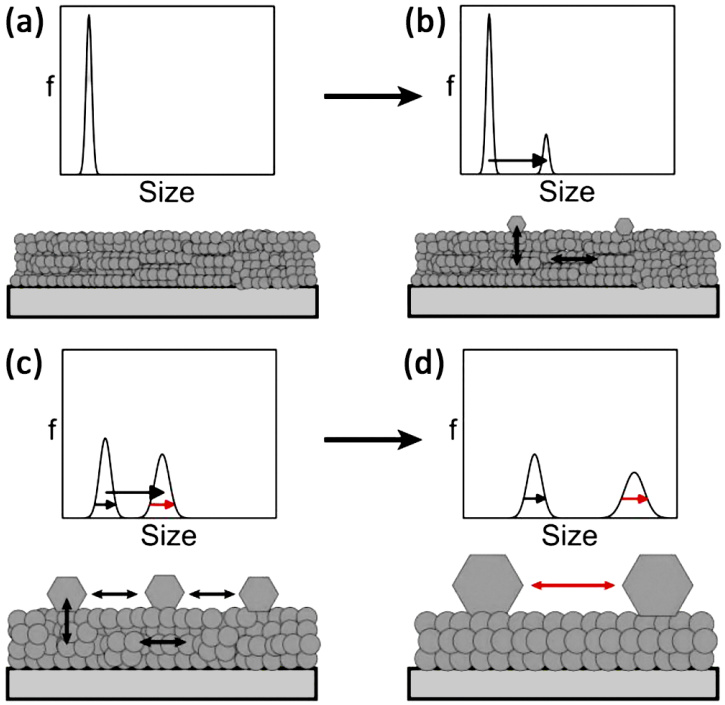

Fig. 3.4: Schematic of the grain growth model by Chernomordik et al. [22]. Starting from a layer of uniform nanoparticles (a), the size distribution f becomes bimodal as the annealing time is progressing. This is due to material transport towards the film surface and the nucleation of abnormal grains on top of the absorber layer (b). Continuing material transport from the bottom allows the abnormal grains to grow further. The normal grains in the floor layer increase in size as well, but to a lower extent. Larger grains start to consume material from the smaller ones so that the proportion of bigger crystallites increases (c). The final film consists of two layers of grains with different average crystallite size (d). Slightly adapted from [22].

Apart from the transport mechanism itself, however, finding out what determines the kinetics is also essential to improve control of the grain formation.

Chernomordik et al. identified the decrease of the total free energy as the driving force responsible for the non-uniform grain size development [22]. With proceeding annealing time, the nanocrystals grow which reduces their surface-to-volume ratio and is hence energetically favourable. Especially in case of abnormal grain growth, the initially very high normalised surface energy of the small particles is rapidly decreasing as they gain volume, which is the reason behind the occurrence of these grains that are significantly larger in size than the others. Nonetheless, the interfaces' contribution to the overall free energy of the film is in turn continuously being lowered, so that the driving force for abnormal grain growth is reduced, slowing down the growth rate as the time moves on. The density of abnormal grains as a function of time initially increases before reaching a maximum and

then falling again, which can be understood in a similar fashion [22]. In the first stage, the surface-to-volume ratio is still large allowing for a high material flux. The decrease in the second stage might be thermodynamically related to a decrease of the diffusion rate from the floor layer and to the relative decrease of available diffusion paths because the grains have become larger in size and the normalised surface area has been reduced. Larger abnormal grains start to consume material from the smaller ones resulting in a decreasing abnormal grain density. Their final size was found to be the larger the higher the temperature is [22], probably due to enhanced diffusion rates. This growth model is illustrated in Figure 3.4. Finally, it is also important to highlight that the normal and abnormal growth mechanisms are coupled. Abnormal grains occur, because their growth is associated with a reduction of the total energy due to the smaller surface-to-volume-ratio as explained above. When normal grain growth is accelerated, abnormal grain growth can be slowed down because the energy difference decreases and hence also the driving force is reduced [22].

The experiments of Chernomordik et al. additionally showed that an increase of the sulphur pressure induces a significant enhancement of the growth rates of either growth mechanisms and of the abnormal grain density [22]. This correlation has been validated by other studies [88]. Two explanations are proposed by Chernomordik et al. stating that the amount of sulphur vapour available is either leading to an enhancement of the thermodynamic driving force for grain growth or to an acceleration of the kinetics [22]. On the one hand, the sulphur vapour may enhance the removal of carbon, an issue that is discussed further in Section 3.3.4, through reaction into volatile compounds. On the other hand, solid diffusion of the growth-limiting species, identified as sulphur, may be accelerated. Not only could both of these mechanisms explain grain growth enhancement with increasing sulphur vapour pressure, also they would fit the observation of abnormal grains at the film surface, since this is where the sulphur concentration in the surrounding gas starts to reveal its impact first [22, 83]. However, the search for a conclusion which of the two proposed explanations does hold is being complicated by the fact that grain size and carbon concentration are linked to one another. The lower carbon concentration measured on the films annealed at higher sulphur pressure could either be the reason for the enhanced grain growth if its removal is facilitated by the sulphur vapour, or it could be a result of the enlarged absolute surface area of the grains, where most of the carbon residuals are expected [22, 88]. It is thus not completely clear which mechanism or which combination of effects causes the enhanced grain growth at higher sulphur pressures. The following two

sections are coming back to the interrelation between crystallite size and carbon content of the film by looking at these two properties separately.

3.3.3. Role of Nanoparticle and Ink Properties

There are some studies on the impact of other parameters not directly related to the annealing itself, such as the effect of nanocrystal size on the grain growth which has been investigated by Williams et al. [88]. Small nanocrystals (5 nm) led to films with micrometre-sized grains on top of film surface, i.e. abnormal grains. The larger nanocrystals (35 nm) in contrast developed a uniform grain size. This is a bit surprising, since Chernomordik et al. [22] used nanoparticles with a size of about 35 nm for their study discussed above as well, where they observed abnormal grain growth. However, this dissimilar behaviour could be due to slight differences in the parameter selection and the study design. Coming back to the investigations related to the nanocrystal size by Williams et al., a strong dependency was observed between nanocrystal size or, more precisely, their surface area and the carbon concentration [88]. Due to this relation it is unfortunately difficult to clearly distinguish between cause and effect as already mentioned above. One of the authors' conclusions is, however, that the rate of abnormal grain growth can be affected by the size even if the amount of carbon is similar [88]. Only when a certain threshold value of carbon concentration is exceeded, there is abnormal grain growth irrespective of the nanocrystal size – although the growth proceeds faster for the smaller nanocrystals in that case. The enhanced growth rate for smaller particles has been attributed to the larger total surface area of the crystallites implying a higher total surface energy, as well as to an increased diffusion rate along the grain boundaries [88]. In terms of the nanocrystal size there are, in conclusion, two fundamental effects: The large normal surface area of small particles allows for more ligands and therefore for a higher carbon concentration. In addition, fine-grained films have a larger free energy which drives grain growth [88]. Even though the initial particle size is not varied in the context of this study, the above-mentioned effects could also apply to the grains during their growth process.

Further parameters potentially relevant to grain growth are the absorber layer thickness and the solvent used for ink fabrication. Abnormal grains can reach sizes larger than the initial film thickness [22]. Also, it has been observed that the initial film thickness is slightly decreasing as a consequence of sintering and the material transport to the film surface, where the abnormal grains start to

grow [88]. It is therefore conceivable that layer thickness and cross-sectional morphology are interrelated. Although different solvents have been used for ink fabrication already, for example toluene or hexanethiol, it would be interesting to investigate specific characteristics such as the influence of the polarity of the solvent in order to understand the effect of this choice more clearly. The ligands on the nanoparticle surfaces certainly play a significant role in this context as well. Nevertheless, details of these questions are beyond the scope of this study. The carbon content of the film, which is not only related to the nanocrystal size as pointed out above but also to the solvent used, has already been studied by different groups as mentioned before and is discussed in the following section.

3.3.4. Residual Carbon

Carbon left over from organic solvents used for nanocrystal synthesis and for ink fabrication is a controversial topic as becomes apparent later in this section. The as-synthesised nanoparticles are usually coated with a layer of capping ligands as explained in Section 3.1.2, unless they are completely removed or replaced by other ligands via a suitable exchange procedure [6]. It is commonly thought that capping ligands would be detrimental to charge transport and can hence lower the device efficiency [6]. This is related to the fact that carbon as well as other solutes are known to pin grain boundaries and this way impede grain growth [22, 90, 91]. However, the complete removal of the capping ligands can also induce surface defects which serve as traps for charge carriers if the film is not completely transformed into a polycrystalline film [6]. In any case, it is worth investigating how the ligands respond to heat treatment. It is often reported that the initial carbon content decreases during annealing [22, 84]. There could be different explanations, namely evaporation, thermal decomposition, or a reaction with the sulphur vapour provided as summarised by Chernomordik et al. [22]. Different approaches to systematically investigate the effects of carbon on the absorber layer formation have been described in literature already; either the usually ligand-capped nanocrystal surface or the solvent used to redisperse the particles can be manipulated.

Engberg et al. [84] investigated the consequences of residual carbon by comparing ligand-free with ligand-coated nanoparticles as well as nanocrystal ink with dry powder. They observed only moderate grain growth for films made of nanocrystal inks with some grains appearing on top of the film surface, whereas annealing of nanoparticle powders, where no solvent was added for deposition, allowed for

micron-sized grains. Also, those films fabricated with ink were porous in contrast to those fabricated with powders. It is consequently advised to use less solvent for the deposition where possible [84], for example by use of highly concentrated nanoparticle ink. Ligand-free nanocrystals exhibited larger grains than ligand-coated ones [84]. All of these observations indicate that carbon residues might be detrimental. By means of thermogravimetric analysis and mass spectrometry, Engberg et al. could substantiate thermal decomposition of residual solvents during annealing. Specifically, oleylamine capping ligands disaggregated into smaller fragments above 270 °C. This also indicates that ligand decomposition starts below the boiling point of the solvent oleylamine at 364 °C, which was used as stabilising agent during particle synthesis in Engberg's study as well as in this work. In reducing atmosphere, in this case H_2 in Ar, the decomposition rate appeared to be slightly enhanced [84]. Engberg et al. mention that a mass loss has also been observed for those particles to be deemed as ligand-free which may relate to a small amount of amines unintentionally left over as suggested by mass spectroscopy data [84]. However, there are also other studies which argue that the weight loss of CZTS detected above 300 °C is not related to the thermal decomposition of organics remaining in the films [92]. Instead, sulphur evaporation is suspected to be partly responsible for the continuing decrease of mass [84]. Leaving aside this matter, the work by Engberg et al. suggests that capping ligands decompose during the high-temperature treatment in a step-wise manner and that less solvent as well as nanoparticles with fewer ligands are generally favourable in terms of large-grained and dense films [84].

Not only ligand-free and ligand-coated nanocrystals can be compared in order to analyse the effects of carbon residuals, but also the solvent can be used to precisely manipulate the carbon concentration in the films. Tiong et al. [83] compared various solvents with different carbon content per molecule while using the same nanoparticles and a sulphur-rich atmosphere. They found that the photoactivity tended to be the larger the smaller the carbon content was. Also, the rate of grain growth during the sulphurisation process increased with decreasing carbon content, which coincides with the findings of the study presented above. However, based on the observation that large grains formed preferably on the film surface, the authors assume that the sulphur vapour present during annealing can help to remove the residual carbon instead of mere thermal decomposition. Williams et al. [88] used another way to investigate the effect of the carbon concentration in the solvents. The as-synthesised particles have been treated with additional washing steps in order to remove ligands and decrease the carbon content or

different amounts of polystyrene have been added to the nanoparticle dispersion in order to increase it. This manipulation of the carbon content while keeping the sulphurisation atmosphere and the nanocrystal size constant allowed to conclude that a higher carbon concentration leads to a larger number of abnormal grains with a larger average size. The other way round, a complete turnaround towards normal grain growth is reached at sufficiently low carbon concentrations [88]. This is further supported by other experiments [76]. Too much carbon, however, slows down all grain growth [88]. Hence, the carbon content does not simply impede grain growth as suggested by the studies from Engberg et al. [84] and Tiong et al. [83], but can control the growth mechanism and also its driving force [88].

Williams et al. also concluded from their study that carbon plays a more complex role in the formation of the final absorber layer than commonly thought and that it may even have some side benefits since it aids rapid grain growth [88]. As mentioned in Section 3.3.3, they highlighted the interdependency between the nanocrystal size and the carbon content. Due to the fact that the surface-to-volume ratio increases with decreasing particle size, more carbon remains in the films when initially small nanocrystals are used. This is consistent with the considerations of Chernomordik et al. that the lowered carbon amount after annealing could not only indicate the removal of carbon, but could also be the result of the enhanced grain growth observed [22] as discussed in Section 3.3.2. This dependency between crystallite size and carbon concentration, as well as the control of the growth mechanism described in the previous paragraph both suggest a complex effect of carbon on the film development. Whereas less carbon seems to be better for uniform grain growth, large grains can be obtained in a relatively short time with a modest carbon content, which may be useful in the fabrication process.

More conclusions can be drawn from another well-known phenomenon within CZTS absorbers – a layer of small grains appearing at the interface between CZTS and the rear contact after sulphurisation or selenisation [93]. It is sometimes also referred to as nanocrystal floor layer [22] as described in Section 3.3.2. Its occurrence is generally undesirable since it is suspected to cause significant recombination losses [7], although it has been claimed by other authors that this small-grained layer in the vicinity of the rear contact has no negative impact on the chemical and electronic properties of the film [88, 94]. More important in this context is the possibility that it may come along with a higher carbon concentration [88]. That means that a bilayer structure resulting from carbon

segregation at the rear contact can be observed [89, 95, 96]. However, Williams et al. [88] noted that the carbon-rich, fine-grained interlayer is only formed during selenisation, not during sulphurisation annealing. This supports the assumption that the presence of sulphur vapour aids the carbon removal. Engberg et al. [84] pointed out that the fine grain layer between the back contact and the absorber layer seems to occur only in case that the latter one is composed of ligand-coated nanoparticles, since ligand-free particles do not show this behaviour. It is hence very likely that the organic residuals play a role in this layer formation with an increased carbon concentration in the vicinity of the rear contact indeed. This would be consistent with an improved removal of residual ligands due to the sulphur-rich environment considered before, because small-grained layers caused by a too high carbon content could be prevented by a sulphur-rich environment if it actually aids the removal. Assuming that, it would stand to reason that a lower sulphur concentration is required in case the starting carbon concentration is lower already. In their own study, Engberg et al. inferred the occurrence of thermal decomposition from annealing experiments without sulphur addition so that this theory seems to be valid as well. It is hence likely that the mechanisms of thermal decomposition of carbon and reaction with the sulphur vapour both contribute to the decrease of the carbon content during annealing. However, the interdependency between crystallite size and carbon concentration still imposes a problem in interpreting the results and needs to be taken into consideration for further investigations.

Although the carbon content is monitored in the experiments reported in this study as well, this is not the key subject. Notwithstanding this, the observation of layer formation broached above leads to the next important topic, i.e. interfacial features of the absorber layer, which is investigated in this work to some extent.

3.3.5. Interface between Absorber and Substrate

Apart from the bulk of the absorber layer, also the absorber layer surface and the interfaces with the substrate or rear contact layer and with the buffer layer are crucial for the resulting device performance [7, 13]. The most studied interface in CZTS-based devices so far is probably that to the rear contact layer, which is often made of molybdenum (Mo) as this material has also been used in the similar, but already more advanced CI(G)S-based solar cells [7]. Since the work described in this thesis does not focus on the fabrication of complete devices, the following section only elaborates on the choice of the substrate and the interface

between absorber and contact layers. The interface between absorber and buffer layer is discussed elsewhere [7, 63].

Firstly, it is notable that the chosen substrate can significantly influence the grain structure within the absorber layer even if it is covered by a rear contact layer. Chernomordik et al. [22] compared the substrate materials soda lime glass (SLG) and fused quartz, i.e. substrates with and without impurities, in the original form as well as covered by a Mo layer respectively. SLG is a commonly used type of glass which is also used as window glass, for bottles and similar objects and which is much cheaper than highly pure fused quartz glass. It is interesting to note that normal grain growth is enhanced by use of SLG, presumably due to the diffusion of sodium (Na) impurities into the layer of growing CZTS nanocrystals [22]. These results agree with the studies of Prabhakar et al. who investigated the effect of sodium diffusion by comparing SLG and Na free borosilicate glass as well as with the findings of Johnson et al. working on grain growth under the presence of alkali-metals such as sodium (Na) and potassium (K), both of which are contained in SLG [46, 49, 88]. Similar observations have been made with CI(G)S [22] but it is also worth to notice that additional Na beyond that supplied by the SLG substrate was not found to be advantageous and can even lower the performance [97]. Some more information on specific effects of Na impurities can be found in Section 2.2.2 but it remains to be seen by which particular mechanisms Na influences the dynamics of crystal growth such as the mobility of grain boundaries or material transport. Based on the evidence available, Chernomordik et al. concluded that impurities introduced by the substrate can reduce the temperature as well as the sulphur pressure needed to obtain a large-grained absorber due to the resulting grain growth enhancement [22].

Leaving aside the enhancement of grain growth, SLG may offer additional benefits as compared to impurity free substrate materials. Liu et al. [7] considered that the beneficial effect of sodium on the electrical properties might even be more significant than the effect on grain growth in terms of achieving higher device efficiencies. Specifically, Na can passivate grain boundaries leading to a reduction of non-radiative recombination processes [48]. The accumulation of Na at the grain boundaries has been verified and EBIC measurements (i.e. electron-beam-induced current) directly showed an improved carrier collection at these interfaces [50]. Sodium also increases the hole concentration [7, 46]. Overall, Na diffusing out of the substrate into the absorber layer can hence help to reach a higher open circuit voltage [7]. The improved electrical characteristics support the use of relatively

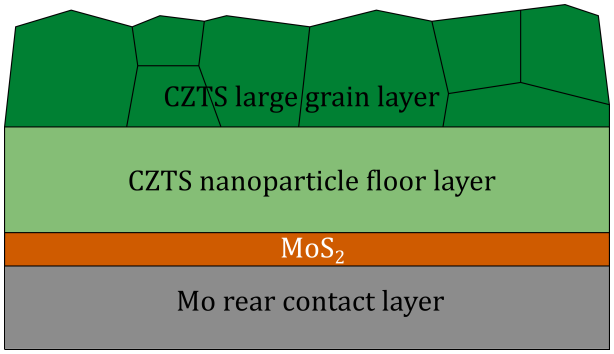

Fig. 3.5: A schematic illustration of a cross-section through a thin film of CZTS nanoparticles on top of a molybdenum layer is shown which has been annealed, leading to the formation of an intermediate layer of MoS_2.

low-cost SLG substrates in addition to the accelerated grain size development, so that it is used also within this work.

When adding a rear contact layer, usually made of molybdenum [7], between the absorber and the substrate as it is required for device fabrication, the film formation process is changed. This is briefly looked at in this study, too. Whereas the intermediate $MoSe_2$ layer at the back contact of CIGS devices can improve the performance [7, 98, 99], the corresponding phenomenon in CZTS devices lowers it [7, 63, 100]. In particular, CZTS(e) tends to decompose and to partly react with Mo forming $MoS(e)_2$ if the materials are jointly processed at high temperatures [101]. A schematic illustration of the resulting cross-sectional morphology can be found in Figure 3.5. The forming interlayer can cause losses in the open-circuit voltage V_{OC}, the short-circuit current I_{SC}, and the fill factor FF. Seo et al. [100] observed that the device performance is mainly determined by the MoS_2 layer if it is larger than 350 nm, rather than by the grain size as discussed earlier. Two main approaches to counteract the detrimental reaction of the layer components were proposed in literature, replacing Mo by another suitable rear contact material or using an intermediate layer in-between CZTS and Mo [101].

Indeed, several studies on alternative contact materials and barrier layers have been done on CIGS as well as CZTS already, details of which were reviewed elsewhere [7]. Regarding CZTS, gold (Au) and tungsten (W) seem to be particularly suitable for the rear contact layer. However, Mo is still the superior material with respect to the resulting device performance [7], which is why it is also used here. Moreover, various materials have been tried out to serve as a barrier between Mo and CZTS [7]. Due to the fact that carbon seems to be important for the morphology of the films as mentioned above, the option of an intermediate carbon layer is

a particularly interesting approach. There have been indications that carbon within the small grain layer, although itself detrimental, may at least improve its conductivity [102] and the positive effect of such a barrier on the device performance has been demonstrated indeed [103]. In this context, an additional effect of carbon on the MoS_2 layer should be mentioned in that the carbon content of the solvent influences the interlayer's thickness [83]. This again underlines the interplay between different parameters and observations, leading to the conclusion that the rear contact, as an essential part of a solar cell, as well as its interface with the absorber need to be investigated further.

3.3.6. Alteration of the Opto-electronic Properties

Apart from the morphology of the final film and other aspects such as residual carbon which have been discussed in the previous sections, the resulting opto-electronic properties are of high importance as the aimed application is in solar cells. However, there are not many truly systematic studies on the development of these characteristics during annealing and their dependency on the processing parameters chosen, especially with regard to the band gap energy. Proper understanding of the mechanisms is still limited [15]. In this context, it has to be taken into account that the opto-electronic properties are critically dependent on the chemical composition as it can be inferred from Section 2.3 in combination with Section 2.1.2 and they may be additionally affected by secondary phases discussed in section 2.2.1. Consequently, these characteristics cannot be investigated in isolation from one another which makes the analysis quite complex.

One particular study by Long et al. [14] reported a decrease of the band gap energy with increasing sulphurisation temperature. This result might be related to an alteration of the composition. A loss of Sn was observed, going along with an increase of the Zn/Sn and S/metal ratios as well as with a decrease of the Cu/(Zn+Sn) ratio. Indications of secondary phases were additionally found in the Raman spectra. The publication itself, however, does not pay much attention to the explanation of the significant changes in the band gap energy. The proposition that residual organics could be responsible for a higher band gap energy is not well supported by evidence. It also might be worth to mention that the authors observed a hole mobility in their samples which is different from that reported by other groups [14]. Unlike the samples made from nanocrystal inks used in the present work, the CZTS thin films of Long et al. had been prepared by the sol-gel method, where precursor solutions are annealed in a gas mixture of nitrogen and

H_2S. For that CZTS processing approach, the authors proposed 500 °C as the optimum temperature regarding the opto-electrical properties [14]. Using another technique of fabrication, however, might lead to another conclusion.

Mamedov et al. [42] studied the impact of secondary phases, in this case Cu_2S and SnS, on the optical properties in more detail by means of first principles calculations. According to their study, Cu_2S lowers the band gap energy of CZTS leading to an improved light absorption throughout the whole range of wavelengths from the spectrum of the incident solar radiation. SnS was found to change the optical properties as well, but since this does not apply to energies within the relevant range, the effect can be neglected. Nevertheless, this study suggests that secondary phases do not necessarily have a detrimental effect on the device performance as usually assumed. Secondary phases may form upon annealing, for example, Cu_2S above annealing temperatures of about 350 °C [42] which is why the effects of such compounds on the band gap energy, for instance, are relevant to the experiments presented in this thesis.

3.4. Aim of this Study

The preceding sections demonstrated that there is a huge scope for further investigations in different areas. This thesis focusses on the processing step of annealing. In particular, the choice of annealing temperature is investigated, supplemented by an analysis of varying durations of annealing for a constant temperature by way of example. Cross-sectional analysis is also briefly done but without looking at different annealing parameters. Since sample preparation is crucial for meaningful experiments, the reproducibility of the nanoparticle synthesis is looked upon as well. The strength of this study lies in the availability of a significant number of measurement methods allowing for the analysis of various material characteristics and for comparison of the results from complementary techniques. This improves understanding of the complex mechanisms and interdependencies broached before.

4. Sample Preparation

The samples used in this study are based on nanocrystals consisting of the material of interest, copper zinc tin sulphide. Sample preparation begins with the synthesis of these particles which is described in Section 4.1. In the context of solar cells, they are used to fabricate thin films which provide the absorber layer of the final device. The preparation of the glass substrates including the deposition of the molybdenum rear contact is covered in Section 4.2.1. How to fabricate a nanocrystal ink from the nanoparticle powder obtained by the synthesis described before is explained in Section 4.2.2, where also the spin-coating procedure is described. Subsequently, the samples are further processed by annealing in a furnace as explained in Section 4.3.

4.1. Nanocrystal Synthesis via Hot-injection Method

The nanocrystals used to fabricate the inks are synthesised based on a hot-injection method which has firstly been described by Guo et al. [23] in 2009. Slight adaptations have been made including the precursor ratios and the centrifuging procedure as indicated below.

The precursors used for copper (Cu), zinc (Zn), and tin (Sn) are copper(II) acetylacetonate (99.99 %), zinc acetylacetonate (99.995 %), and tin(IV) bis(acetylacetonate) dichloride (98 %), all of which are from the supplier Sigma-Aldrich and are in powder form. They are measured out according to the desired molar ratios. In this work as in a later study by Guo et al. [24], 1.332 mmol, 0.915 mmol, 0.75 mmol of the Cu, Zn, and Sn precursors have been used in order to synthesise Cu-poor/Zn-rich particles. This corresponds to 348.7 mg, 241.2 mg, and 290.9 mg respectively. It is worth to note that the molar ratio of the precursors does not exactly represent the molar ratio of the as-synthesised nanocrystals due to the fact that the precursors are not incorporated into the growing particles at the very same rates. Sulphur (S) is provided in elemental form and is added later on, separately from the other precursors. 4 mmol corresponding to 128.3 mg of S powder is weighed out and dissolved in 10 ml oleylamine ($C_{18}H_{35}NH_2$; from Aldrich, technical grade) in an ultrasonic bath. For the later injection, a glass syringe with a metal needle sealed by silicon tape is prepared.

Together with another 10 ml oleylamine, the stabilising agent which is commonly used [21], the respective amounts of the above-mentioned Cu, Zn, and Sn precursors

are added into a three-neck flask with a stirring bar in it. The flask is placed on a hot plate with a thermally conductive, hemispherical attachment. Two of the accessions are connected to a Schlenk line in order to allow for evacuation and for the addition of argon (Ar) gas. The remaining accession is closed with a rubber bung through which the test prod of a thermometer is put into the mixture to control the temperature. To minimise temperature fluctuations and to ease quick heating-up, the flask is covered with several layers of tin foil from the outside.

To start with, the three-neck flask is evacuated and the initially bluish or turquoise mixture is heated up to 130 °C. After having reached this temperature it is held for 30 min. Subsequently to this degassing step, the precursor solution is purged with Ar gas twice for 5 min respectively, using a small disposable needle pushed into the bung in order to compensate for the pressure. In between and after these steps, the flask is evacuated for 5 min respectively. After the third iteration of filling the flask with Ar, the purging is completed and the temperature is increased to 225 °C whilst the solution stays under a constant stream of the inert gas. This gas flow is kept up until the very end of the procedure. As soon as the injection temperature of 225 °C is reached, the S solution prepared beforehand is introduced to the flask with the aid of the syringe. Due to the sulphur addition, small particles immediately begin to nucleate. The reaction time during which the crystals grow is 30 min in this case, but could be varied in order to influence the resulting particle size. The colour of the mixture is changing to brown and later to black. The setup is symbolically shown in Figure 4.1.

After finishing all of the steps described above, the mixture is cooled down by taking the flask from the hot plate and by removing the tin foil mantle. In order to remove the oleylamine and to collect the synthesised nanoparticles this way, hexane and ethanol are added to the dispersion in 1 : 1 ratio, 25 ml each. The whole content of the three-neck flask is then divided into two tubules and centrifuged with 10 000 rpm (rounds/revolutions per minute) for 10 min. After cautiously and slowly decanting the supernatant, the precipitate in each of the tubules is re-dispersed in a mixture of hexane and isopropanol in 1 : 2 ratio, i.e. 10 ml of hexane and 20 ml of isopropanol, and then centrifuged another time with 8 000 rpm for 10 min. The last step is repeated once. This washing process as a whole is a combination of two slightly differing procedures used by Guo et al. [23, 24] as described below. Afterwards, the synthesised nanoparticles are remaining at the bottom of the tubules and are dried in a vacuum desiccator over night (with lids left loose). The accumulated particles are carefully ground with

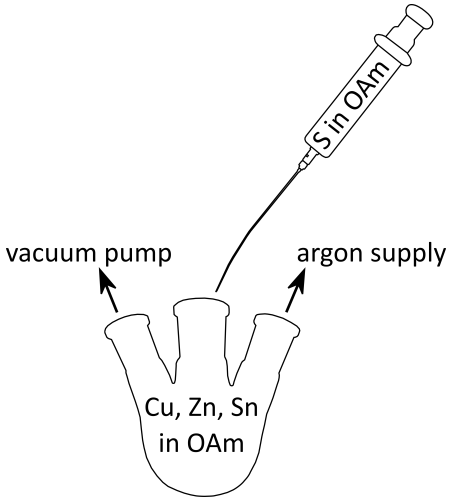

Fig. 4.1: The setup for the nanocrystal synthesis essentially consists of a three-neck flask which is connected to a Schlenk line to provide vacuum and argon gas (Ar) when needed. Initially, the reaction vessel contains only the precursors for copper (Cu), zinc (Zn), and tin (Sn) (for sake of simplicity indicated by the chemical symbols instead of the full precursor names) and oleylamine (OAm). Sulphur (S) is injected later on by use of a syringe. For this purpose, the elemental S powder is dissolved in OAm as well. Details of the procedure are provided in the main text.

mortar and pestle to finally obtain a fine powder of nanocrystals.

Typically, about 200 mg particles are produced during one synthesis as described above. The nanoparticle powder can then be used for the fabrication of a nanocrystal ink for thin film deposition which is described in Section 4.2.2. The synthesis parameters are kept constant throughout all of the experiments described in this work as the focus is on the variation of the annealing parameters. Section 6.1 comments on the reproducibility of the as-synthesised particles and their properties.

The procedure described above has been applied in the particle synthesis for the specimens used in the annealing experiments presented later on in this thesis. However, the original procedure involved another combination of chemicals for the washing step in the centrifuge, namely mixtures of toluene and isopropanol [23]. In that article, the so collected particles were re-dispersed in toluene to form an ink. This ink solvent was changed to hexanethiol in a later publication [24] in combination with alternative chemicals for the centrifuging procedure – ethanol, hexane, and isopropanol as adopted in the above described variant. Own laboratory work revealed that particles collected with toluene and isopropanol can be used for ink fabrication with hexanethiol as well, but that this procedure

frequently results in an ink that either is relatively grainy or that does not adhere properly to the glass surface. These observations during the thin film deposition could not be traced back to the cleaning procedure of the substrates, their surface roughness or any other causes such as the parameters of spin-coating.

Such problems did not occur with ethanol, hexane, and isopropanol used for the washing procedure. Also, re-centrifuging in the alternative set of chemicals can make those particles from a non-adhering ink usable. It is assumed that the centrifuging chemicals are crucial for the quality of the removal of residual oleylamine and/or for the surface ligands and hence the interaction of the particles with hexanethiol. A first observation is that the collection of the synthesised particles with these alternative centrifuging chemicals seem to be significantly more effective as a higher amount of particles is finally obtained. It should be noted that this could be related to a broader size distribution of the particles. Secondly, the hexanethiol-based ink produced from those nanocrystals is much more stable than ink made with toluene and no problems of adherence occurred. As a result, more uniform and more dense absorber layers could be reproducibly fabricated. The different combinations of centrifuging chemicals discussed have been tested by using constant speeds and times in the centrifuge according to the parameters from reference [23].

Although there are alternative routes to produce CZTS nanocrystals such as arrested precipitation [104], the advantage of hot-injection methods is that they are generally usable to obtain highly uniform particles of various compounds [105]. Also, there are more recipes for the hot-injection synthesis of CZTS particles apart from the one proposed by Guo et al., for example one by Riha et al. [106] with another stabilising agent for improved uniformity or one by Mirbagheri et al. [107] for ligand-free particles to mention only a few. In every case, the injection results in immediate and simultaneous nucleation of the particles abetted by a high level of supersaturation in the precursor solution [105]. This initial formation of nuclei is hence temporally separated from the subsequent growth process. As small particles tend to grow faster than larger ones in the diffusion-controlled growth mode, further size focusing takes place. Such high monodispersitivity can also be achieved by simpler heat-up methods, however these are more difficult to control [105]. Another advantage of synthesis by injection is the precise size control that it allows for. This has been explicitly demonstrated for CZTS nanocrystals [71].

4.2. Thin Film Deposition

4.2.1. Substrate Preparation and Sputtering of Rear Contact

The substrate of choice is soda lime glass (SLG) as it has been discussed in Section 3.3.5. Apart from the option to deposit thin films on the plain glass slides, a rear contact layer can be added beforehand as well. Most of the measurements presented in this study have been done on samples without such an intermediate layer between glass and absorber material. However, in order to study the interfacial structure of CZTS and the rear contact, also some molybdenum (Mo) coated substrates have been used.

In each case, the squared pieces of SLG glass with about 25 mm edge length have to be cleaned at first in order to eliminate any residual solvents or other surface contaminations originating from the fabrication process. This is done by a three-step washing procedure in an ultrasonic bath using acetone, methanol, and distilled water for 10 min each. Subsequently, the slides are blow-dried with a nitrogen gun and placed into a hot-air drying cupboard.

For those samples used for the interface study, a layer of molybdenum is then deposited onto the cleaned substrates by means of DC magnetron sputtering with an argon plasma. Sputtering belongs to the group of physical vapour deposition (PVD) techniques for thin film deposition [108]. The process takes place in a high vacuum chamber that also reduces any contamination to a minimum. During the actual deposition process, a typically inert sputtering gas such as argon is introduced. A direct current (DC) voltage is applied to a pure target of the material to be deposited, here Mo. In consequence, a plasma environment is created, in which argon ions set free Mo atoms from the surface of the target. In the specific case of magnetron sputtering, electromagnetic fields are used in addition in order to confine the plasma to the vicinity of the target which enhances the deposition rate. Molybdenum settles down on the surface of the substrates fixed above the target where it slowly builds up a layer, the thickness of which is controlled via the deposition time.

In this work, a home-built system was used. At a vacuum level of $10^{-6} - 10^{-7}$ Torr, a Mo layer with a thickness of about 600 nm is deposited. According to a deposition rate of about 1 $\text{Å}/\text{s}$, the required deposition time is 100 min. The DC voltage on the target is $280 - 380$ V and the current is $0.10 - 0.11$ A.

(a) Synthesis **(b)** NC ink **(c)** Thin film

Fig. 4.2: The fabrication process of the CZTS samples used in this study is shown schematically. It starts from nanocrystal synthesis via the hot-injection method (a). The nanocrystal powder is then re-dispersed in hexanethiol to obtain an ink (b), which is used for the thin film deposition on a SLG substrate by spin-coating (c). Subsequently, the sample may be annealed.

4.2.2. Ink Fabrication and Spin-coating

In order to fabricate thin films, the as-synthesised nanocrystals are re-dispersed in a solvent so that the dry powder becomes a so-called ink. In this study, the solvent chosen is hexanethiol [$CH_3(CH_2)_5SH$; from ACROS Organics, 96 %]. In the earliest attempts, toluene ($C_6H_5CH_3$) was used instead [23]. The dispersion is then thoroughly mixed in an ultrasonic bath for about one hour.

The ink is deposited on the substrates to obtain a thin film by means of spin coating. This is done at room temperature. A substrate is placed onto the rotating plate of the spin coater (WS-400 Lite Series Spin Processor from Laurell Technologies) where it is held by vacuum. In order to obtain a sufficiently thick absorber layer, about five consecutive deposition steps are necessary in this procedure, where the nanocrystal ink has a concentration of 200 $^{\mathrm{mg}}/_{\mathrm{ml}}$. In each step, 40 μl of ink are measured with a pipette and are then dropped centrally onto the substrate through a hole in the middle of the spin coater lid. To avoid premature surface drying, the spinning process is started immediately afterwards. The parameters chosen are a spinning speed of 1 000 rpm for 10 s with a ramp rate of 800 rpm. After each of these deposition steps, the sample is placed onto a hot plate with a temperature of 150 °C for 30 s and then transferred to another one with a temperature of 300 °C for another 30 s. This ‘soft-baking’ procedure for drying the layers has been adopted from Qu [109].

During the ongoing project it has been noted that even a well-adhering ink that produces a uniform and dense first layer might not lead to ideal final films of sufficient thickness. This is due to the fact that previously deposited layers might be (partly) removed again when more layers are added on top. Reason for this is an incomplete evaporation of the solvent during the intermediate drying step. It was found that the temperature is much more significant than the duration of

soft-baking. Interestingly, although the boiling point of hexanethiol is at around 150 °C, a significantly higher temperature of 300 °C is necessary. This might be a consequence of adhesion of the solvent to the nanoparticle surfaces. Initially, a blow dryer has been used instead of hot plates but this caused reduced uniformity of the drying process. Some parts of the previous layer being dryer than others can introduce non-uniform build-up of the film in the course of subsequent layer depositions. The procedure described before led to the best results.

Among the alternatives to spin-coating are methods such as dip-coating, spray-coating, slot-coating, die-coating, doctor blading, and roll-to-roll coating [6, 8], although some of these require flexible substrates. For industrial upscaling, printing techniques are of particular interest [8]. High-throughput and low cost are general benefits of solution-based processing. In order to study the film development during annealing, the deposition technique itself is not of major importance, but spin-coating provides a reproducible method for uniform films.

4.3. Annealing Procedure

Annealing is performed in a home-built furnace comprising the CTF 12/65/550 model from Carbolite Gero with a quartz tube to hold the samples. In the heating-up stage, the temperature is increased at a ramp rate of 10 $^{\circ C}/_{min}$ until the target temperature is reached. This is varied between 400 °C and 600 °C throughout this study (see Sec. 6.2). The annealing time refers to the duration of the fixed temperature stage and is chosen between 30 min and 3 h here (see Sec. 6.3). Finally, the furnace and the samples are cooled down to room temperature naturally over night, by switching off the heating power. The half-life period is about 3:15 h.

As mentioned earlier, the annealing atmosphere used is sulphur-rich. Specifically, gaseous hydrogen sulphide (H_2S) and nitrogen (N_2) are used in a 20:80 ratio. After inserting the samples into the furnace tube manually and sealing the end caps with silicon grease, the tube is evacuated and repeatedly flushed with pure nitrogen. After that, the gas mixture for the annealing procedure is introduced. The pressure is regulated in such a way that it does not exceed 75 Torr/10 kPa/0.1 atm in order to keep the setup airtight. Once the furnace is filled, the gas supply is closed and the heating process is started. After having finished annealing and leaving the furnace to cool down to about 280 °C (which is below the temperature of soft-baking), it is flushed with nitrogen. Any remainders of H_2S are thoroughly removed before finally venting the furnace and removing the samples.

5. Analysis Methods

The following chapter introduces the measurement techniques used in the context of this study. The as-synthesised nanoparticles as well as the resulting thin films (prior to and after the annealing step) are analysed with respect to opto-electronic properties, crystal structure, chemical composition, and morphological aspects. Through the combination of X-ray diffraction, Raman spectroscopy, SEM imaging, SEM-EDX analysis in conjunction with mass spectroscopy, UV-vis spectroscopy, and photoluminescence measurements, a comprehensive picture of the material properties can be developed. This is essential to allow for a proper understanding of such a complex compound as CZTS with many interrelations between individual parameters and properties.

5.1. X-ray Diffraction (XRD)

Diffraction experiments are a powerful tool to analyse the structural properties of crystalline materials. Single crystal analysis is more commonly used for this purpose, but also powder patterns, a method introduced by Debye and Scherrer in 1916, reveal a lot of information [110]. Particularly X-ray diffraction (XRD), which can be easily set up in nearly any laboratory, is widely used. An alternative would be the use of neutrons, which provides patterns of high information content. Instead of interacting with the electrons in the atoms as in case of X-rays, neutrons interact with the nucleus and exhibit weaker absorption. The latter approach is advantageous in case that close neighbours and isotopes have to be discriminated or light elements need to be detected. Neutron diffraction also has been used previously to analyse disordering phenomena in CZTS [11]. However, cation disorder is not studied in this thesis so that the resolution of common XRD spectra is sufficient for the purpose of structural analysis.

X-ray diffraction patterns can be described by Bragg's law [111]

$$2\,d \cdot \sin(\theta) \;=\; \mathrm{n} \cdot \lambda \qquad (\mathrm{n} \in \mathbb{N})\;. \tag{5.1}$$

The parameter d is the interplanar spacing, which depends on the crystal structure of the material investigated and on the set of lattice planes considered. θ is the diffraction angle (or 2θ the Bragg angle) and λ the wavelength of the light diffracted, where X-rays have a wavelength of the order of an ångström [110]. The natural number n indicates the order of diffraction.

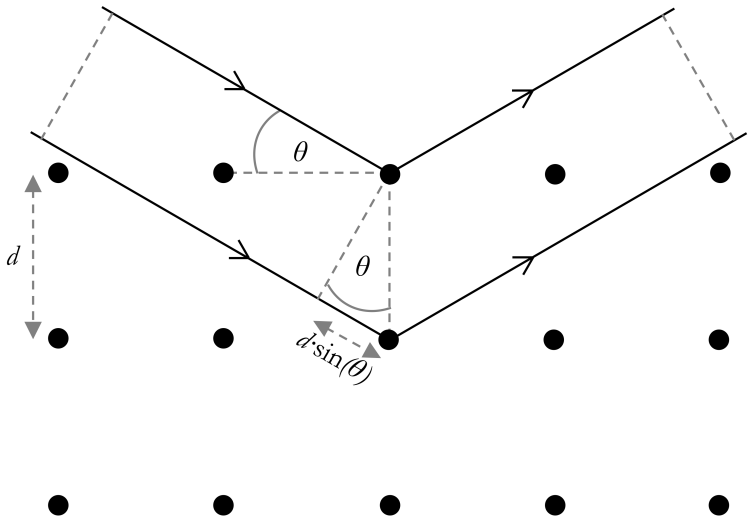

Fig. 5.1: Graphical representation of Bragg's law (Eq. 5.1). Waves that have a path difference of $2d \cdot \sin(\theta)$ after their diffraction at a lattice plane interfere constructively and lead to a diffraction peak. Otherwise they are extinguished. Here, the first order of diffraction is shown, but similar arguments hold for deeper lattice planes. Illustration from [26].

Bragg's law, as illustrated in Figure 5.1, provides a condition for constructive interference of radiation reflected at consecutive lattice planes. Nevertheless, even though it works for X-ray analysis to some extent indeed, this equation assumes reflection at the lattice planes just as it would happen with visible light at a mirror. In this simplified model, the reflections originating from the whole set of parallel crystal planes are assumed to interfere since they are all reflected into the same direction which results in the characteristic pattern. This way, the peak positions of a diffraction pattern can be predicted; however, in order to get information about the peak intensities, it is necessary to look at the elastic scattering process of the incident X-rays at the electrons of the atomic shells that actually takes place. These considerations are commonly undertaken in reciprocal space. In this case, the Bragg condition is represented via the Ewald construction and is mathematically expressed by the equivalent equation

$$| \vec{G_{\mathrm{hkl}}} | = | \vec{k} - \vec{k_0} | \tag{5.2}$$

with the reciprocal lattice vector $\vec{G_{\mathrm{hkl}}}$ and the wave vectors of incident and scattered beam k_0 and k respectively [110]. Again, this alone only takes into account the lattice function (i.e. the Bravais lattice or space group) describing the crystal structure analysed with other relevant terms still neglected.

Further contributions to the diffraction pattern originate from the potential

presence of more than one atom per basis and from the fact that the diffraction centres are not dot-like in reality. Firstly, a more than one-atomic basis changes the modulation function of the peaks, that means the relative intensities [110]. This is because the intensity, i.e. the squared amplitude of the total wave, depends on the phase shift if more than one wave contributes, scattered at atoms at different positions. In reciprocal space, this is described by the so-called structure factors which take into account the arrangement of atoms within the unit cell and can be represented by a Fourier series. Secondly, the reflections are broadened out to some extent due to the fact that the electron density has a certain spatial distribution around the position of the atomic core. This is taken into account via the atomic scattering factors or form factors that are part of the structure factor just discussed [110]. Another consequence is a general decrease of intensity towards higher scattering angles. In addition to these two contributions, thermal oscillations of the atoms described by the exponential Debye-Waller factor are taken into consideration for the total intensity as well. Overall, this quantum mechanical treatment of X-ray diffraction as outlined above is able to explain the peak positions as well as the intensities observed.

A powder sample ideally consists of randomly oriented crystallites so that all orientations are present, which has multiple effects. Most importantly, many more peaks are to be expected as compared to the diffraction pattern of a single crystal. In the latter case, the lattice is continuous and the orientation of the single crystal relative to the direction of the incident radiation determines which sets of lattice planes with their respective lattice spacings d fulfil the Bragg condition. The powder has millions of such crystallites which are not aligned and it is hence much more likely that the angle of the incoming beam fits one of these orientations causing a Bragg reflection. More precisely, these reflections are arranged in rings around the direction of the incident beam as visible in a 2D pattern [110]. As a consequence of the increased number of peaks, a powder pattern is more likely to contain overlaps [110]. This is complicated by the effect that the peak width increases with decreasing crystallite size. That relation is discussed in more detail in Section 5.1.2 along with the useful estimation of the domain size to be derived from it. A practical advantage of powder diffraction is that the randomly distributed crystallites do not have to be aligned as single crystals have to.

Laboratory X-ray diffractometers usually use sealed-tube sources which generate electromagnetic radiation by bombarding a metal target with high-energy electrons in a vacuum environment. The excited metal atoms emit X-rays whilst

returning into their ground state via a series of electronic transitions. Above a certain threshold, the continuum X-rays, also known as white radiation or 'Bremsstrahlung', discrete peaks appear in addition [110]. They result from the ejection of inner-shell electrons when their states are filled-up again by electrons from higher energy levels. These transitions are accompanied by the emission of photons with respective wavelength typical for the target material. These so-called characteristic X-rays are used as source radiation for the diffraction experiments. The wavelength typically chosen lies in the range of 0.1 - 5 Å and the most common target metals are copper (Cu) and molybdenum (Mo) [110]. It is important to note that these wavelengths are just of the order of magnitude of lattice spacings which is why their application in diffraction experiments is so useful. Apart from this, Cu in particular has the advantage of good thermal conduction, so that relatively high power can be used to increase the intensity of the incoming radiation [110]. Its emission spectrum is shown in Figure 5.2. The generated radiation undergoes additional steps through slits, mirrors, filters, single crystals, and other optical elements in order to obtain a focussed and monochromatic beam [110]. Finally hitting the sample, two main measurement geometries can be used, the reflection mode or the transmission mode. The spectrum of diffracted X-rays is then collected with a detector.

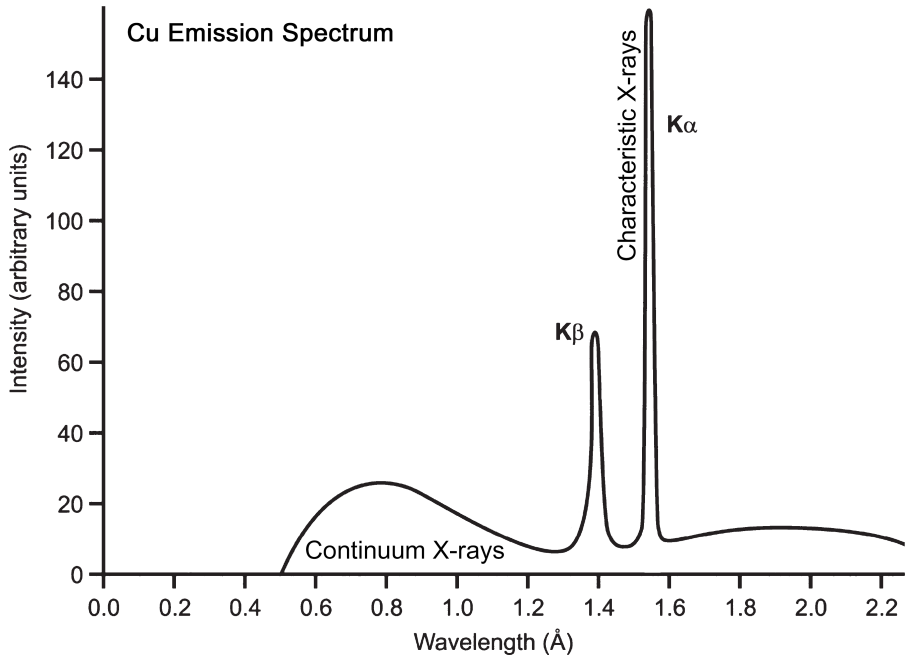

Fig. 5.2: Cu emission spectrum with the continuum and characteristic X-rays. The K_α line is commonly used as source radiation for XRD. Adapted from [110].

The XRD spectra within this study are measured with the commercial instrument D8 Advance from Bruker. It uses the Cu - K_α line ($\lambda = 1.5406\,\text{Å}$) and measures in reflection mode with a point detector. The sample remains at the same position throughout the whole measurement whilst the source and the detector are scanning the spectrum. The scans cover a range from 10° to 90° and are measured in 0.3 s to 0.9 s steps under continuous rotation of the sample to diminish any impact of inhomogeneities. The specimen of CZTS are either in the form of the as-synthesised nanocrystal powder on a flat-plate sample holder made of glass or in the form of thin films on SLG slides.

In the analysis of a measured diffraction pattern, peak identification and indexing, i.e. assignment of peaks to the respective Miller indices, is an important step. Often, some corrections have to be undertaken before, such as the removal of background signals. Indexing involves deducing the crystal geometry in three-dimensional reciprocal space from the one-dimensional pattern given and is hence a complex process of many steps. Full pattern analysis such as the Rietveld refinement developed in 1969 are powerful tools for a complete analysis of diffraction patterns measured [110]. Unlike in the analysis of individual Bragg reflections, overlapped or degenerate peaks cause less problems in the analysis and peak-broadening effects as well as background contributions of the sample and the set-up are taken into account. Via a least-square fitting approach including lattice parameters and atomic positions, the diffraction pattern is completely fitted and the crystal structure is solved in Rietveld refinement. However, this procedure requires detailed modelling of the crystal structure and is not pursued here.

In this case, the XRD measurements are used in a 'fingerprint approach' in order to compare the measured patterns with other spectra of CZTS from a database containing verified spectra from the academic literature. This allows to verify that the samples consist of the desired compound and provides the peak indices at the same time. For the X-ray diffraction patterns of CZTS and the most common secondary phases see Figure 5.3. However, it is important to note that XRD patterns are not sufficient for secondary phase identification in CZTS since the patterns of the kesterite and stannite crystal structures are far too similar [39]. Other compounds can only be identified by careful analysis of all the minor peaks and this becomes increasingly difficult with decreasing contribution from these. This is the main reason for the additional application of Raman spectroscopy introduced in Section 5.2 which is much more sensitive in this regard. Further analysis of the XRD patterns beyond peak identification is done by fitting of

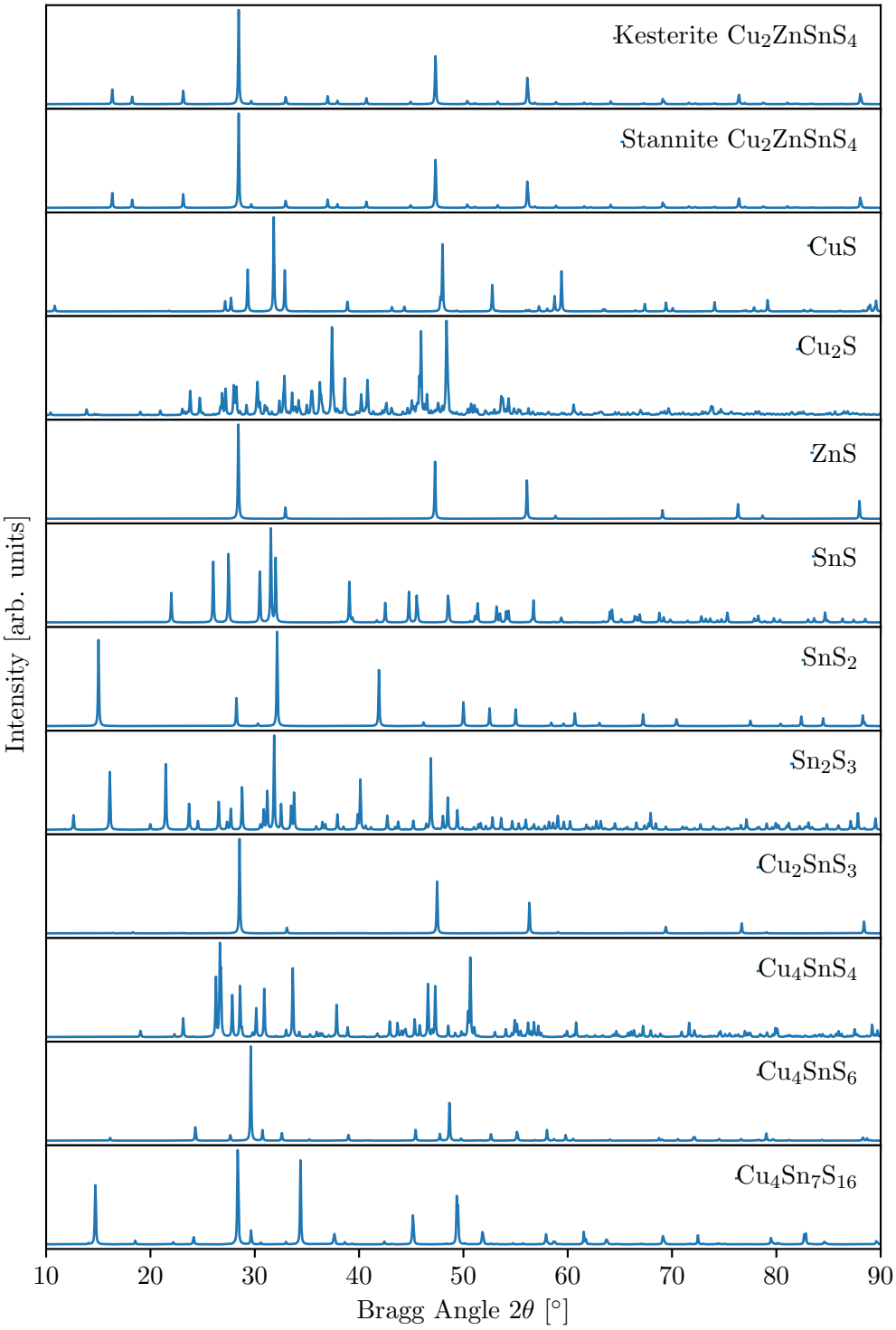

Fig. 5.3: The XRD spectra of CZTS as well as of related binary and ternary phases for a Cu-K_α X-ray source are shown. They have been obtained by use of corresponding CIF files for the different crystal structures from the Inorganic Crystal Structure Database (ICSD); the collection codes from top to bottom are 239683, 239684, 67581, 100333, 77090, 24376, 252197, 31995, 50965, 833, 88972, and 154696. Based on these, the diffraction patterns have been simulated with the freeware Mercury from the Cambridge Crystallographic Data Centre. It should be emphasised that the spectra for kesterite and stannite CZTS are nearly identical as it becomes apparent above. Similar illustration in [26].

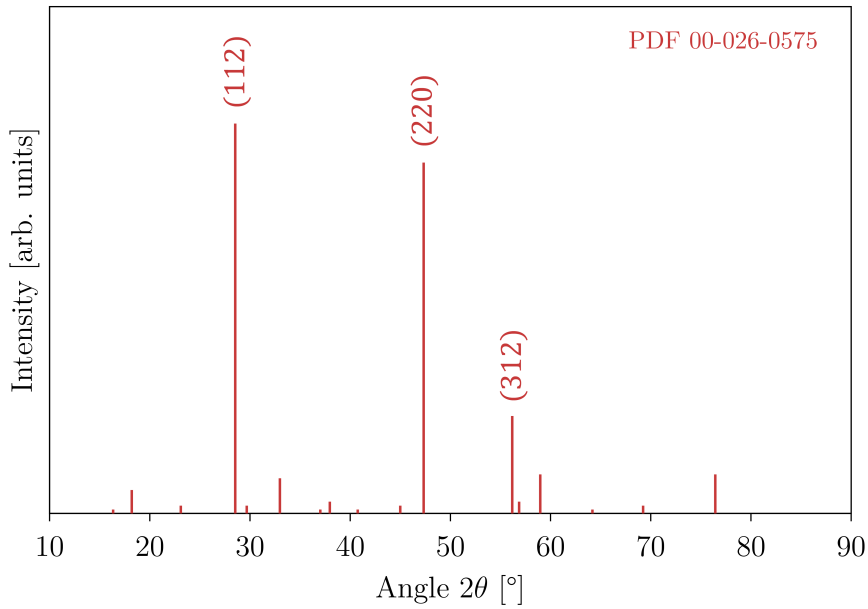

Fig. 5.4: A reference pattern from the ICDD database for kesterite Cu_2ZnSnS_4 frequently used in corresponding literature is shown (PDF 00-026-0575). The main peaks are (112) at 28.531°, (220) at 47.332°, and (312) at 56.178°. As the kesterite and stannite structures have nearly identical XRD patterns, the (220) peak is often marked with a second index (204) and the (312) peak with (116).

some individual peaks. Common functions used to model the peak shapes are Lorentzians, squared Lorentzians, Voigt curves, or related functions [110]. The fitting parameters can then be used for the determination of the lattice parameters and the domain size as described in the following two sections.

In this study, the evaluation of the XRD patterns is partly performed with DIFFRAC.EVA (V 4.2.1) with access to the database PLU 2015 of the International Centre for Diffraction Data (ICDD) to compare the spectra measured with reference patterns as mentioned before. An indexed reference pattern of kesterite CZTS (PDF 00-026-0575) is shown in Figure 5.4. The software EVA is also used to remove the background signal. Least square fitting of the main peaks is performed by use of MagicPlot and Lorentzian curves in order to obtain peak positions, widths, and intensities.

5.1.1. Calculation of the Lattice Parameters

The previous section has demonstrated that the features in an XRD pattern reflect the crystal lattice. For cubic crystal structures, there is a fairly easy way to calculate the sole lattice constant a from a diffraction pattern. However, in case of more complex ones such as the tetragonal lattice of kesterite or stannite CZTS,

where two lattice constants are present, a more sophisticated approach has to be pursued. The starting point is Bragg's law (Eq. 5.1). Rearrangement, considering the first diffraction order with n=1, leads to

$$d = \frac{\lambda}{2 \cdot \sin(\theta)} \,. \tag{5.3}$$

Using the Miller indices (h k l) for indicating the different crystal planes, another expression for the interplanar spacing d is obtained. In case of a tetragonal crystal structure with the lattice parameters a and c, it is [110]

$$d = d_{\mathrm{hkl}} = \left(\frac{\mathrm{h}^2 + \mathrm{k}^2}{a^2} + \frac{\mathrm{l}^2}{c^2} \right)^{-1/2} \,. \tag{5.4}$$

This expression can be equated with Formula 5.3, so that one obtains

$$\frac{\lambda}{2 \cdot \sin(\theta)} = \left(\frac{\mathrm{h}^2 + \mathrm{k}^2}{a^2} + \frac{\mathrm{l}^2}{c^2} \right)^{-1/2} \,. \tag{5.5}$$

For a given XRD spectrum, where the peaks have already been indexed, this formula can be used to calculate the lattice parameters a and c. The indices h, k, and l, as well as the peak position θ (or $2\,\theta$) are known. λ is the wavelength of the incident X-rays and is also known. Since Equation 5.5 has two unknowns, a and c, it is a minimisation problem that cannot be solved straightforward, but numerically. For this purpose, starting values for a and c close to the true parameters are chosen (in this case, they have been taken from literature on CZTS). The optimisation procedure is then carried out by an appropriate software package or program.

In this work, a script written in the programming language Python is used. The code is provided in Section B.1 in the appendix. For the analysis of the spectra, the three main peaks – (112), (220), and (312) – are analysed as described above. The respective results for a and c are then averaged.

5.1.2. Estimation of the Domain Size

In the framework of line profile analysis, XRD spectra can also be used to draw conclusions on the so-called domain size τ, which corresponds to the size of a single crystallite and is hence smaller or equal to the particle size. In order to do so, the diffraction peaks need to be analysed with respect to their shape, since the domain size is inversely dependent on the peak width. The sharpest

peaks arise from perfectly ordered single crystals. In finite crystallites, radiation with an incident angle slightly deviant from Bragg's condition will not result in completely destructive interference due to an insufficient number of scattering centres involved. The missing long-range order in a multicrystalline powder prevents perfect cancellation of the contributions from the different lattice planes in this way and the intensity peaks are broadened over a wider angular range as compared to a single crystal [110]. The smaller the crystallites, the more pronounced the effect of peak broadening will be.

The peak width can be quantified by the full width at half maximum (FWHM) and is symbolised by β in the following. The mathematical relation used is the Scherrer equation [110]

$$\tau = \frac{K\,\lambda}{\beta \cdot \cos(\theta)} \,, \tag{5.6}$$

where K is a dimensionless factor depending on the shape of the crystallites analysed and usually being in the range of 1. For the CZTS nanoparticles investigated here, $K = 0.9$ corresponding to the assumption of an approximately spherical shape was used as done by other authors working on the same material [110, 112, 113]. As above, λ is the wavelength of the incident X-rays and θ the Bragg angle of the respective peak. Features of a diffraction pattern represent an average over the whole sample. Accordingly, the domain size determined in the way presented above is sometimes also referred to as 'apparent domain size' or, more precisely, as 'volume-weighted mean size' [110].

Similar to the determination of the lattice parameters, the domain size is calculated by applying this procedure to all of the three main peaks and subsequent averaging of the results.

5.2. Raman Spectroscopy

Different from X-ray diffraction, Raman spectroscopy is based on inelastic scattering processes. The Raman effect has been theoretically predicted by Smekal in 1923 and then experimentally demonstrated by Raman in 1928 [114–116]. When a molecule absorbs a photon and is consequently brought into an excited state, it might not directly relax into the ground state by emission of a photon with unchanged frequency – even though this is most probable. This is the elastic Rayleigh scattering. Instead, the molecule might only relax into an intermediate energy level under emission of a photon with lower energy or frequency than the

incident photon. Another option is photon absorption by a molecule already being in an excited state so that the photon emitted during the return into the ground state has a higher energy or frequency than the incident photon [116]. If the photon frequency is changed in one of these ways the process is called Raman scattering and the difference in energy is compensated via phonons [117]. In case that a phonon is absorbed, radiation energy is gained leading to an anti-Stokes shift of the photon frequency towards higher frequencies; in case that a phonon is emitted, radiation energy is lost and the photon frequency is lowered or Stokes shifted. This terminology for the distinction of up- and down-shifted frequencies originates from Stokes rule of fluorescence [116]. The processes described follow the conservation rules of energy and momentum [117], which are

$$\omega_\mathrm{s} = \omega_\mathrm{i} \pm \Omega \tag{5.7}$$

and

$$\vec{q_\mathrm{s}} = \vec{q_\mathrm{i}} \pm \vec{K}. \tag{5.8}$$

Here, ω stands for the frequencies and $\vec{q}$ for the wave vectors of incident radiation (index i) and scattered radiation (index s) respectively. Ω and $\vec{K}$ are the frequency and the wave vector of the phonon involved in this inelastic scattering process [117]. The elastic and inelastic scattering processes mentioned are graphically illustrated in Figure 5.5. A Raman spectrum conventionally shows the measured intensities versus the Raman shift, i.e. the difference between incident and frequency-shifted light, which means that the frequencies have already been corrected for the wavelength of the excitation light or, put another way, the incident wavelength is taken as zero [118]. The peak positions correspond to the normal frequencies or eigenmodes of the material, in case of crystalline structures the lattice modes, and they do not depend on the excitation wavelength [118].

In contrast, the peak intensities do depend on the excitation wavelength, so that its choice can change the visibility of spectral features [118]. The resonance Raman effect is addressed below in particular. First, the general case is discussed. The experimental determination of scattering cross-sections of Raman bands is very difficult [118]; however, the intensity ratio of Stokes and anti-Stokes lines can be derived and it follows the relation [118]

$$\frac{I_\text{anti-Stokes}}{I_\text{Stokes}} = \left(\frac{\nu_0 + \nu_\mathrm{ab}}{\nu_0 - \nu_\mathrm{ab}}\right)^4 \mathrm{e}^{\nu_\mathrm{ab}/k_\mathrm{B}T}\,, \tag{5.9}$$

where ν_0 indicates the frequency of the incident radiation and ν_ab the frequency shift. Stokes shifts are more intense than anti-Stokes shifts. This is related to

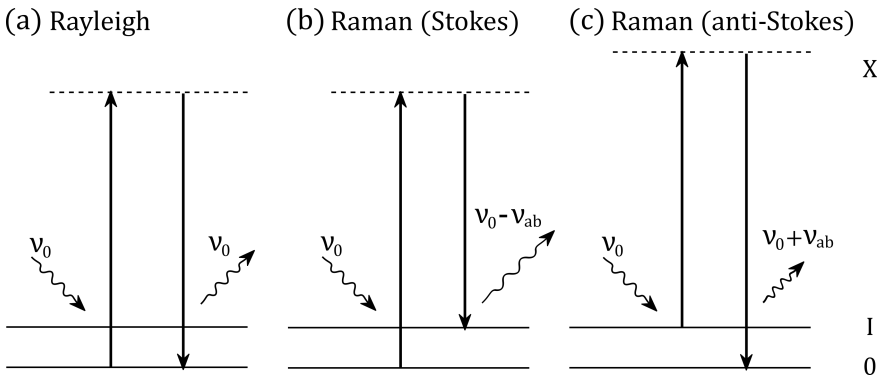

Fig. 5.5: Illustration of scattering processes, where 0 signifies the energetic ground state, I an intermediate energy level, and X the excited state. Elastic Rayleigh scattering: (a) A photon is absorbed and without any change of energy emitted again when the atom returns into the ground state. Inelastic Raman scattering: (b) Stokes shift, where a phonon is emitted after previous light absorption and the photon frequency hence lowered. The atom is left behind in an intermediate energy level. (c) Anti-Stokes shift that starts with an atom being in an intermediate energy level. A phonon is absorbed during the return into the energetic ground state and the photon frequency is hence increased. Adapted from [116].

the fact that most molecules are in the ground state rather than in excited states unless the temperature is relatively high as one can conclude from the Boltzmann distribution [116]. The difference in the intensities from Stokes and anti-Stokes lines increases with the vibrational frequency [116].

To fully describe Raman scattering, a more comprehensive theoretical description is necessary which is why line-shape analysis is less commonly done. A simplified classical picture can be used instead [117]. But although it provides a correct prediction of the existence of the effect itself as well as the dependence on the frequency of the exciting light, it is not suitable to explain why finally not all of the normal frequencies result in a Raman peak [118]. For the purpose of determining the spectroscopically active modes, a quantum mechanical approach would have to be chosen. Regardless of these considerations, also inactive normal modes do have an effect since they can, for example, lead to peak broadening in XRD spectra or contribute to the specific heat [118].

It is worth to mention that the analysis of normal modes is based on the assumption of perfect simple harmonic motion. However, although only weak in intensity, overtones or combinations of fundamental modes can be observed [118]. Apart from phonons, also free carriers and impurities may become apparent in the Raman spectra [117]. Collective oscillations of carriers or plasmons have characteristic

frequencies that vary with carrier concentration. In interaction with phonons, Raman-active coupled modes can occur [117]. In addition, charge carriers from impurity levels can be exited by so-called electronic Raman scattering, which is also dependent on the carrier concentration [117].

As compared to reflection, transmission, absorption, and Rayleigh scattering, Raman scattering is very weak [117] since only a small share of the incident light is scattered inelastically [118]. However, in case that the excitation wavelength is close to the fundamental gap of the semiconductor analysed, energy transfer to the crystal lattice is much more probable so that Raman scattering is significantly enhanced and relatively high peak intensities can be observed [117]. This situation is also known as resonant excitation or resonant Raman effect and can facilitate the detection of hidden features in the spectra, especially in the case that the spectra are overlaid by fluorescence.

The shape of the Raman band peaks is usually approximated by use of Gaussian or Lorentzian functions, both of which are symmetrical around the peak position [118]. They account for homogeneous and inhomogeneous broadening respectively. The full width at half maximum (FWHM) as a measure of the peak width can help to estimate the sample quality as inhomogeneities broaden the spectral features and as the intensity correlates with the degree of long-range order in the crystal [117]. Fitting a spectrum can be difficult when the peaks are less than their FWHM apart from one another. Also, it becomes apparent that the experimentally measured Raman peaks may not fit these functions at their wings as good as around their centre [118]. Here, a Lorentzian curve shape is chosen for fitting because it shows the best agreement with the peaks measured.

In the measurement of Raman modes, an excitation laser of suitable energy illuminates a small spot on the sample surface. The Raman scattered light is passing a monochromator and is then measured with a detector. In this case, not a single monochromator but a double monochromator containing two gratings is used in order to allow for sufficient dispersion of the spectrum to detect for the small Raman shifts and to prevent a distortion of the measurements by the undesired Rayleigh peak originating from the large, unshifted portion of the incoming radiation [117]. Also, a double monochromator holds back stray radiation from the exciting laser light more effectively. Nevertheless, fluorescence of the sample may be observed in Raman spectra in form of a smooth and continuous background signal [118].

For the measurements presented in this study, a Horiba JY LabRAM-HR Raman microscope in backscattering configuration is used. The acquisition time is 15 s and ten of these spectra are accumulated in order to eliminate any peaks originating from cosmic rays or other noise rather than from the sample itself. Two excitation wavelengths, 532 nm and 785 nm are chosen. About 1.5 mW and 2.5 mW of laser power arrive at the sample surface respectively. The estimated spot size is 15 - 20 µm.

5.2.1. Secondary Phase Identification in CZTS

In the context of this work, Raman spectroscopy is used in a fingerprint approach, where the measured spectra are compared to peak positions known from literature in order to identify secondary phases that may be present in the samples. The reference values used are listed in Table 5.1. As mentioned above, the laser wavelengths used include resonant excitation in order to promote the relevant modes. This allows at least for qualitative identification of unwanted phases that may be present in the samples in addition to Cu_2ZnSnS_4 [39]. An exemplary curve measured on a CZTS sample fitted with a series of Lorentzians is shown in Figure 5.6. It has been shown previously that Raman spectroscopy is clearly superior to other techniques in terms of secondary phase identification [39] and is hence the method of choice for the experiments presented later on.

5.3. Scanning Electron Microscopy (SEM)

In order to investigate nanoscale structures morphologically, the resolution of light microscopes is generally insufficient since it is limited by the wavelength of visible light. An electron's de Broglie wavelength is significantly smaller than that of visible light and this is why electron microscopes can be used for the analysis of much smaller structures [119]. Here, a scanning electron microscope (SEM) is used. An SEM can not only be used to analyse a specimen's morphology, but, among others, also for compositional analysis by energy-dispersive X-ray (EDX) analysis as discussed in Section 5.3.2. Further examples are cathodoluminescence (CL, which is similar to photoluminescence discussed in Section 5.6) and electron-beam-induced current (EBIC) both of which are not used in this study though. A special type of an SEM is one with an integrated focused ion beam (FIB) which can be used for the preparation of cross-sectional views, e.g. of a layered device.

The components of an electron microscope are placed inside a high vacuum system

Tab. 5.1: Raman peaks of CZTS and some of its secondary phases for phase analysis of the spectra measured. Table taken from [26, p. 139] and references therein.

Compound	**Raman modes [cm^{-1}]**
Cu_2ZnSnS_4	286, 300, 337 (A), 82, 84, 97, 98, 247, 248, 252, 264, 313, 319, 352, 373 (B), 67, 83, 141, 147, 160, 165, 255, 272, 293, 300, 347, 365 (E), 331 (disordered)
CuS	137, 265, 472
Cu_2S	475
ZnS	273, 276, 290, 352, 386, 422
SnS	96, 160, 190, 219, 288
SnS_2	215, 314
Sn_2S_3	52, 60, 71, 87, 183, 234, 251, 306
Cu_2SnS_3	290, 352
Cu_3SnS_4	318
Cu_4SnS_4	317
$Cu_4Sn_7S_{16}$	78, 94, 182, 192, 274, 305, 311, 350, 365, 466

with a beam column and a sample chamber. Emitted from an electron gun, most commonly a thermionic emitter which is particularly powerful, the electrons are focused into a fine beam. This is done by a double condenser lens system consisting of a condenser lens which is often associated with the spot size (because it is primarily changed by this lens) and another one which is commonly known as the objective lens and associated with the focus (although it also contributes to lowering the spot size a bit) [119]. Further components such as deflection coils are used to guide the beam vertically and in the optical axis of the microscope column. Furthermore, such coils are used to scan the beam over the sample surface, analysing one point at a time, in order to assemble them into a line scan or 2D image in the end [119]. This is where the name scanning electron microscope comes from. The distance between objective lens and sample surface is called the working distance and can be varied. Prior to a measurement, an alignment procedure with stationary spot has to be undertaken in order to tune the different components for an optimum result. The parameters of contrast and brightness are controlled electronically [119]. Where they hit the surface of the specimen, the incident electrons interact with the material in multiple ways. Different kinds of detectors are used to collect secondary electrons, backscattered electrons, X-rays, and so forth which are used for different purposes.

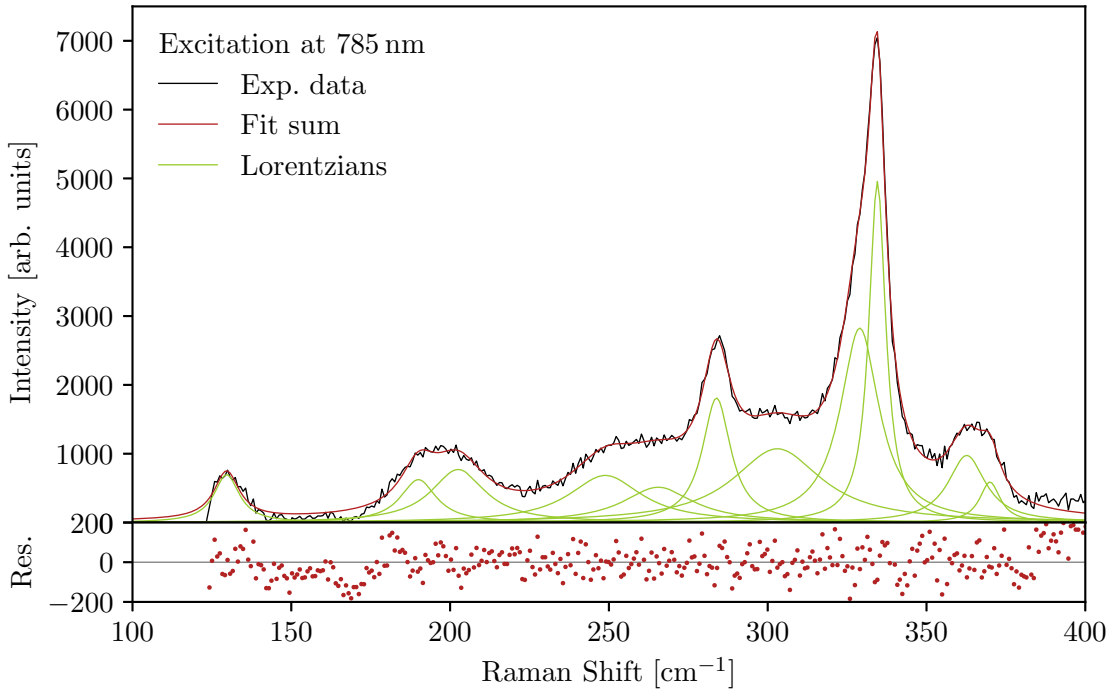

Fig. 5.6: An exemplary fit of a Raman spectrum with resonant excitation at 785 nm measured on an annealed CZTS thin film from nanocrystal ink is shown (see also Figure 6.15, p. 100). It has been corrected for background contributions by subtracting a straight line. The lower section of the graph shows the residuals. In this specific case, a peak at around 190 cm^{-1}, unexpected for CZTS, might for instance indicate the presence of the secondary phase SnS.

5.3.1. SEM Imaging

The electron-beam-specimen interactions can be classified into elastic and inelastic events [120]. Imaging is usually done with secondary electrons (SE), which are called so since they do not originate from the incident beam itself, but are ejected from the material under investigation via interaction of the incident high-energy electrons with the solid [120]. SEs result from inelastic scattering events where a small amount of energy (only a few eV) from the incident electrons is transferred to the atoms of the specimen. This can set free some of the loosely bound conduction electrons which mainly provide topographical information. This arises from the angular dependence of SE generation, whereas there is nearly no dependence on the atomic number of the material under investigation [120]. Different signal intensities at different spots on the sample surface create a monochrome picture with contrast similar to a usual photograph, just with a much higher spatial resolution.

In contrast to SEs as described above, backscattered electrons (BSE) come from

elastic scattering events, where electrons of the incident beam undergo a significant change in direction and hence exit the sample surface again. This happens to about 30 % of the electrons of the incoming beam [120]. BSEs have significantly higher energy than SEs and hence the information depth of BSEs appears to be about 100 times larger than that of SEs [120]. Other than that, the number of BSEs generated per unit area is much lower than that of SEs. In addition to topographic contrast, a backscattered image contains compositional information due to the atomic number contrast (or Z contrast/compositional contrast) [120]. Regions of different brightness in the resulting monochrome image indicate different atomic number and therefore different abundance of elements or phases. In particular, the higher the atomic number the more likely backscattering events become [120]. Apart from that, the fraction of incident electrons that is backscattered also depends on the angle of the incident beam with respect to the sample surface but hardly on the energy.

It has to be emphasised that, although one seems to obtain an image of the sample surface, the signal originates also from near-to-surface regions inside the specimen. This is related to the penetration depth of the electron beam which depends on the electron energy and on the type of signal investigated [119]. The electron energy is controlled via the accelerating voltage. On the one hand, lower voltages can limit charging effects of the sample surface if it is not sufficiently conductive and can thereby improve the image quality. Other precautions are described in Section 5.3.3. On the other hand, higher voltages improve the resolution obtainable. The optimum value lies in between and depends on the sample [119, 120].

Apart from optical limitations of the instrument due to diffraction and chromatic/spherical aberration, the resolution of the final image is mainly determined by the diameter of the beam hitting the specimen [119]. As mentioned above, the lens settings and the condenser lens in particular strongly influence the spot size, but also the working distance has a certain impact [119]. However, a smaller beam diameter or probe size also means a smaller beam current which can principally induce higher background noise and the optimum value depends on the magnification chosen as well as the other parameters [119]. Other limitations are imposed by the specimen itself. In case of backscattered electrons, it also has to be considered that they may exit the sample surface at a significant distance from the spot where the beam originally impinged on the specimen [120]. This leads to a loss in resolution as compared to secondary electrons which have a smaller interaction volume.

The SEM images presented in this study are made with a Hitachi SU-70 FEG SEM. Mostly, they are taken at an acceleration voltage of 12 kV. The condenser and objective lenses are set to the values 3 respectively and the working distance is chosen to be 9 mm. The magnification depends on the respective purpose of the image. In Section 6.4, also some cross-sectional views are presented which have been made by Mr Leon Bowen (Department of Physics, Durham University). They are prepared on a FEI Helios Nanolab 600 FIB microscope.

5.3.2. Energy-dispersive X-ray Spectroscopy (EDX)

Energy-dispersive X-ray spectroscopy (EDX or EDS) is a common technique used in combination with SEM, also referred to as SEM-EDX, and a powerful tool for determining the chemical composition of a sample with spatial resolution. This X-ray microanalysis is based on inelastic scattering events, where incident electrons with an energy higher than the ionisation energy are able to eject inner-shell electrons. The vacancy thus left behind is filled up by electrons from higher energy levels. During the decay of the ionised atom back into its ground state, characteristic X-rays following to the rule of energy conservation are emitted [120]. In contrast to the continuous spectrum of X-rays emitted due to a different process (also known as deceleration radiation or 'Bremsstrahlung'), the characteristic lines mentioned before can be used for compositional analysis since their energy depends on the distinctive energy differences between the atomic levels [120].

K, L, or M lines may be used for the purpose of element identification [120], where the capital letter indicates the destination shell of the corresponding radiative transition. Greek letters in the index show from which shell the electron relaxed, e.g. the K_α originates from the transition from the L to the K shell, whereas the K_β line originates from the transition from the M to the K shell. Further number sub-indices indicate the intensity, beginning with the strongest lines [120]. This line splitting is due to the division of shells into subshells with different probabilities of a transition.

Two different types of analysis can be distinguished; firstly, qualitative analysis which focuses on the identification of the elements present, and secondly, quantitative analysis where the actual concentration of elements is determined by looking at the intensity ratios of the peaks attributed to the different elements [120]. In either case, the instrument has to be operated under such conditions that give sufficient X-ray counts for a satisfying signal-to-noise-ratio. Also, the X-ray spectrometer

should be calibrated prior to measurement by use of a pure element standard, e.g. cobalt (Co), under identical conditions. Another important consideration, especially for quantitative analysis, concerns the spectral resolution of neighbouring peaks. If neighbouring peaks overlap too much, accurate determination of the composition is not possible because the intensity ratios might contain errors [120]. Remedy might be provided by choosing other line series of the elements of interest. Tables of the X-ray lines can for example be found in [120, p. 641 ff.].

In this study, EDX measurements are performed at an accelerating voltage of 12 kV. The condenser lens is set to 3 and the objective lens is set to 2. A working distance of 15 mm is chosen. X-ray microanalysis can either be performed on a spot or on a small area selection over which the signal is averaged to calculate the material's composition, or EDX mapping can be performed. For usual composition determination, measurements in this study are done at a magnification of 500 × with a dwell time of 35 µs and SEs as input signal. The results of three or four areas distributed over the sample surface are averaged, where each of these is additionally divided into 12 subareas. This procedure is particularly useful to look at inhomogeneities. As mentioned above, caution has to be taken in choosing the line series used for the element identification. As suggested by reference [14], the Cu_K and Zn_K lines are used instead of the lines of the L series, as well as Sn_L and S_K. Experiments in the context of this project have shown that the choice of the X-ray lines has a significant impact on the result indeed and the best choice of parameters has been established by comparison with ICP-MS measurements as discussed within Section 6.1.3. An exemplary EDX spectrum with the respective lines is shown in Figure 5.7. The microscope used is the same as that used for imaging, a Hitachi SU-70 FEG SEM, in combination with the X-Max^N 50 Silicon Drift Detector and the analysis software AZtec 3.2 from Oxford Instruments. At the beginning of each measurement session, a beam measurement with a cobalt (Co) standard is performed to assure proper calibration.

5.3.3. Sample Preparation

Nonconductive samples are prone to charging effects during SEM analysis. If the electric charge building up in consequence of the incident high-energy electrons cannot drain off, image distortion or even thermal and radiation damage can occur [120]. A commonly used approach to prevent this is to apply a conductive coating to the specimen in order to enhance the surface conductivity and to thereby inhibit the accumulation of electrostatic charge. This is often realised by vacuum

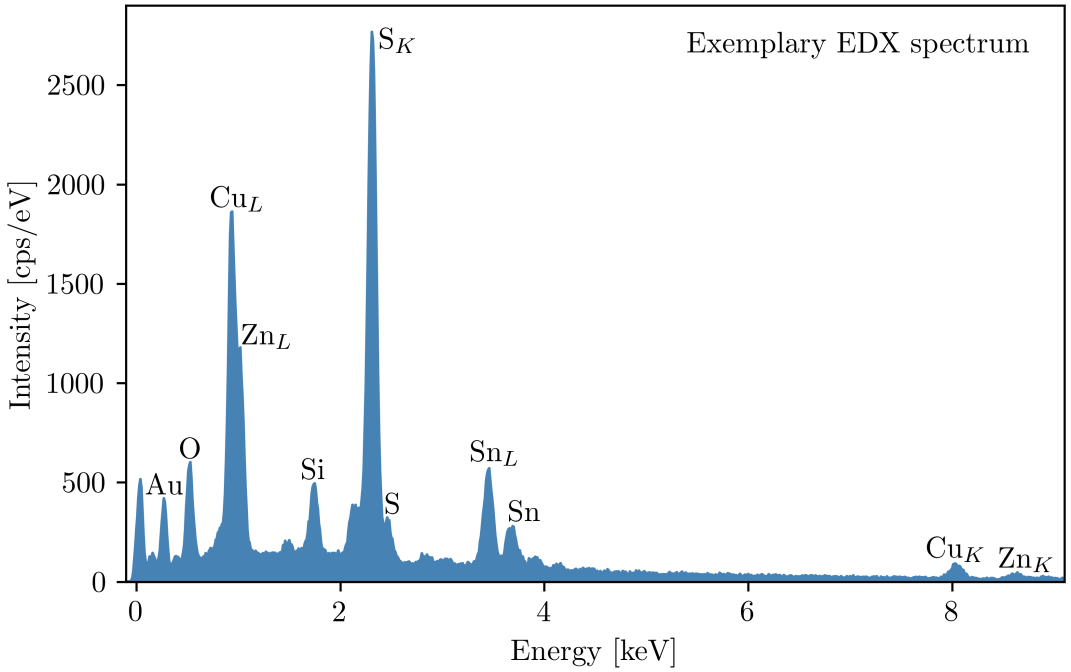

Fig. 5.7: An exemplary EDX spectrum is shown as it is collected on the SEM. This example represents a Cu-poor/Zn-rich sample of CZTS with cation ratios of Cu/(Zn+Sn)=0.84 and Zn/Sn=1.25. Also the underlying Si wafer substrate and the Au coating become apparent through their corresponding peaks. Where relevant to the main text, the corresponding lines (K or L) are specified.

evaporation or by sputter coating, where the latter technique has the advantage that the resulting layer is continuous regardless of the specimen's surface topology and roughness since also areas will be covered that do not lay in line of sight of the target [120]. A typical coating material for this purpose is gold (Au).

In this study, two different kinds of samples are used. The as-synthesised nanocrystals are analysed by use of a drop of nanoparticle ink drop-casted on a small piece of silicon wafer as a substrate. In addition, thin film samples on SLG prepared by spin-coating are investigated by SEM-EDX after annealing in the furnace as well. Either kind of samples are coated with an approximately 15 nm thick Au layer. It is deposited with a Cressington Sputter Coater (108 auto) with argon gas supply using a deposition time of 300 s. The so prepared samples are attached to the sample holder by use of conductive adhesive in order to ground it electrically.

5.4. Inductively Coupled Plasma Mass Spectroscopy (ICP-MS)

Mass spectroscopy is, so to say, an extremely precise method of weighing. It is used to determine the (weight) percentages of different elements in a sample similarly to EDX discussed before, but it principally can even distinguish the isotopes since they slightly differ in mass. One possible method is to use a plasma, which means an ionised gas, in which the sample material is introduced. In inductively coupled plasma mass spectroscopy or spectrometry (ICP-MS) in particular, this plasma is generated by a high-frequency field applied to a coil [121]. The ionised gas is usually argon, which is inert so that it does not react with the material under investigation and has a high ionisation energy itself, so that the produced plasma can excite and ionise a huge share of the elements [121]. The hereby ionised atoms originating from the sample have then to be focussed into a beam and transferred into a mass analyser [121]. By use of perpendicular magnetic (B) and electric fields (E), a Wien filter initially allows to select ions of certain velocity v since only those particles with $v = {}^{E}/_{B}$ move straight through and can be selected by passing through a circular aperture. Subsequently, these ions are directed into a magnetic field which is aligned perpendicular to the beam direction. The particles are therefore forced into a circular motion whose radius depends on their mass to charge (${}^{m}/_{z}$) ratio. An ion detector at a known radial position finally enables to determine the relative abundance of these ions of specific ${}^{m}/_{z}$. The detector scans the whole range of radii and the result is a spectrum of ion counts versus mass to charge ratio. This is the basic principle of operation; instrumental details are discussed elsewhere, see for instance reference [121].

For the purpose of ICP-MS analysis, powder samples of 5 - 10 mg CZTS are dissolved in 50 ml of nitric acid (HNO_3) and are then diluted 1000 times prior to analysis. Nitric acid is particularly useful for decomposition of sulphides [121]. Within this study, ICP-MS is used to determine the atomic ratios rather than to perform a quantitative analysis of specific elements or to analyse their isotopes. Also, the amount of sulphur cannot be determined via this method and thus has to be taken from the EDX measurements. For the other three elements, copper, zinc, and tin, the results from ICP-MS and EDX measurements have been compared for a set of samples as discussed in Section 6.1.3 in order to find and confirm the best choice of X-ray lines for the EDX analysis on the SEM as mentioned before. The ICP-MS measurements on the samples from this study have been kindly carried out by Dr Chris Ottley (Department of Earth Sciences, Durham University).

5.5. UV-visible Absorption Spectroscopy (UV-vis)

Another spectroscopic technique used in this study is absorption spectroscopy. In case that the incident light is resonant with a transition from the ground to an excited state of the material, i.e. if the photon energy matches the energy difference of the two energy levels involved, light of this wavelength is absorbed by the atoms in the solid [122]. According to the wavelength range investigated, the technique can be referred to as UV-visible (or UV-vis) spectroscopy, which means that the spectrum ranges from the far-ultraviolet (ca. 10 - 200 nm) or near-ultraviolet (ca. 200 - 380 nm) to the visible region (ca. 380 - 780 nm) [116]. Sometimes, commercial instruments also cover the near-infrared (NIR) region (ca. 780 - 2500 nm).

When light enters a medium, the intensity is attenuated exponentially with the penetration depth x so that it can be written as [122]

$$I = I_0 \cdot \exp(-\alpha\, x) \ . \tag{5.10}$$

This equation is the Beer-Lambert law, where I_0 stands for the original intensity of the incident beam and x the depth at which the remaining intensity I is measured. α is a material specific and frequency dependent parameter and is called the absorption coefficient. The Beer-Lambert law (Eq. 5.10) can be rearranged to

$$\alpha = -\frac{\log_{10}(I/I_0)}{x \cdot \log_{10}(\mathrm{e})} \ . \tag{5.11}$$

This leads to the definition of the optical density [122]

$$\mathrm{OD}_\lambda = -\log_{10}(T) \tag{5.12}$$

with the transmittance

$$T = \frac{I}{I_0} = 10^{-\mathrm{OD}_\lambda} \ . \tag{5.13}$$

The absorption coefficient in Equation 5.11 can hence also be written as

$$\alpha = \frac{\mathrm{OD}_\lambda}{x \cdot \log_{10}(\mathrm{e})} \ . \tag{5.14}$$

Usually, not α itself but the absorbance A is measured in dependence of the

wavelength λ of the incoming light. This magnitude is defined as [122]

$$A = 1 - T = 1 - 10^{-\mathrm{OD}_\lambda} \ . \tag{5.15}$$

In case of low optical densities (i.e. $\mathrm{OD}_\lambda \leq 0.2$), the transmittance in Equation 5.13 can be approximated via a first-order Taylor series expansion and together with the definition of the absorbance in Equation 5.15 it appears that [122]

$$A \approx 1 - (1 - \mathrm{OD}_\lambda) = \mathrm{OD}_\lambda \ . \tag{5.16}$$

Consequently, the absorbance spectrum A versus λ is similar to the actual absorption spectrum α versus λ (since $\alpha \propto \mathrm{OD}_\lambda$ according to Eq. 5.14) if the optical density of the sample is sufficiently small, but not otherwise. The term 'absorption spectrum' is sometimes used for both types of graphs in the literature.

The measurement of an absorbance spectrum is performed with a spectrophotometer, whose main components are a light source, a monochromator, a sample holder, and a suitable detector [122]. In order to cover the whole wavelength range of interest, several lamps for different ranges may have to be used. An exchangeable grating of suitable grid size (or a prism or a combination of these) within the monochromator that disperses the incoming light allows to scan the spectrum and to select specific wavelengths with the aid of a narrow slit [67]. This light of known wavelength and intensity shines on the sample. From the intensity remaining after traversal of the specimen, the absorbance can then be determined.

The instrument used in this study is the UV-vis-NIR spectrophotometer UV-3600 from Shimadzu in combination with the software UVProbe. It is operated at medium scan speed with a slit width giving a spectral resolution of 8.0 nm. The light source and the grating are set to be automatically changed at 390 nm and 850 nm. The sampling interval is 0.5 nm. In order to determine the high-wavelength/low energy limit of the absorbance, which is a constant value, the spectra are measured to an upper boundary of 1800 nm (NIR). The lower wavelength boundary is usually chosen as 450 nm (visible). In this wavelength range, the instrument is operated with a halogen lamp. The samples investigated are thin films on SLG substrates. Alternatively, also CZTS nanoparticle powder dissolved in toluene within a quartz cuvette can be used. Since the instrument is a double-beam spectrophotometer, a reference sample without the material of interest, i.e. a plain glass slide (or an identical cuvette filled with mere toluene) is placed in a second beam pass in order to correct for any contributions of the substrates (or containers).

5.5.1. Determination of the Band Gap Energy

In order to derive the band gap energy from an absorbance spectrum, the data is represented in a so-called Tauc plot, where the squared absorbance A^2 is plotted against the photon energy [122]

$$E_{\mathrm{Ph}} = \mathrm{h}\nu = \frac{\mathrm{hc}}{\lambda} \tag{5.17}$$

with the Planck constant $\mathrm{h} \approx 6.62 \cdot 10^{-34}\,\mathrm{J\,s}$. On such a plot, a straight line fit can be performed and the intersection of the extrapolated line with the x axis corresponds to the band gap energy E_{g} [122]. This is shown for an exemplary measurement in Figure 5.8. However, this exact procedure is only valid for direct band gap semiconductors. Indirect semiconductors require a plot of $\sqrt{A}$ versus E_{Ph}. This is based on the respective expressions for the absorption coefficient α. In case of a direct band gap material, it holds that [5]

$$\alpha = \alpha_0 \sqrt{\frac{\mathrm{h}\nu - E_{\mathrm{g}}}{E_{\mathrm{g}}}} = \alpha_0 \sqrt{\frac{E_{\mathrm{Ph}} - E_{\mathrm{g}}}{E_{\mathrm{g}}}}\,. \tag{5.18}$$

Consequently, it is also valid that

$$\alpha^2 = \alpha_0^2 \frac{E_{\mathrm{Ph}} - E_{\mathrm{g}}}{E_{\mathrm{g}}} = \underbrace{\frac{\alpha_0^2}{E_{\mathrm{g}}}}_{\equiv\, a} \cdot E_{\mathrm{Ph}} \underbrace{- \alpha_0^2}_{\equiv\, b}\,, \tag{5.19}$$

which is an equation linear in E_{Ph} with slope a and intercept b. The corresponding graph is the Tauc plot mentioned above. Now consider the case $E_{\mathrm{Ph}} = E_{\mathrm{g}}$. According to the previous equation, it is $\alpha^2 = 0$ then, so that the intersection of the straight line described by Equation 5.19 with the x axis must just be at E_{g}. In mathematical terms, one has

$$a \cdot E_{\mathrm{Ph}} + b = 0 \;\Leftrightarrow\; E_{\mathrm{Ph}} = -\frac{b}{a} \tag{5.20}$$

at the intersection of the fitted straight line and the x axis. Plugging in the definitions of a and b from above then shows that

$$E_{\mathrm{g}} = -\frac{b}{a}\,. \tag{5.21}$$

By performing a straight line fit of the form $a \cdot E_{\mathrm{Ph}} + b$ on a Tauc plot of an absorbance spectrum, the band gap can hence be obtained easily. Error

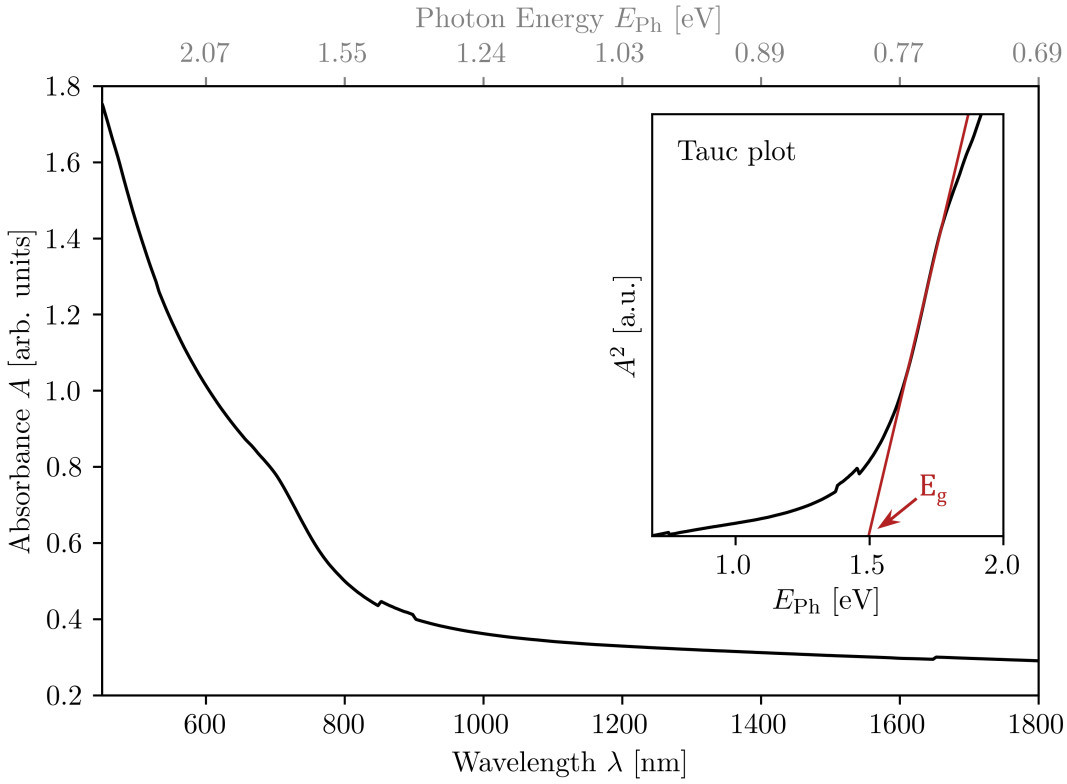

Fig. 5.8: An exemplary absorbance spectrum versus λ measured on an annealed thin film sample of CZTS nanoparticles is shown where also the constant long wavelength limit of A becomes apparent. The small jump discontinuities between 800 nm and 1 000 nm originate from automatic changes in the instrument, e.g. of the grating, during the scan. The inset demonstrates the determination of the band gap energy via a Tauc plot. In addition, band tailing is visible below E_g.

propagation leads to

$$\sigma_{E_g} = \sqrt{\sigma_a^2 \frac{b^2}{a^4} + \sigma_b^2 \frac{1}{a^2} - 2\,\sigma_{ab} \frac{b}{a^3}}\ , \tag{5.22}$$

where σ_a and σ_b are the uncertainties in a and b respectively. $\sigma_{ab} = \rho_{ab}\,\sigma_a\,\sigma_b$ is the covariance of the two parameters a and b derived from the off-diagonal element ρ_{ab} of the correlation matrix.

For $E_{\mathrm{Ph}} < E_g$, the absorption is expected to be at zero, i.e. $\alpha = 0$ [122]. This means that also A^2 has to be zero which can be seen from Equations 5.14 and 5.15. Nevertheless, the Tauc plot of measured data might exhibit a kind of tail for such low energies below the band gap value. In the long wavelength/low energy limit, a constant value of A is approached rather than zero as it can be seen in Figure 5.8. Considering the previous statement of $\alpha = 0$, this constant value has to be subtracted from the curve in order to obtain the correct band gap energy

via the method described above. This is done already in the Tauc plot shown.

The phenomenon of band tailing which causes absorption below the band gap energy to some extent has already been discussed in Section 2.3 with respect to the material CZTS. In addition, it should be mentioned that in general, the band edge of a semiconductor shifts with temperature and the energy levels are broadened due to lattice expansion and increased oscillation of the atoms around their equilibrium positions with rising temperature [67]. In the context of this work, the absorption spectra are measured at room temperature. Most important is the exponential variation of the population of states with temperature, but also optical excitation or electron bombardment have a significant influence on the electron and hole populations of the bands. High concentrations of free carriers can lead to perturbation of the band edge and band tailing similar to that induced by impurities discussed in the above-mentioned section [67]. Free-carrier absorption means that a carrier moves inside the same band via an additional interaction with a phonon or an ionized impurity, so that the momentum remains conserved. If present, this type of absorption becomes increasingly apparent with increasing wavelength or decreasing photon energy [67]. Another aspect already mentioned in Chapter 2 is a distortion of the deduced band gap energy by the presence of secondary phases. Corresponding E_g values are included in Table 5.2 (p. 72).

5.5.2. Estimation of Absorber Layer Thickness

As mentioned earlier, absorption follows the Beer-Lambert law (see Eq. 5.10) which describes the remaining intensity as a function of the depth x into the material in terms of the material and wavelength specific absorption coefficient α. Assume that the intensity is measured after the light passed an absorber layer of thickness l (i.e. $x = l$), for example a thin film of CZTS on a transparent glass substrate. Equation 5.14 can be rearranged to give

$$\alpha \approx 2.303 \cdot \frac{\mathrm{OD}_\lambda}{l} \tag{5.23}$$

or

$$l \approx 2.303 \cdot \frac{\mathrm{OD}_\lambda}{\alpha} \,. \tag{5.24}$$

In typical experiments, either the pathlength l or the absorption coefficient $\alpha(\lambda)$ of the material investigated are known. This way it is possible to estimate the other of these two parameters by using the value of A at a specific wavelength to calculate $\mathrm{OD}_\lambda = -\log_{10}(1 - A)$ (this follows from Eq. 5.15).

Here, α is taken from literature. As the applicability of the method is restricted to wavelengths close to the absorption edge, $\lambda = 855\,\mathrm{nm}$ (about $1.45\,\mathrm{eV}$) is chosen. For this value, it is $\alpha = 2.44 \cdot 10^4\,\mathrm{cm}^{-1}$ in case of CZTS [66]. Based on the absorbance A measured at the chosen wavelength, the absorber layer thickness l of the CZTS nanocrystal ink thin films is then estimated. Section 6.4.1 within the results chapter includes a brief comparison of the experimentally determined thickness values from this approach and from cross-sectional images of the films prepared on the FIB microscope.

5.6. Photoluminescence Spectroscopy (PL)

Luminescence can, more or less, be understood as the inverse process to absorption [122]. Basically, a previously radiatively excited material is relaxing back into its ground state accompanied by the emission of photons. Different excitation mechanisms are suitable for this purpose. If light is used, the process is called photoluminescence (PL); among the alternatives is, for instance, cathodoluminescence (CL) which uses electron bombardment instead [122]. In any case, the energy input brings electrons within the atoms of the specimen into an excited state. The transitions from the higher energy levels back to the ground state lead to the emission of photons with the respective energy (radiative transition). This is recorded in the form of a spectrum which shows fingerprint peaks according to the energy of the material's energy levels [117]. Two different types can be distinguished – emission and excitation spectra [122]. For the recording of an emission spectrum, the excitation wavelength is constant and the material's response is represented over a certain wavelength range. Different from this, the excitation wavelength is being varied for the recording of an excitation spectrum while only one emission wavelength is considered.

An excited atom can not only can relax into its ground state by emission of a photon, i.e. a radiative transition, but also by non-radiative processes. The most important ones are multiphonon emission and energy transfer to another recombination centre in the vicinity which will then be lifted into an excited state [122]. Non-radiative recombination counteracts luminescent emission and increases with temperature, leading to thermal quenching of luminescence. This is due to the fact that higher vibrational levels are occupied by more and more electrons as the temperature rises, which are going back into the ground state by non-radiative processes afterwards [122]. As a consequence, luminescence might be extinguished if the temperature is too high, so that PL measurements are

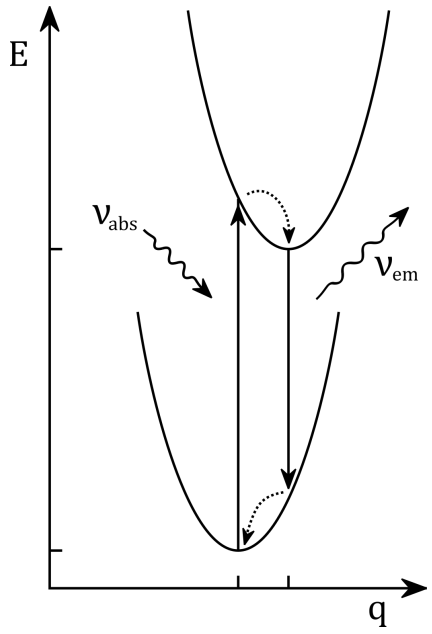

Fig. 5.9: The energy states in this configuration coordinate diagram of a two-level system are parabolas of energy versus real space position, taking into account the vibrating lattice following the rules of a simple harmonic oscillator as distinct from the horizontal energy levels in a rigid lattice. In case of down-conversion luminescence, the incident photon has a higher energy or frequency (ν_{abs}) than the emitted photon (ν_{em}). This is known as a Stokes shift. The radiative transitions involved are illustrated by vertical errors. The dotted lines signify non-radiative relaxation processes involving phonons. Adapted from [122].

preferably done at lower temperatures, e.g. by use of a cryostat. This way, not only nonradiative processes are reduced, but also the thermal peak broadening of about 25 meV at room temperature is lowered and impurity centres are less likely to be ionised [117].

Non-radiative transitions are also responsible for the fact that PL peaks do not necessarily occur at identical energies as observed in the absorption spectrum [122]. In the simplest case it is assumed that the atoms are part of a rigid lattice, but they are rather vibrating around an equilibrium position. This means that, instead of thinking of distinct energy levels, a continuum of states lying on a parabola of energy versus position, see Figure 5.9, has to be taken as appropriate model. As described before, a photon is absorbed while conserving the crystal momentum, but the excited electron does not need to be in the equilibrium position of the respective energy state, yet. This is reached by phonon emission leading to the respective change in energy and wave vector $\vec{q}$. From there, the electron undergoes a radiative band-to-band transition which is becoming visible in the PL spectrum. Back in the ground state, the equilibrium position is reached again

by nonradiative processes. The latter transitions lead to an effective reduction of the energy difference covered by the radiative transition and hence the PL peak occurs at a lower frequency than in the absorbance spectrum [122]. This is called Stokes shift, also referred to as down-conversion luminescence. Other than that, also an anti-Stokes shift or up-conversion luminescence can occur, when two photons of same frequency are sequentially absorbed by a multilevel system. If the excited electron is non-radiatively transferred to a lower level prior to the radiative band-to-band transition, the emitted photon has a higher energy than those being absorbed, leading to a PL peak at a higher frequency as compared to the absorption spectrum [122].

Absorption and therefore luminescence can take place across the band gap, but also when an electron is transferred from a neutral donor to the conduction band or from the valence band to a neutral acceptor, as well as when it is transferred from an ionized acceptor to the conduction band or from the valence band to an ionized donor [117]. It is consequently possible to make conclusions on the band gap as well as on impurity levels, where the latter is probably the most important application of PL spectroscopy [117]. Also excitonic processes can influence the PL peaks [117]. These originate from bound states of electron-hole pairs and result in spectral features below the band gap energy.

Although there is a close analogy between absorption and radiative emission, PL spectra tend to show much clearer features as compared to absorption spectra, because recombining electrons and holes have well-defined energy values leading to narrow peaks and making PL more appropriate for material characterisation than absorption spectroscopy [117]. Another difference concerns the band gap. Whereas the band gap energy determined by means of absorption spectroscopy gives the energy difference between the top of the valence band and the Fermi level, i.e. the optical band gap, PL spectroscopy rather gives values between the latter and the conduction band gap, i.e. the energy difference between the top of the valence band and the bottom of the conduction band [117]. Especially in case of highly doped materials, the Fermi energy does have a significant impact so that the optical band gap will be larger than the conduction band gap and comparisons between the results of absorption and PL spectroscopy have to be done carefully.

The light source commonly used for photoluminescence is an excitation laser; the alternative would be a lamp in combination with a monochromator. The light

re-emitted by the material under investigation passes another monochromator to allow for analysis of its spectral distribution and is then recorded by a detector [122]. Focusing lenses are incorporated in the beam path as well. Commercial setups for these types of measurement are called spectrofluorimeters [122]. The home-built setup chosen for the measurements presented here makes use of a green 514 nm laser operated at 200 mW with a 570 nm and a 550 nm glass filter (cut-off above 2.18 eV) between sample and detector. Additional spectra are collected by excitation with a 375 nm UV laser operated at 60 mW with a 400 nm and a 395 nm filter in the beam path (cut-off above 3.10 eV). The monochromator has a 250 µm wide entrance slit and a diffraction grating of 150 cm^{-1} as the dispersive element. A CCD camera is used for the signal detection and an exposure time of 60 s is chosen. Most of the measurements presented in this thesis are performed at room temperature but by use of a cryostat, a temperature range from room temperature down to about 3 K is realised for an exemplary measurement series.

Not only can PL and Raman spectra be obtained from nearly the same setups but also, both techniques are very surface-sensitive as compared to infrared spectroscopy for example [117]. This is due to the fact that the absorption coefficient α depends not only on the material investigated but also on the wavelength of the incident light. The absorptivity of the material in the given spectral region determines the decay of light intensity and hence the penetration depth defined as the depth into the material where the intensity has decreased to $1/e$ of the incident intensity [117]. In addition to this, the spot on the specimen investigated is relatively small since a focussed laser beam is used for the measurements. These limitations have to be taken into account when interpreting PL or Raman data.

5.6.1. Secondary Phase Identification in CZTS

PL can also aid secondary phase identification in CZTS in addition to Raman spectroscopy, especially in case of Cu_2SnS_3 as it shows a well separated peak [123]. The expected peaks for some of these compounds are summarised in Table 5.2. However, problems with this approach have been reported previously [26, 39]. An example for a photoluminescence spectrum measured on CZTS nanoparticles and fitted with a series of Gaussians is shown in Figure 5.10.

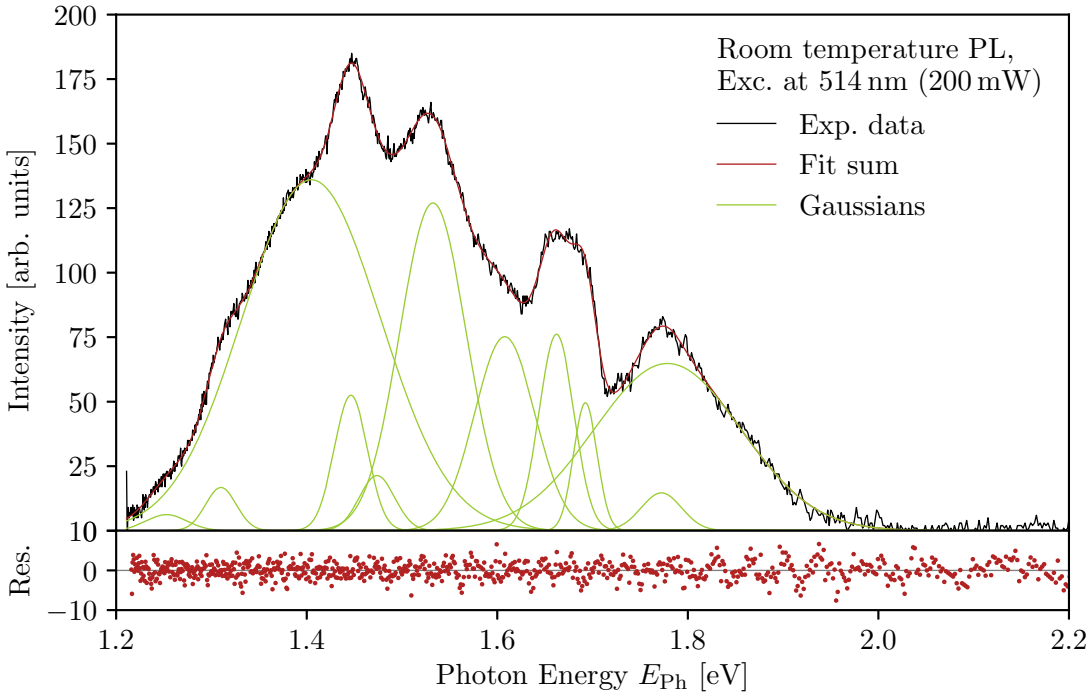

Fig. 5.10: An exemplary PL spectrum of an annealed CZTS nanoparticle ink thin film measured at room temperature by excitation with the green laser (514 nm) is shown (see also Figure 6.21, p. 107). The experimental data has been fitted with a set of Gaussian curves. The residuals of the fit sum are shown in the lower part of the graph. No background removal has been performed.

Tab. 5.2: Photoluminescence peaks and band gap energies of CZTS and some of its secondary phases. Table taken from [26, p. 145] and references therein.

Compound	**PL peaks [eV]**	$\boldsymbol{E_g}$ **[eV]**
Cu_2ZnSnS_4	0.66, 1.23, 1.35, 1.48	1.5
CuS	2.38, 2.50, 2.56, 2.71	1.0
Cu_2S	1.22	1.2
ZnS	1.80, 1.94, 2.09, 2.34, 3.02	3.8
SnS	0.75, 1.12, 1.23, 1.47	1.3
SnS_2	1.77, 2.25	2.2
Sn_2S_3	2.08, 2.38, 2.50, 2.64, 2.82, 3.03	2.1
Cu_2SnS_3	0.95	1.4
Cu_3SnS_4	3.38	1.2

6. Results and Discussion

The following chapter presents and analyses the experiments done in the context of the project in four sections. Firstly, the reproducibility of the CZTS nanoparticle fabrication is briefly discussed in Section 6.1. Based on this, more emphasis is put on the fabrication step of annealing. In particular, Section 6.2 looks at the effects of different temperatures as the main results part of this thesis. This is complemented by Section 6.3 discussing the relevance of the duration of the constant temperature stage. In both cases, CZTS nanocrystal ink thin films on plain SLG glass substrates are used. Results from this are finally compared with exemplary films on a Mo rear contact layer in a cross-sectional analysis in Section 6.4. The content of those sections is divided into subsections according to different characteristics such as structural, chemical, and optical properties, where different measurement methods are considered in some cases. In this way, findings from different techniques can support each other and data interpretation can be verified. The respective measurement parameters are specified in Chapter 5. The very last part of this chapter, i.e. Section 6.5, elaborates on potential sources of error in the different measurement methods and on implications for data interpretation.

6.1. Reproducibility of Nanocrystal Synthesis

Sample preparation is crucial for the design of meaningful experiments. Therefore, this first results section briefly compares the properties of some nanocrystal (NC) synthesis batches, eleven in number, prepared via the method described in Section 4.1. The thin film samples analysed later on are prepared from some of these CZTS nanoparticles. As indicated in Chapter 4, some steps in the sample preparation including the chemicals used for collecting the as-synthesised particles from the OAm mixture by centrifuging have been changed in the course of the ongoing experiments. Specifically, the change from the combination of toluene and isopropanol in centrifuging towards ethanol, hexane, and isopropanol was made in between the synthesis batches Syn04 and Syn05. Beside other findings, this section will demonstrate that no significant changes are observed in the spectra measured with particles obtained by these two different approaches – although it is not pointed out explicitly for each analysis method discussed. The centrifuging chemicals have an influence mainly on the film quality obtainable by spin-coating, whereas data shown in the figures of this section and the corresponding tables does not show any systematic dependence.

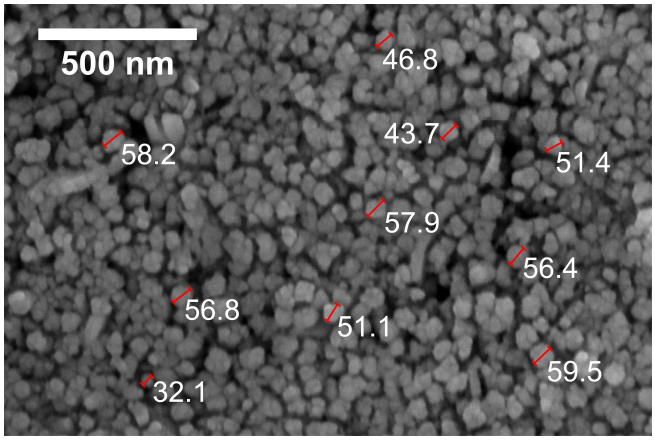

Fig. 6.1: Exemplary SEM image of some nanocrystals from synthesis batch Syn01 at a magnification of $\times$ 50k. The diameter of some particles has been measured by use of the software ImageJ and is noted in units of nanometres. The average with corresponding standard deviation is (51 ± 9) nm. The crystallite domain size inferred from PXRD is $\tau = (41.7 \pm 1.9)$ nm.

6.1.1. Nanoparticle Size

By way of example, Figure 6.1 presents an SEM image of particles from batch Syn01. It becomes apparent that the particle size with an average value of (51 ± 9) nm is of the same order of magnitude as the average crystallite domain size, which is $\tau = (41.7 \pm 1.9)$ nm in this particular case. The crystallite domain size is, in general, smaller than (or equal to) the actual particle size as mentioned in Section 5.1.2 so that the slight difference between the two values is as expected. This is because one particle may consist of more than one crystal domain. Nevertheless, the SEM particle size and the XRD domain size overlap within the margin of the errors and the particles may hence still be single crystals. Apart from this, the nanocrystals have a certain size distribution as revealed by the standard deviation stated. Fortunately, the presence of heterogeneity in size does not necessarily impose any problems upon film fabrication and may even entail benefits [5, 72].

Powder X-ray diffraction is used to estimate the average domain size for all of the synthesis batches considered in this chapter. The results are based on the spectra shown in Figure 6.2 in the following section and are summarised in Table A.2 (p. 149). The values lie roughly between 19 nm and 42 nm, the average with corresponding standard deviation of all batches being (31 ± 7) nm. Despite of same growth times, the crystallites resulting from the different syntheses therefore differ in size, apparently. Reason for this could, for instance, be slight variations in the cooling stage after completion of the synthesis whose control might need improvement in future. In any case, it remains important to keep in mind that the

domain sizes reported can only give an indication of the particle size as discussed above and the actual particle (or grain) size may be a bit larger.

6.1.2. Crystallinity

The results for the tetragonal lattice parameters are also deduced from the XRD spectra and are summarised in Table A.2 (p. 149). The corresponding spectra of all batches are shown in Figure 6.2. Peaks are found at the same positions in each case, confirming that the syntheses consistently produce material of the same crystal structure. The more or less constant position of the main peaks leads to roughly the same lattice parameters with a weighted mean of $a = (5.404 \pm 0.003)$ Å and $c = (10.867 \pm 0.002)$ Å, differing from the literature values reported in [5, p. 65] by only 0.43 % and 0.04 % respectively. The visible variations in peak widths correspond to the varying domain sizes of the batches discussed earlier.

The mentioned figure also includes a simulated reference spectrum for kesterite CZTS. Even though most of the peaks agree fairly well, the experimental spectra contain an additional side peak left to the most intense Bragg reflection (112) at around 28° which is not expected. It may originate from a secondary phase, but taking into account their reference spectra in Figure 5.3, the fingerprint approach pursued for XRD in this study is not sufficient to identify the corresponding compounds. More informative secondary phase analysis based on Raman spectroscopy is presented in Section 6.1.4. Importantly, the mentioned side peak disappears upon annealing as shown in Figure 6.6 in Section 6.2. Minor peaks visible in the reference spectrum are not necessarily visible in the experimental ones due to background contributions from the sample mounting system and residual carbon as well as due to peak broadening in the nanocrystalline material.

6.1.3. Chemical Composition

The chemical composition of the samples has been analysed mainly by means of EDX but for six batches also by means of ICP-MS performed by Dr Chris Ottley* in order to verify the results and instrumental parameters used, the X-ray lines chosen for the different elements in particular. Table A.3 (p. 150) provides a summary of the measured atomic percentages and Table A.4 (p. 151) contains the empirical formulas of CZTS as well as the cation ratios, Cu/(Zn+Sn) and Zn/Sn, derived from both of these methods.

*Department of Earth Sciences, Durham University

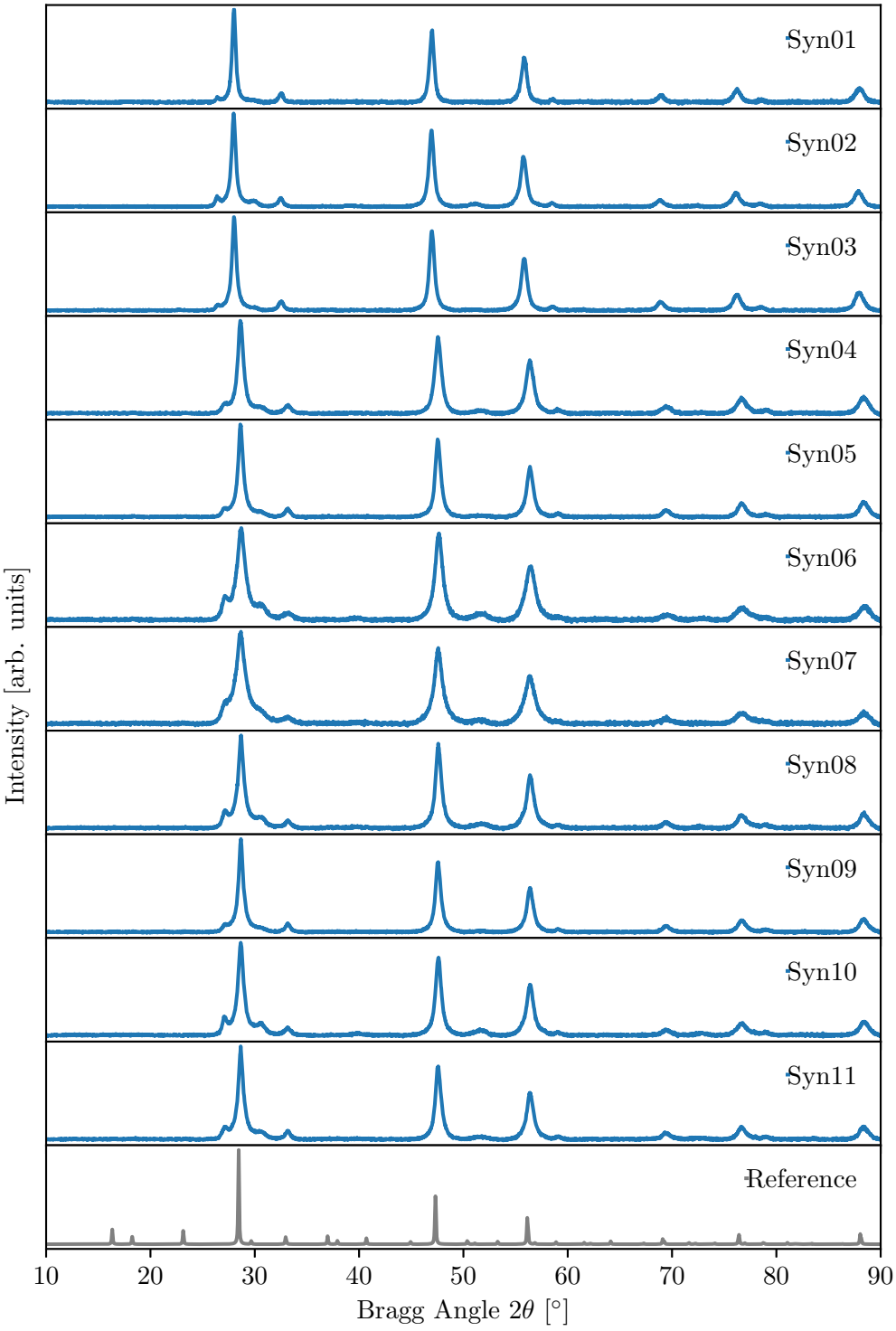

Fig. 6.2: The XRD spectra of the as-synthesised nanocrystals from the different synthesis batches are shown. The spectra are measured by use of nanoparticle powder samples (in distinction from the as-deposited thin films). The derived domain sizes and lattice parameters are listed in Table A.2 (p. 149) in the appendix. In the bottom row, the simulated reference pattern for kesterite CZTS is shown (same as in Figure 5.3). Peaks appear sharper in this case since they refer to a bulk sample with larger crystal domains.

It becomes apparent that most of the samples are very poor in Cu and very rich in Zn, i.e. Cu/(Zn+Sn) $\ll 1$ and Zn/Sn $\gg 1$. The average cation ratios with corresponding standard deviations for all batches as determined by EDX are Cu/(Zn + Sn) = (0.67 ± 0.10) and Zn/Sn = (1.9 ± 0.6). Even though the precursor ratios have been kept constant, significant variations in the resulting compositions are observed. Consequently, even small differences in the synthesis procedure seem to have a big impact. However, it is important to consider that the comparison with the results from ICP-MS indicates limited precision of the measurements themselves. The cation ratios calculated based on ICP-MS are Cu/(Zn + Sn) = (0.72 ± 0.06) and Zn/Sn = (1.9 ± 0.3). In the bottom row of Table A.3, also the averages and standard deviations of the elemental concentrations for both methods are given. In general, ICP-MS indicates that smaller fluctuations of the composition are present than assumed based on the EDX measurements but in the case of ICP-MS only a smaller number of measurements is available for comparison. In terms of the different elements, the Sn content is particularly stable (smallest standard deviation) – in terms of the different syntheses analysed by the same method as well as in terms of comparative measurements with the two techniques. Since the Cu/(Zn+Sn) ratio is more constant throughout the different syntheses than the Zn/Sn ratio, confirmed by both methods, the Zn content appears to have the biggest fluctuations.

Both methods average over a certain but limited volume of material. Sources of error might, for example, be small particles getting lost during the transfer into the instrument, in case of ICP-MS in particular. Particles of different size are known to have potentially different compositions and these or any other compositional inhomogeneities in the samples may cause systematic deviations in the measurements. Further considerations of potential sources of errors can be found in Section 6.5.3. The results chapters dealing with varying annealing temperatures and times investigate thin film samples, which is why ICP-MS is much less practical for compositional analysis in that case since it requires powder samples. Therefore, EDX is used for this purpose but it should be kept in mind that ICP-MS might indicate smaller changes of composition in comparison. The measurement parameters used for EDX, particularly the X-ray lines specific to the different elements, have been chosen in a way that the measurement results are stable with respect to repeated measurements of the same sample and that the measurement values agree with to the results from ICP-MS as good as possible. The resulting choice of X-ray lines is specified in Section 5.3.2 about EDX analysis.

6.1.4. Phase Purity

Secondary phase analysis of the different syntheses by means of Raman spectroscopy is presented in Table A.5 (p. 152), assigning the Raman shifts identified to the respective compounds. Intensity ratios are not considered and no quantitative analysis is done since the peak intensities depend relatively much on the background fitting which is realised via straight line subtraction for the data presented here. The corresponding spectra can be found in Figures 6.3 and 6.4 for the excitation wavelengths of 785 nm and 532 nm respectively.

First of all, it is notable that the spectra of the latter excitation wavelength look very similar for all of the syntheses and show the expected peaks for CZTS. In contrast, spectra measured with 785 nm resonant excitation do exhibit some differences among the batches and in particular, Syn10 and Syn11 seem to be quite different. These two spectra contain more noise than the others even though the same measurement parameters have been used. This could be caused by an increased concentration of residual carbon. Also, peaks with smaller Raman shifts are much more intense as compared to the CZTS main peaks in case of these two batches. The table of peak positions reveals that the visual differences of the spectra partly originate from the relative intensities, meaning that present peaks may simply be too weak to stand out. A quite notable peak is observed at $195\,\mathrm{cm^{-1}}$ - $200\,\mathrm{cm^{-1}}$ which can possibly be assigned to the secondary phases SnS (expected at $190\,\mathrm{cm^{-1}}$) and/or $Cu_4Sn_7S_{16}$ (expected at $192\,\mathrm{cm^{-1}}$) even though there would be a systematic upwards shift as compared to the respective reference peaks which calls into question this interpretation. The same peak is not only found in batches Syn10 and Syn11 but also in all the others; for those it just has a much weaker intensity compared to the typical CZTS peaks.

In case of Syn10 and Syn11, the relative intensities change dramatically with annealing which significantly promotes the kesterite CZTS phase as discussed below in Sections 6.2.4 and 6.3.4 in the context of different annealing temperatures and times. This high-temperature processing step causes the Raman spectra of Syn10 and Syn11 to become similar to those of the other batches and improves the crystal quality. This indicates that the here observed deviant appearance of the Raman spectra measured with resonant excitation is not related to problems with the success of further processing steps and that the material is still suitable for use in photovoltaic absorber layers. This is supported by the 'usual' appearance of the 532 nm spectra of the as-synthesised particles from batches Syn10 and Syn11.

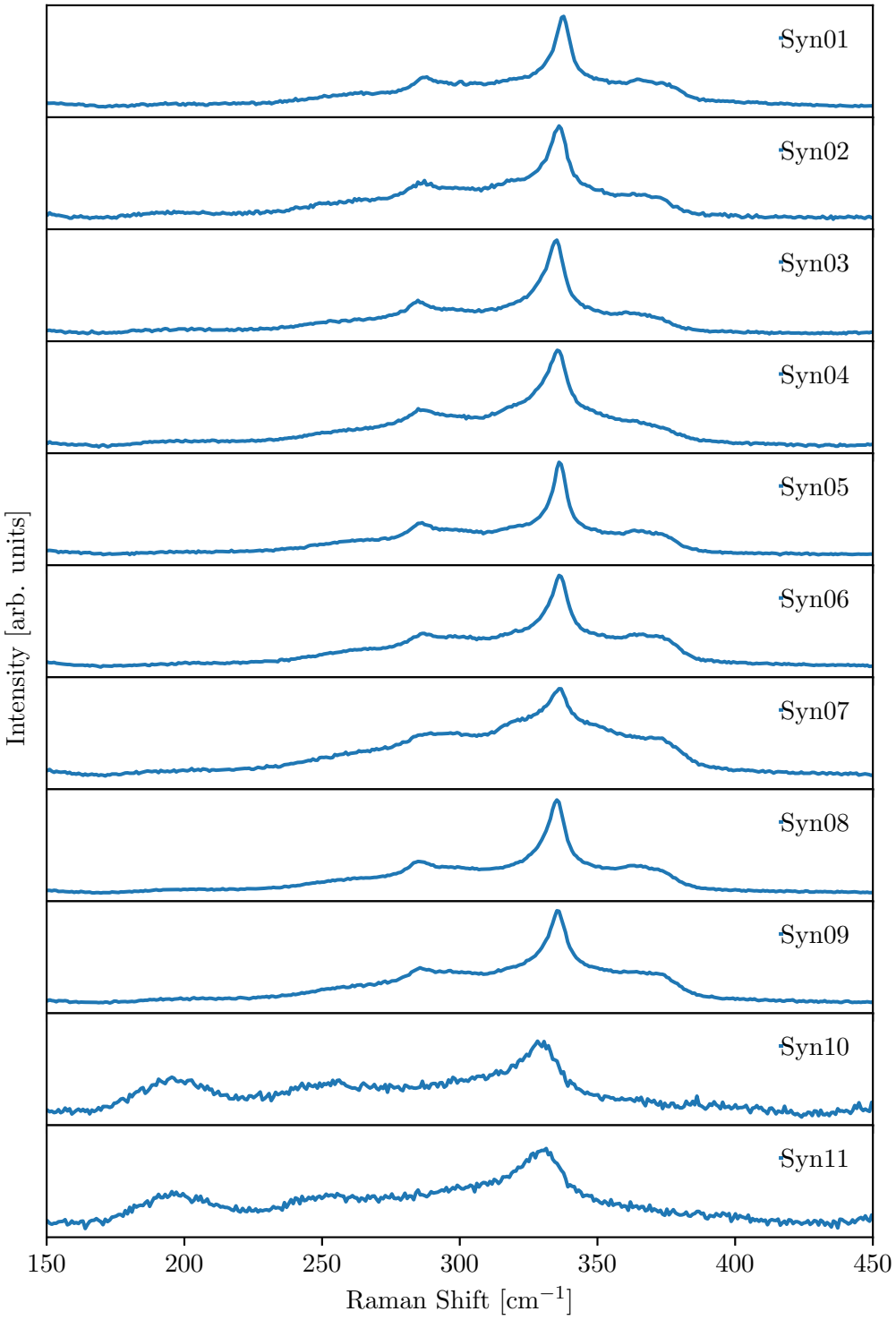

Fig. 6.3: The Raman spectra of the as-synthesised nanocrystals measured with 785 nm excitation wavelength are compared in order to search for differences in phase purity of the different synthesis batches. The peak positions are listed in Table A.5 (p. 152). The spectra from the last two syntheses batches have a deviant appearance from the other batches even though this is mainly due to changes in the relative intensities as revealed by curve fitting. Annealing transforms these anomalous Raman spectra into similar ones to those observed for the other batches as discussed later in Section 6.2.4.

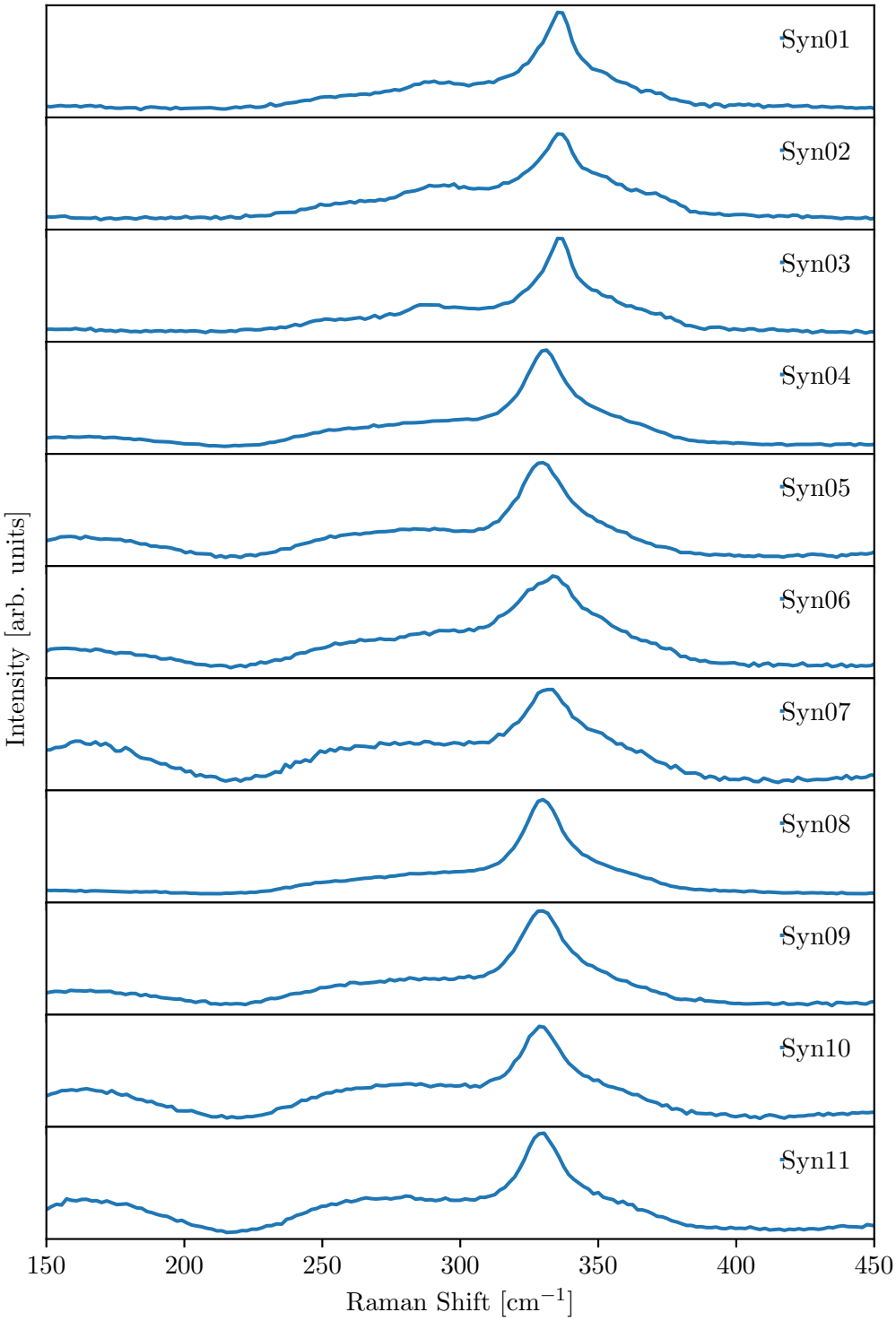

Fig. 6.4: The Raman spectra of the as-synthesised nanocrystals from the different synthesis batches measured with a 532 nm laser are shown. Fewer features are observed compared to the measurements from resonant excitation shown in Figure 6.3. Most importantly, the last two batches have nearly the same spectra as all the other syntheses in this case. The positions of the main peaks are given in Table 6.1 and are compared to those from 785 nm excitation. Here, features at Raman shifts smaller than about 220 cm^{-1} should be interpreted with care because of their dependence on background fitting.

All the spectra in Figure 6.3 show indications of disordered CZTS in the form of a peak at around 330 cm^{-1}. Usually, this is a side peak at the left of the main Raman mode expected at 337 cm^{-1} which has the largest intensity. Batch Syn07 has a similar side peak but it is found at a comparatively low Raman shift, 322.2 cm^{-1}, leading to a more pronounced shoulder. In case of the last two batches, the contribution of disordered CZTS is particularly pronounced meaning that the main peak seems to be shifted to the left. Overall, hardly any secondary phase is found in the spectra of the different synthesis batches with certainty, except from maybe some SnS and/or $Cu_4Sn_7S_{16}$ as mentioned before, but due to peak overlaps between CZTS and other compounds no definite statement can be made as to their presence. Table A.5 (p. 152) contains more detailed information about these ambiguities. Neglecting those aspects, the Raman data suggests that no significant amounts of unwanted compounds are present as intended, even though disordered CZTS is detected. The latter is assumed to be common for most specimen used in studies from the academic literature [30].

Tab. 6.1: The position of the main Raman peaks of the different synthesis batches measured with excitation at 785 nm (from Table A.5) and at 532 nm are compared. The corresponding spectra are displayed in Figures 6.3 and 6.4.

NC batch	**Position main peak [cm^{-1}]**	
	785 nm	532 nm
Syn01	337.53 ± 0.04	335.4 ± 0.5
Syn02	335.9 ± 0.04	336.1 ± 0.6
Syn03	335.0 ± 0.04	336.0 ± 0.5
Syn04	335.9 ± 0.1	331.1 ± 0.4
Syn05	336.30 ± 0.03	330.3 ± 0.3
Syn06	336.32 ± 0.03	332.2 ± 0.3
Syn07	335.97 ± 0.09	332.2 ± 0.4
Syn08	335.35 ± 0.03	330.5 ± 0.4
Syn09	335.66 ± 0.04	330.0 ± 0.3
Syn10	329.58 ± 0.18	329.8 ± 0.4
Syn11	330.1 ± 0.3	330.0 ± 0.4

Table 6.1 compares the position of the CZTS main peak expected at 337 cm^{-1} in the spectra measured with 785 nm and 532 nm excitation wavelength from Figures 6.3 and 6.4. The variations observed are not truly systematic although the measurement with 532 nm excitation tends to result in a smaller Raman shift. In any case, this comparison indicates that the errors obtained from least-

square fitting underestimate the true errors. This may be partly due to a small impact of background subtraction as well as of the excitation wavelength itself on relative peak intensities. Since resonant excitation allows for much better peak identification, the other results chapters will only look at the explicit peak positions for measurements with the 785 nm laser. Deviations of experimentally determined Raman shifts from the literature values do not seem very surprising in the light of the varying peak positions obtained by using different excitation wavelengths and the resulting uncertainties.

6.1.5. Opto-electronic Properties

For the purpose of comparing the different synthesis batches, the analysis of the opto-electronic properties is restricted to band gap determination by use of Tauc plots based on UV-vis spectroscopy. The results are summarised in Table A.2 (p. 149) in the appendix. For discussing the influence of different annealing parameters in Sections 6.2 and 6.3, PL spectroscopy will be taken into consideration in addition.

All of the syntheses batches seem to have a relatively low band gap energy of $E_g = (1.14 \pm 0.13)\,\text{eV}$ on average as compared to the 1.4 - 1.5 eV theoretically expected for kesterite CZTS. The values lie roughly in between 0.86 eV (Syn03) and 1.26 eV (Syn08). A possible explanation for the systematic deviation could be the presence of secondary phases. Their band gap energies can be found in Table 5.2 but according to the previous section, no significant amounts of those compounds are contained in most of the samples. Nevertheless, the presence of some SnS and/or $Cu_4Sn_7S_{16}$ having band gap energies of 1.3 eV [124] and 0.8 eV [125] respectively could possibly explain the systematic shift observed. The band gap energy of the latter compound would agree better with the magnitude of the deviation observed. Another suitable explanation is the reduction of the band gap energy induced by an increasing level of cation disorder [58, 65]. This would be consistent with the indications of disordered kesterite in the Raman spectra discussed before. However, some observations made in the context of the present research project may put into question the reliability of the band gap values derived from the UV-vis spectra. Those aspects are discussed further in Section 6.5.4. They may be partly responsible for the differences between observations and expectations as well.

6.1.6. Conclusions

There is only scarce information available on the reproducibility of the synthesis methods in corresponding publications. The previous section, which briefly discusses this issue, reveals that the chemical composition in particular appears to vary significantly despite constant precursor ratios. The comparison of two methods for compositional analysis, EDX and ICP-MS, additionally showed that the measurements might not be straightforward but that the standard procedures need some modifications. Crystallographically, the synthesised material is quite similar from one batch to another: Even though the particles have a certain size distribution, the average domain size of different batches is fairly similar. The overall crystal structure as determined by XRD does not change and the lattice parameters inferred agree well with the expectations from literature. For most of the batches, the vibrational modes revealed by Raman spectroscopy are very similar to one another and close to the expectations for CZTS but there are indications of secondary phases in a few instances. This applies to the compounds SnS and/or $Cu_4Sn_7S_{16}$ in particular. Secondary phases are suppressed upon treatment in the furnace and the desired kesterite CZTS phase is promoted as discussed in the following two results sections dealing with the annealing experiments. Solely resonant excitation was found to be able to detect deviant intensity ratios in the Raman spectra of the different batches. Absorption spectroscopy systematically indicates a lower band gap energy as compared to the literature value for CZTS. However, potential sources of error discussed in Section 6.5.4 definitely need to be taken into consideration as some observations put the reliability of the UV-vis analysis into question. Other than that, the relatively low band gap energies would agree with the presence of disordered kesterite as also indicated by Raman spectroscopy. Overall, the methods available confirm that CZTS nanocrystals have been successfully synthesised but also show that further improvements of the synthesis procedure and the analysis techniques for the application in CZTS nanoparticle thin films are yet to be made.

6.2. Influence of Annealing Temperature

Annealing is an important step in the preparation of solar cell absorber layers made of nanoparticle inks. In this section, the effect of temperature is analysed by comparing the as-deposited with the annealed films using a range of different measurement methods. A fixed annealing time of one hour was chosen for this purpose. Section 6.3 suggests that this duration is sufficient to reach the final state

of the thermally induced changes in the material. Temperatures between 400 °C and 600 °C were tested in 50 °C steps, as well as an intermediate temperature of 575 °C to look in more detail at a sudden grain growth enhancement observed. For the interpretation of data presented later on, it should be mentioned that the sample annealed at 600 °C was slightly bent after the treatment in the furnace. The temperature-dependent viscosity of SLG hence determined the maximum temperature that could be tested [126]. Annealing or sulphurisation was done as described in Section 4.3 by use of a mixed N_2/H_2S atmosphere.

The thin films investigated have a thickness of about half a micron according to estimations based on their absorbance. However, Section 6.4 discussing exemplary cross-sectional images indicates that the actual thickness is rather about one micron. The thickness was achieved by depositing five layers of ink in the way described in Section 4.2.2 on top of plain glass substrates. This allows for absorbance measurements and band gap determination prior to and after the annealing which would not be possible with similar but opaque Mo-coated substrates. All of the six samples have been prepared from the same ink using particles from synthesis batch Syn11. For a summary of some properties of the individual as-deposited films refer to Table A.6 (p. 153).

6.2.1. Film Morphology

Visually, the films annealed at temperatures up to 500 °C look smooth and have a shinier surface than the as-deposited films, whereas the surface of the films annealed at 550 °C or more seems to be a bit rough and matt. This fact might be related to an enhancement of surface grain size observed with the electron microscope. On the SEM images shown in Figure 6.5, it is visible that abnormal grains appear when the temperature is increased from 450 °C to 500 °C. They have an edged shape resulting from their crystalline structure and they grow in size as the annealing temperature is increased. The most pronounced difference is observed between the annealing temperatures 575 °C and 600 °C. Micron-sized abnormal grains present after annealing at 575 °C seem to merge and finally build little ‘islands’, several microns in diameter, that cover the nanoparticle floor layer to a significant extent after annealing at 600 °C.

The images presented in Figure 6.5, especially those for the lower annealing temperatures, reveal some round ‘bumps’ which are different from the edged surface grains appearing at higher temperatures only. Those bumps have also been

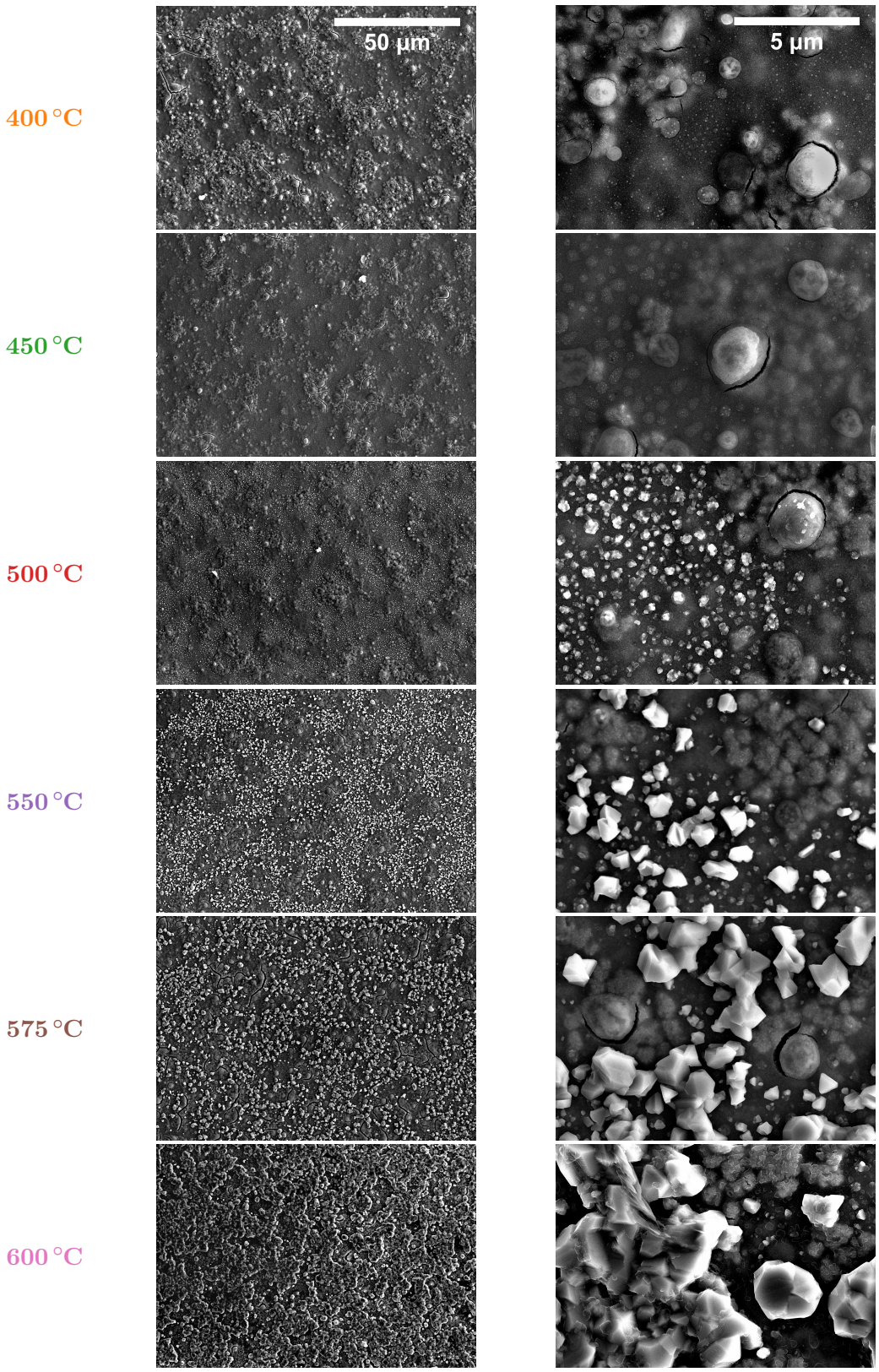

Fig. 6.5: Some SEM images (secondary electrons) of the samples annealed at different temperatures are shown, at a magnification of × 1k in the left-hand column and of × 10k in the right-hand column respectively. The abnormal grains appearing above 500 °C seem brighter in contrast which is presumably due to the difference in height as they grow on top of the darker-appearing nanocrystal floor layer.

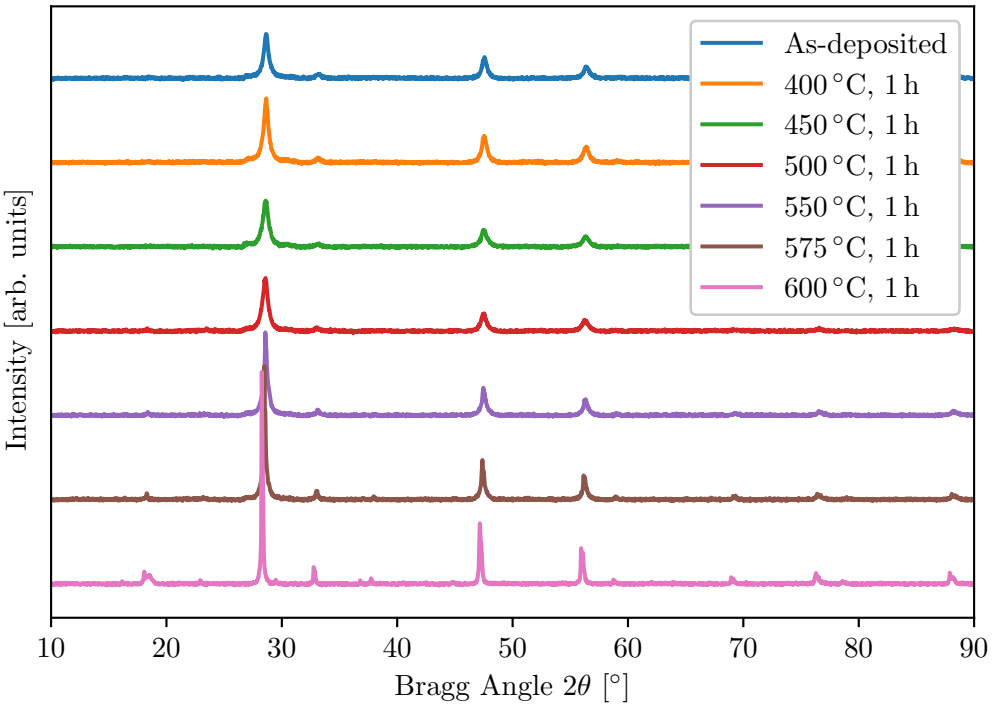

Fig. 6.6: The XRD spectra of the films annealed at different temperatures are compared. The background signal mainly originating from the amorphous glass substrates has been subtracted and the different spectra have been shifted vertically for clarity. The 600 °C annealed sample was bent due to the annealing so that the alignment in the instrument was ambiguous leading to a peak shift that is most likely not related to changes in the crystal structure.

observed on as-deposited films and they do not result from the annealing treatment. It is therefore strongly assumed that they originate from some nanoparticle accumulations that could not be disjointed prior to ink fabrication.

The observation of abnormal grain growth on top of a fine-grained layer described before is consistent with work of other authors discussed in detail in Section 3.3.2. Explanatory models are described therein as well. Related film properties such as the carbon concentration and the presence of sodium are analysed with respect to the present study later on in this section in order to assess whether carbon decomposition and sodium diffusion from the substrate play a role in the grain growth mechanism as suggested by corresponding literature.

6.2.2. Crystallinity

The main source of information on the crystal structure are the XRD spectra. Figure 6.6 shows that the peaks become sharper and sharper and that they increase

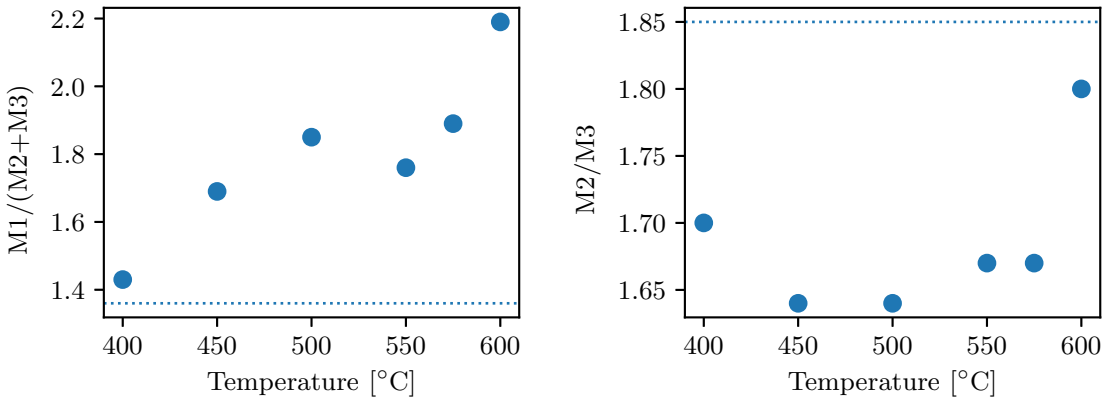

Fig. 6.7: The intensity ratios of the main peaks – M1 (112), M2 (220), and M3 (312) – are plotted in dependence of the annealing temperature. The horizontal line indicates the level measured on an as-deposited film. The corresponding XRD spectra are presented in Figure 6.6.

in absolute intensity when the annealing temperature is increased, indicating crystallite growth and improved crystal quality. As the background level is lowered, possibly due to carbon removal, minor peaks become better visible as well. Furthermore, even though the peak positions do not change significantly with varying annealing temperature as discussed later, the relative intensities do.

Figure 6.7 illustrates the height ratios of the main peaks, namely (112) at about 28.5°, (220) at 47.3°, and (312) at 56.2° denoted as M1, M2, and M3 respectively (in order of increasing Bragg angle). It appears that M1 becomes more pronounced in intensity as compared to the other two peaks. The M1/(M2+M3) ratio increases from about 1.4 to 2.2 from the as-deposited film to the film annealed at 500 °C. The increase of M1 as compared to the other two peaks is not completely monotone and has a dip between 500 °C and 550 °C. This may be because M2 and M3 increase in intensity, too, but change their ratio. Up to 500 °C, the intensity of M2 is decreasing as compared to M3, whereas from this temperature upwards, the relative intensity of M2 is increasing again and nearly reaches the original M2/M3 ratio of 1.85 of the as-deposited film. These observations indicate the presence of changes in the crystal structure, but these do not seem to be related to a transition between stannite and kesterite CZTS as suggested by the simulated XRD patterns shown in Figure 5.3 not revealing any difference in peak intensities. Instead, the shift in relative intensities due to annealing may be interpreted as influence of additional atoms in the lattice on the relative intensities of the Bragg reflections. These might be sodium atoms or could be related to a range of defects such as vacancies or antisites forming in the proximity of certain lattice planes.

Tab. 6.2: Comparison of the peak positions from a reference pattern (PDF 00-026-0575, kesterite Cu_2ZnSnS_4) and those of the sample annealed at 600 °C, where the minor peaks are much better visible than without annealing or annealing at lower temperatures. The latter peaks have been located by use of the software DIFFRAC.EVA. The main peaks are indicated in bold font.

Miller indices	**Bragg angle 2θ [°]** Reference	Measured
(002)	16.338	16.157
(101)	18.205	18.146
		18.469
(110)	23.101	22.935
(112)	28.531	28.298
(103)	29.676	29.466
(200)	32.990	32.833
(202)	37.026	36.796
(211)	37.967	37.733
(114)	40.759	-
(105)	44.997	44.824
(220)	47.332	47.162
(312)	56.178	56.076
(303)	56.860	58.793
(224)	58.971	-
(314)	64.179	-
(008)	69.231	69.037
(332)	76.445	76.300
(?)	-	87.978
(?)	-	88.174

Also the presence of small amounts of secondary phases potentially influences the peak intensities. A comparison with reference spectra from a database does not seem to be suitable to add clarity as the there observed differences in relative peak heights are rather significant and the diversity of sample-specific properties reported is too wide-spread.

Full-pattern fit approaches such as Rietveld refinement would be able to assess the above-made hypotheses more profoundly and could, in particular, also detect small indications of secondary phases in the minor peaks of the XRD spectra. As mentioned before, Raman spectroscopy is the method of choice for secondary phase identification in the present work. However, in case of the sample annealed at 600 °C where the peaks are visible most clearly, a detailed comparison of the experimentally determined peak positions with a reference spectrum (PDF 00-026-0575) for kesterite CZTS, shown in Figure 5.4, has been done including the minor peaks. This is summarised in Table 6.2. Even though this approach does not provide as much information as Rietveld refinement solving the entire crystal structure, it gives an impression of the agreement between experiment and expectation. It is observed that the measured values have a systematic tendency to occur at lower angles. However, Figure 6.6 also shows that this is only the case for this specific sample which has been annealed at 600 °C. In result of this comparably high temperature, the substrate has been bent slightly, causing difficulties in sample alignment and potentially a systematic error in peak position. This is because height displacement of the specimen is a major source

of error in determining XRD line positions [127]. The focus of analysis is put on the assignment of the peaks to the appropriate Miller indices here, similarly applicable to the samples annealed under other conditions which exhibit even better agreement in terms of the Bragg angles measured. Only a small side peak left to the Bragg reflection (112) which has the largest intensity disappears with increasing annealing temperature and is not found after annealing at 600 °C anymore. This could be related to suppression of a secondary phase as speculated in Section 6.1.2.

In case of the 600 °C annealed film, the (101) peak at around 18.3° is split into two, maybe due to a secondary phase or the simultaneous presence of ordered and disordered CZTS. It is unclear whether this is the same for the other annealing temperatures. Almost all of the following peaks are found in the measured spectrum. Only (114), (224), and (314) at about 41°, 59°, and 64° are missing, but it is important to note that especially the first and last-mentioned peak have very small intensities in the reference spectrum (1 % of strongest line). Lots of other reference spectra for CZTS apart from that one used exist, most of them exhibiting slight differences in peak positions and sometimes notable differences in intensities. It is therefore not surprising that some of the smaller peaks are not visible at the resolution available. An additional double peak is found at around 88° in the sample investigated which is not contained in the reference spectrum but this is assumed to be a result of the smaller range of Bragg angles covered. The feature in question is visible in the simulated patterns of CZTS shown in Figure 5.3 indeed. Since according to this, no additional peaks are found in the experimental data as compared to the expectations for CZTS there seem to be no significant amounts of secondary phases. No statement can be made concerning ZnS and Cu_2SnS_3 because their patterns are too similar to that of CZTS. Overall, there is reasonably good agreement between the measured XRD spectrum and the reference spectrum. More detailed phase analysis is pursued in the following subsections, especially by means of Raman spectroscopy.

Mainly based on the peak positions, the widths of the unit cell can be extracted from the XRD spectra. Although the lattice parameters plotted in Figure 6.8 seem to increase slightly with increasing annealing temperature, this is not at all certain. This is because the slightly bent surface of the sample annealed at 600 °C can introduce significant shifts in the peak positions observed in this particular case since not the whole substrate can be placed in the correct vertical position within the measurement setup as mentioned above. Also the relatively

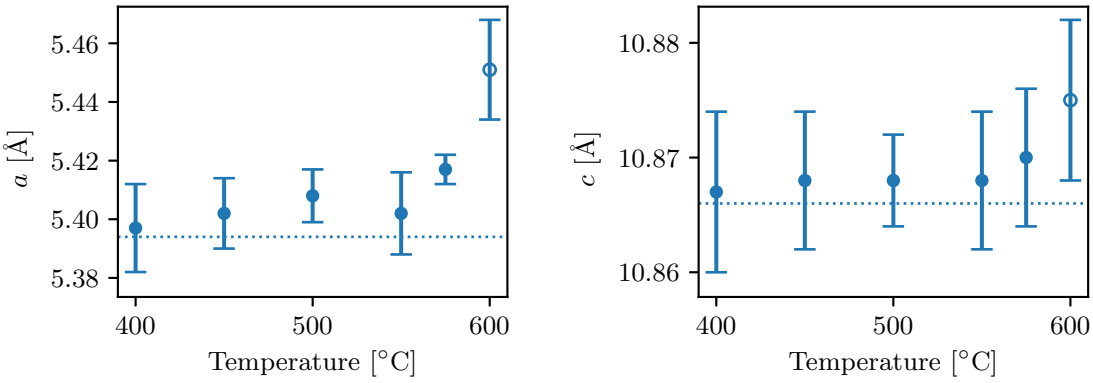

Fig. 6.8: Based on the XRD spectra shown in Figure 6.6, the tetragonal lattice parameters a and c have been determined for the films annealed at different temperatures. It is important to note that the reliability of the data for the film annealed at 600 °C is questionable, since the substrate was slightly bent which induces a possible error in the peak position. Leaving aside this last data point and considering the error bars, no significant trend is observed – although there might be a slight tendency of an increase as compared to the lattice parameters measured on an as-deposited sample indicated by a horizontal line.

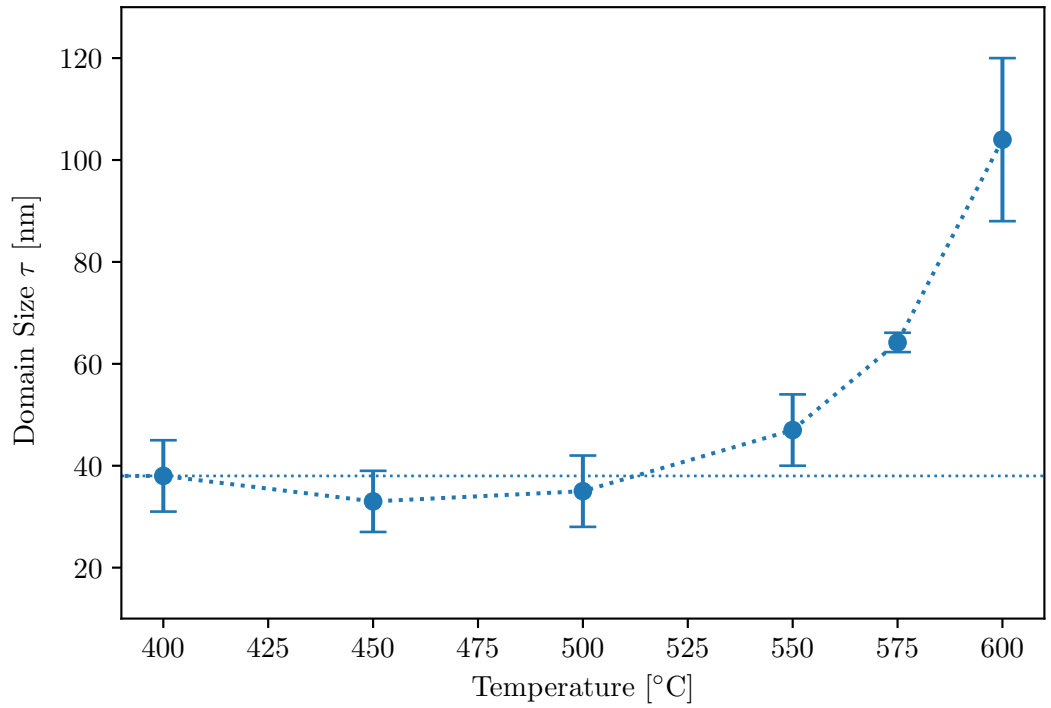

Fig. 6.9: The average domain size τ has been inferred from the XRD data plotted in Figure 6.6. There is a clear upwards trend with increasing annealing temperature, highlighted by the dotted line segments. The horizontal line is at the level of the domain size determined for an as-deposited film.

large error bars as compared to the variations in a and c suggest that the lattice parameters stay more or less the same with changing annealing temperature. As compared to the starting value, a slight increase of the lattice constants may be present. Incorporation of Na into the lattice structure would have such an effect for example, also consistent with the change in relative peak intensities discussed above. However, the change in the lattice parameters derived is not very pronounced.

Of big interest is the development of the domain size τ displayed in Figure 6.9 which can be deduced from the XRD data as well. Annealing between 400 °C and 500 °C does not have an obvious effect on the domain size as compared to the as-deposited material with a domain size of about 38 nm, considering the error bars. The apparent initial decrease may indicate recrystallisation of the material. However, τ clearly starts to increase between 500 °C and 550 °C. This development is accelerated as the temperature rises and the domain size changes significantly from roughly 64 nm to 104 nm by going from 575 °C to 600 °C. This is an important fact to consider in the context of the desired large-grained absorber layers. Sugimoto et al. [128] reported similar observations in this temperature range for annealed CZTSe nanoparticle thin films. Due to the fact that the thin films investigated were deposited on SLG, it is unclear to what extent increased sodium diffusion from the substrates contributed to the observed grain growth enhancement though. Also, it is important to be aware of the fact that the abnormal surface grains described in the previous section are part of the average domain size value as well. The biggest change of the surface morphology was observed in the same temperature range. Coming back to the above-mentioned bent substrate of the film annealed at 600 °C, the calculation of the domain size is supposed not to be affected by the systematic error of the peak position as much since the peak width is much more significant in this case. The data hence reliably indicates a clear upwards trend of the average domain size with the most significant grain size enhancement between 575 °C to 600 °C.

6.2.3. Composition and Carbon Residues

According to EDX data, the cation ratios, namely Cu/(Zn+Sn) and Zn/Sn shown in Figure 6.10, remain relatively constant or, at least, do not show a trend. This is most prominent in the case of the Cu/(Zn+Sn) ratio; in case of Zn/Sn a slight tendency of decrease may be present but the films annealed at 550 °C and 575 °C do not fit this trendline well. The results from the as-synthesised particles are

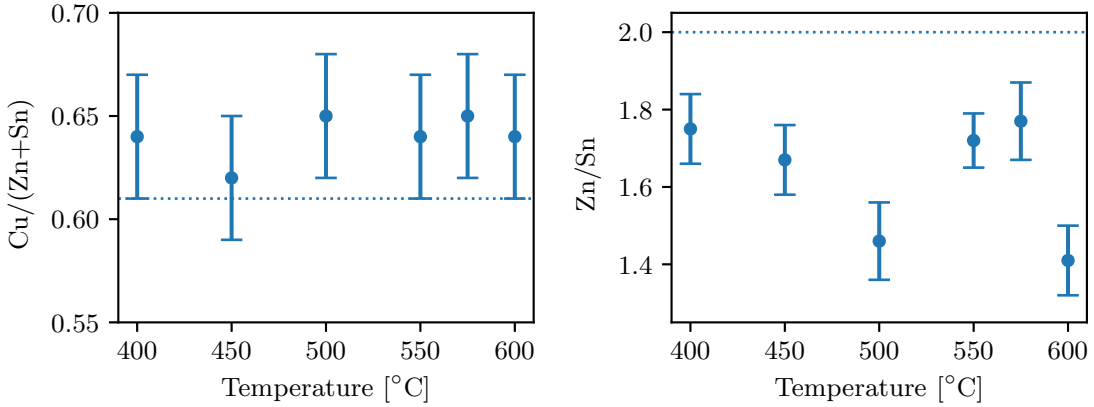

Fig. 6.10: The cation ratios Cu/(Zn+Sn) (left graph) and Zn/Sn (right graph) are plotted against the annealing temperature with error bars from propagation of the uncertainties in the measured concentrations. The horizontal lines indicate the ratios measured on the as-synthesised particles.

indicated by horizontal lines, adding some information to the previous statements. The Cu/(Zn+Sn) ratio is not notably shifted by annealing. The Zn/Sn ratio of the annealed material is systematically lower than that of the as-synthesised particles. However, the as-synthesised particles are measured as drop-casted on a piece of silicon wafer instead of thin films on SLG glass so that the measurement conditions are slightly different. The normalised percentages of all four main elements in the films are also illustrated in the form of pie charts in Figure 6.11, confirming that the average composition is relatively constant except from some random fluctuations and a slight increase in the sulphur content. The latter increase, however, does not progress further when the annealing temperature is increased beyond 450 °C. This may suggest that a slightly lower H_2S concentration could be sufficient. For example, two studies on the effect of the H_2S concentration in the annealing atmosphere have been presented by Maeda et al. [86, 87] being in favour of less sulphur-rich annealing atmospheres. However, it is also interesting to note that sulphur levels they reported did not follow a monotone trend with changing H_2S concentration, surprisingly, indicating that further investigations might be advised. In contrast to those studies, a higher sulphur amount in the surrounding vapour may help to prevent decomposition of CZTS as broached in Section 3.3.2. In line with this, excess sulphur in the final material was found to suppress secondary phases [129].

In addition to copper, zinc, tin, and sulphur, some carbon, oxygen, and sodium are present in the films investigated as well. The development of their concentration is illustrated in Figure 6.12. Minor elemental components of very low concentrations,

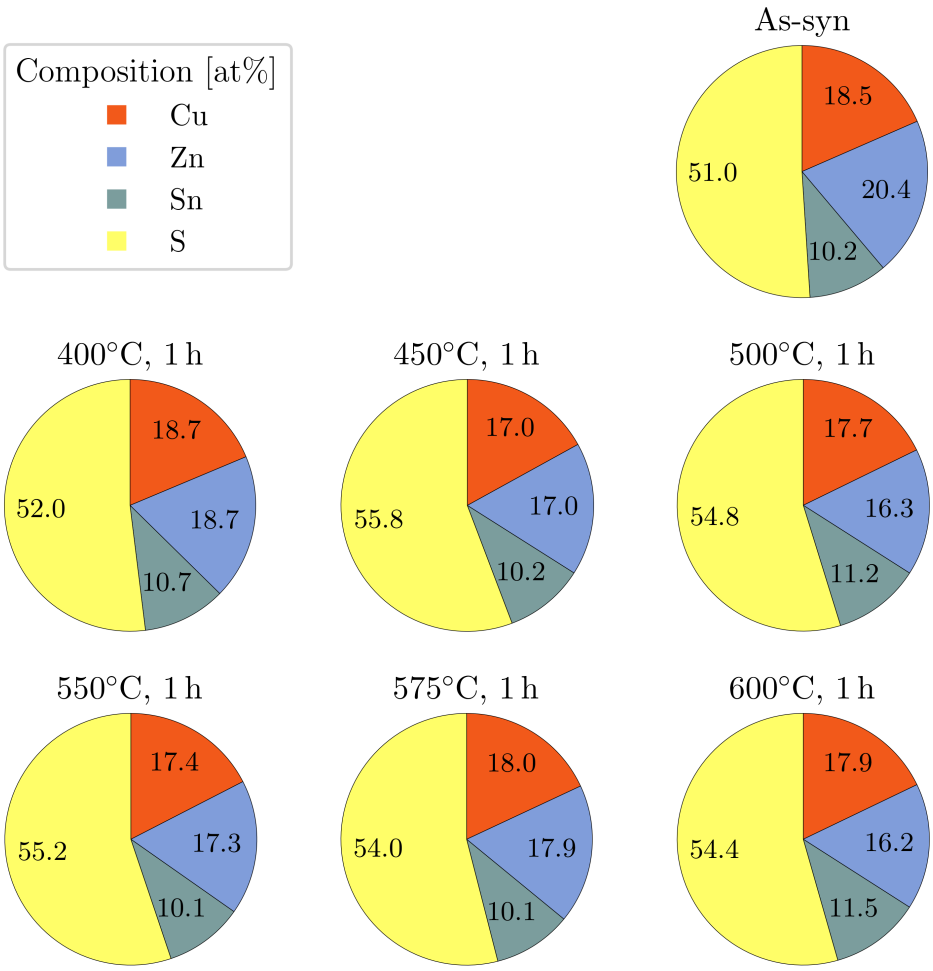

Fig. 6.11: These pie charts illustrate the normalised composition of the as-synthesised CZTS particles and the annealed films with varying annealing temperature, relative to the subgroup of elements under consideration. The former are measured as drop-casted on a piece of Si wafer whereas the latter are analysed as deposited on a glass substrate. Similarly to the cation ratios shown in Figure 6.10, there is no clear trend of the elemental concentrations to be observed. The Sn content is particularly stable. However, it becomes apparent a tendency of an increased sulphur content due to annealing in the sulphur-rich atmosphere but it is saturated for annealing temperatures of 450 °C or more.

for example some residuals from the precursor compounds, are not taken into consideration here. As discussed in Chapter 3, the carbon is a remainder of organic solvents used during nanoparticle and ink fabrication. The measurements reveal that all of the annealed films have a lower level of carbon as compared to the as-synthesised particles and that the amount is continuously decreasing with increasing annealing temperature indicating decomposition of residual organics. The reduced background level in different spectra of the annealed films as compared to the as-deposited samples is therefore likely to be partly related to the reduced carbon concentration.

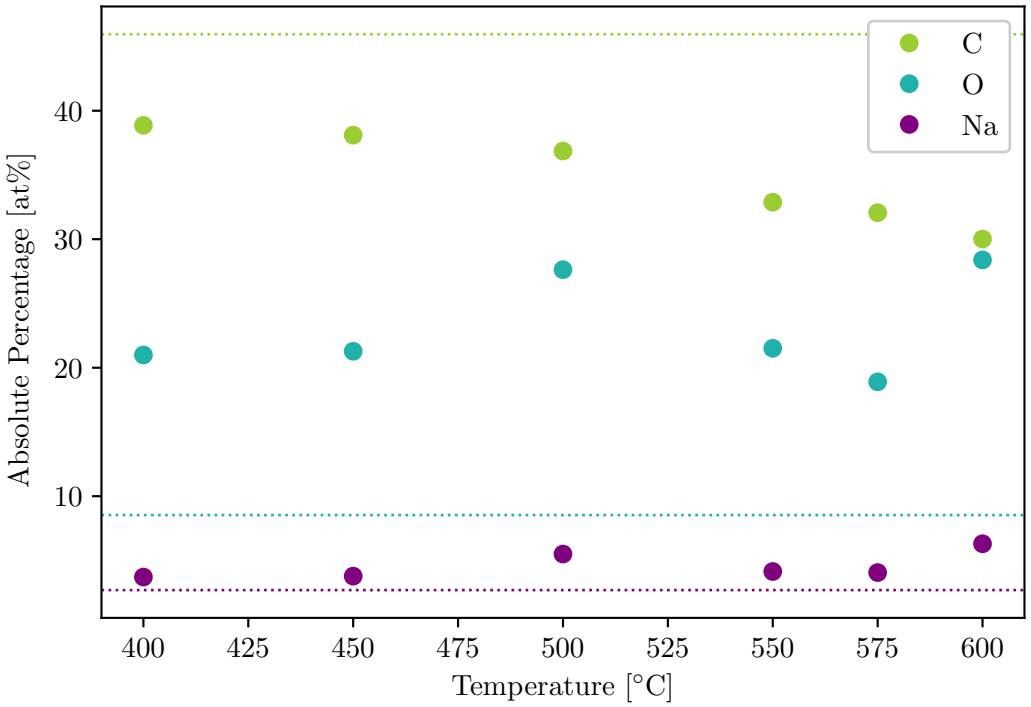

Fig. 6.12: Supplementary to the normalised CZTS composition illustrated in Figure 6.11, the total portion of other major elements present in the films is shown here. Namely, these are carbon (C), oxygen (O), and sodium (Na). The horizontal lines indicate the amount of the respective elements in the as-synthesised particles (measured on a piece of Si wafer instead of on a SLG substrate).

Oxygen can potentially be introduced to the particles during synthesis. Even though they are prepared in a flask that is either evacuated or filled with an inert gas (argon), the acetylacetonate precursors contain some oxygen. However, much more significant is probably the film deposition procedure where the layers are dried at a temperature of 300 °C in air in order to remove the liquid solvent prior to the next deposition step. This might explain why the oxygen content of the as-synthesised particles is significantly lower in comparison to all of the

annealed films. The composition of the as-synthesised particles has been measured with a small amount of ink drop-casted on a piece of silicon dried in air as well but at lower temperatures. The annealed films have an increased oxygen level, but no systematic dependency of the annealing temperature is observed and in addition, no further oxygen can be introduced during annealing in the furnace as it has been thoroughly evacuated of any residual air prior to filling it with the $H_2S : N_2$ mixture. The observations described suggest that the drying procedure during film deposition increases the oxygen content of the films. Consequently, it might be advised to develop alternative approaches of drying the films in-between spin-coating steps in an inert atmosphere rather than in air.

Sodium can diffuse into the films from the glass substrates during annealing. However, only a slight tendency of increasing Na concentration is observed with increasing annealing temperatures in this case. Furthermore, some Na is also contained in the as-synthesised particles. The latter are measured by drop-casting on a piece of Si wafer so that measurement artefacts due to penetration of the electron beam through the CZTS layer into the underlying, sodium-containing glass substrate can be excluded in this particular case. This is different for the annealed films on SLG but as discussed in Section 6.5.3 the penetration depth seems to be sufficiently small not to cause measurement errors. Consequently, Na is certainly contained in the nanoparticles themselves from the beginning, possibly contaminations from the precursor chemicals or diffusion from the reaction vessel. It remains the question whether the apparent increase in Na concentration is actually related to sodium diffusion from the substrates during heating in the furnace and to what extent the additional Na influences grain growth.

In contrast to the concentrations of Cu, Zn, Sn, and S which have been measured with specific X-ray lines in the EDX analysis to avoid any side effects of peak overlaps and the like, this has not been done in the measurement of the C, O, and Na concentrations. Hence, the results have to be interpreted with care and can only indicate some trends of the average amounts of these elements. As discussed later in the context of EDX map analysis in more detail, there are indications of a non-uniform distribution of sodium and oxygen across the film but this is also the case with respect to the constituents of CZTS themselves.

In particular, a non-uniform distribution of the elemental components might be related to abnormal grain growth. Figure 6.13 shows a comparison of the composition of the grains appearing on the film surface during annealing above a

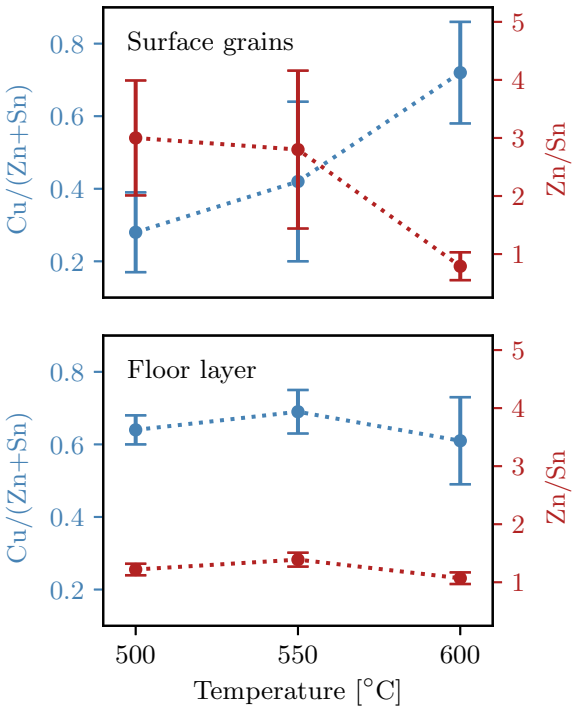

Fig. 6.13: Compositional comparison by means of the cation ratios – Cu/(Zn+Sn) in blue and Zn/Sn in red – between the surface grains (top) and the underlying nanoparticle floor layer (bottom). Dotted lines as guide to the eye. The measurement of this data set is illustrated in Figure 6.14 and the atomic percentages of the elements including sulphur are listed in Table 6.3.

temperature of 500 °C with the floor layer of nanoparticles underneath. For this purpose, a magnification of × 5k has been chosen with the other settings being the same as for standard measurements of the composition as specified in Section 5.3.2. Each sample has been analysed on three different sites and on each of these sites, five spot measurements of the composition of the surface grains and five spot measurements on the floor layer have been taken respectively to give an average value. During the measurement time, the area analysed shifted slightly, but by capturing a second image subsequent to the compositional analysis it has been verified that the measurement points were still on the area of interest, i.e. either on the selected surface grain or the floor layer. An image of an exemplary site analysed in this way is shown in Figure 6.14 for demonstration.

Whereas the Cu/(Zn+Sn) and Zn/Sn ratios of the floor layer remain relatively constant from 500 °C to 600 °C, the surface grains show some trends. However, it is also important to note that the standard deviation of the elemental percentages measured and hence of the cation ratios are much higher in case of the surface grains indicating that there is a wider spread of compositions present as compared

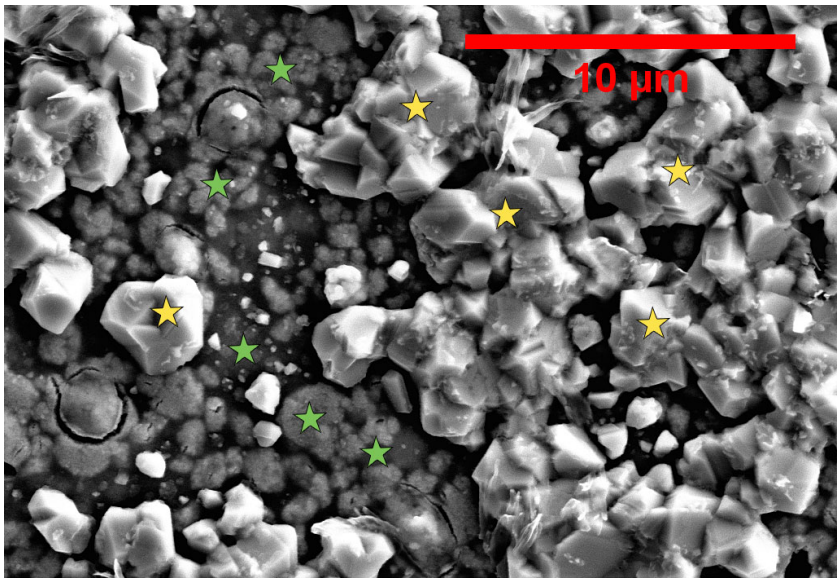

Fig. 6.14: SEM image of one exemplary measurement site on the sample annealed at 600 °C corresponding to the analysis of spatial differences in composition presented in Figure 6.13 and Table 6.13. Measurement spots on surface grains are indicated in yellow and spots on the floor layer in green. The results of three of these sites have been averaged for each sample.

to the more uniform bottom particle layer. The Cu/(Zn+Sn) ratio of the surface grains increases with increasing temperature, whilst the Zn+Sn ratio decreases. This indicates that they lose zinc in particular, even though the most commonly reported problem is a loss of Sn during annealing of CZTS as discussed in Section 3.3.1. As almost no change in composition is observed for the floor layer it is unlikely that the change in the surface grain composition is related to transport from or to the bottom of the film. Instead, the floor layer is probably less affected by the heating up and the interaction with the surrounding annealing atmosphere because it is less exposed to the gas environment. This way, elemental losses are prevented and the composition is more stable. At lower annealing temperatures (500 °C), the surface grains are richer in Zn (and potentially poorer in Cu) than the particles underneath. Towards higher annealing temperatures (600 °C), the concentrations measured for the surface grains surprisingly approach the values of the floor layer, finally resulting in nearly the same cation ratios. This may be related to enhanced diffusion rates under such conditions.

Table 6.3 presents the atomic percentages of the elemental components of CZTS divided into surface grains and the floor layer. In that data, the trends discussed above are less clearly visible due to the fact that the sulphur amount is not particularly stable and is neglected when considering the cation ratios. Nevertheless,

Tab. 6.3: The compositions of surface grains and floor layer are compared in terms of the normalised atomic percentages of the elemental components of CZTS for the samples investigated. The corresponding cation ratios are plotted in Figure 6.13 and an exemplary measurement site is shown in Figure 6.14.

Temp.	**Area**	**Normalised amounts [at%]**			
		Cu	Zn	Sn	S
500 °C	Surface	8.46 ± 2.89	23.01 ± 5.88	7.67 ± 1.62	60.86 ± 2.2
	Bottom	16.08 ± 0.72	13.85 ± 1.12	11.34 ± 0.32	58.73 ± 1.19
550 °C	Surface	13.93 ± 6.11	24.59 ± 9.82	8.78 ± 2.42	52.7 ± 2.75
	Bottom	18.19 ± 1.21	15.43 ± 1.22	11.12 ± 0.28	55.27 ± 0.77
600 °C	Surface	16.76 ± 2.44	10.27 ± 3.06	13.07 ± 1.07	59.9 ± 1.32
	Bottom	14.53 ± 2.71	12.26 ± 0.86	11.42 ± 0.72	61.78 ± 3.31

it becomes apparent again that the values of surface grains and floor layer lay closer to one another when the annealing temperature is increased. Taking the differences between these areas of the sample into consideration, the average compositions of the sample as a whole discussed earlier can only be interpreted as far as overall elemental losses are concerned. Off-stoichiometric, Zn-rich and Cu-poor surface grains are more likely to contain secondary phases such as ZnS for example. One indication for this could be the above-discussed deviations in composition. However, further analysis methods are necessary to analyse this in more detail, for example Raman spectroscopy and EDX mapping addressed within the following section. The latter also includes a brief discussion of the distribution of sodium and oxygen across the surface.

6.2.4. Phase Purity

Phase purity has mainly been checked by means of Raman spectroscopy. As it can be seen from the syntheses comparison in Section 6.1.4, the 785 nm Raman spectra of the nanocrystal batch used looks slightly different from the others. This may be partly due to an increased amount of carbon in the as-deposited films which increases the level of background signal. Also, the peak observed at around 190 cm^{-1} visible in the as-deposited films of this nanoparticle batch indicates the potential presence of the secondary phases SnS and/or $Cu_4Sn_7S_{16}$. It is very interesting to see in Figure 6.15 (a) that annealing with increasing temperatures reveals more and more of the expected peaks in the Raman spectra. Annealing hence promotes the formation of the kesterite CZTS phase. This process starts

between 400 °C and 450 °C. Carbon removal and a lowered background level could contribute to the changing appearance of the spectra as well since organic residuals start to decompose as confirmed in the previous section.

In contrast to the observations just described, there is nearly no difference in the spectra obtained with 532 nm excitation shown in Figure 6.15 (b). Already the as-deposited films clearly show the characteristics of a Raman spectrum of CZTS. This supports the assumption discussed earlier that non-resonant single-wavelength excitation is not sufficient to analyse the compound in question. The focus of further analysis is therefore on the measurements with 785 nm excitation.

The experimentally determined peak positions for the as-deposited and the annealed films can be found in Table A.7 (p 154). In addition, compounds that can be assigned to these peaks are given as well. It is important to be aware of the fact that some of these peaks are relatively weak in intensity and overlap with each other. It is therefore not only difficult to estimate the amount of detected secondary phases quantitatively but also occasionally possible that peaks are present but not identified. As the XRD spectra suggest that the samples consist of Cu_2ZnSnS_4, it is likely that secondary phases only occur in very small amounts. Their detection by means of Raman spectroscopy is most sensitive to the surface region, although this mainly applies to the excitation wavelength of 532 nm. 785 nm excitation probes more into the bulk of the sample. In addition to the CZTS peaks, there are indications of SnS and/or $Cu_4Sn_7S_{16}$ at about 190 cm^{-1} in the Raman spectra not only of the as-deposited but also of the annealed films. Their peak intensity decreases with increasing temperature as compared to Raman modes characteristic for CZTS. Also, no additional secondary phases are emerging upon annealing which is as desired.

Nevertheless, quite a few of the peaks assigned to CZTS are very close to those reported for some secondary phases such as SnS, Sn_2S_3, CuS, and $Cu_4Sn_7S_{16}$ so that their presence cannot be entirely excluded. Peaks found at about 127 - 131 cm^{-1}, 202 - 205 cm^{-1}, and 392 - 400 cm^{-1} could neither be associated to CZTS nor to any of the most common secondary phases. A further interesting observation is that a peak at about 330 cm^{-1} assigned to disordered CZTS (rather than kesterite CZTS) is contained in all spectra. Not all peaks found show clear correlations to the processing conditions. However, it is clear indeed that a main peak characteristic for kesterite CZTS expected at 337 cm^{-1}, here at around 335 cm^{-1}, is consistently present for annealing temperatures of 575 °C and 600 °C. This indicates the

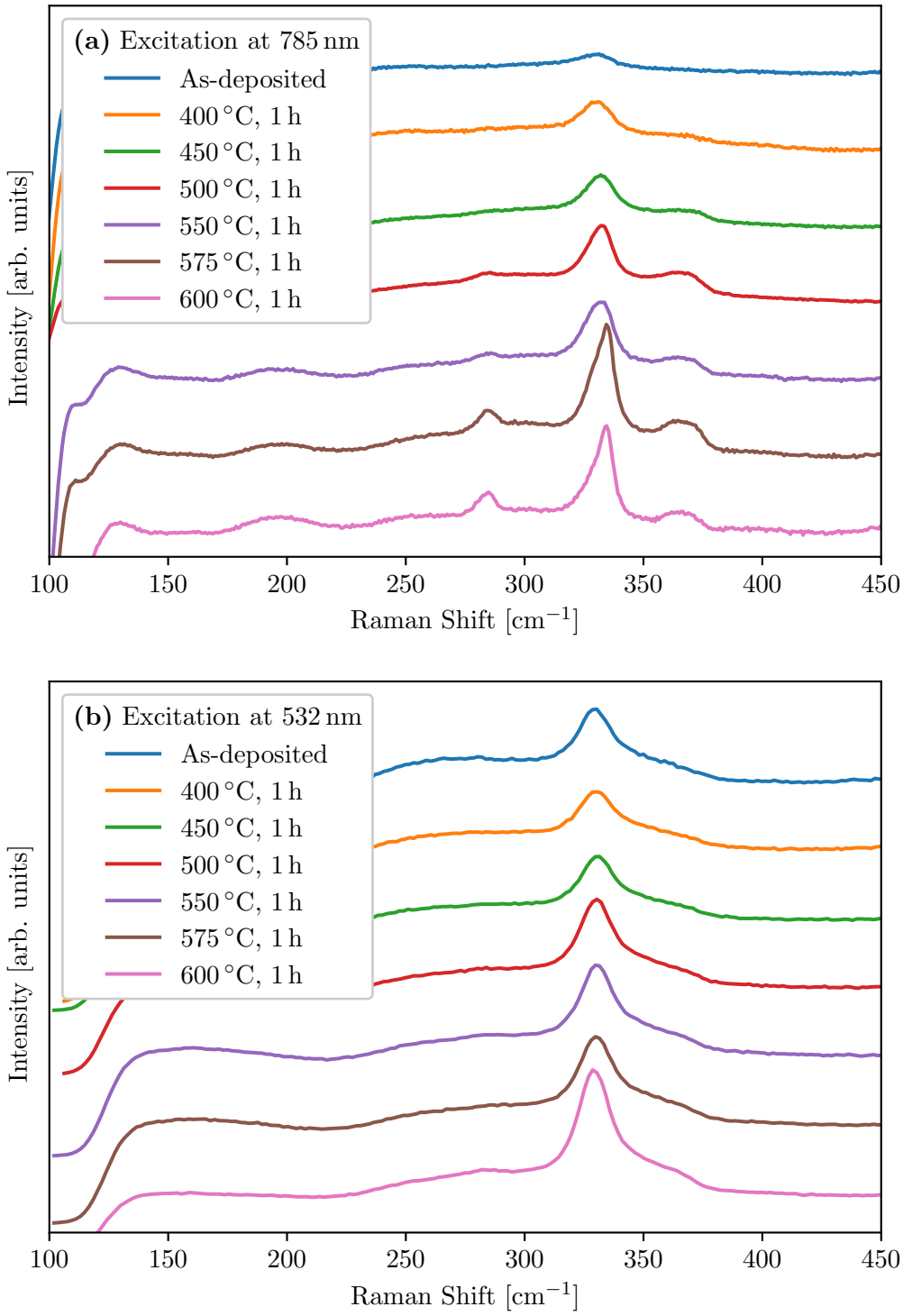

Fig. 6.15: The background-corrected Raman spectra measured with 785 nm (a) and 532 nm (b) excitation wavelength are shown respectively, where the different curves are shifted vertically for the purpose of clarity. For the analysis in terms of secondary phases refer to the main text and Table A.7 (p. 154) where the peak positions determined by fitting a series of Lorentzians are listed and assigned to the corresponding Raman modes. The fitted spectrum of the 600 °C annealed sample from part (a) is shown in Figure 5.6 (p. 57) as an example for peak analysis.

establishment of the desired phase at these higher annealing temperatures. Table A.7 provides further details.

EDX analysis has been taken into consideration for the analysis of phase purity as well. Exemplary mapping is shown in Figures 6.16 (SE and BSE images), 6.18 (maps of Cu, Zn, Sn, and S), and 6.17 (maps of O and Na) for the samples annealed at 500 °C and 600 °C. The instrumental settings correspond to those summarised in Section 5.3.2. The surface grains visible with the SEs can also be identified with the BSEs and some parts on the surface seem to be a bit brighter than the underlying nanoparticle floor layer. This might suggest the presence of secondary phases since BSEs also reveal compositional contrast. Generally, secondary phases are more likely to occur at higher annealing temperatures due to decomposition of CZTS. However, differences in contrast which are not related to the surface topography appear to be more pronounced at the lower annealing temperature. Seeming surprising at first, it fits the observation described in the previous section that the composition of floor layer and surface grains becomes more similar with increasing annealing temperature within the range investigated.

The distribution of Cu, Zn, Sn, and S in the colour maps of Figure 6.18 seems to be slightly more uniform for annealing at 500 °C, but nevertheless, the film heated to 600 °C also does not show significant correlations between the elemental distribution and the surface grains visible on the corresponding images. This points towards a relatively uniform phase despite of the slight contrast changes between floor layer and surface grains or other features on top of the film visible in the BSE images. These may be due to further elements contained in some parts of the absorber instead of being due to secondary phases. Figure 6.17 reveals a visible tendency of an increased sodium and oxygen level in some surface features (not necessarily abnormal grains) as compared to the nanocrystal floor layer, in case of 500 °C annealing in particular. Regions of interest are highlighted in the diagram. The observations may partly explain differences in BSE contrast despite of uniform distribution of the constituents of CZTS. The surface roughness of the samples, of the one annealed at 600 °C in particular, complicates the interpretation since compositional and topographic contrast are more difficult to distinguish.

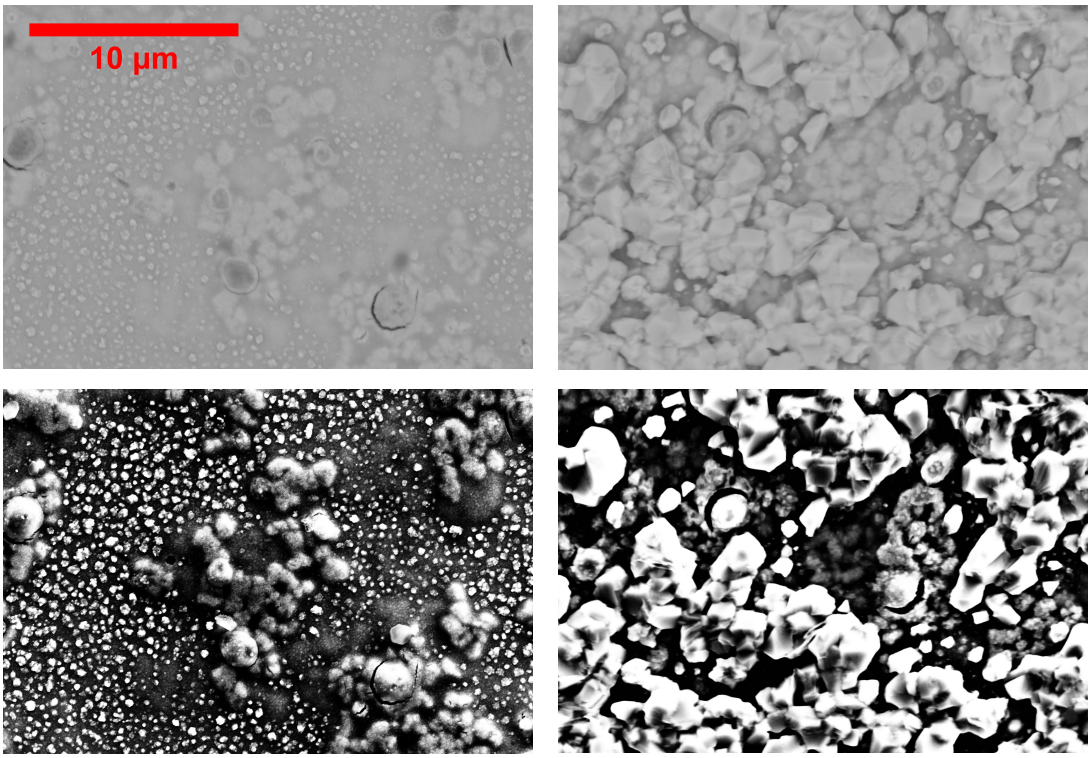

(a) Annealing at 500 °C **(b)** Annealing at 600 °C

Fig. 6.16: This figure presents the BSE images (top row – mainly compositional contrast) and SE images (bottom row – mainly topographic contrast) of one site on the 500 °C (a, left column) and on the 600 °C (b, right column) annealed film respectively. These sites investigated at a magnification of × 5k were analysed by EDX mapping as well, with corresponding colour maps in Fig. 6.17, 6.18.

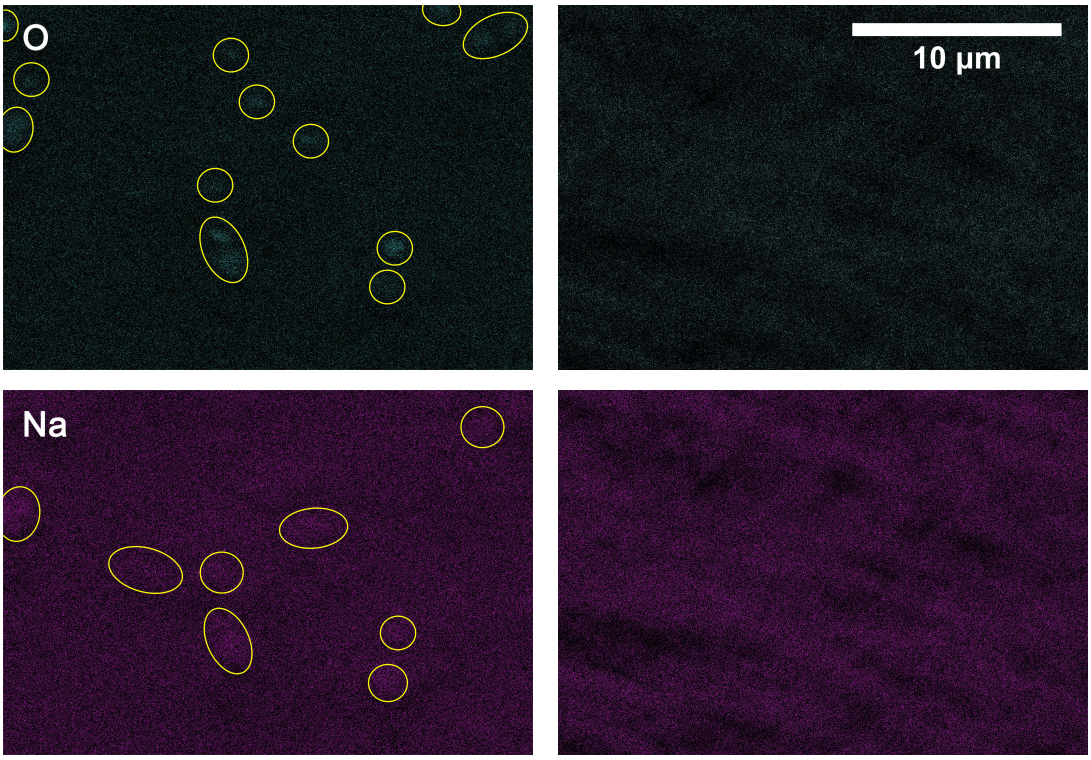

(a) Annealing at 500 °C **(b)** Annealing at 600 °C

Fig. 6.17: EDX colour maps of oxygen (O) and sodium (Na) corresponding to Fig. 6.16.

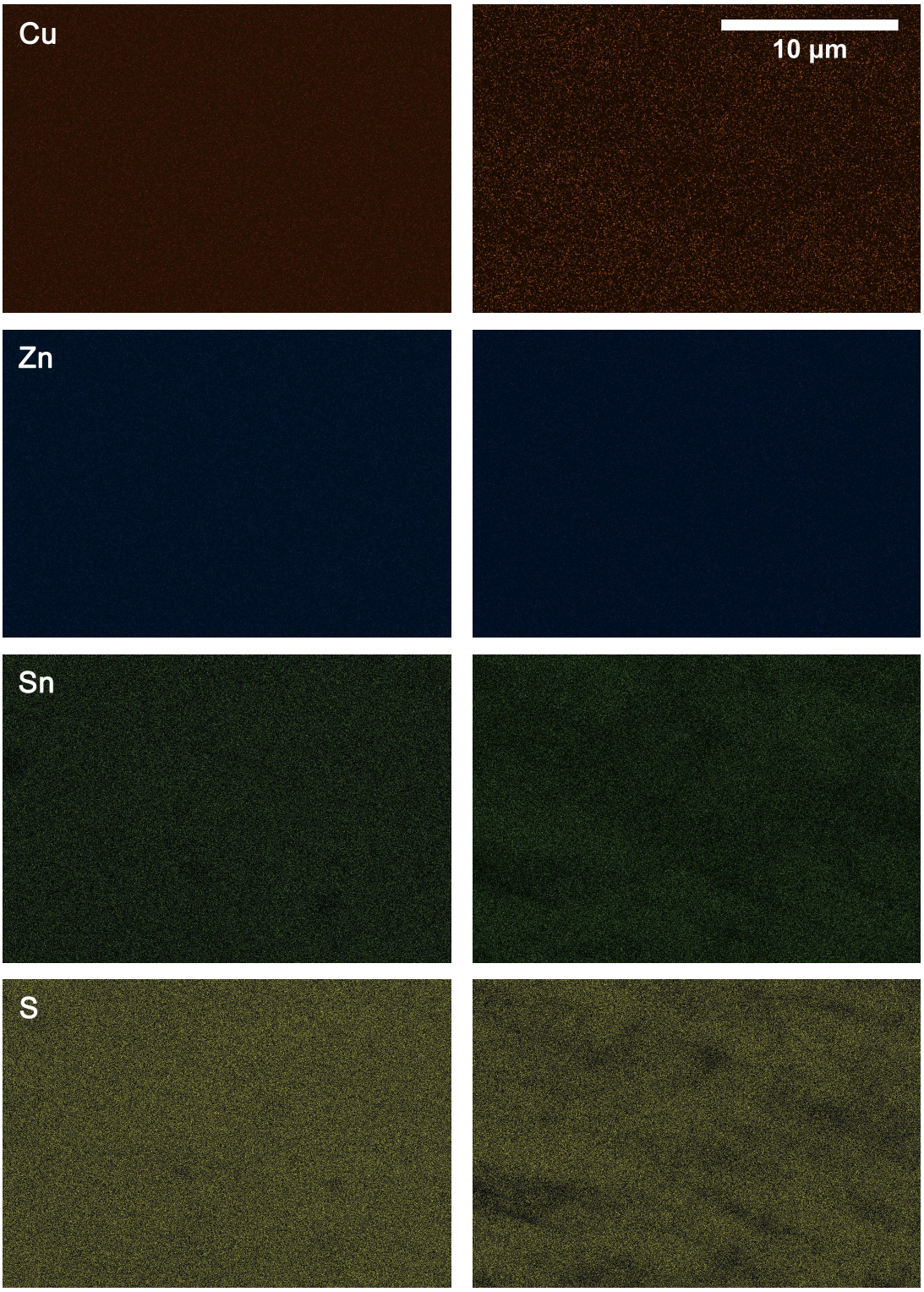

(a) Annealing at 500 °C **(b)** Annealing at 600 °C

Fig. 6.18: EDX colour maps of Cu, Zn, Sn, and S – the main components of the desired compound CZTS – corresponding to the SE and BSE images in Figure 6.16.

6.2.5. Opto-electronic Properties

Absorption spectroscopy as well as photoluminescence measurements with two different excitation lasers have been performed to investigate the opto-electronic properties which are crucial in the light of the potential application of CZTS absorbers in thin film solar cells.

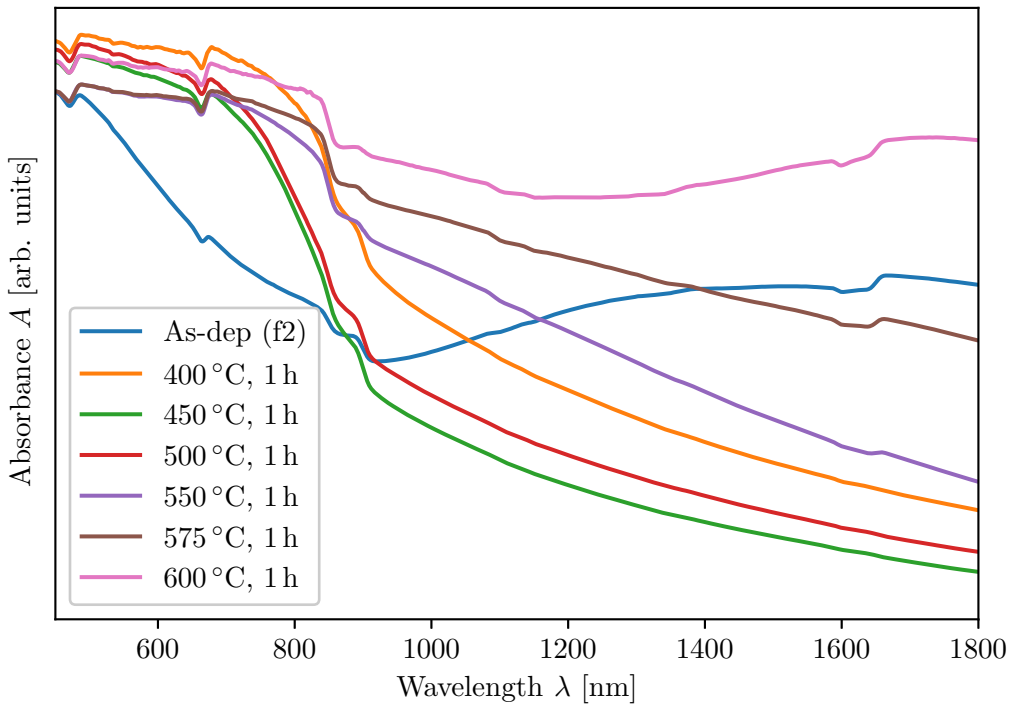

Fig. 6.19: This graph presents the UV-vis spectra for different annealing temperatures. The spectra of all as-deposited samples are shown in Figure A.1 (p. 153) supplemental to the example of film 2 (f2) shown here.

The absorbance spectra prior to and after the annealing step at different temperatures can be found in Figure 6.19. Already the as-deposited films have an unusual shape as compared to curves reported elsewhere – although the wavelength range displayed or measured is often smaller than it is here. Specifically, the curves from this experiment have a minimum at around 900 nm instead of approaching a constant value in the long wavelength limit. In this context it is very important to note that the features observed appear only after adding more than one layer to the film, which is discussed in detail in Section 6.5.4. The small discontinuities apparent in the spectra partly result from changing instrument parameters during the running scan as stated at the same place. Here, the focus is on the curve development due to annealing. The pronounced minimum observed for the as-deposited films disappears upon the high-temperature treatment, indicating that

absorption below the band gap energy is reduced significantly. Nevertheless, the absorbance does not approach a constant value but continues to decrease towards high wavelengths. In addition, the film annealed at the highest temperature of 600 °C has a distinct curve with a relatively flat shape having a minimum that does not fit the previously mentioned trend.

Section 3.3.4 discusses that annealing induces partial decomposition of the residual organics. However, also the hypothesis that decomposing ligands can cause trap states is mentioned in Section 3.1.2. As reported before, the present experiments reveal potential ligand removal by a lower carbon concentration in the annealed films indeed. However, the number of defect or trap states in the band gap decreases by annealing as it can be concluded from the fact that absorbance below the band gap is being reduced. Consequently, ligand decomposition does not seem to have detrimental effects in this case. The presence of defect states and band tailing in CZTS is supposedly not due to the level of cation ordering but rather due to band-gap fluctuations which have been attributed to nanoscale variations in the chemical composition [64, 65]. Slight fluctuations in composition have been discussed before and they may cause variations in band gap energy which are observed in the context of this study. The latter will be discussed below.

Due to the fact that the linear section in the Tauc plots is extremely narrow, the band gap determination from these spectra is difficult. There may also be some doubt about the reliability of the data set because even as-deposited films of the very same nanoparticle batch have a certain spread in the calculated band gap energies significantly larger than the statistical errors resulting from straight line fitting of the Tauc plots. Under the assumption of relatively uniform particles, this observation contradicts the expectation. Corresponding results of the as-deposited samples used for the present measurement series are summarised in Table A.6 (p. 153). For further discussion of potential errors in the UV-vis measurements see Section 6.5.4. In Figure 6.20, the band gap energy is illustrated as a function of annealing temperature. Each of the annealed thin film samples is directly compared with the as-deposited one in order to minimise the impact of any initial deviations.

The data presented may suggest that there is no clear trend in band gap energy which is induced by the annealing procedure, in particular considering the above-mentioned and later discussed sources of error in the absorption measurements. An alternative interpretation of Figure 6.20 would be an increase of ΔE_{g}, the

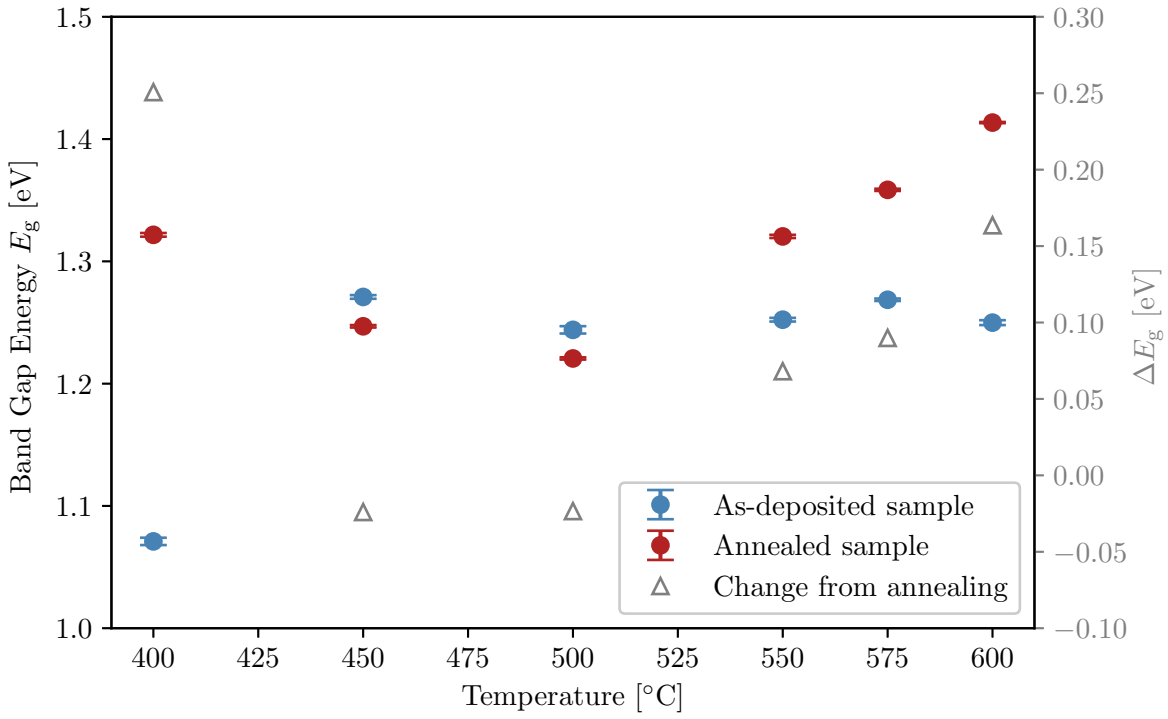

Fig. 6.20: The band gap energy E_g has been inferred from the UV-vis data plotted in Figure 6.19. It is important to be aware that quite different results were obtained even from the as-deposited films all of which were fabricated in the very same manner. Therefore, both the value measured on the respective as-deposited and on the annealed film are plotted at the corresponding annealing temperature as well as their difference $\Delta E_g = E_{g,\,\text{annealed}} - E_{g,\,\text{as-dep}}$ from one another (on the right-hand axis) which is expected to represent the change in band gap energy induced by annealing.

change in band gap energy induced by annealing, for annealing temperatures above 500 °C with no systematic dependency below this temperature. This assumption is consistent with initial experiments done in the context of this project and presented on a conference [130], suggesting that there is a trend of an increasing band gap energy with increasing annealing temperatures. However, this in turn would be in contradiction with findings from Long et al. [14]. Also, the present data set in Figure 6.20 exhibits a negative change of E_g at annealing temperatures of 450 °C and 500 °C. This not only contradicts the development observed for higher temperatures but also the large increase after annealing at 400 °C, which is the maximum of ΔE_g in the entire range investigated. In consequence, the trendline of increasing ΔE_g with increasing annealing temperatures is not truly consistent considering data points at 500 °C and lower. Also, there is no obvious correlation with the random fluctuations of the chemical composition discussed in Section 6.2.3.

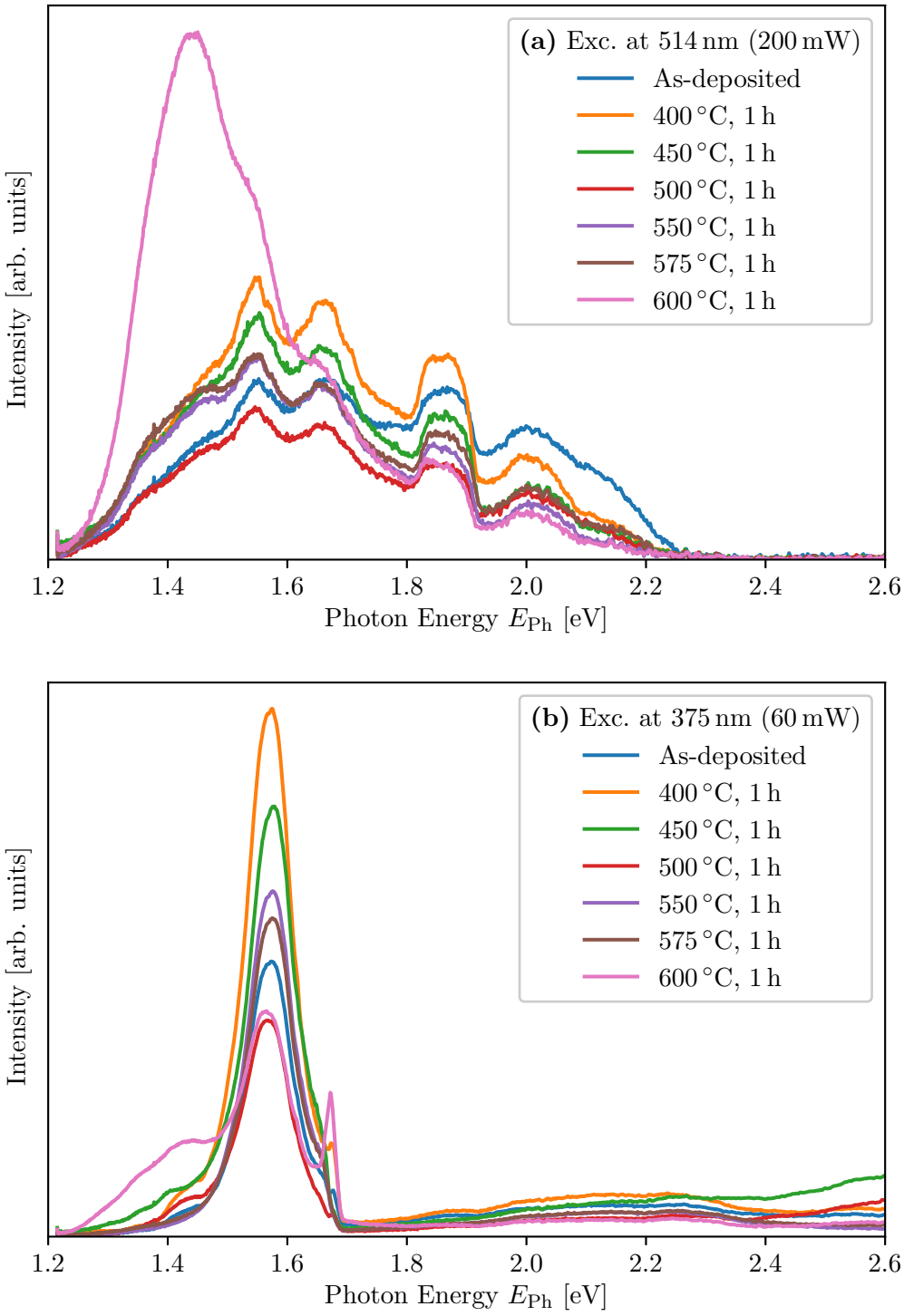

Fig. 6.21: Room temperature PL spectra of the samples annealed at different temperatures have been measured with a green excitation laser of $\lambda = 514\,\text{nm}$ (a) and a UV laser of $\lambda = 375\,\text{nm}$ (b) respectively. The peak positions of former spectra are given in Table A.8 (p. 155). Peak analysis by curve fitting is shown at the example of the spectrum of the 500 °C annealed sample from part (a) in Figure 5.10 (p. 72).

The annealed films have also been analysed by means of PL spectroscopy. Hönes [123] previously presented results from some annealing trials at $T = 500 - 540\,°C$ with $Cu_2ZnSnSe_4$ prepared by PVD, suggesting that annealing can change the PL spectrum significantly. This also becomes apparent in this study, where the effect of annealing temperature on the properties of Cu_2ZnSnS_4 nanoparticles is investigated more systematically. Figure 6.21 (a) shows the room temperature spectra resulting from an optical excitation with a green laser in the visible region (514 nm ≈ 2.41 eV, 200 mW). The corresponding peak positions derived from fitting a series of Gaussians to the curves are listed in Table A.8 (p. 155). The origin of the various peaks observed will be discussed below, for example with respect to different transition mechanisms, the influence of cation disorder, secondary phases, interference effects, and the influence of ligands. In general terms, the peaks occur in a PL band between 1.2 eV and 2.2 eV. The spectra of the as-deposited film and the films annealed at up to 575 °C have remarkable resemblance to one another regarding the peak positions and intensities, whereas the relative intensities in the spectrum of the film annealed at 600 °C are quite different. With the other analysis methods, for example Raman spectroscopy, minor changes were observed in this temperature range but not such a distinct change as in this case. Specifically, a formerly weak feature at about 1.43 eV becomes prominent in the PL spectrum in case of 600 °C annealing. The fact that this feature, which is presumably one of the characteristic CZTS peaks, dominates only in case of high annealing temperatures, indicates that these are necessary in order to promote the desired phase ordering and to suppress competing recombination mechanisms by modifications in the crystal structure.

It has been pointed out by others that the interpretation of the transitions in CZTS is not consistent in academic literature and that it has changed over time [26]. For example, Tanaka et al. [131] attributed the peaks found at 1.23, 1.35, and 1.48 eV to band-to-acceptor, band-to-tail, and band-to-band emission respectively. In contrast, Grossberg et al. [132] assumed that similar peaks observed at 1.27 eV and 1.35 eV are both due to band-to-impurity recombination based on the same deep acceptor defect, but arising from different types of Cu_2ZnSnS_4 with divergent lattice occupancy, i.e. from ordered and disordered kesterite. Support comes from more recent, systematic studies on Cu-Zn disorder, showing that the PL spectra of CZTS are highly dependent on the level of cation ordering, the main peak lying between 1.32 eV and 1.43 eV [30] or between 1.21 eV and 1.35 eV [133] shifting to higher energies going from disordered to ordered kesterite respectively. Scragg et al. [30] also anticipate that the peak would shift further up to about 1.5 eV,

the fundamental band gap energy, if optimum order could be reached. However, based on the fact that the peak is usually reported to be at 1.3 eV - 1.35 eV, they conclude most specimens discussed in publications contain disordered CZTS.

In this study, as it can be seen from Table A.8, one peak at 1.32 eV - 1.38 eV and another one at 1.46 eV - 1.5 eV are found within the energy range just discussed. They can hence either be assigned to band-to-impurity and band-to-band recombination respectively or they can both be assigned to band-to-impurity recombination with diverging energies due to areas with different degrees of structural disorder present in the polycrystalline CZTS films. One peak below at 1.27 eV-1.28 eV and one in-between at 1.43 eV-1.45 eV appear additionally in some cases. Neglecting the above-mentioned ambiguity of peak interpretation, the observation of the specified peaks could suggest that the nanocrystals synthesised represent a mixture of particles with different levels of Cu-Zn order with tendency towards a disordered kesterite structure. This would agree with the present signs of disordered CZTS in the Raman spectra. As the annealing temperature does not affect the peak positions in a systematic manner, it may be assumed that no significant change of the band gap energy is induced, being in agreement with one of the possible interpretations of the results from UV-vis spectroscopy.

Many publications not mentioned yet deal with the theoretical explanation of the broad PL band around 1.3 eV in CZTS. These include for example the model of fluctuating potentials stating that, as in heavily doped semiconductors, band edges are broadened out by a high density of charged impurities in the band gap leading to tail states [60, 61]. Optically active impurity states can, for example, be related to intrinsic defects including antisites, vacancies, and interstitials. Recent examples include the application of the deep donor - deep acceptor pair model, the donor being an interstitial Zn atom and the acceptor a Cu_{Zn} antisite defect [134] and the quasi-donor acceptor pair model [135] to mention only a few. However, the data presented here is influenced by further contributions as well as by potential measurement artefacts discussed later. This is why the models just mentioned are not evaluated in more detail.

In addition to the CZTS peaks discussed earlier, more spectral features, especially at energies well above the band gap, are found in this study. Some of these peaks might originate from secondary phases, literature values for which are summarised in Table 5.2 (p. 72). By comparison with the experimentally determined peak positions it becomes apparent that the spectral features observed do not necessarily

coincide with the expected ones. However, as insinuated before, material-inherent properties such as cation order and disorder, but also temperature and laser power can shift the peaks. Due to these relations, the published peak positions can only provide approximate reference values. Based on these, possible candidates for secondary phases according to the peaks found are ZnS, SnS_2, and Sn_2S_3. However, not all peaks expected for these compounds are detected. The detailed assignment of the measured peaks to the different compounds is given in Table A.8 (p.155). It is conceivable that the particles or grains are not quite homogeneous and that they consist of different phases which become apparent as additional peaks in the CZTS PL spectra. The search for features at lower energies to check for any indications of other secondary phases only yields a flat curve as visible in Figure 6.22. Higher energies, i.e. lower wavelengths could not be tested due to the cut-off wavelength of the glass filters used to block reflections from the excitation light.

However, the difficulty to identify secondary phases by means of PL spectroscopy has been pointed out by others already [26]. Many of the peaks can be assigned to more than one compound and Cu_2S as well as SnS in particular cannot necessarily be distinguished from Cu_2ZnSnS_4. In the context of this study, it should be emphasised that – except potentially from a small amount of SnS and/or $Cu_4Sn_7S_{16}$ – no other secondary phases could be detected with certainty by Raman spectroscopy as analysed in Section 6.2.4. This would disagree with the compounds supposedly identified by PL even though Raman spectroscopy is more established for secondary phase identification in CZTS. The above-described interpretation of the PL spectra is therefore to some degree to be considered as questionable. Alternatively, some of the Raman peaks assigned to CZTS may partly originate from the indicated secondary phases with overlapping reference peaks.

Additional PL spectra of the annealed films have been measured with excitation in the UV region (375 nm $\approx$ 3.31 eV, 60 mW) resulting in another response of the electronic structure of the material investigated. This is shown in Figure 6.21 (b). In contrast to the appearance of the spectra measured with the green laser discussed above, excitation at this lower wavelength or higher energy results in one dominant recombination pathway for all annealing temperatures. Again, the as-deposited film as well as all samples annealed at up to 575 °C have very similar spectra whereas after annealing at 600 °C, another feature at about 1.45 eV, probably related to kesterite Cu_2ZnSnS_4, appears. This is similar to the observations in the

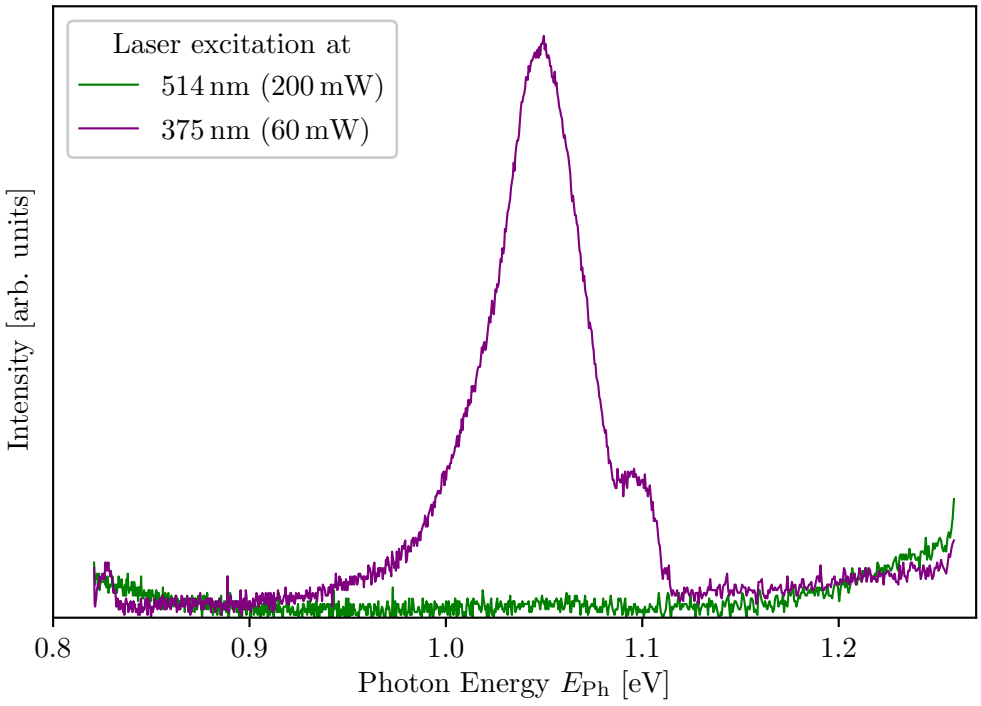

Fig. 6.22: The PL spectra have been checked for features at lower energies with both, the green (514 nm) and the UV (375 nm) excitation laser. In contrast to some overlapping peaks observed for the UV laser, no signal is detected with the green laser in this regime. For these room temperature measurements, a 10-layer thick, as-deposited thin film on Mo-coated SLG glass with CZTS particles from batch Syn11 has been used. The Mo layer does not contribute and is expected to exclude contributions from the underlying substrate as light cannot transmit through.

context of the previous excitation wavelength, but in this case the appearing peak is less pronounced in terms of relative intensity and it is less intense than the main peak at around 1.57 eV. The latter is neither one of the peaks expected for Cu_2ZnSnS_4 nor can it be related to a secondary phase. As a general observation, the relative intensities are clearly different and not all of the peaks are visible as compared to the spectra from excitation in the visible region. However, the peaks present could also be found in the spectra taken at the other excitation wavelength analysed before. The more detailed analysis in terms of secondary phases done for the excitation with the green laser is hence not repeated. In contrast to the excitation in the visible region with the green laser, an additional feature is found at lower energies or higher wavelengths in case of UV excitation. This is demonstrated for an exemplary sample in Figure 6.22. In case of the UV laser, three overlapping main peaks are found at 1.0417(6) eV, at 1.0508(2) eV, and at 1.1002(3) eV. These could potentially correspond to the secondary phases SnS

(reference peak at 1.12 eV) or alternatively Cu_2SnS_3 (reference peak at 0.95 eV). The former compound was consistently identified by Raman spectroscopy but nevertheless, the latter in particular was mentioned to be easily distinguished by PL spectroscopy [123]. It is worth mentioning that no contribution of this peak is visible in case of excitation with the green laser at all. This fact may suggest that in case PL spectroscopy shall be applied to secondary phase identification in future studies, more than one excitation wavelength should be used for this purpose similar to the procedure used in Raman spectroscopy.

It should also be noted that the UV laser and the green laser have different penetration depths due to their wavelengths and the related absorption coefficient of the material under investigation. It is conceivable that the nanocrystals consist of a core and an outer shell of different phases with varying properties such that the two types of laser probe different areas of the particles effectively. As an alternative explanation, it could be the ligand coating which leads to an alteration of the recombination paths. Campbell et al. [135] recently presented a study about the influence of different ligands on opto-electronic properties. By using PL spectroscopy, CZTSSe particles with ligands originating from oleylamine and formamide were found to exhibit similar transitions at low temperatures whereas at higher temperatures, the former revealed another process of recombination. As PL measurements were performed at room temperature in this study and the particles are OAm capped, a relation between the presence of ligands, the penetration depth of the different excitation lasers, and the resulting spectra is conceivable.

Despite of all the interpretative approaches from above, the spectra measured still contain more peaks at around 1.55 eV, 1.67 eV, 1.85 eV, and 1.89 eV for which no explanation has been proposed so far, mainly in case of excitation in the visible region. Furthermore, it was surprisingly found that the PL spectra hardly change when the measurement temperature is lowered from room temperature down to 3 K. This is shown in Figure 6.23. The intensities vary slightly, but there are no systematic changes at all. The peak positions can be considered as constant too. Usually, the intensity should increase significantly with decreasing temperature as thermal quenching is a prominent effect in photoluminescence. Corresponding mathematical relations are for instance summarised in [26]. Taking this into account, it is worth to look at other characteristics of the specimen that could result in peak-like features in the emission spectrum.

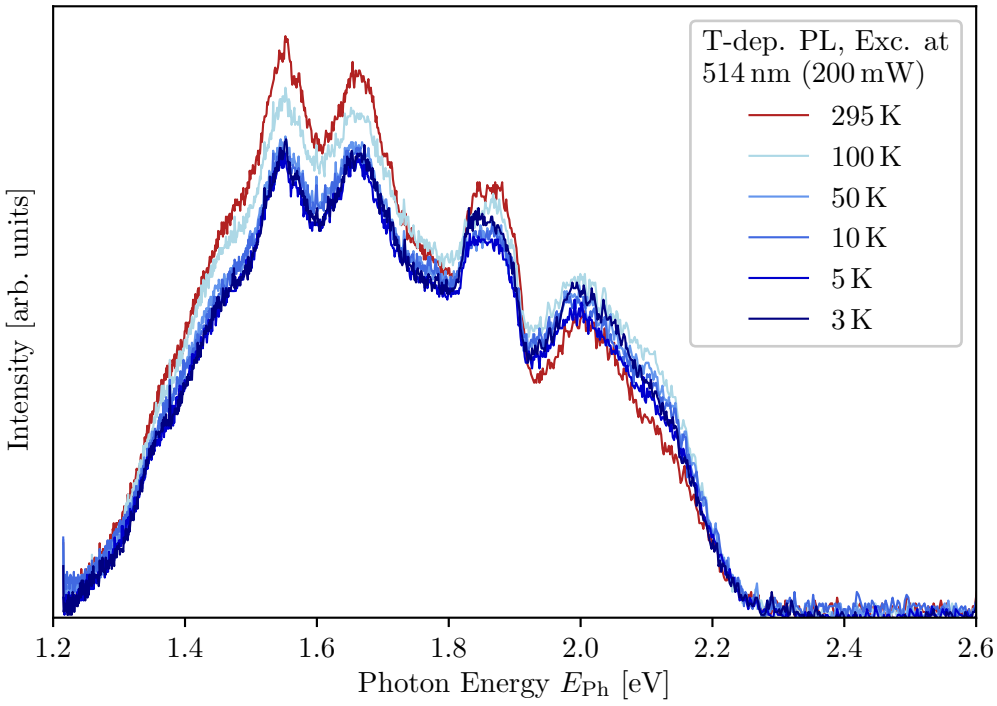

Fig. 6.23: The temperature dependency of the PL intensity has been measured with the 514 nm green excitation laser in a range from room temperature down to 3 K. The sample was an as-deposited film of the CZTS nanocrystal batch Syn11 on SLG. Surprisingly, the intensities do not increase with decreasing temperature as one would expect. This may indicate that at least some of the spectral features are not originating from the material itself as explained in the text.

An important aspect to be considered arises from interference effects. Larsen et al. [136] demonstrated experimentally as well as with the aid of simulations that the usage of thin films can result in peak-like features or 'fringes' within the spectra at the example of CZTS absorber layers. This is shown in Figure 6.24. The extent of the effect depends on the layer thickness. The authors suggest to use layers thicker than 10 microns in order to avoid any distortions of the PL spectra. As this is not satisfied, the films used in this study may suffer from these interference effects as well which is crucial for the interpretation of the peaks. This calls into question the analysis presented above. These suspicions may explain the absent temperature dependence of the PL intensity discussed in Section 6.5.5 since interference effects are not suspected to depend on the temperature. They may also be the reason why some of the peaks could not be assigned to CZTS or any other compound. Furthermore, the spectra with UV excitation might be less effected by the interference due to the different wavelength.

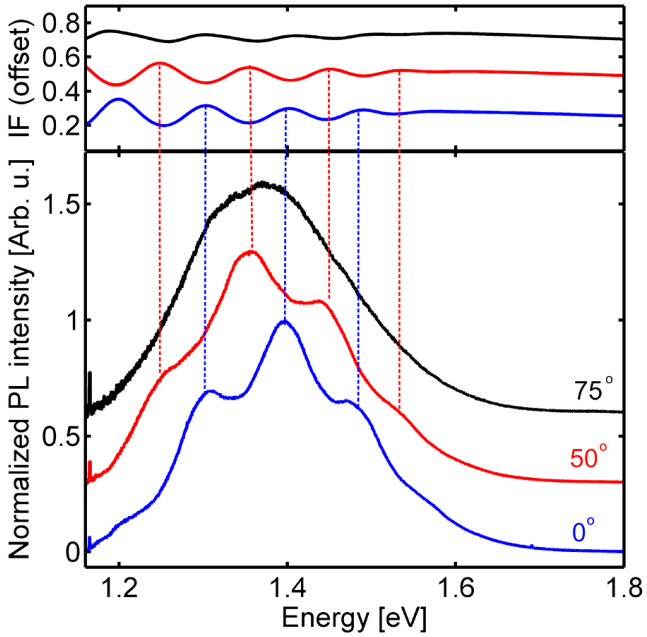

Fig. 6.24: Illustration of interference effects in PL spectra of thin films and its dependence on the tilt angle (relative to the surface normal). The upper part shows the calculated interference function IF. The lower spectra have been measured at room temperature on a CZTS thin film sample. If the specimen is tilted by 75°, nearly no interference effects appear in the spectrum. However, if it is not tilted but mounted perpendicular to the incident beam as it is typically done, the peaks clearly coincide with those in the interference function, revealing the origin of the intensity modulation measured. Illustration from Larsen et al. [136].

It is, however, important to note that Larsen et al. used a different approach to material fabrication as compared to this study. Their sulphurised layers prepared by reactive sputtering may be smoother and more uniform than films from the nanoparticle approach used here. In consequence, interference effects are less likely to occur in the present work. The surface morphology of the annealed samples has been described in Section 6.2.1. For annealing temperatures up to 500 °C, the resulting film surface was observed to be smooth and shiny, changing to a rougher surface for 550 °C or higher annealing temperatures. Since the PL spectra do not exhibit significant changes in this temperature region but only when increasing it from 575 °C to 600 °C, surface roughness apparently does not play a role for the peaks detected. If interference effects were present, in contradiction, changes in film roughness would be expected to change interference patterns [136]. From this it can be concluded that interference effects are not very likely to be present in the experimental data discussed here. Instead, surface ligands may provide a more suitable explanation as discussed further below.

If interference was confirmed to have caused the mentioned observations, careful elimination of similar effects in the other measurement techniques would have to be implemented. In terms of PL spectroscopy, the question remains why luminescence is detected in a band well above the band gap whereas it is usually reported to appear at lower energies in CZTS. Interference only imposes a modulation of the intensity. Maybe the actual spectrum does not only consist of the broad PL band of CZTS but overlaps with one or more peaks of secondary phases in addition. This appears to be difficult to verify on the basis of the data available. Irrespective of these considerations, the confirmed promotion of the kesterite CZTS phase due to annealing at 600 °C is probably still valid, as the film thickness is not expected to change significantly during annealing so that interference effects do not change. A similar argument holds for the small band of peaks found at higher wavelengths in case of UV excitation assigned to SnS and/or Cu_2SnS_3. The former compound has more peaks at higher energies (see Tab. 5.2) which would contribute to the set of modulated peaks observed upon excitation with the green laser, supporting the assignment of the peak to SnS.

Not many PL studies have been published so far on nanoparticle-based CZTS absorber layers. Hamanaka et al. [137] did present such a study on CZTS nanoparticles on quartz substrates that had been synthesised via another solution-based method. They are relatively small (approx. 7 nm) and have an approximately stoichiometric composition. No annealing procedure was involved. The authors observe a broad asymmetric PL band with an intensity maximum at 1.22 eV which roughly spans the energy range between 1 eV and 1.5 eV. As this emission is below the band gap, the authors concluded that band-to-level transitions lead to the photoluminescence measured; the intraband levels are probably due to some point defects as inferred from the relatively low temperature and excitation power dependence of the spectra measured. Here, the PL bands span a wider range including energies above the band gap. In addition, the peak-like features found are not present in the spectra of Hamanaka et al., although they mention that peak overlaps are likely due to the asymmetry of the PL band. No conformance between calculated ionisation energies for possible intrinsic defects in CZTS and the experimental results could be substantiated by their group. Based on this, Hamanaka et al. conjecture that the defects in question and the resulting PL emission might originate from the solution-based synthesis, in particular on the nanocrystal surfaces. For example, these might have dangling bonds, vacancies, and external adatoms [137]. If this assumption of artefacts from the synthesis approach chosen is true, similar effects could contribute to the spectra within the

framework of the present study. This also relates to the dependence on different ligands studied by Campbell et al. [135] which has been discussed in the context of penetration depths already.

Whereas Campbell et al. [135] looked at differences of relevant transitions in the PL spectra comparing two types of ligands, another study by Zaberca et al. [138] investigated surfacant-free nanocrystals where PL spectroscopy revealed low defect concentration. In both cases, a single PL peak is observed which is different from the emission spectrum consisting of a series of peaks observed in the present experiments. Unfortunately, not many studies on the effect of ligands on the PL spectra of CZTS nanoparticles have been published so far apart from those just mentioned. It remains an open question whether ligands could be responsible for some of the additional peaks observed which are not generally expected for CZTS. Nevertheless, other observations partly discussed in Section 3.1.2 of the effects of ligands on the electronic interaction of individual particles, opto-electronic and transport properties, carrier recombination, band alignment, as well as on the performance of complete solar cell devices [75, 76, 139–142] underline that further investigations in terms of photoluminescence are strongly recommended. These will involve ligand exchange and removal procedures.

6.2.6. Conclusions

The experiments presented in the previous chapter clearly show that the annealing temperature, in this case investigated in a range between 400 °C and 600 °C, is an important parameter to influence the material properties of a thin film made of CZTS nanocrystal ink. Between 450 °C and 500 °C, abnormal grains start to grow on top of the nanoparticle layer. Their growth is enhanced with increasing annealing temperatures, particularly when raising it from 575 °C to 600 °C. At 575 °C, the abnormal grains have a size in the micrometre range already and at 600 °C, they cover a significant portion of the sample surface in the form of 'islands' with a diameter of several microns. Coverage may be enhanced by choosing a longer annealing time. The enhanced grain growth comes along with an accelerated increase of the average domain size of the crystallites above 500 °C, finally reaching a value of 104 nm as measured in these experiments for an annealing temperature of 600 °C. Since large-grained absorber layers heretofore were found to be favourable in terms of the currently achievable device efficiencies as discussed in Section 3.3.1, the observations suggest the use of annealing temperatures around 600 °C. Similar developments in the film morphology by abnormal grain growth have been

observed in other studies as well, some of which are broached in Section 3.3.2.

The grain growth mechanism is generally assumed to be influenced by carbon decomposition and sodium diffusion from the substrates as explained in Sections 3.3.4 and 3.3.5 respectively. In the present study, a decrease of carbon concentration with increasing annealing temperature was confirmed. This might also explain the lowered background level in different spectroscopic measurements on the annealed films. The average concentration of sodium in the films increases only very little upon annealing; however, it accumulated in certain features on the film surface. The latter finding may indicate diffusion from the bottom to the top of the absorber layer. Nevertheless, the fact that the overall Na content does not increase much casts doubt on whether significant amounts of this element were introduced to the material by the substrates or whether the sodium comes from the particles themselves instead. The oxygen content does not depend on the annealing temperature, but it is found to be at a higher level than that of the as-synthesised material and is detected at increased concentration in some surface features, too. The oxygen is probably introduced by soft-baking in air during spin-coating. It may be worth to refine the measurement procedure of C, Na, and O for future studies in order to reach similar confidence as in the analysis of the elemental components of CZTS itself, e.g. by considering potential peak overlaps.

In terms of copper, zinc, tin, and sulphur, the average composition and the cation ratios in particular are relatively constant with respect to the annealing temperature despite some random fluctuations. The sulphur content is increasing as compared to the as-synthesised particles and low annealing temperatures, but stays more or less constant from 450 °C upwards. However, there are indications of a non-uniform distribution of these elements which is related to the abnormal surface grains. Whereas the floor layer exhibits relatively constant cation ratios, the surface grains, which are more exposed to the annealing atmosphere, show a wider spread of values as well as a loss of Zn in particular with increasing annealing temperature. Interestingly, floor layer and surface grains have more similar compositions at an annealing temperature of 600 °C than at a lower temperature of 500 °C. EDX mapping with the measurement parameters chosen appears to be less effective to detect the tendencies discussed as compared to spot measurements on the areas of interest. Nevertheless, the EDX measurements are able to confirm that annealing at 600 °C results in a more uniform distribution of elements than at 500 °C, which would be advantageous in terms of fabricating devices based on such films. Furthermore, BSE images indicated the potential

presence of secondary phases and/or the accumulation of other elements in specific areas on the sample surface for 500 °C annealing in particular.

The results from Raman spectroscopy as the main tool for secondary phase identification, clearly confirmed a promotion of the desired kesterite phase by increasing the annealing temperature, starting between 400 °C and 450 °C. These developments could only be detected with resonant excitation, underlining the importance of its application. Small amounts of SnS and/or $Cu_4Sn_7S_{16}$ could be detected in the samples; peaks of other potential secondary phases coincide with those assigned to CZTS and can hence not be identified with certainty. The low portion of unwanted compounds agrees with the fact that no additional peaks were found in the XRD spectra. A potential reason for a suppression of decomposition during annealing is the relatively high sulphur concentration of the annealing atmosphere used as compared to other studies. Secondary phases are likely to occur mainly on some isolated areas on the sample surface as suggested by BSE imaging. There are indications of disordered kesterite in the Raman measurements which may also explain a peak splitting observed in XRD and shifts of a characteristic PL peak discussed earlier. This would agree with the assumption from other authors that the predominant part of CZTS specimen used for academic studies has a high level of disorder [30] and that thermal treatment is not suitable to improve this [143].

Changes of the relative peak intensities in the XRD spectra indicate structural changes in the atomic basis according to which the unit cells are occupied. Nevertheless, the peak positions are in good agreement with the expectations for the compound CZTS, meaning that the lattice system itself is maintained. The peaks do hardly shift with changing annealing temperature which indicates relatively stable lattice parameters. Only a slight tendency towards a widened structure may be present that could potentially be related to the incorporation of impurity atoms, e.g. sodium. Such defects could also be the reason for a change in the structure factors determining the modulation function of the Bragg reflections and hence the relative peak intensities.

Below-band-gap absorption in the as-deposited films revealed by UV-vis spectroscopy decreases upon annealing, even though the expected long-wavelength constant limit of the absorbance is still not observed. Nevertheless, the observations indicate that defect density is reduced. The reliability of the data set is put into question regarding the derivation of the band gap energy. The band gap

energies determined from different films made of the same nanocrystal ink and with the same procedure show unexpected deviations from one another indicating necessary adjustments of the measurement procedure to eliminate any artefacts in the data. As good as it can be concluded from the Tauc plots having a relatively narrow linear section, the band gap does not show a completely consistent trend with changing annealing temperature. Random fluctuations in band gap energy without systematic changes would agree with findings from PL spectroscopy. Only for temperatures higher than 500 °C, the change in band gap energy induced by annealing increases monotonically with increasing annealing temperature as indicated by absorption spectroscopy.

The characteristic CZTS features in the PL spectra slightly below the band gap energy measured with 514 nm excitation wavelength do not exhibit shifts with varying annealing temperature. However, the relative intensity of these peaks compared to other spectral features are changed significantly at a temperature of 600 °C indicating a suppression of competing recombination mechanisms and a promotion of the desired CZTS phase. Devices with high efficiencies presented in the literature were reported to exhibit a single dominant PL transition as well [5, 144, 145] so that also in this regard, the observations of the present study are in favour of relatively high annealing temperatures. It should be mentioned that different from this, an earlier study looking at the opto-electronic properties of sulphurised CZTS from sol-gel deposition suggested 500 °C as the optimum value but importantly without considering data from PL measurements [14]. Differences in the results may be partly due to the other approach to fabrication. In the present study, a number of additional features detected that are not expected for CZTS, including peaks at energies well above the band gap of the material investigated, complicate the interpretation of the PL spectra obtained. A possible explanation is that the solution-based synthesis approach causes surface states on the particles' outside potentially related to ligands. Considering findings from academic literature mentioned in Section 5.6.1 and the discussion of the results from the present study, the assignment of secondary phases to the peaks seems to be questionable. It is, in contrast, conceivable that the actual PL band is modulated by interference effects of the thin films. This would also explain the absent temperature dependence of the peak intensities. However, considering the surface roughness of the samples used, the impact of ligands seems to be a more appropriate explanation than interference effects.

Despite of these considerations, a PL peak at lower energies detected by measure-

ment with a 375 nm UV laser indicates the presence of some SnS or Cu_2SnS_3. The detection of former compound agrees with the findings from Raman spectroscopy mentioned before. The comparison with a second wavelength to induce photoluminescence most importantly revealed the domination of significantly different recombination paths, one particular in the UV region. It is conceivable that this is due to particles with inner and outer shells of different material composition. These would be probed by different lasers of differing penetration depth. Ligands left behind on the particle surfaces from synthesis and altered during annealing could impact the corresponding PL spectra in this way as well. Alternatively, the observation of one dominant recombination path in case of UV excitation as compared to excitation in the visible region might be due to a limitation of interference effects in the particular case of the about half a micron thick films used. In this case, using other excitation wavelengths, if not restricted by opto-electronic characteristics of the material, could be an alternative way to limit interference effects in PL studies of thin films in addition to those proposed by Larsen et al. [136]. Overall, however, the impact of ligands may be considered a more likely explanation than interference effects.

Opto-electronic properties and their impact on device performance were discussed in Section 3.3.6. According to this, secondary phases do not necessarily have a detrimental effect. They are found in small amounts in this study, but SnS is the only one confirmed by Raman as well as potentially by PL spectroscopy. SnS has a band gap of 1.3 eV (see Table 5.2) close to that of CZTS and is one of the secondary phases which does not harm efficiency as much as commonly assumed [42].

In summary, the results of the different measurement techniques used in the present study are reasonably consistent. However, some observations need further clarification for a profound interpretation of the data. For example, the complex effects of the annealing on the ligands originating from particle synthesis require more attention. Within the limits of this particular study, sulphurisation of CZTS nanoparticle ink thin films is advised to be performed at annealing temperatures around 600 °C since grain growth is fostered, the formation of crystalline CZTS is supported as compared to other phases, and the carbon content of the films is reduced.

6.3. Influence of Annealing Time

In addition to the study on the annealing temperature presented in the previous section, different annealing times of 0.5 h, 1 h, 1.5 h, 2 h, and 3 h are compared in a similar approach in the following. The times stated refer to the stage of constant temperature rather than to the whole procedure comprising the heating-up and cooling-down stage as well. The latter are the same throughout this project with details given in Section 4.3. The target temperature is fixed to a moderate value of 500 °C for the annealing experiments presented in this section. Table A.9 (p. 156) summarises some properties of the as-deposited samples such as their respective thickness. Based on the corresponding UV-vis spectra, it is estimated to be around half a micron for all of the samples which have been deposited in five layers on top of SLG substrates. However, Section 6.4 exploring some exemplary cross-sections indicates that the films are rather about one micron thick. The samples are similar to those used for the experiments reported in Section 6.2 but in this section, the nanocrystals are from synthesis batch Syn10. It shall be noted that the analysis of varying annealing times is presented in less detail since the annealing temperature is assumed and found to be more significant in terms of inducing changes to the material properties. Also, the discussion of the results presented in this section follows similar lines of argumentation as in the previous chapter.

6.3.1. Film Morphology

All the annealed thin films look consistently smooth and shiny, similar to the 500 °C sample from Section 6.2. Some SEM images of the films are shown in Figure 6.25. The sample annealed for 1 h (at 500 °C) can be compared to the corresponding sample from Syn11 treated under the same conditions in the context of the annealing temperature series previously discussed. It becomes apparent that in the former case, abnormal surface grains are not emerging yet in contrast to the latter case. Here, in case of Syn10, abnormal grains do form but only after longer times of annealing. They emerge in between 2 h and 3 h. This is presumably due to the fact that particles of two different synthesis batches have been used for either of the measurement series. However, as it can be seen from the synthesis comparison in Section 6.1, batch Syn10 and Syn11 are quite well comparable and do not show significant differences in the as-synthesised state. Furthermore, the subsequent sample preparation has been done according to the very same procedure. It can be concluded from this observation that even minor

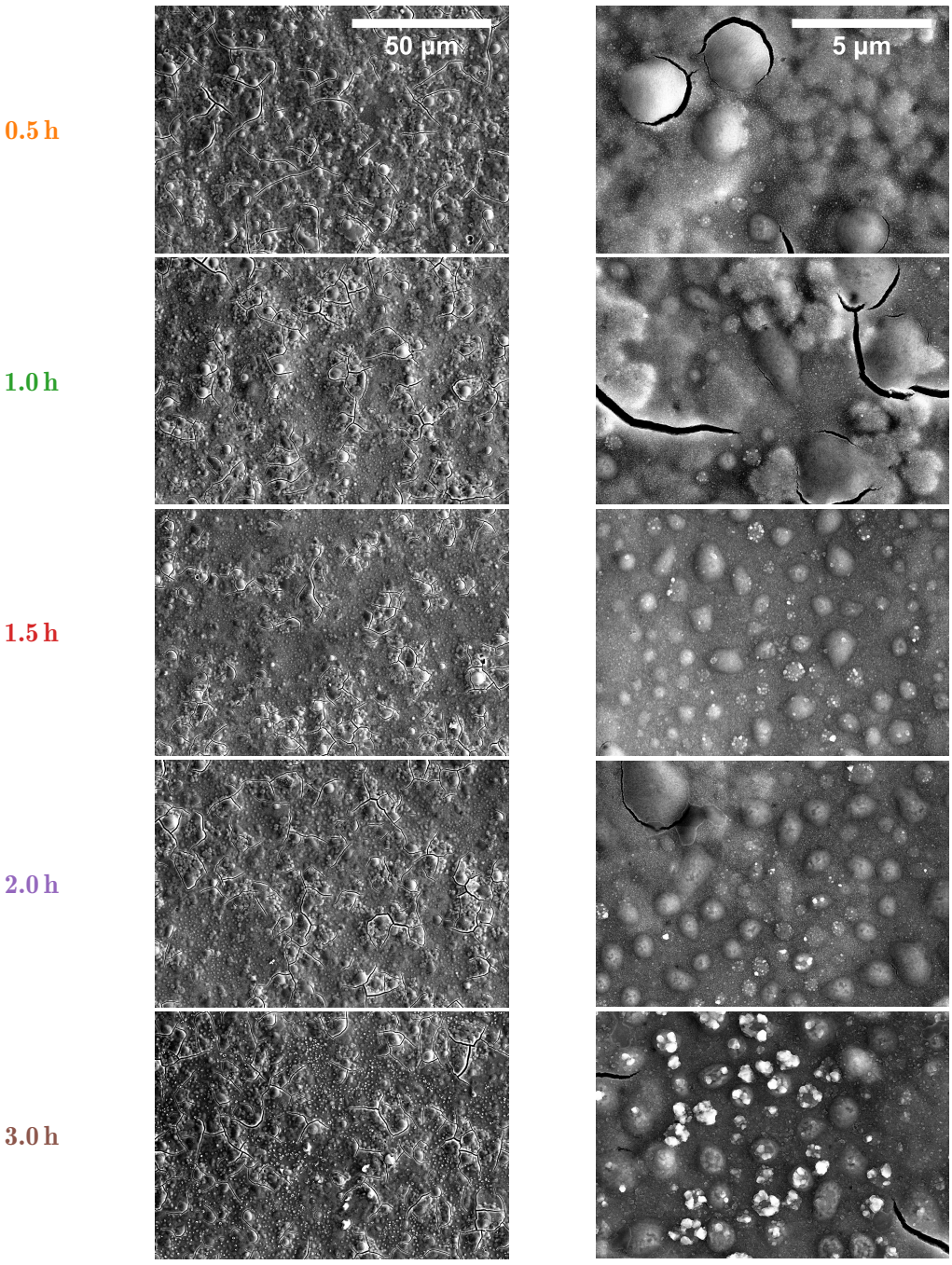

Fig. 6.25: The surface morphology of films processed with different durations of annealing is analysed in the SEM at magnifications of $\times$ 1k (left column) and $\times$ 10k (right column).

differences in the starting material that might not be detected can lead to notable differences in the final films.

6.3.2. Crystallinity

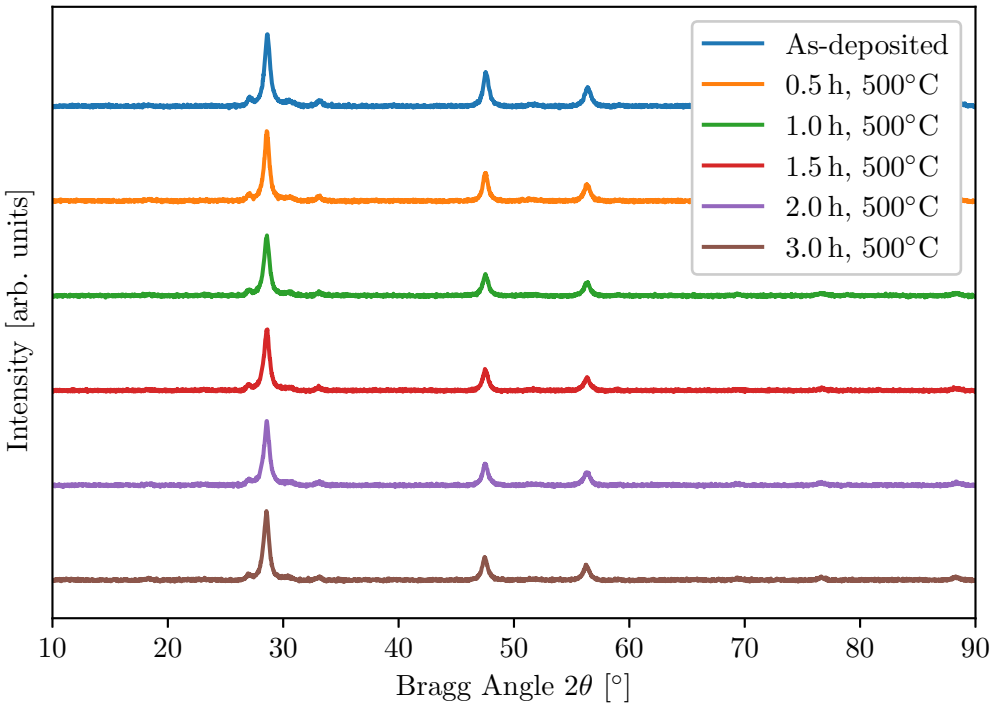

Fig. 6.26: The XRD spectra of the films annealed for different times are shown. They are background-corrected and vertically shifted for clarity.

Figure 6.26 shows the XRD spectra of the films under investigation. Unlike varying annealing temperature, varying annealing time does not induce any notable changes in the spectra concerning peak intensities and widths. This observation comes along with an approximately constant domain size as illustrated in Figure 6.27. The tetragonal lattice parameters derived from the spectra are plotted in Figure 6.28. Parameter c is quite constant but parameter a exhibits a slight upwards trend with increasing annealing times. This may potentially indicate a widening of the crystal structure but the comparatively large error bars make assessment difficult.

6.3.3. Composition and Carbon Residues

Compositional analysis of the samples has been performed by means of EDX. The calculated cation ratios are graphically shown in Figure 6.29. The Cu/(Zn+Sn) ratio lays systematically lower as compared to the annealed films but does not

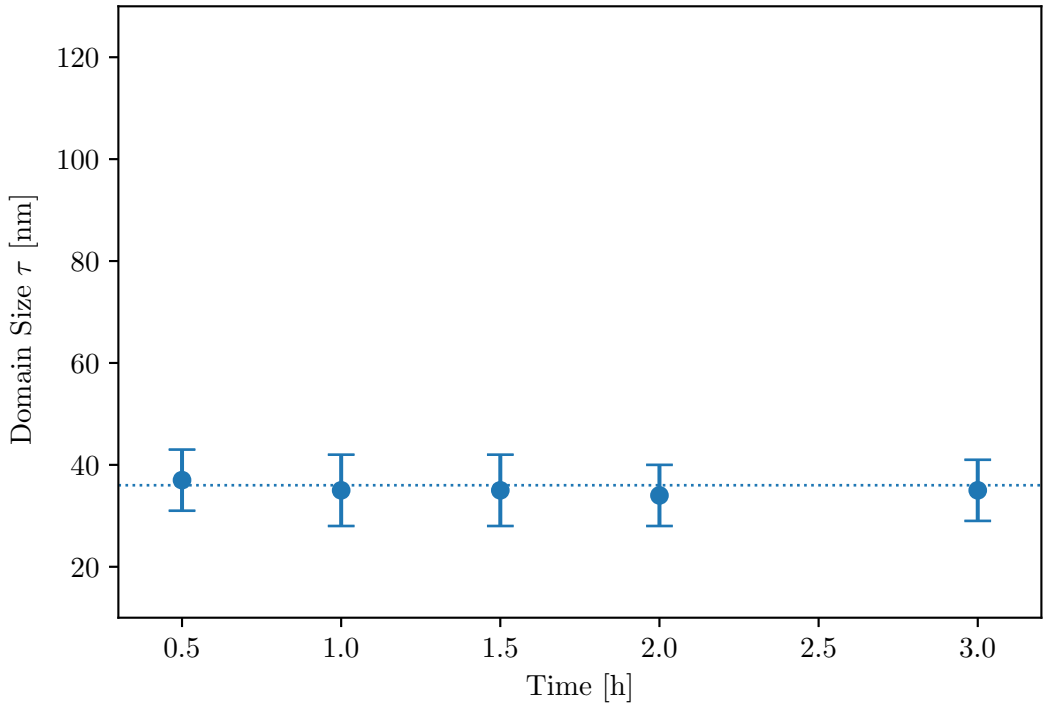

Fig. 6.27: The development of the domain size derived from the XRD spectra in Figure 6.26 is shown in dependence of the annealing time. The scale chosen is the same as in the domain size plot for the temperature series (see Fig. 6.9) in order to ease comparison. Here, no significant change as compared to the domain size calculated for an as-deposited film represented by the horizontal line can be seen.

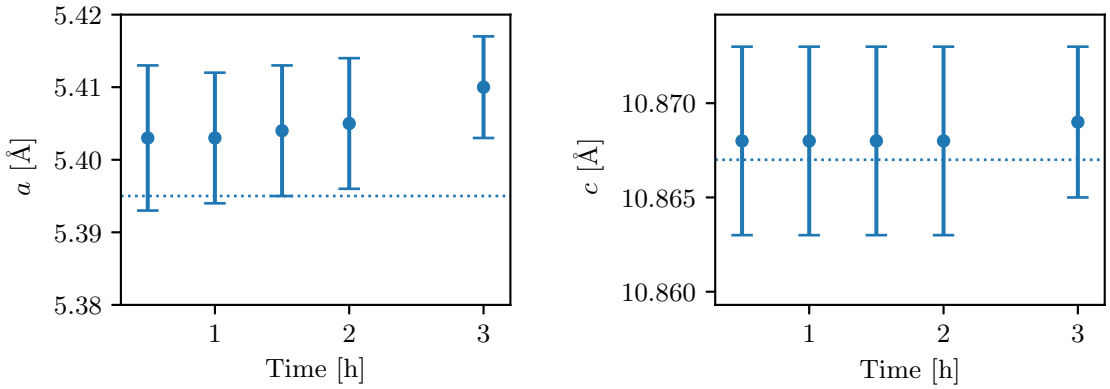

Fig. 6.28: The tetragonal lattice parameters a and c are plotted against the annealing time. The values are inferred from the XRD spectra. The horizontal lines indicate the parameters calculated for the as-deposited films.

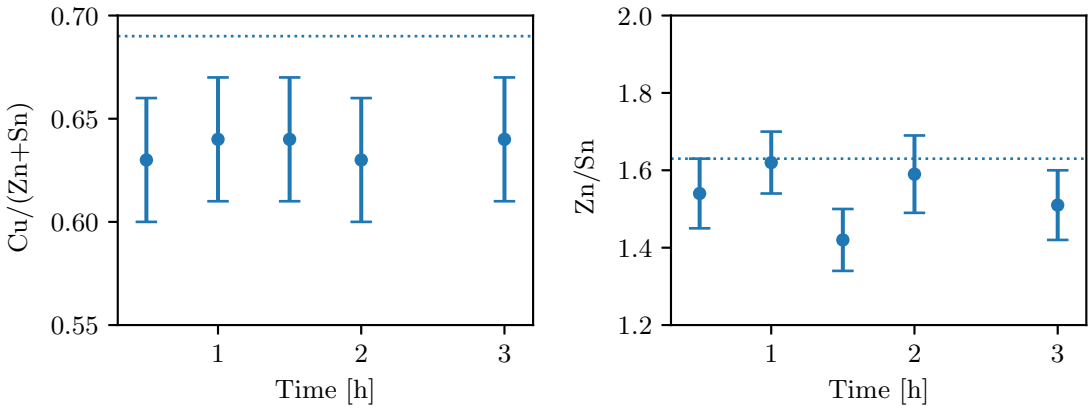

Fig. 6.29: The cation ratios Cu/(Zn+Sn) and Zn/Sn and their dependence on the annealing time are shown. The horizontal lines refer to the as-synthesised particles.

show any trends otherwise. The Zn/Sn has slightly larger fluctuations, however, no systematic change is observed either. An increased sulphur content is present in all of the annealed films as compared to the as-synthesised particles which can be seen from the pie charts in Figure 6.30. The observations are in agreement with the results from the study on varying annealing temperature.

Similarly consistent with previous statements is the observed development of the amount of other major elements contained in the films which are carbon, oxygen, and sodium. The level of carbon in the annealed films lies significantly lower than in the as-synthesised particles, possibly related to thermally induced decomposition of carbon. The carbon concentration also slightly decreases with increasing annealing time but it is unclear whether this small change is significant. As discussed before, the increased concentration of oxygen regardless of the annealing time is probably to be traced back to the soft-baking steps during spin-coating. The sodium level increases as compared to the as-synthesised particles and may also slightly increase with increasing duration of annealing but again, the magnitude of this might not be considered significant. Reason for the increase itself may be sodium diffusion from the substrates. The observation could also be provoked by the fact that the as-synthesised particles have not been measured on SLG substrates containing Na themselves but on a piece of Si wafer. The measurement data discussed is shown in Figure 6.31.

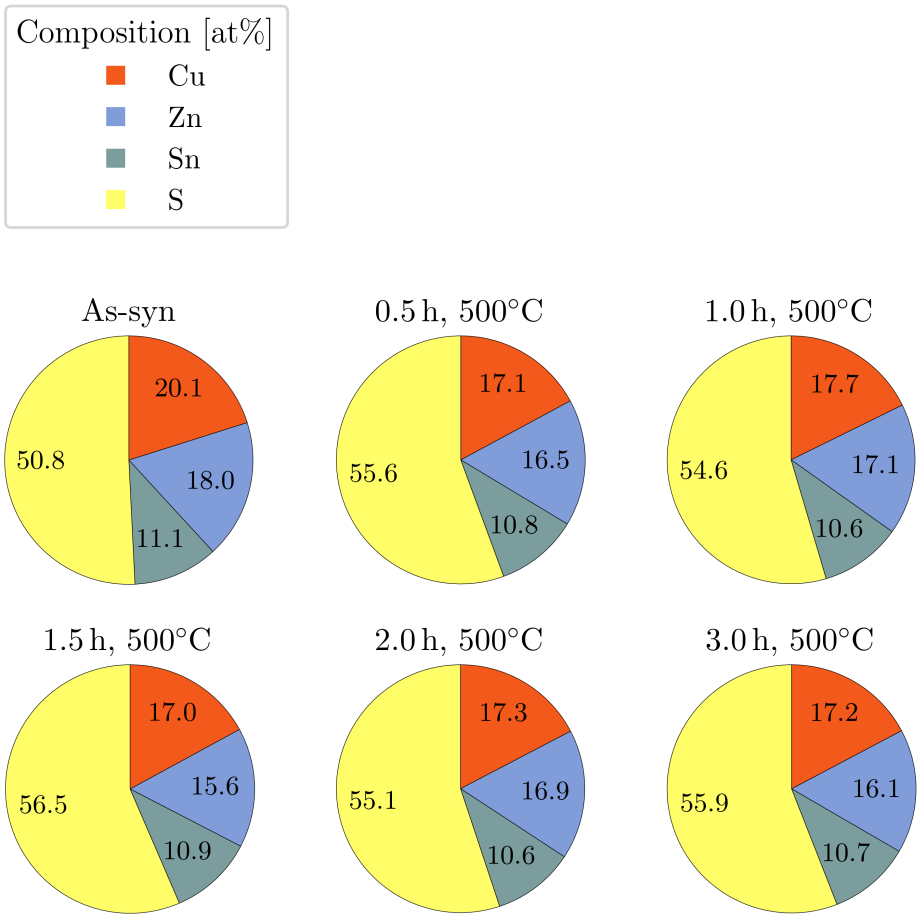

Fig. 6.30: The normalised concentrations of the different elemental components of CZTS are illustrated for the films annealed at different annealing times in comparison with the as-synthesised particles.

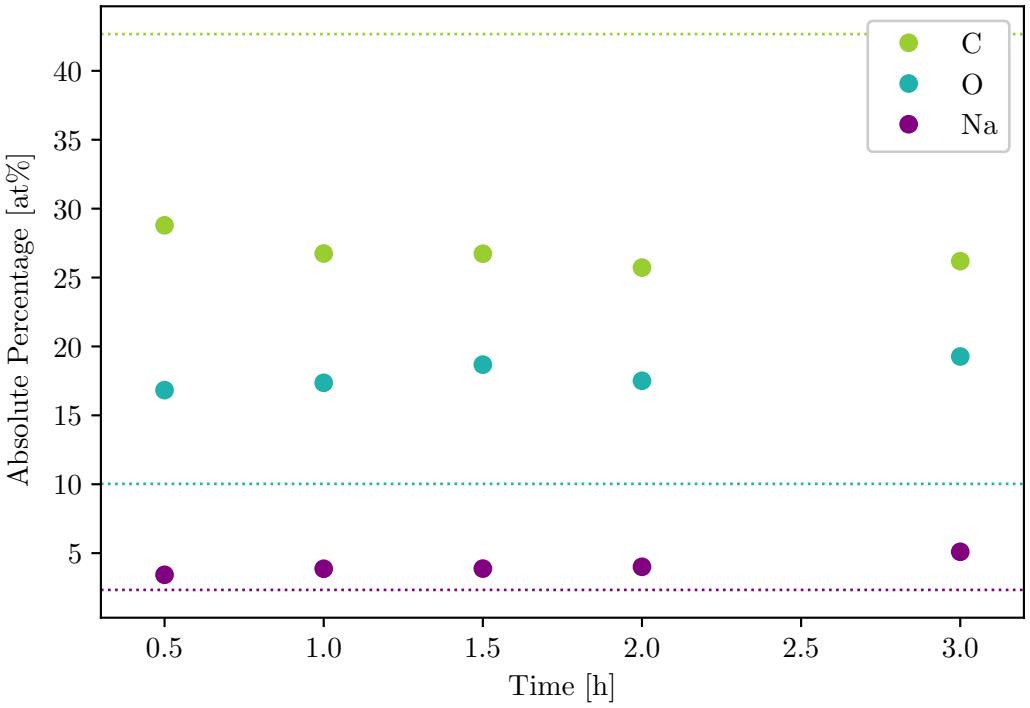

Fig. 6.31: The total portion of major elements present in the samples except from copper, zinc, and tin is plotted in dependence of the annealing time. These components are C, O, and Na. The horizontal lines indicate how much of the respective elements is contained in the as-synthesised particles (measured on a piece of Si wafer).

6.3.4. Phase Purity

Raman spectra measured with excitation wavelengths of 785 nm and 532 nm are presented in Figures 6.32 (a,b). Whereas the film annealed for only 0.5 h is still relatively similar to the as-deposited film and does not have very pronounced CZTS features, the typical Raman modes are easy to identify in the spectra of all of the films annealed for 1.0 h or longer and they resemble each other very much. As in the previous chapter studying the annealing temperature, the promotion of the desired kesterite CZTS phase can be seen clearly. Reaching this state is found to take 0.5 h to 1.0 h of annealing (at the temperature of 500 °C chosen). No further improvement of the film properties is observed when annealing is continued for longer.

Similarly to the measurement series with variation of the annealing temperature, nearly no changes can be seen in the spectra obtained with 532 nm excitation, except for slightly increasing peak intensities. The analysis of the peak positions in the spectra measured with 785 nm excitation with regard to secondary phases is

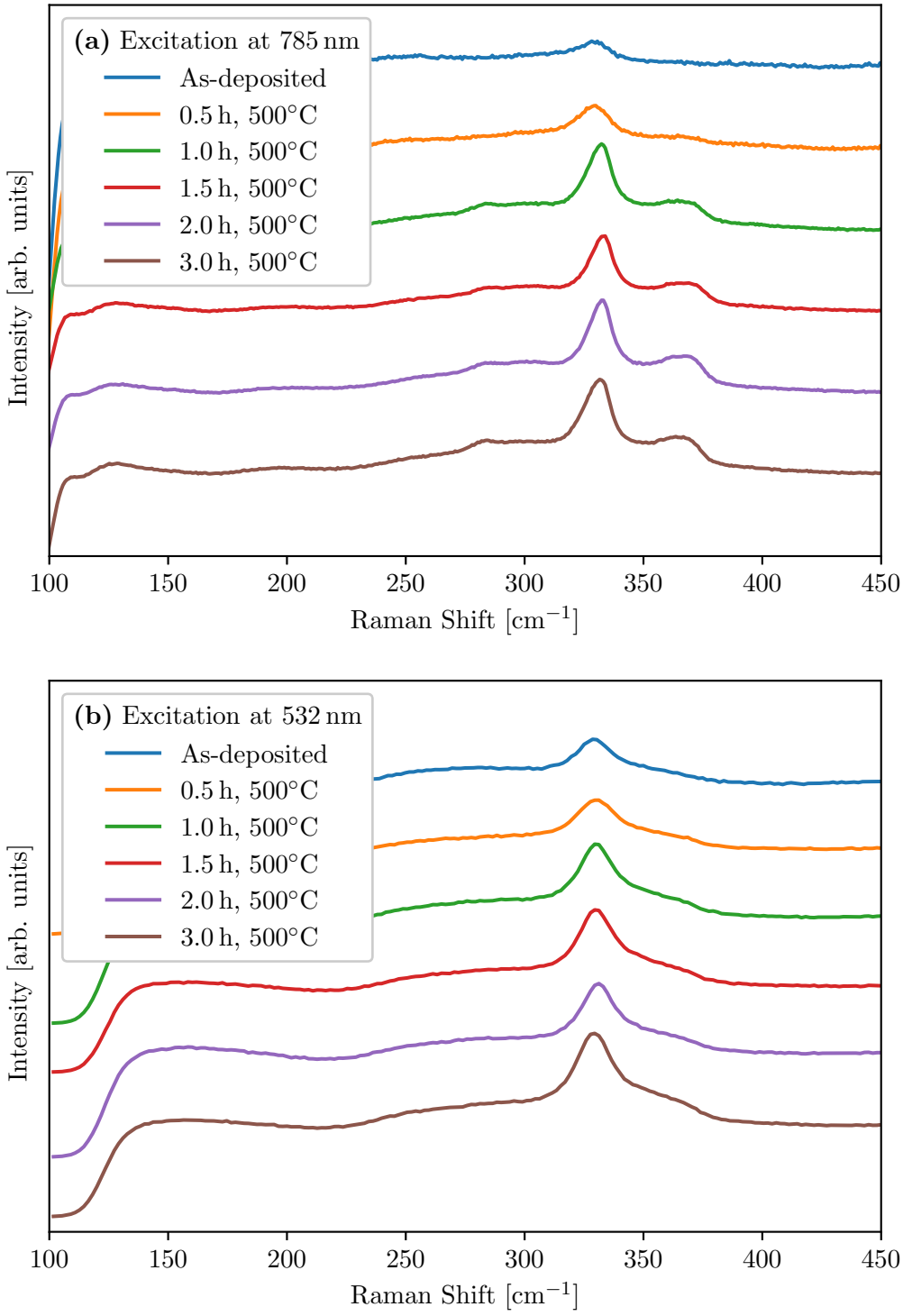

Fig. 6.32: The background-corrected and vertically shifted Raman spectra of the samples annealed for varying times measured with 785 nm (a) and 532 nm (b) excitation wavelength respectively are compared. The peak positions of the spectra in part (a) can be found in Table A.10 (p. 157).

presented in Table A.10 (p. 157). The potential presence of SnS and/or $Cu_4Sn_7S_{16}$ already discussed in the context of the as-synthesised particles of batch Syn10 (and Syn11) remains the same across all annealing times tested. Also, disordered CZTS is still detected in all cases. Some peaks disappear but also, further CZTS peaks arise upon annealing and they increase in their relative intensities, both of which are positive findings with respect to an improved crystal structure. Similar to previous observations, several secondary phases with peak overlaps to kesterite CZTS might be present but a definite conclusion is not possible. Nevertheless, none of these is formed due to the annealing treatment as far as it can be concluded from the information available. Further can be found in the given table.

6.3.5. Opto-electronic Properties

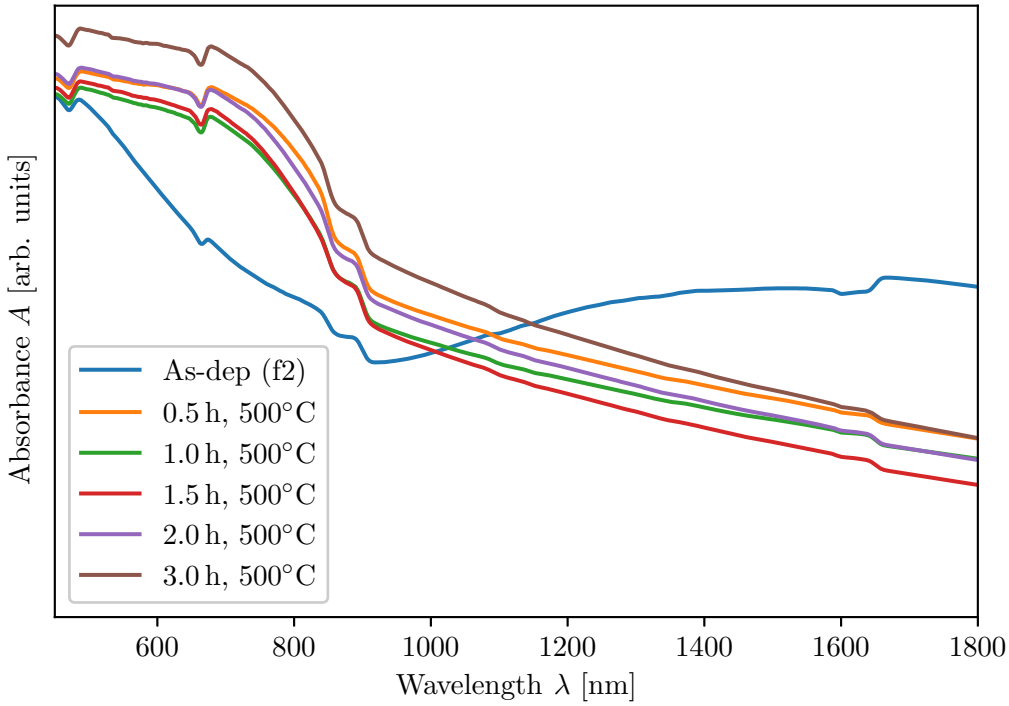

Fig. 6.33: Illustration of the UV-vis spectra measured for different durations of the annealing process. Figure A.2 (p. 156) shows the spectra of all as-deposited films in addition to the example of film 2 (f2) included in this graph.

Figure 6.33 reveals that even after only 0.5 h of annealing, the final state regarding changes in the absorbance spectrum is reached already. Below-band gap absorption is reduced and all of the annealed samples have nearly the same absorbance curve without a minimum. Figure 6.34 presents the band gap energies deduced from these UV-vis spectra. The annealed material seems to have a systematically larger band gap value than the as-deposited material. This increase in E_g is of the

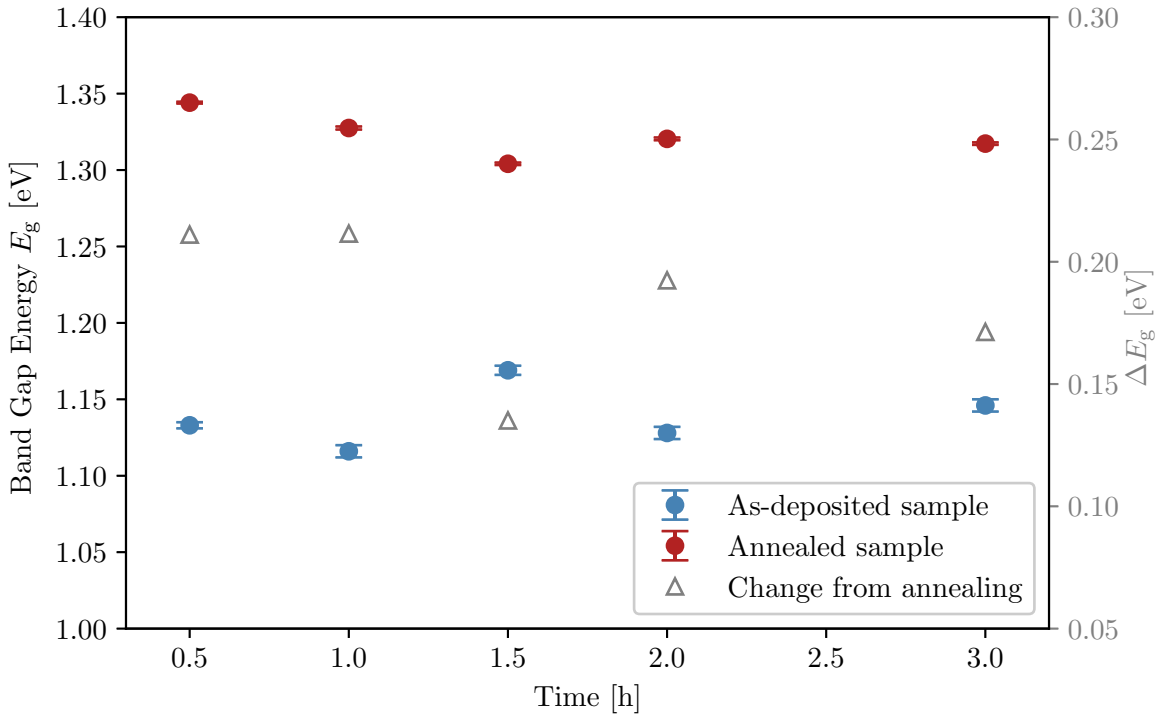

Fig. 6.34: The band gap energies derived from the UV-vis spectra from Figure 6.33 are shown and compared to the original values measured on the as-deposited films. In addition, the difference $\Delta E_g = E_{g,\,\text{annealed}} - E_{g,\,\text{as-dep}}$ between each pair of values is indicated on the right-hand axis.

same order of magnitude for all durations tested. Solely the film annealed for 1.5 h has a smaller increase in band gap energy. These observations may put a different complexion on the band gap variations reported in the context of varying annealing temperatures. Since the upwards shift seems to be reproducible in terms of varying annealing times, the changes due to different temperatures discussed earlier may not be as random as thought.

In addition to UV-vis spectroscopy, photoluminescence measurements are presented in Figures 6.35 (a,b). They have been performed at room temperature using a 514 nm green laser operated at 200 mW and a 375 nm UV laser operated at 60 mW. The detailed analysis of the different peaks has already been done in Section 6.2.5 in the context of varying annealing temperature. Since the peak positions of the samples discussed here, as summarised in Table A.11 (p. 158), are about the same as those discussed before. Since the previous analysis revealed distortion of the measurements by interference effects as likely root cause, this discussion is not repeated in detail. In this sense, the secondary phases assigned to the peaks within the mentioned table may not be necessarily related to these compounds, that is if the observations partly originate in measurements artefacts indeed. The compounds in question are ZnS, $SnSn_2$, and Sn_2Sn_3, which are not directly indicated by Raman spectroscopy as broached in the previous section. This disagreement puts the assignment of the PL peaks to secondary compounds further into question.

More general, varying annealing times do not lead to a significant change in the spectra – in contrast to the transition observed from 575 °C to 600 °C in the previous chapter. However, it can be seen from the illustration in Figure 6.35 that the relative intensities change from the as-deposited to the annealed films, independent of the duration to about the same extent. Peaks at lower energies are enhanced as compared to peaks at higher energies. It could be speculated that this may be due to a subtle enhancement of CZTS band-to-band emission as the increased intensity lies in the range of the expected band gap energy of 1.4 eV - 1.5 eV. Looking closely, the same observation can be made in Figure 6.21 from the temperature series as well when comparing the as-deposited to any of the annealed samples. Here, the shift of relative intensities is not promoted further when increasing the annealing time and slight changes still observed do not correlate systematically with annealing time for excitation with either laser.

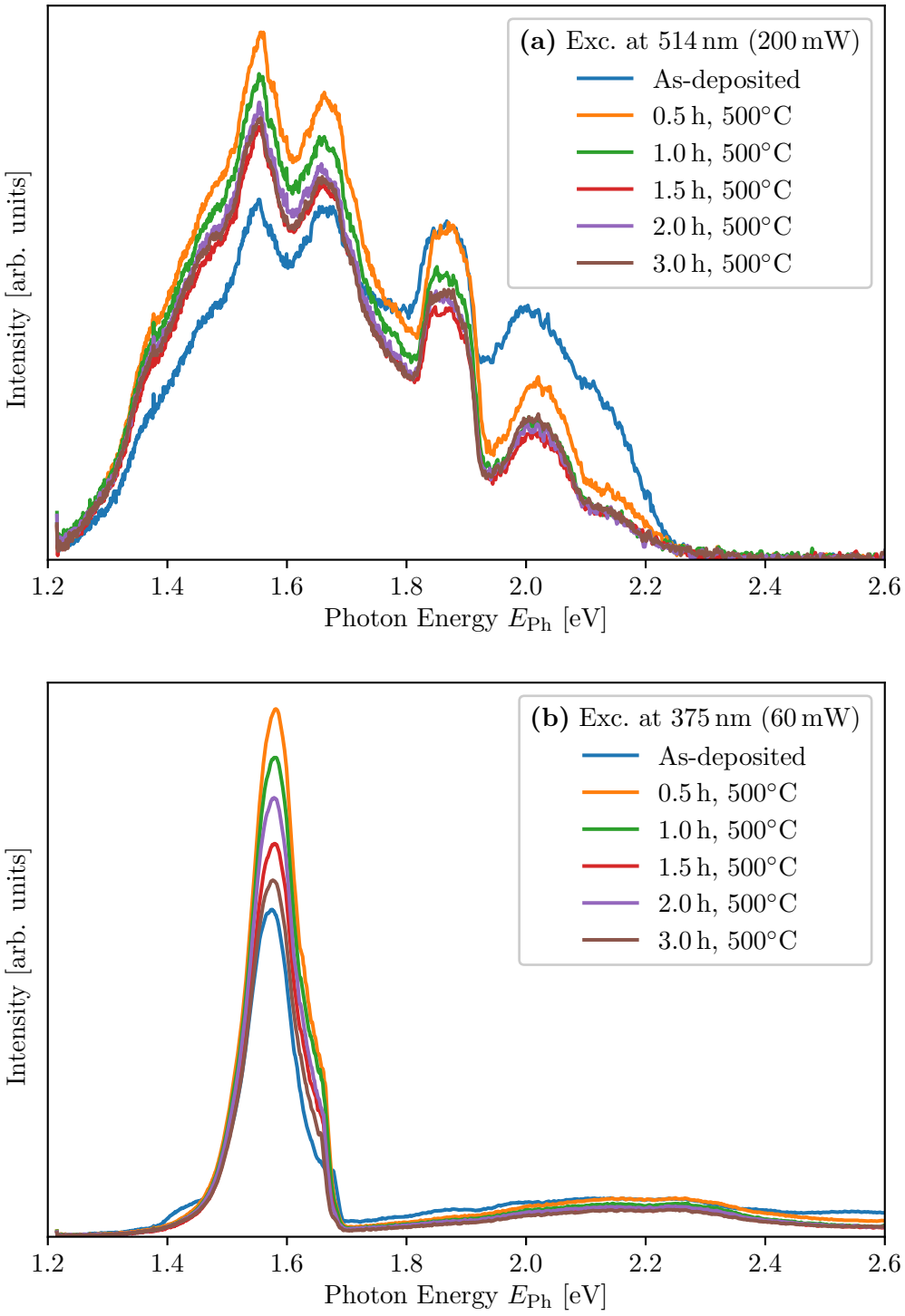

Fig. 6.35: Room temperature PL spectra of the samples from the study on varying duration of annealing have been measured with 514 nm green (a) and 375 nm UV laser excitation light (b) respectively. The peak positions of the fitted spectra in part (a) are listed in Table A.11 (p. 158).

6.3.6. Conclusions

This chapter demonstrates that varying the duration of annealing has a smaller impact on the properties of the resulting films than the choice of the annealing temperature. Considering that many of the processes in the formation process are thermally activated this might not be surprising. Most of the changes occur in the first half an hour or hour of annealing so that longer durations are not advised with respect to energy expenditure of the fabrication process. Material properties and film development should mainly be regulated via the annealing temperature.

However, it should be noted that the present investigations focused on one annealing temperature only. It remains to be seen whether similar observations are made at temperatures different from 500 °C. For example, another combination of temperature and time may lead to a longer transition phase during which the changes in material properties take place. Based on Section 6.2, temperatures around 600 °C should be studied further in particular while considering the development of the films over time. Other relevant parameters in this context may be the ramp rates of the heating-up and cooling-down stages during annealing.

6.4. Layer Study with Rear Contact

Making a step from the absorber layer itself towards its application in a solar cell, a Mo rear contact is added in between SLG substrate and the CZTS thin film for a layer study presented in this chapter. One 10-layer film of batch Syn11 (same batch as used for the study on annealing temperature in Sec. 6.2) and one 5-layer film of batch Syn10 (same batch as used for the study on annealing time in Sec. 6.3) are analysed with respect to their cross-sectional morphology. Imaging on the FIB microscope has kindly been carried out by Mr Leon Bowen[*].

The film properties have been checked by the same methods used in the previous chapters and no notable differences were found – except from some additional peaks assigned to Mo, for instance in the XRD spectra. Absorption spectroscopy is the only method not applied to these samples as the rear contact does not let any light come through, making this measurement impossible.

[*]Department of Physics, Centre for Materials Physics, Durham University

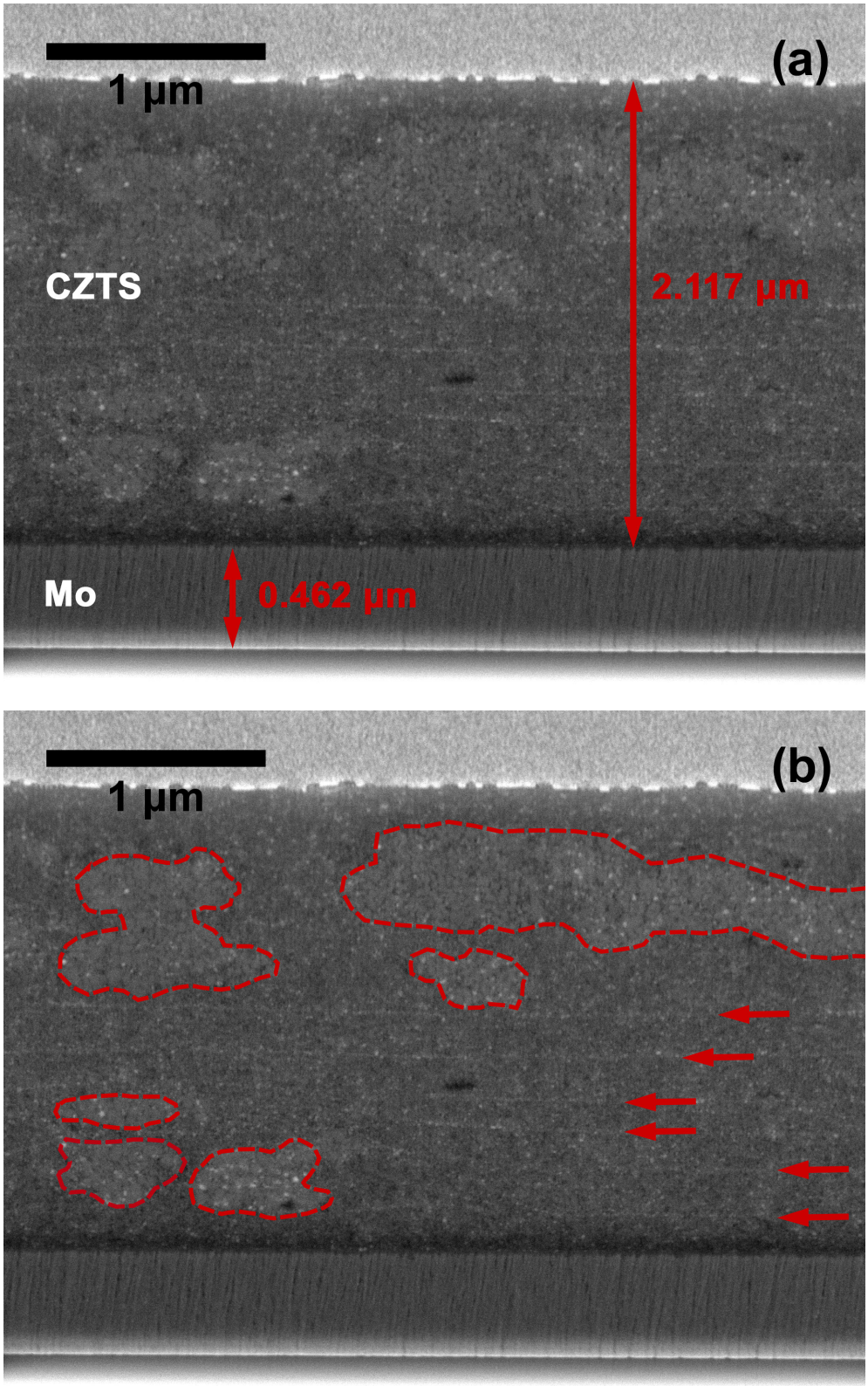

Fig. 6.36: Cross-section of a 10-layer film made of particle batch Syn11 on a Mo-coated SLG substrate and annealed at 500 °C for 3 h. (a) Exemplary thickness measurements of the Mo rear contact layer and the CZTS absorber layer, (b) Agglomerations of larger crystallites in some areas of the absorber surrounded by red dashed lines for clarity and presumed artefacts of subsequent layer deposition indicated by arrows. Both images have the same field of view using a magnification of × 65k.

6.4.1. Layer Thickness

Estimations of the film thickness based on the UV-vis spectra of the samples from Section 6.2 and 6.3 (see Tab. A.6 and A.9) suggest that the deposition of five layers result in a film with an approximate thickness of about half a micron. This would mean that ten layers would be about one micron thick and hence suitable for an efficient absorber layer in a photovoltaic device. However, as it can be seen from the example shown in Figure 6.36 (a) and the more detailed Table 6.4, the cross-sectional view reveals a thickness of (2.05 ± 0.07) µm on average which is approximately twice as much as expected. Also the 5-layer film is, with an average thickness of (1.07 ± 0.19) µm, about twice as thick as originally assumed. This may indicate issues of data interpretation concerning the absorption measurements on the specific type of samples used. Potential errors in the analysis of the UV-vis spectra are discussed in Section 6.5.4.

The summary of all corresponding measurements in Table 6.4 indicates that the 5-layer samples is less uniform than the 10-layer film. However, this is most likely due to the fact that the former was prepared from a rest of ink that contained some agglomerations of particles and is not comparable to the samples used in the other sections of this study. The much more uniform 10-layer film is more representative for the deposition procedure followed. The measured Mo layer thickness, (470 ± 8) nm in average, is relatively uniform across the samples but has a small systematic deviation from the targeted value of 600 nm. A solar cell using such a Mo thickness previously demonstrated a particularly high device efficiency [146] but the details of optimum device fabrication are beyond the scope of this study.

6.4.2. Absorber Uniformity

Figure 6.36 (b) highlights some notable features in the cross-section of the annealed absorber layers. First of all, some zones stand out by a lighter tone of grey as compared to the rest of the CZTS layer and by larger crystallites. These areas, surrounded by dashed lines for better visibility, are neither solely located on top of the film nor solely at the Mo - CZTS interface but they are randomly distributed in the absorber. However, it should be noted that under the chosen annealing conditions of 500 °C for 3 h no abnormal grains formed on the film surfaces. The regions described could be related to secondary phases that appear upon annealing. Alternatively, their distinct appearance may simply be due to randomly occurring,

Tab. 6.4: Summary of the thickness measurements based on cross-sectional images from the FIB. The values have been obtained with ImageJ and the estimated error of a single measurement is smaller than $\pm 0.010\,\mu m$. The bottom line contains the average values with the corresponding standard deviations. The Mo thicknesses are taken from both of the samples investigated.

	CZTS thickness [µm]		**Mo thickness [µm]**
	5 layers	10 layers	
	0.934	2.123	0.481
	0.801	2.117	0.468
	0.917	1.977	0.459
	1.111	2.076	0.471
	1.120	2.104	0.462
	1.086	1.972	0.474
	1.167	2.029	0.474
	1.386	2.018	0.469
Average:	1.07(19)	2.05(7)	0.470(8)

enhanced grain growth in these areas. This would be interesting to look at in more detail in future studies.

In addition, faint horizontal lines are visible. It is assumed that they originate from the subsequent deposition of multiple layers by spin-coating. As described in Section 4.2.2, each layer is dried in air at 300 °C for 1 min in total. The previous parts of this study indicated that this process introduces oxygen to the films. This may become apparent through the change in contrast at the borders of these layers. If this assumption is true, the vertical distance between the lines shows that the different layers have about the same thickness and that their deposition procedure is hence reasonably reproducible. This is confirmed by some UV-vis measurements performed layer after layer as presented later in Section 6.5.4.

Finally, there is a slightly darker region at the interface between the Mo contact and CZTS. This possibly indicates the formation of a MoS_2 interlayer but further analysis would be necessary to confirm this.

6.4.3. Conclusions

The analysis of exemplary cross-sections allowed for cross-check of the absorber thickness of the samples used and revealed that it is underestimated based on the UV-vis spectra. The large deviation by a factor of two indicates that the absorbance values measured on this specific type of samples need to be interpreted

with care as discussed further in Section 6.5.4. In future studies, the use of a profilometer could provide alternative means for determination of the film thickness. It can be concluded from the present investigations that the film deposition procedure used (see Sec. 4.2.2) only requires five layer depositions in order to reach one micron in thickness suitable to absorb the major part of the incident sunlight within a solar cell. In consequence, it may be assumed that the samples analysed in Section 6.2 and 6.3 have a thickness in this range, too, so that the corresponding observations are well applicable to 'real-world' solar cell design.

Furthermore, there are possible signs of secondary phases that are randomly distributed in the absorber layer. The corresponding regions also exhibit larger average grain sizes indicating accelerated growth. Further studies on the cross-sectional uniformity involving similar investigations on the dependence of the layer structure on different annealing conditions are advised. In the context of this study, only a very brief insight is given.

6.5. Sources of Error in the Experiments

To some degree, the previous chapters analysing the experimental results already included some discussion of potential sources of error. Further issues considered relevant are broached in this chapter, without making a claim to be complete. ICP-MS is left out since it is only used for the purpose of comparison and as a way to verify the EDX measurements done in the context of this work. Also, general problems relevant to several techniques such as matters of error propagation, the choice of the optimum functions for peak fitting and the corresponding variance in FWHM, peak overlaps, or the fact that reference patterns might have been measured under deviant conditions that affect the peak positions (e.g. concerning temperature or laser power) are not covered explicitly for each method.

6.5.1. XRD Measurements

The position of XRD peaks is quite susceptible to the vertical position of the samples that means incorrect alignment in the instrument can cause systematic shifts [127]. In turn, the deduction of the lattice parameters is influenced by this to a higher degree than the calculation of the domain size as it can be seen from the equations in Sections 5.1.1 and 5.1.2. This source of error has been mentioned in the context of a bent sample earlier in this thesis already.

Apart from this, XRD measurements can either be performed on powder samples or on as-deposited films. As the same kind of particles is used in either of these approaches, the results are expected to be the same. However, there are small deviations between these two approaches, particularly in the peak widths and consequently in the domain sizes deduced from them. The values obtained from the two different samples types, nevertheless, mostly lie within the margin of error of one another. The peak positions and therefore also the inferred lattice parameters do not depend on the sample type chosen as much. A possible explanation for these observations could be related to preferred crystallite orientations depending on the way of preparing the sample [110]. On a glass slide covered with NC ink by spin coating, edged particles may align in a particular way with respect to the flat substrate, according to the local direction of the forces during spin-coating, destroying the aimed random orientation. The sticky undercoat of vaseline used to fix NC powder on top of the respective holders may, in contrast, be less prone to this kind of texture effects. In addition to this, errors can originate from differences in surface roughness and different contributions of absorption effects from the substrates and/or sample holders when X-rays partly transmit through the layer of CZTS [110].

The domain size determination is mainly dependent on the peak width. The latter is also influenced by instrumental broadening effects; however, standard laboratory equipment usually allows to measure domain sizes up to 200 nm with sufficient accuracy [110]. This requirement is fulfilled for the data presented here. Further sources of error in peak width are, for example, broadening effects of strain in an imperfect crystal lattice that can contain various defects [110], as well as of inactive Raman modes [118]. Both could contribute to the spectra presented in the context of this study but should not depend on the sample type.

The Scherrer equation which is based on Bragg's law is commonly used in order to calculate the domain size from powder diffraction data, also in the context of nanocrystalline CZTS. However, it is important to note that the applicability of this approach is constrained to a certain range of crystallite sizes [110]. If they are too small, the assumption of an infinite periodic lattice does not hold any more. Nanoscale particles may hence need to be treated with the so-called Debye equation instead in order to obtain accurate results [110]. Contributions of diffuse scattering need to be taken into consideration, besides other effects. This results in the total scattering method which would be more precise and could therefore add value to future studies. In a first step, also the use of the Scherrer equation

could be improved by choosing the constant factor K more deliberately based on an analysis of the actual shape of the crystallites as the exact value of K depends on the particle shape as discussed in Section 5.1.2.

6.5.2. Raman Measurements

It has been mentioned before that Raman spectroscopy is a rather surface-sensitive technique. Secondary phases occurring deeper in the absorber might hence not be detected. Furthermore, the spot size restricts the area analysed to only 15 - 20 µm in diameter. Different spots on some exemplary samples have been compared to check how reproducible the results are. It was found that only the background level changes, possibly due to a non-uniform carbon distribution and/or variations in fluorescence background, and that peak intensities vary slightly (maybe related to the first-mentioned aspect), whereas the peak positions remain the same. Since the latter is in the focus of the investigations presented, the impact of the location of the randomly chosen measurement spot on the sample surface can be neglected. Moreover, the observations indicate a relatively homogeneous phase throughout the sample surface. Secondary phase identification in CZTS by means of Raman spectroscopy could potentially be improved by using more different excitation wavelengths, e.g. 325 nm which is resonant to ZnS and has been proved to be useful for its identification in a CZTS sample even in amounts as small as 10 % [39]. Another, more advanced approach is the application of Raman imaging that can be used for phase analysis with spatial resolution.

If polycrystalline material is investigated, with crystal sizes below 50 nm in particular, phonon confinement effects can induce peak broadening and peak shifts in the Raman spectra [147, 148]. Peak positions are also dependent on strain in the crystal lattice. It may be worth to take this into consideration for more profound analysis because the particles used for the present work have crystal sizes just at the border to be influenced by the effects in question. Fluctuations in grain and particle size may be partly responsible for slight variations in peak positions among the samples and as compared to the literature values.

6.5.3. EDX Measurements

As specified in Section 5.3.2, certain X-ray lines have been chosen in order to avoid errors in the determination of the composition by overlapping peaks. This follows suggestions in reference [14]. The effectiveness of the approach was checked by

means of ICP-MS in the context of the present study and this confirmed that quantitative measurements with the K lines for Cu, Zn, and S and with the L line for Sn led to the closest results as compared to mass spectroscopy. An exemplary comparison of both the techniques was included in Section 6.1.3. For instance, it was found that ICP-MS indicates a higher stability of the elemental concentrations as compared to EDX when looking at different batches prepared under the very same conditions. This could be one of the reasons for the presumably random fluctuations in composition reported in the context of the measurement series on varying annealing conditions (see Sec. 6.2.3 and 6.3.3). The application of other methods than EDX for the purpose of verification is recommended for future investigations.

Another aspect of importance is the choice of the acceleration voltage used. Figure 6.37 illustrates the simulated interaction volume of secondary electrons entering a CZTS (bulk) sample with a thickness of about one micron using values of 12 keV and 15 keV respectively. It becomes apparent that 12 keV are suitable to restrict penetration of the electrons to the absorber layer rather than letting them go into the underlying SLG substrate. In the latter case, EDX measurements could be disturbed by signals from the elements contained in the glass or by scattering at the interface between the CZTS layer and the substrate. This is why a setting of 12 keV is chosen for the measurements presented, suiting the 5-layer films of the measurements series on temperature and time of annealing which are about one micron thick according to the cross-sectional analysis in Section 6.4.

These considerations are a first level approximation. A more precise simulation would have to take the fact into account that the material under investigation is nanocrystalline and has a rough surface. The so-called mass effect is relevant for particles with diameters smaller than five microns and at beam energies below 20 keV [120]. Electrons can escape from such particles through all of their sides and the X-ray intensity measured depends on the particle diameter. Additionally, the so-called absorption effect occurs due to the fact that the absorption pathway is changed in comparison to a monocrystalline material. Specifically, the surface curvature of small particles, i.e. particles which are smaller than the interaction volume, reduces absorption so that the X-ray intensity increases [120]. From the aspects just discussed it is clear that the criteria for a relevant impact of the mass and the absorption effect apply to the samples investigated in this study. The acceleration voltage is below 20 keV and the particles/grains are significantly smaller than 5 µm as well as smaller than the interaction volume. Therefore,

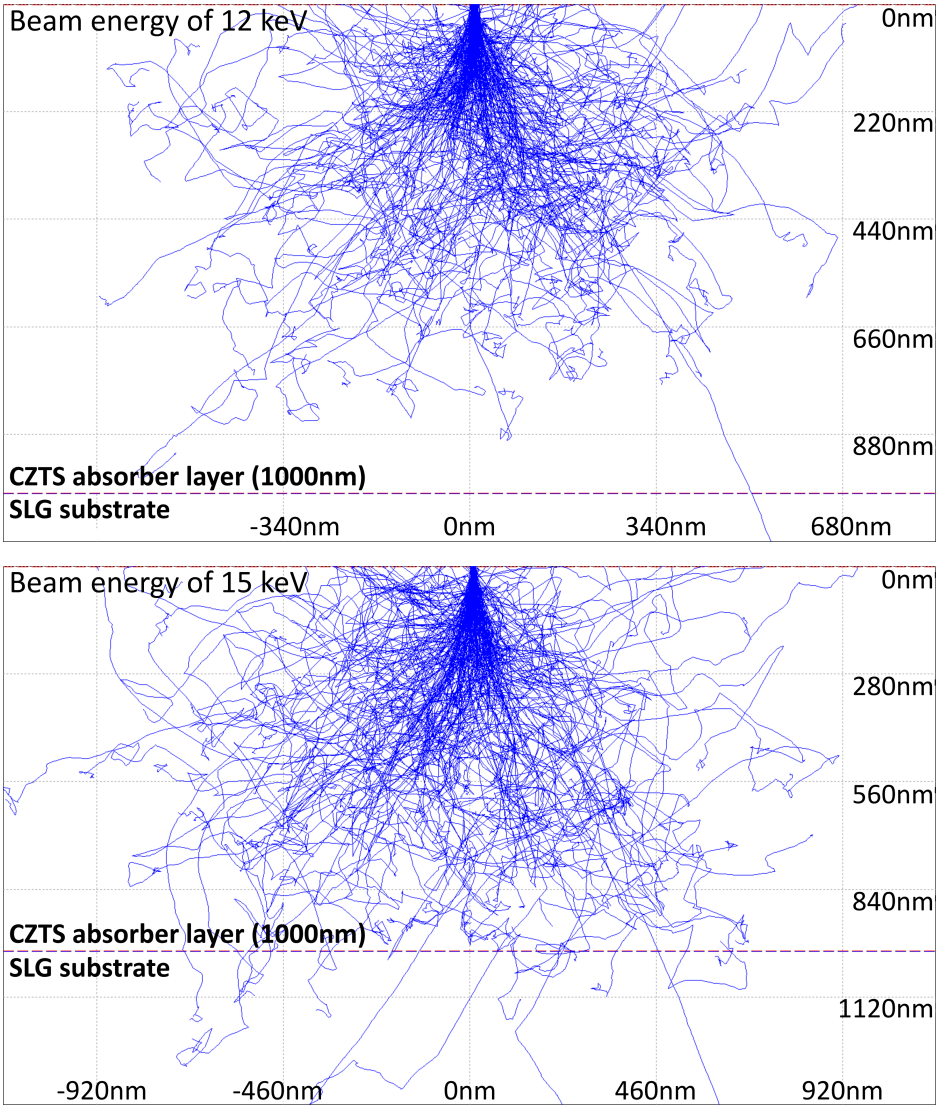

Fig. 6.37: The interaction volume of the primary electron beam (in blue) for a one micron thick CZTS layer on a SLG substrate is simulated for a beam energy of 12 keV (top) and 15 keV (bottom). The dashed line indicates the border between absorber layer and substrate. The software used, CASINO (version 2.51), has been developed as a tool for 'Monte **Ca**rlo **si**mulations of electro**n** trajectories in s**o**lids' by D. Drouin et al. (Université de Sherbrooke, Sherbrooke, Quebec, Canada). For more information refer to references [149, 150].

some distortion of the EDX measurements has to be assumed. Particularly when investigating grain growth, the extent of the effects might even vary from sample to sample as the relevant magnitude of particle or grain size is deliberately changed, by choosing different annealing conditions. The compositional variations reported in the previous chapters and the remaining deviances of the EDX data from ICP-MS may partly be related to these issues.

In terms of data interpretation it should be kept in mind that due to the procedure followed in the EDX measurements, an average value despite of any inhomogeneities is obtained and hence statements on the presence of secondary phases may be difficult to make. By employment of spot measurements and EDX mapping, this fact may be circumvented as partly done in Sections 6.2.3 and 6.2.4 and a non-uniform distribution of the elements was found by this approach indeed. This could lead to inaccurate average values if no sufficiently large number of measurement spots is taken into consideration.

6.5.4. UV-vis Measurements

First of all, there are some uncertainties in fitting of the Tauc plots, which is for instance complicated by relatively narrow linear sections and by jump discontinuities from the instrument (according to settings, change of light source at 390 nm, of grating at 850 nm, and of detector at 900 nm/1650 nm). There are also some small peak-like features at around 700 nm which are not related to any instrumental changes and may require further investigations. However, other observations concerning the UV-vis spectra require even more attention in order to obtain reliable data interpretation. For instance, it is interesting to see in Figure 6.38 how the UV-vis spectra evolve with the addition of more and more layers during the spin-coating procedure. Whereas the UV-vis curve measured on a single layer approaches a constant lower absorbance limit with increasing wavelengths as expected, the additional layers lead to the formation of a minimum at around 900 nm. The again increasing absorbance above this wavelength indicates below-band-gap absorption as discussed in the context of the band diagram of CZTS, in the analysis methods section about UV-vis spectroscopy, as well as along with the experimental results. Another explanation to consider are interference effects since those are likely to have disturbed the PL spectra measured, too, as discussed in Section 6.2.5.

The thicknesses and band gap energies derived from the UV-vis curves of the

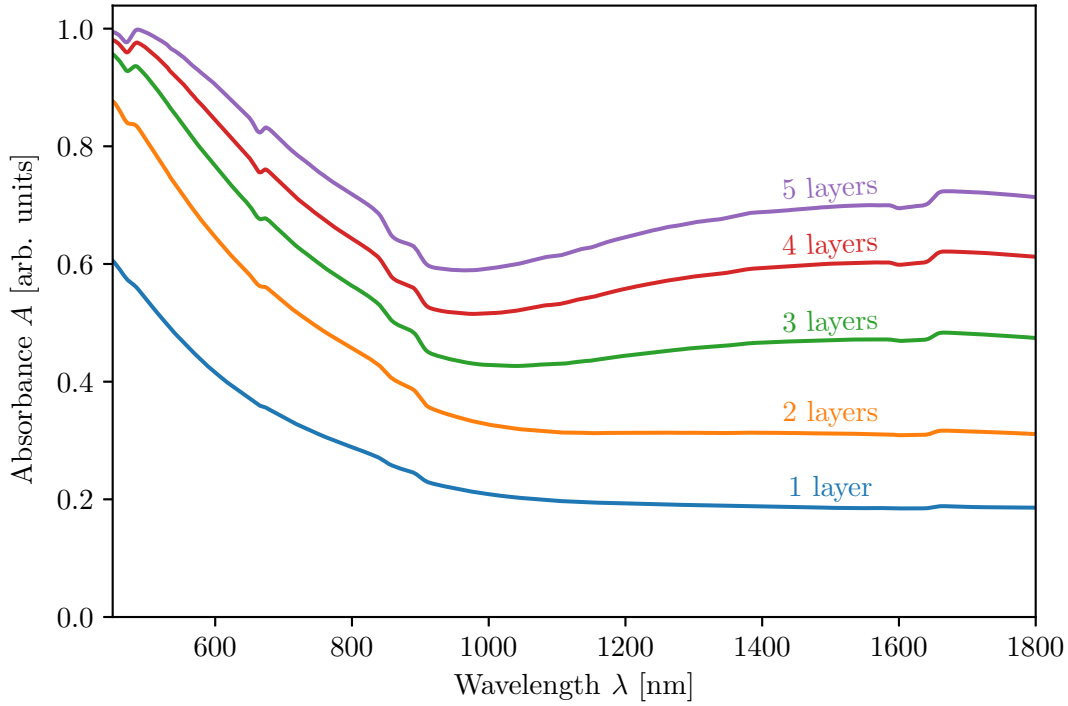

Fig. 6.38: This figure demonstrates how the UV-vis spectra evolve when more and more layers are added. The spectrum of the one-layer film approaches a constant value towards high wavelengths as expected. With increasing number of subsequent layers, a minimum at around 900 nm appears. Some of the discontinuities are related to changes inside the instrument, namely of the lamp and the grating which is done automatically. The curves shown have been measured during the deposition process of film f6 from particle batch Syn11. Parameters derived are summarised in Table 6.5.

different number of layers in Figure 6.38 are summarised in Table 6.5. The shift of the spectra towards higher absorbance values with the addition of layers corresponds to an increasing thickness and is relatively reproducible in its magnitude. However, it becomes apparent that also the results for the band gap energy change. The latter variations are not systematic since, even though the values increase at first, the band gap energy seems to decrease again after deposition of the fifth layer. In any case, no variations in band gap energy are expected with varying absorber thickness since this material-dependent property should only depend on the nanocrystals used themselves. The deviations between the measurements on different layers are more significant than the extremely small statistical errors which are based on straight line fitting. Therefore, the errors indicated are underestimated and should be interpreted with care. This scepticism is reinforced by the varying band gap values deduced from the spectra of similarly thick films of the same NC batches which does not have an obvious physical reason, see Tables A.6 and A.9. The observation of the varying band gap energies from stacks

Tab. 6.5: The total film thicknesses and the band gap energies derived from the UV-vis spectra in Figure 6.38 in dependence of the number of layers are listed.

Layers	Thickness [nm]	Band gap energy [eV]
1	125	1.2030 ± 0.0013
2	219	1.2249 ± 0.0011
3	295	1.2636 ± 0.0011
4	364	1.2821 ± 0.0011
5	441	1.2686 ± 0.0010

with different numbers of layers may partially be related to surface oxidisation during the soft-baking in between subsequent steps of spin-coating that has been considered in Section 6.4 in the context of the cross-sectional analysis as well.

Another aspect to note is that the addition of more than five layers, as tested with another sample, did not lead to a further up-shift of the UV-vis curve even though the layer thickness clearly increased based on how much light can been seen shining through. The absorbance A measured did not increase to more than approximately 1.2 [arbitrary units]. Problems with the instruments have been excluded by testing with other samples. Possibly, effects of carbon residuals and ligands or surface oxidisation of the subsequently deposited layers as broached in Section 6.4.2 are related to these observations.

In future experiments, more focus could be put on the comparison of UV-vis measurements of thin films and of nanoparticles in solution (usually toluene). Early experiments done in the context of this study indicated that the band gap energies derived from measurements in NC dispersion lie in the same range as those from thin films. However, slight deviations showed also in this case that the statistical errors from the Tauc plots largely underestimate the true uncertainties in the results. For further experiments, ligand exchange procedures might be necessary in order to improve the dispersibility of the as-synthesised particles in toluene (if ethanol, hexane, and isopropanol are used for the collection of the as-synthesised particles in the centrifuge) and to enable the measurement of the particle dispersion in the spectrophotometer in this way.

6.5.5. PL Measurements

Different spots on the same sample have been compared to check for the reproducibility of the PL spectra measured by way of example and no significant changes were found. However, signals have been measured emitted by a mere

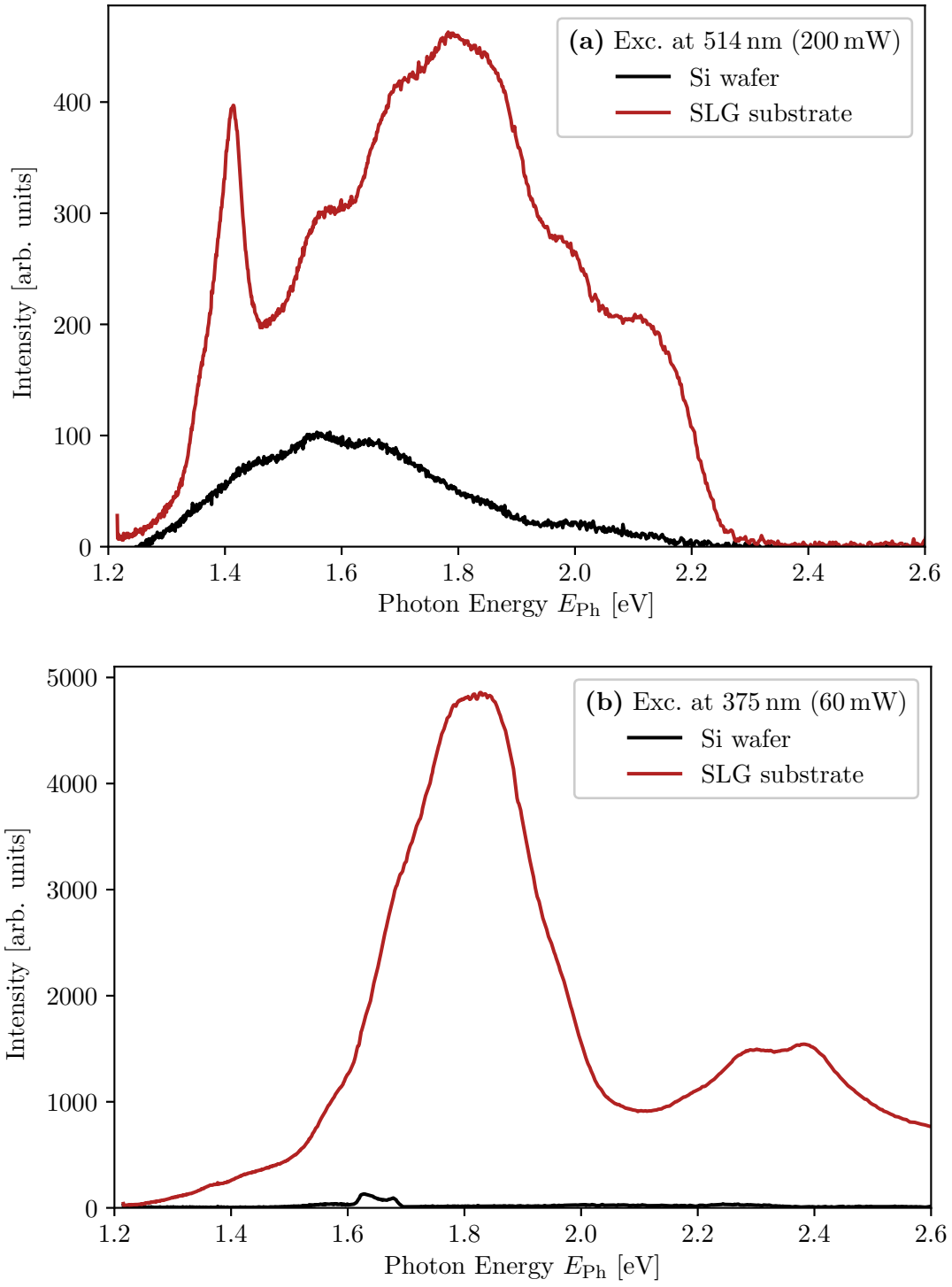

Fig. 6.39: SLG and a Si wafer are part of the experimental setup as detailed in the text. This graph shows their contributions to the PL spectra in case of excitation with the 514 nm green laser (a) and with the 375 nm UV laser (b) respectively. The spectra have been measured at room temperature.

glass substrate and by a plain Si wafer respectively. The latter is usually placed between the glass substrate of the thin film sample and the sample mount of the setup to avoid background signals. The potential contributions to the spectra of both, the SLG and the Si, are shown in Figure 6.39. With both excitation lasers, the green and the UV laser, the glass emission is significantly higher and has a more modulated intensity than the emission of Si in the region of interest. Nevertheless, probably no significant distortion by these two materials is present in the measurement data because the CZTS layer reduces the incident light intensity on the SLG and the Si wafer underneath to a minimum. In the same way, the small amount of emitted light is attenuated in the other direction because a one micron thick film of CZTS should nearly absorb all light due to the high absorption coefficient of $\alpha > 10^4\,\mathrm{cm}^{-1}$ [29]. However, the findings suggest that thinner layers on SLG substrates are less suitable for use in PL measurements.

The discussion of the PL spectra of films annealed at different temperatures in Section 6.2.5 concluded that interference effects are likely to have influenced the spectra measured. These effects could potentially be reduced by tilting the specimen in relation to the incident beam direction which is one of the ideas proposed and tested by Larsen et al. in order to avoid measurement errors [136]. Figure 6.24 (p. 114) demonstrates this. Also, interference only occurs in case of fairly smooth layers and can thus be diminished by increasing surface roughness. The third option suggested is to correct for interference by experimentally determining the reflectance or a calculated interference function [136]. In the conclusion of Section 6.2 of this study, the application of excitation lasers with other wavelengths was mentioned as further option to consider.

Looking back on the discussion of potential errors in EDX measurements in Section 6.5.3, it is conceivable that not only interference occurs in PL but also that mass and absorption effects similar to those in EDX due to the nanocrystalline material occur in the context of PL emission. This would alter the relative peak intensities. Furthermore, it is known that side effects of strain can potentially be seen within PL spectra, also known as strain-excited/strain-stimulated luminescence or triboluminescence [67]. It cannot be excluded that strain is present in the nanostructured thin films used. Finally, as already mentioned briefly, ligands can influence the PL spectra of CZTS [135]. Quenching of the measured PL intensity due to ligand adsorption has been reported for nanocrystals of other materials in combination with amines and thiols [74, 151, 152]. Such chemicals are used in the sample preparation in the context of this work as well.

7. Summary and Outlook

The outcome of the present experiments is now briefly summarised. More detailed conclusions from the different measurement series can be found in Sections 6.1.6, 6.2.6, 6.3.6, and 6.4.3, finishing the corresponding parts of the results chapter. Since successful experiments rely on reproducible fabrication of samples, several nanocrystal syntheses prepared by the approach chosen for this project were compared, showing that CZTS nanoparticles are successfully synthesised with adequate reproducibility. Most importantly, the impact of varying annealing temperatures was analysed in detail by use of a number of different methods in order to understand the development of various material properties. The results, overall, suggest to use rather high annealing temperatures of around 600 °C. In addition, varying annealing times were tested at a moderate temperature of 500 °C showing that the final state is already reached after one hour at maximum. By way of example, a cross-sectional analysis of two annealed samples on a Mo rear contact layer was performed, indicating that the absorber is densely packed but not completely uniform regarding grain sizes and/or phase.

In terms of future studies, it is first of all recommended to extend the investigations on issues broached in Section 6.5 about potential sources of error in the experiments. In particular, interference effects and the complex influences of ligands require better understanding. This will allow for more profound conclusions from UV-vis and PL spectroscopy but also from other techniques used in the context of CZTS nanoparticle thin films. The success of future investigations will also depend on the reproducibility of sample preparation so that a higher level of parameter control is desired. This study looked at different annealing temperatures and times but especially in the latter case the analysis needs to be extended to higher annealing temperatures as the temporal development is likely to depend on this choice. Other annealing parameters such as the sulphur concentration in the surrounding gas atmosphere and the ramp rates of heating-up/cooling-down should be investigated as well. More focus should additionally be put on the properties of the interface between absorber layer and rear contact. In the long term, the preparation of complete photovoltaic devices will be useful so that direct effects on cell performance can be studied. Certain experiments involving the above-mentioned suggestions have already been presented in the academic literature but due to the complex interdependencies between various properties and processing parameters open challenges persist towards whose mastery this work attempted to make a small contribution.

A. Supplemental Figures and Tables

This appendix contains a number of tables and some graphs in addition to those provided within the main text. Uncertainties on the last figures may be indicated in brackets where space is rare. Average values are mainly stated for the purpose of looking at the standard deviation of the different samples, especially in the context of NC synthesis reproducibility. They need to be interpreted with care. Peak tables for Raman and PL measurements include the assignment to compounds according to Tables 5.1 (p. 56) and 5.2 (p. 72) respectively. If reference peaks for CZTS and secondary phases lie close together, the peak has been considered as a CZTS peak within the analysis but the alternative compounds are given in brackets in the tables. In addition, it is important to note that all peaks found are listed but that some of them are doubtful due to sometimes low peak intensities and due to peak overlaps which complicate fitting. Sorting of the peaks may be ambiguous since they are observed at varying positions for different samples.

A.1. Additional Background Information

Tab. A.1: Expected composition including the elemental ratios for stoichiometric as well as Cu-poor/Zn-rich CZTS to facilitate comparison between different ways of representing the measurement results of elemental analysis.

	Stoichiometric	Cu-poor/Zn-rich
Cu/(Zn+Sn)	1	0.8
Zn/Sn	1	1.2
Empirical Formula	Cu_2ZnSnS_4	$Cu_{1.76}Zn_{1.2}SnS_4$
Cu	25.0 at%	22.1 at%
Zn	12.5 at%	15.1 at%
Sn	12.5 at%	12.6 at%
S	50.0 at%	50.2 at%
Cu	28.9 wt%	25.6 wt%
Zn	14.9 wt%	17.7 wt%
Sn	27.0 wt%	27.3 wt%
S	29.2 wt%	29.4 wt%

A.2. Reproducibility of Nanocrystal Synthesis (Sec. 6.1)

The horizontal line dividing nanocrystal (NC) batches Syn04 and Syn05 within the following tables indicates the change in the combination of chemicals used for collecting the as-synthesised particles from the OAm mixture by centrifuging.

Tab. A.2: In terms of the comparison between different NC batches, the tetragonal lattice parameter a and c as well as the domain sizes τ deduced from the XRD spectra in Figure 6.2 (p. 76) are listed in this table. They have been measured with NC powder samples. In addition, the band gap energies inferred from UV-vis measurements on as-deposited thin films from these particles are given. For the last two batches, Syn10 and Syn11, the E_g value stated is the average over a number of films whose individual results are summarised in Tables A.6 and A.9 respectively. The error stated in this particular case is the standard deviation of the different films which is significantly higher than the statistical error obtained from the fitting of the Tauc plots as indicated in case of the other syntheses listed. In the bottom line of this table, the weighted mean with corresponding error for the lattice parameters and the average value with corresponding standard deviation for the domain sizes and band gap energies are given respectively.

NC batch	**Lattice parameters**		**Domain size**	**Band gap energy**
	a [Å]	c [Å]	τ [nm]	E_g [eV]
Syn01	5.407 ± 0.003	10.869 ± 0.004	41.7 ± 1.9	1.108 ± 0.003
Syn02	5.403 ± 0.007	10.868 ± 0.005	36 ± 4	1.2382 ± 0.0019
Syn03	5.402 ± 0.007	10.868 ± 0.005	37 ± 4	0.856 ± 0.003
Syn04	5.395 ± 0.016	10.866 ± 0.007	28 ± 4	1.0776 ± 0.0008
Syn05	5.394 ± 0.017	10.866 ± 0.008	32 ± 6	1.2514 ± 0.0014
Syn06	5.386 ± 0.020	10.865 ± 0.009	22 ± 6	1.0067 ± 0.0015
Syn07	5.394 ± 0.017	10.866 ± 0.008	19 ± 6	1.2565 ± 0.0009
Syn08	5.390 ± 0.020	10.866 ± 0.009	28 ± 6	1.2624 ± 0.0003
Syn09	5.392 ± 0.020	10.866 ± 0.008	33 ± 4	1.0933 ± 0.001
Syn10	5.392 ± 0.017	10.866 ± 0.008	29 ± 6	1.14 ± 0.03
Syn11	5.392 ± 0.018	10.866 ± 0.008	30 ± 5	1.23 ± 0.09
Average:	5.404 ± 0.003	10.867 ± 0.002	31 ± 7	1.14 ± 0.13

Tab. A.3: EDX and in some cases also ICP-MS has been used to determine the composition of the as-synthesised particles. In this table, the normalised atomic percentages of the elemental components of CZTS are compared. Since from ICP-MS the amount of sulphur is not known, it is taken from EDX (by normalising all values to the Sn content which is known from both measurement techniques giving similar results) in order to make the concentrations obtained from ICP-MS comparable to the EDX results. The bottom line contains the average values with corresponding standard deviations in order to look at the stability of the elemental concentrations in terms of the different synthesis batches prepared via the same method.

NC batch	**Composition from EDX**				**Composition from ICP-MS**			
	Cu [at%]	Zn [at%]	Sn [at%]	S [at%]	Cu [at%]	Zn [at%]	Sn [at%]	S [at%]
Syn01	19.0(1.2)	25.2(1.5)	8.6(0.3)	47.2(1.1)				
Syn02	23.0(1.2)	18.5(1.3)	12.2(0.4)	46.3(0.4)	23.86	16.42	12.47	47.26
Syn03	19.7(1.7)	25(3)	9.6(0.4)	46(3)	20.78	21.13	10.12	47.97
Syn04	24.3(1.0)	15.9(1.2)	12.2(0.4)	47.6(1.0)				
Syn05	20.1(1.2)	20.7(1.6)	11.1(0.4)	48.1(1.2)				
Syn06	20.1(1.0)	19.3(1.1)	10.9(0.3)	49.7(0.8)				
Syn07	20.6(0.9)	16.1(1.2)	12.5(0.3)	50.8(1.2)				
Syn08	17.2(0.6)	18.9(0.7)	10.0(0.3)	53.9(0.7)	20.29	18.68	9.57	51.47
Syn09	19.0(0.4)	17.8(0.5)	10.61(0.15)	52.6(0.4)	20.69	18.69	10.17	50.45
Syn10	20.1(0.7)	18.0(1.1)	11.1(0.3)	50.8(0.7)	21.84	19.92	10.41	47.84
Syn11	18.5(0.8)	20.4(1.0)	10.2(0.3)	51.0(0.8)	20.72	20.11	9.83	49.34
Average:	20(3)	20(4)	10.8(1.2)	49(3)	21.4(1.4)	19.2(1.7)	10.4(1.1)	49.1(1.7)

Tab. A.4: Based on the results from Table A.3, the empirical formulas (based on the EDX measurements) are summarised where sulphur is used as basis (i.e. the value of S is set to 4 as expected for stoichiometric CZTS). The cation ratios from EDX as well as ICP-MS where available are given in addition. The average values and standard deviations are stated in the bottom line.

NC batch	**Empirical formula from EDX** with S as basis	**Cation ratios from EDX**		**Cation ratios from ICP-MS**	
		Cu/(Zn+Sn)	Zn/Sn	Cu/(Zn+Sn)	Zn/Sn
Syn01	$Cu_{1.61(11)}Zn_{2.14(13)}Sn_{0.73(3)}S_{4(.13)}$	0.56(5)	2.92(20)		
Syn02	$Cu_{1.98(11)}Zn_{1.59(12)}Sn_{1.06(04)}S_{4(.13)}$	0.75(6)	1.51(12)	0.83	1.32
Syn03	$Cu_{1.72(17)}Zn_{2.2(3)}Sn_{0.84(6)}S_{4(.3)}$	0.57(7)	2.6(3)	0.67	2.09
Syn04	$Cu_{2.04(10)}Zn_{1.34(11)}Sn_{1.03(4)}S_{4(.12)}$	0.86(6)	1.30(11)		
Syn05	$Cu_{1.67(11)}Zn_{1.73(14)}Sn_{0.92(4)}S_{4(.14)}$	0.63(6)	1.87(16)		
Syn06	$Cu_{1.62(9)}Zn_{1.56(10)}Sn_{0.88(3)}S_{4(.09)}$	0.67(5)	1.77(12)		
Syn07	$Cu_{1.63(8)}Zn_{1.27(10)}Sn_{0.98(4)}S_{4(.13)}$	0.72(5)	1.29(11)		
Syn08	$Cu_{1.27(5)}Zn_{1.40(6)}Sn_{0.744(20)}S_{4(.07)}$	0.59(3)	1.89(9)	0.72	1.95
Syn09	$Cu_{1.44(4)}Zn_{1.35(4)}Sn_{0.807(13)}S_{4(.04)}$	0.67(3)	1.68(6)	0.72	1.84
Syn10	$Cu_{1.58(6)}Zn_{1.42(9)}Sn_{0.87(3)}S_{4(.08)}$	0.69(4)	1.63(11)	0.72	1.91
Syn11	$Cu_{1.45(7)}Zn_{1.60(8)}Sn_{0.80(3)}S_{4(.09)}$	0.61(4)	2.00(12)	0.69	2.05
Average:		0.67(10)	1.9(6)	0.72(6)	1.9(3)

Tab. A.5: The Raman spectra in Figure 6.3 (p. 79) are used for secondary phase analysis. Here, the peak positions for excitation at 785 nm are listed and the main peaks are highlighted in bold font. The values have been obtained by fitting a series of Lorentzians. In the bottom line, the assigned compounds are given.

NC batch	**Peak positions [cm^{-1}] for excitation at 785 nm**											
	L1	L2	L3	L4	L5	L6	L7	L8	L9	L10	L11	L12
Syn01	194.2(1.3)		259.0(7)	**287.27(15)**	305.6(1.7)		333.9(1.2)	**337.53(4)**	351.0(8)	365.9(6)	376.1(5)	
Syn02	195.6(1.0)		260.1(9)	**285.7(4)**	299.4(1.2)		322.7(6)	**335.9(4)**	350.0(6)	364.0(6)	373.0(5)	
Syn03	197.6(1.3)		258.8(9)	**284.7(3)**	301.8(1.1)		328.4(1.3)	**335.00(4)**	348.6(7)	361.7(5)	371.2(5)	
Syn04	199.7(1.1)		259.9(1.0)	**286.1(4)**	300.6(8)	318.0(1.0)	329.8(9)	**335.9(1)**	349.0(5)	367.5(5)		
Syn05	198(3)		261.7(7)	**285.55(19)**	298.7(9)		325.3(6)	**336.30(3)**	350.0(5)	364.5(3)	374.0(3)	
Syn06	201.8(1.1)		261.9(9)	**285.8(3)**	298.7(1.4)		328.0(8)	**336.32(3)**	351.0(6)	364.9(4)	374.6(3)	
Syn07	202.3(1.5)		261.3(1.2)	**286.4(1.1)**	299.0(1.2)		322.2(4)	**335.97(9)**	349.8(6)	363.1(7)	374.1(5)	
Syn08	199.8(8)		258.7(8)	**284.97(10)**	298.3(9)		331.1(8)	**335.35(3)**	350.2(7)	363.9(3)	373.6(3)	
Syn09	200.1(1.2)		260.9(1.6)	**284.97(20)**	296.8(1.5)		327.7(1.1)	**335.66(4)**	349.9(8)	363.7(5)	373.8(4)	
Syn10	196.1(4)	250(3)		**278(7)**	310(3)		**329.58(18)**			362.5(1.8)		392(3)
Syn11	196.7(4)	249.8(2.0)		**277(8)**	307(4)		**330.1(3)**			363.5(2.0)		394(3)
Phases:	SnS, $Cu_4Sn_7S_{16}$	CZTS (Sn_2Sn_3)	CZTS (CuS)	CZTS (SnS)	CZTS (Sn_2Sn_3, $Cu_4Sn_7S_{16}$)	CZTS (SnS_2, $Cu_{3/4}SnS_4$	disord. CZTS	CZTS	CZTS (ZnS, Cu_2SnS_3, $Cu_4Sn_7S_{16}$)	CZTS ($Cu_4Sn_7S_{16}$)	CZTS	

A.3. Influence of Annealing Temperature (Sec. 6.2)

Tab. A.6: Information on the samples for the measurement series on annealing temperature, including an attribution of the different films to the annealing conditions used. All samples are prepared from particles of nanocrystal batch Syn11. General characteristics of the as-synthesised nanocrystals are included in Section A.2. Here, the respective thicknesses and the band gap energies E_g measured with the *as-deposited films* are summarised. They have both been inferred from the UV-vis spectra in Figure A.1.

Annealing	Film	Thickness [nm]	Band gap energy [eV]
400 °C	f1	773	1.071 ± 0.003
450 °C	f4	434	1.2709 ± 0.0015
500 °C	f2	417	1.244 ± 0.003
550 °C	f5	422	1.2523 ± 0.0015
575 °C	f6	441	1.2686 ± 0.0010
600 °C	f3	413	1.2499 ± 0.0020

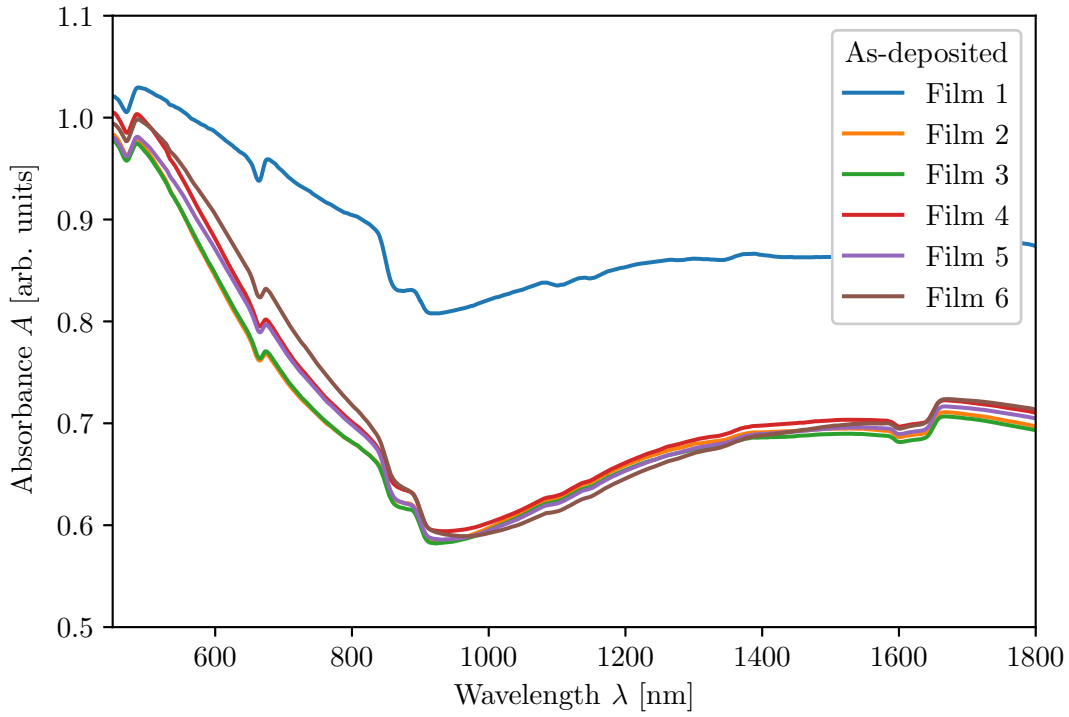

Fig. A.1: The absorption spectra of the as-deposited samples for the annealing experiments with varying temperature are presented. The curve of film 1 (f1) is shifted upwards as it is slightly thicker and therefore absorbs more light. Apart from this, the spectra appear to be very similar to one another. Characteristic parameters deduced from this graph are summarised in Table A.6.

Tab. A.7: Positions of the Raman peaks of samples annealed at different temperatures via fitting of a series of Lorentzians to the curves in Figure 6.15 (a) on p. 100 measured with 785 nm excitation wavelength. The compounds assigned to these peaks are indicated at the bottom of the table.

	Raman peak positions [cm^{-1}] for excitation at 785 nm												
	L1	L2	L3	L4	L5	L6	L7	L8	L9	L10	L11	L12	L13
As-dep			196.7(4)		249.8(2.0)		277(8)	307(4)	330.1(3)		363.5(2.0)		394(3)
400 °C	128.5(3)	151.3(1.4)	194.8(5)		251(1)			297.1(9)	330.29(9)		364.8(5)		
450 °C	129.8(4)		193.2(8)	205.4(9)	254.1(1.4)		284(3)	306(3)	331.83(7)		361.2(1.0)	371.7(5)	
500 °C	126.5(7)	147(4)	196(1)		251.0(1.1)		283.9(4)	296.4(1.3)	331.92(3)		361.3(7)	370.1(3)	
550 °C	130.4(3)		190.3(8)	202.4(1.2)	247.4(1.8)	263.6(1.7)	283.6(7)	303.6(1.6)	331.33(6)		365.3(3)		399.6(1.4)
575 °C	131.2(3)		189.9(7)	201.5(9)		259.6(6)	284.30(14)	302.0(5)	331.26(15)	335.19(5)	363.0(4)	371.22(20)	
600 °C	129.6(3)		190.0(7)	202.5(1.1)	249(3)	266(3)	283.90(15)	303.0(7)	329.0(5)	334.53(5)	362.7(9)	370.0(6)	
Phases:		CZTS	SnS, $Cu_4Sn_7S_{16}$		CZTS (Sn_2S_3)	CZTS (CuS)	CZTS (SnS)	CZTS (Sn_2S_3, $Cu_4Sn_7S_{16}$)	disord. CZTS	CZTS	CZTS ($Cu_4Sn_7S_{16}$)	CZTS	

Tab. A.8: Positions of the PL peaks of samples annealed at different temperatures via fitting a series of Gaussians to the curves in Figure 6.21 (a) on p. 107 measured at room temperature by excitation with the green laser (514 nm, 200 mW). Assigned compounds are listed in the bottom line.

	PL peak positions [eV] for excitation with green laser													
	G1	G2	G3	G4	G5	G6	G7	G8	G9	G10	G11	G12	G13	G14
As-dep			1.452(6)	1.471(4)	1.5479(7)		1.6685(18)		1.793(3)	1.8432(19)	1.8855(18)	1.9952(15)		2.143(4)
400 °C	1.282(3)	1.3544(8)		1.497(5)	1.545(8)	1.58(3)	1.6605(19)	1.771(6)		1.8414(11)	1.8840(8)	1.979(19)	2.037(7)	2.110(13)
450 °C		1.3585(7)		1.5(3)	1.5522(8)		1.67(14)	1.780(7)		1.852(1)	1.8942(9)	1.94(14)	2.017(5)	2.148(3)
500 °C	1.274(4)	1.3540(9)		1.487(7)	1.545(12)	1.58(4)	1.666(6)	1.771(9)		1.8471(14)	1.8895(13)	2.0012(18)	2.0103(19)	
550 °C	1.284(5)	1.3558(14)		1.463(2)	1.5516(6)		1.6614(19)	1.772(8)	1.7932(18)	1.841(2)	1.8871(18)		2.0027(17)	2.12(3)
575 °C		1.3573(8)	1.445(5)	1.4701(18)	1.5505(9)		1.660(3)		1.782(3)	1.8472(13)	1.8900(13)		2.0058(8)	2.156(3)
600 °C			1.4276(10)		1.5491(6)	1.598(10)	1.6632(17)			1.848(3)	1.8879(14)	1.90(6)	2.012(3)	
Phases:	CZTS (Cu_2S, SnS)	CZTS		CZTS (SnS)				SnS_2	ZnS, SnS_2			ZnS	ZnS, Sn_2S_3	ZnS, Sn_2S_3

A.4. Influence of Annealing Time (Sec. 6.3)

Tab. A.9: Information on the samples for the measurement series on the annealing time, including an attribution of the different films to the annealing conditions used. All samples are prepared from particles of nanocrystal batch Syn10. General characteristics of the as-synthesised nanocrystals are included in Section A.2. Here, the respective thicknesses and the band gap energies E_g measured with the *as-deposited films* are summarised. They have both been inferred from the UV-vis spectra in Figure A.2.

Annealing	Film	Thickness [nm]	Band gap energy [eV]
0.5 h	f3	608	1.133 ± 0.002
1 h	f4	526	1.116 ± 0.004
1.5 h	f5	532	1.169 ± 0.003
2 h	f6	537	1.128 ± 0.004
3 h	f7	567	1.146 ± 0.004

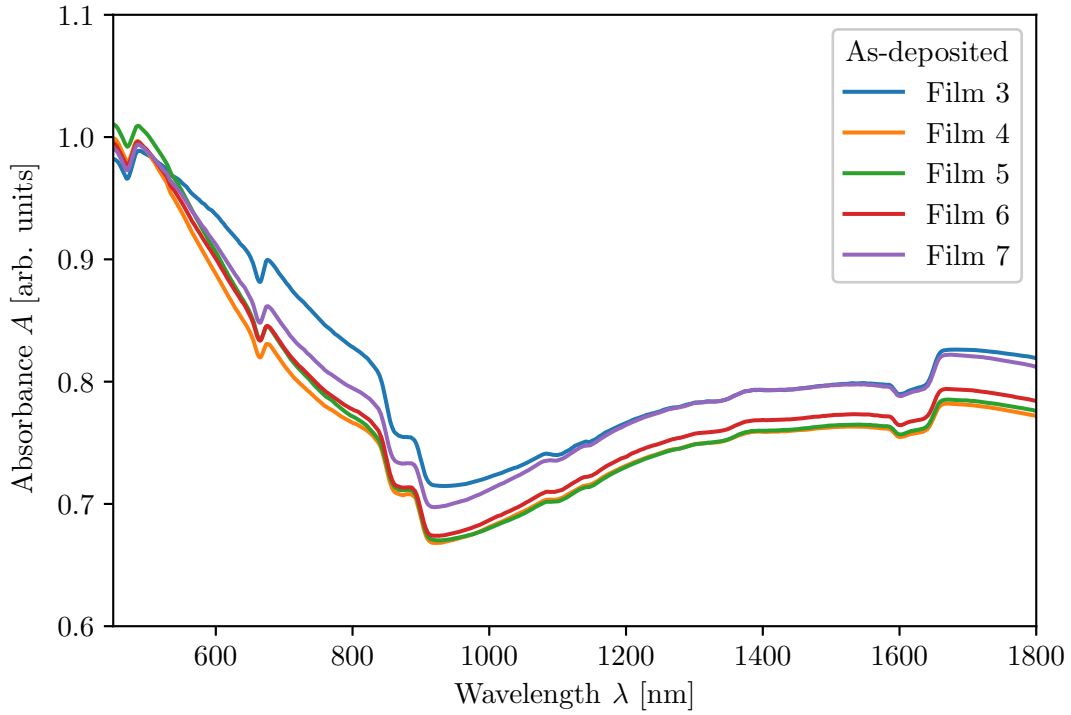

Fig. A.2: The absorption spectra of the as-deposited samples prepared for the measurement series on the annealing time are shown. Table A.9 lists the film thicknesses and band gap energies from these curves.

Tab. A.10: The Raman peak positions of samples annealed for different durations have been determined by fitting of a series of Lorentzians. This table summarises the results for the curves shown in Figure 6.32 (a) on p. 128 measured at 785 nm excitation wavelength and also includes the assignment to the corresponding compounds.

	Raman peak positions [cm^{-1}] for excitation at 785 nm											
	L1	L2	L3	L4	L5	L6	L7	L8	L9	L10	L11	L12
As-dep	196.1(4)	250(3)	278(7)			310(3)		329.58(18)		362.5(1.8)		392(3)
0.5 h	195.3(0.4)	250.7(1.4)	276(4)		301(3)		322(13)	329.9(1.1)	353(4)		367.7(1.6)	393.7(1.9)
1.0 h	196.2(9)	256.6(1.0)		282.5(5)	301.8(1.5)			331.65(4)	350.7(8)	363.5(7)	371.6(4)	
1.5 h	198.1(8)	256.7(9)		282.7(5)	300.3(1.3)			332.60(3)		362.1(6)	371.5(3)	
2.0 h	199.3(1.1)	257.5(1.0)		282.3(5)	300.6(1.2)			332.04(4)		361.0(6)	370.44(20)	
3.0 h	197.3(9)	255.6(1.1)		282.3(6)	301.3(1.9)			330.92(5)		360.3(9)	369.3(4)	
Phases:	SnS, $Cu_4Sn_7S_{16}$	CZTS (Sn_2S_3)	CZTS (ZnS, $Cu_4Sn_7S_{16}$)	CZTS (SnS)	CZTS (Sn_2S_3, $Cu_4Sn_7S_{16}$)	CZTS ($Cu_4Sn_7S_{16}$)	CZTS	disord. CZTS	CZTS (ZnS, Cu_2SnS_3, $Cu_4Sn_7S_{16}$)	CZTS ($Cu_4Sn_7S_{16}$)	CZTS	

Tab. A.11: The PL peaks of samples annealed for different durations are listed and are assigned to the respective compounds. The peak positions refer to the spectra shown in Figure 6.35 (a) on p. 132 and have been measured at room temperature by illumination of the samples with the green laser (514 nm, 200 mW). The spectra have subsequently been fitted with a series of Gaussians.

	PL peak positions [eV] for excitation with green laser												
	G1	G2	G3	G4	G5	G6	G7	G8	G9	G10	G11	G12	G13
As-dep			1.443(17)		1.5496(7)	1.587(6)	1.6700(17)	1.775(6)	1.8481(17)	1.8899(13)		2.0015(17)	2.146(4)
0.5 h			1.426(3)	1.4796(19)		1.5523(6)	1.6647(9)	1.7920(17)	1.8547(14)	1.8973(14)		2.0163(8)	2.165(4)
1.0 h		1.3618(7)		1.5(1.7)	1.50(19)	1.5550(6)	1.674(6)	1.783(3)	1.8551(9)	1.8976(9)	1.98(4)	2.012(5)	2.060(3)
1.5 h	1.284(5)	1.3600(7)		1.495(3)		1.5550(4)	1.6736(15)	1.7879(14)	1.8512(13)	1.8942(13)		2.0102(11)	2.159(6)
2.0 h	1.30(4)	1.3614(9)		1.489(5)		1.5540(4)	1.670(3)	1.7824(17)	1.8536(9)	1.8961(9)	1.93(4)	2.0184(14)	2.151(3)
3.0 h	1.284(5)	1.358(1)		1.485(4)		1.5538(4)	1.6694(15)	1.7792(15)	1.8539(10)	1.8956(9)	2.006(7)	2.008(4)	2.054(3)
Phases:	CZTS (Cu_2S, SnS)	CZTS		CZTS (SnS)	CZTS (SnS)			ZnS, SnS_2			ZnS	ZnS, Sn_2S_3	ZnS, Sn_2S_3

B. Data Evaluation

B.1. Python Code for Lattice Parameter Calculation

Listing 1: XRD_lattice-parameters.py

```
1  ################################################################################
2  #     Determination of the Tetragonal Lattice Parameters from XRD Patterns     #
3  ################################################################################
4
5  # Author: Karen P. Stroh
6  # Institution: Department of Physics, University of Durham, UK
7  # Date: 19/07/2018
8
9  # Filename: XRD_lattice-parameters.py
10 # Python version: 3.6.3
11 # Description: Command line program for the determination of the lattice
       parameters a and c of a tetragonal crystal structure (e.g. of kesterite or
       stannite Cu2ZnSnS4/CZTS) based on X-ray diffraction (XRD) measurements; two
       operating modes can be chosen, either the analysis of a single peak with any
        set of Miller indices, or the analysis and averaging of the three main
       peaks in a XRD pattern of CZTS; before using this program, the respective
       XRD spectrum needs to be analysed in order to determine the peak positions
       and their Miller indices
12 # Background: The expression for the interplanar spacing d of a tetragonal
       crystal structure can be affiliated with Bragg's law in order to eliminate d
       ; the resulting equation depends on the lattice parameters a and c; since it
        is one equation with two unknowns, a minimisation has to be performed to
       solve it
13 # Notes: All lengths are given in the unit Angstrom [A]; this program is written
        for XRD spectra obtained by use of the Cu K-alpha line (wavelength 1.5406 A
       ); the starting values for the minimisation correspond to CZTS; use the
       absolute values of a and c and do not report more than three decimal places
14
15
16 ##################################  Main Program  ##################################
17
18 # Loading of modules necessary for this script:
19 import numpy as np     # Module which contains definition of arrays for the
       storage of the variables
20 import math     # Module for mathematical functions
21 from scipy.optimize import minimize     # Submodule for minimisation procedure
22 import statistics as stat     # Module for statistical calculations
23 import tkinter as tk     # Module for browsing directories and saving results
       file
24 from tkinter import filedialog
25 import time
26 from datetime import date
27
28 # Choice of operating mode by the user:
29 print("Please choose from the following two options:\n1) Analyse a single peak (
       with any set of Miller indices).\n2) Analyse the three main peaks in a XRD
       pattern of CZTS, i.e. the (112), (220), and (312) peaks and calculate the
       average of the results.")
30 mode = int(input('> Option no. '))
```

```
while (mode!=1 and mode!=2):
    print("No valid input, please enter either 1 or 2.")
    mode = int(input('> Option no. '))

# Definition and read in of global variables:
wl = 1.5406     # Cu K-alpha wavelength of X-ray source used to collect the spectra
x0 = np.array([5.427, 10.871])  # [a0, c0], i.e. the starting values for the lattice parameters in Angstrom (correspond to literature values for CZTS from [K. Ito, "Copper Zinc Tin Sulfide-Based Thin-Film Solar Cells", John Wiley & Sons, 2015, p. 65])

# Function to minimise:
def f(x):
    return abs(1/math.sqrt((h**2+k**2)/x[0]**2 + l**2/x[1]**2) - wl/(2*math.sin(theta)))


# Mode 1 (single-peak analysis):
if mode==1:
    answer = 'y'
    while (answer=='y' or answer=='Y'):

        # Definition and read in of variables:
        twotheta = float(input('\nBragg angle 2 theta of peak to analyse (in degree): '))     # Input of peak position
        theta = (twotheta * (math.pi/180))/2     # Calculation of the angle theta in radians
        print("Corresponding Miller indices:")     # Input of the peak index according to the Miller notation (hkl)
        h = int(input('h = '))
        k = int(input('k = '))
        l = int(input('l = '))

        # Minimisation procedure (via the BFGS algorithm, a quasi-Newton method by Broyden, Fletcher, Goldfarb, and Shanno):
        print("\nDetermination of the lattice parameters:\n")
        result = minimize(f, x0, method='BFGS', options={'gtol': 1e-8, 'disp': True})
        # Report on the minimisation process:
        print("\n Result of minimisation:", result, "\n Notation: x[a,c] in Angstrom\n")
        # Output of the final results, i.e. the tetragonal lattice parameters a and c, in a clear manner:
        print("Results:\n", "a = ", result.x[0], "Angstrom\n", "c = ", result.x[1], "Angstrom")

        print("\nDo you want to analyse another peak? (y/n)")
        answer = str(input())

    else:
        if (answer=='n' or answer=='N'):
            ()
        else:
            print("No valid input, please try again.")


```

```
75 # Mode 2 (averaging of three main peaks):
76 elif mode==2:
77     answer = 'y'
78     while (answer=='y' or answer=='Y'):
79 
80         # Definition and read in of peak positions:
81         print("\nPlease enter the Bragg angles (2 theta) of the following peaks
    (in degree):")  # Input of peak positions
82         twotheta_112 = float(input('(112) > '))
83         twotheta_220 = float(input('(220) > '))
84         twotheta_312 = float(input('(312) > '))
85 
86         # Minimisation procedure (via the BFGS algorithm, a quasi-Newton method
    by Broyden, Fletcher, Goldfarb, and Shanno) for each of the peaks:
87         print("\nDetermination of the lattice parameters:\n")
88         # (112) peak:
89         h, k, l = 1, 1, 2
90         theta = (twotheta_112 * (math.pi/180))/2   # Calculation of the angle
    theta in radians
91         result1 = minimize(f, x0, method='BFGS', options={'gtol': 1e-8, 'disp':
    True})
92         # (220) peak:
93         h, k, l = 2, 2, 0
94         theta = (twotheta_220 * (math.pi/180))/2
95         result2 = minimize(f, x0, method='BFGS', options={'gtol': 1e-8, 'disp':
    True})
96         # (312) peak:
97         h, k, l = 3, 1, 2
98         theta = (twotheta_312 * (math.pi/180))/2
99         result3 = minimize(f, x0, method='BFGS', options={'gtol': 1e-8, 'disp':
    True})
100 
101         # Output of the final results, i.e. the tetragonal lattice parameters a
    and c for the different peaks separately:
102         print("\nResults for (112) peak:\n", "a = ", result1.x[0], "Angstrom\n",
     "c = ", result1.x[1], "Angstrom")
103         print("Results for (220) peak:\n", "a = ", result2.x[0], "Angstrom\n", "
    c = ", result2.x[1], "Angstrom")
104         print("Results for (312) peak:\n", "a = ", result3.x[0], "Angstrom\n", "
    c = ", result3.x[1], "Angstrom")
105 
106         # Calculation and output of the average values and standard deviations
    of the lattice parameters:
107         a_average, c_average = stat.mean([result1.x[0], result2.x[0], result3.x
    [0]]), stat.mean([result1.x[1], result2.x[1], result3.x[1]])
108         a_stddev, c_stddev = stat.stdev([result1.x[0], result2.x[0], result3.x
    [0]]), stat.stdev([result1.x[1], result2.x[1], result3.x[1]])
109         print("\nAverage and standard deviation of lattice parameters from above
    :\n", "a = ", a_average, "p/m", a_stddev, "Angstrom\n", "c = ", c_average, "
    p/m", c_stddev, "Angstrom\n")
110 
111         # Storage of results into a file:
112         root = tk.Tk()
113         root.attributes("-topmost", True)
114         file = tk.filedialog.asksaveasfile(mode='w+', defaultextension=".txt",
    initialfile='Lattice-par_CZTS_Eval-%s' % date.isoformat(date.today()))
115         if file is None:  # if dialog box is closed with "cancel"
```

```
116             root.destroy()
117         else:
118             root.destroy()
119             sample = str(input('Name/description of sample (this is written to
    the file in addition to the results): '))
120             file.write("Sample: %s\n" % sample)
121             file.write("\nAverage and standard deviation of lattice parameters
    considering all three main peaks:\na = %s p/m %s Angstrom\nc = %s p/m %s
    Angstrom\n" % (str(a_average), str(a_stddev), str(c_average), str(c_stddev))
    )
122             file.write("\nSingle results for the different peaks:\n")
123             file.write("(112) @ %s deg\n\ta = %s Angstrom\n\tc = %s Angstrom\n"
    % (str(twotheta_112), str(result1.x[0]), str(result1.x[1])))
124             file.write("(220) @ %s deg\n\ta = %s Angstrom\n\tc = %s Angstrom\n"
    % (str(twotheta_220), str(result2.x[0]), str(result2.x[1])))
125             file.write("(312) @ %s deg\n\ta = %s Angstrom\n\tc = %s Angstrom\n"
    % (str(twotheta_312), str(result3.x[0]), str(result3.x[1])))
126             file.write("\nEvaluation on "  + date.isoformat(date.today()) + ", "
     + time.strftime("%H:%M:%S") + " with 'XRD_lattice-parameters.py' (version
    2018-07-19)")
127             file.close()
128 
129         print("\nDo you want to analyse another spectrum? (y/n)")
130         answer = str(input())
131 
132     else:
133         if (answer=='n' or answer=='N'):
134             ()
135         else:
136             print("No valid input, please try again.")
```

References

[1] International Energy Agency (IEA), *Electricity Information 2018: Overview*, Report, 2018.

[2] O. Morton, *Solar energy: A new day dawning? Silicon Valley sunrise*, Nature **443** (2006), no. 7107, pp. 19–22.

[3] International Energy Agency (IEA), *Renewables Information 2017: Overview*, Report, 2017.

[4] A. Zuser and H. Rechberger, *Considerations of resource availability in technology development strategies: The case study of photovoltaics*, Resources, Conservation and Recycling **56** (2011), no. 1, pp. 56–65.

[5] K. Ito (ed.), *Copper Zinc Tin Sulfide-Based Thin-Film Solar Cells*, John Wiley & Sons, Chichester, UK, 2015.

[6] C. J. Stolle, T. B Harvey, and B. A Korgel, *Nanocrystal photovoltaics: A review of recent progress*, Curr. Opin. Chem. Eng. **2** (2013), no. 2, pp. 160–167.

[7] X. Liu, Y. Feng, H. Cui, F. Liu, X. Hao, G. Conibeer, D. B. Mitzi, and M. Green, *The current status and future prospects of kesterite solar cells: A brief review*, Prog. Photovoltaics **24** (2016), no. 6, pp. 879–898.

[8] S. E. Habas, H. A. S. Platt, M. F. A. M. van Hest, and D. S. Ginley, *Low-Cost Inorganic Solar Cells: From Ink To Printed Device*, Chem. Rev. **110** (2010), no. 11, pp. 6571–6594.

[9] American Physical Society, *This Month in Physics History - April 25, 1954: Bell Labs Demonstrates the First Practical Silicon Solar Cell*, APS News **18** (2009), no. 4, p. 2.

[10] J. Ramanujam, A. Verma, B. Gonzalez-Diaz, R. Guerrero-Lemus, C. del Canizo, E. Garcia-Tabares, I. Rey-Stolle, F. Granek, L. Korte, M. Tucci, J. Rath, U. P. Singh, T. Todorov, O. Gunawan, S. Rubio, J. L. Plaza, E. Dieguez, B. Hoffmann, S. Christiansen, and G. E. Cirlin, *Inorganic photovoltaics - Planar and nanostructured devices*, Prog. Mater. Sci. **82** (2016), pp. 294–404.

[11] C. J. Bosson, M. T. Birch, D. P. Halliday, K. S. Knight, A. S. Gibbs, and P. D. Hatton, *Cation disorder and phase transitions in the structurally complex solar cell material Cu_2ZnSnS_4*, J. Mater. Chem. A **5** (2017), no. 32, pp. 16672–16680.

[12] M. A. Green, Y. Hishikawa, E. D. Dunlop, D. H. Levi, J. Hohl-Ebinger, and A. W. Y. Ho-Baillie, *Solar cell efficiency tables (version 52)*, Prog. Photovolt. Res. Appl. **26** (2018), no. 7, pp. 427–436.

[13] J. J. Scragg, T. Ericson, T. Kubart, M. Edoff, and C. Platzer-Björkman, *Chemical Insights into the Instability of Cu_2ZnSnS_4 Films during Annealing*, Chem. Mater. **23** (2011), no. 20, pp. 4625–4633.

[14] B. Long, S. Cheng, Y. Lai, H. Zhou, J. Yu, and Q. Zheng, *Effects of sulfurization temperature on phases and opto-electrical properties of Cu_2ZnSnS_4 films prepared by sol-gel deposition*, Thin Solid Films **573** (2014), pp. 117–121.

[15] W. van der Stam, A. C. Berends, and C. de Mello Donega, *Prospects of Colloidal Copper Chalcogenide Nanocrystals*, ChemPhysChem **17** (2016), no. 5, pp. 559–581.

[16] C. J. Bosson, M. T. Birch, D. P. Halliday, C. C. Tang, A. K. Kleppe, and P. D. Hatton, *Polymorphism in Cu_2ZnSnS_4 and New Off-Stoichiometric Crystal Structure Types*, Chem. Mat. **29** (2017), no. 22, pp. 9829–9839.

[17] H. Katagiri, N. Sasaguchi, S. Hando, S. Hoshino, J. Ohashi, and T. Yokota, *Preparation and evaluation of Cu_2ZnSnS_4 thin films by sulfurization of E-B evaporated precursors*, Sol. Energy Mater. Sol. Cells **49** (1997), no. 1, pp. 407–414.

[18] W. Wang, M. T. Winkler, O. Gunawan, T. Gokmen, T. K. Todorov, Y. Zhu, and D. B. Mitzi, *Device Characteristics of CZTSSe Thin-Film Solar Cells with 12.6% Efficiency*, Adv. Energy Mater. **4** (2014), no. 7, p. 1301465.

[19] W. Shockley and H. J. Queisser, *Detailed Balance Limit of Efficiency of p-n Junction Solar Cells*, J. Appl. Phys. **32** (1961), no. 3, pp. 510–519.

[20] A. Neisser, A. Meeder, F. Zetzsche, U. Rühle, C. von Klopmann, R. J. Stroh, and N. Meyer, *Manufacturing of Large-Area $CuInS_2$ Solar Modules – From Pilot to Mass Production*, EU PVSEC Proceedings (Hamburg, DE), 2009, pp. 2460–2464.

[21] H. Zhou, W.-C. Hsu, H.-S. Duan, B. Bob, W. Yang, T.-B. Song, C.-J. Hsu, and Y. Yang, *CZTS nanocrystals: A promising approach for next generation thin film photovoltaics*, Energy Environ. Sci. **6** (2013), no. 10, pp. 2822–2838.

[22] B. D. Chernomordik, A. E. Béland, D. D. Deng, L. F. Francis, and E. S. Aydil, *Microstructure Evolution and Crystal Growth in Cu_2ZnSnS_4 Thin Films Formed By Annealing Colloidal Nanocrystal Coatings*, Chem. Mat. **26** (2014), no. 10, pp. 3191–3201.

[23] Q. Guo, H. W. Hillhouse, and R. Agrawal, *Synthesis of Cu_2ZnSnS_4 Nanocrystal Ink and Its Use for Solar Cells*, J. Am. Chem. Soc. **131** (2009), no. 33, pp. 11672–1167.

[24] Q. Guo, G. M. Ford, W.-C. Yang, B. C. Walker, E. A. Stach, H. W. Hillhouse, and R. Agrawal, *Fabrication of 7.2% Efficient CZTSSe Solar Cells Using CZTS Nanocrystals*, J. Am. Chem. Soc. **132** (2010), no. 49, pp. 17384–17386.

[25] B. Pamplin, *The adamantine family of compounds*, Progress in Crystal Growth and Characterization **3** (1980), no. 2, pp. 179–192.

[26] C. J. Bosson, *Understanding Cu_2ZnSnS_4 as a Photovoltaic Absorber for the Future of Solar Electricity*, Doctoral thesis, University of Durham, Durham, United Kingdom, 2018.

[27] T. Maeda, S. Nakamura, and T. Wada, *Electronic structure and phase stability of In-free photovoltaic semiconductors, $Cu_2ZnSnSe_4$ and Cu_2ZnSnS_4 by first-principles calculation*, MRS Online Proc. Libr. Arch. **1165** (2009).

[28] X. Liu, J. Huang, F. Zhou, F. Liu, J. A. Stride, and X. Hao, *Spatial Grain Growth and Composition Evolution during Sulfurizing Metastable Wurtzite Cu_2ZnSnS_4 Nanocrystal-Based Coatings*, Chem. Mat. **29** (2017), no. 5, pp. 2110–2121.

[29] C. Persson, *Electronic and optical properties of Cu_2ZnSnS_4 and $Cu_2ZnSnSe_4$*, J. Appl. Phys. **107** (2010), no. 5, p. 053710.

[30] J. J. S. Scragg, J. K. Larsen, M. Kumar, C. Persson, J. Sendler, S. Siebentritt, and C. Platzer-Björkman, *Cu-Zn disorder and band gap fluctuations in $Cu_2ZnSn(S,Se)_4$: Theoretical and experimental investigations*, Phys. Status Solidi B **253** (2016), no. 2, pp. 247–254.

[31] B. G. Mendis, M. D. Shannon, M. C. J. Goodman, J. D. Major, R. Claridge, D. P. Halliday, and K. Durose, *Direct observation of Cu, Zn cation disorder in Cu_2ZnSnS_4 solar cell absorber material using aberration corrected scanning transmission electron microscopy*, Prog. Photovoltaics **22** (2014), no. 1, pp. 24–34.

[32] M. Courel, J. A. Andrade-Arvizu, and O. Vigil-Galán, *Loss mechanisms influence on Cu_2ZnSnS_4/CdS-based thin film solar cell performance*, Solid-State Electronics **111** (2015), pp. 243–250.

[33] S. Chen, J.-H. Yang, X. G. Gong, A. Walsh, and S.-H. Wei, *Intrinsic point defects and complexes in the quaternary kesterite semiconductor Cu_2ZnSnS_4*, Phys. Rev. B **81** (2010), no. 24, p. 245204.

[34] A. Nagoya, R. Asahi, R. Wahl, and G. Kresse, *Defect formation and phase stability of Cu_2ZnSnS_4 photovoltaic material*, Phys. Rev. B **81** (2010), no. 11, p. 113202.

[35] S. Chen, X. G. Gong, A. Walsh, and S.-H. Wei, *Defect physics of the kesterite thin-film solar cell absorber Cu_2ZnSnS_4*, Appl. Phys. Lett. **96** (2010), no. 2, p. 021902.

[36] F. J. Espinosa-Faller, D. R. Conradson, S. C. Riha, M. B. Martucci, Sarah J. Fredrick, S. Vogel, A. L. Prieto, and S. D. Conradson, *Neutron Diffraction and X-ray Absorption Fine Structure Evidence for Local Lattice Distortions and Aperiodic Antisite Substitution in Cu_2ZnSnS_4 Nanoparticles*, J. Phys. Chem. C **118** (2014), no. 45, pp. 26292–26303.

[37] T. Washio, H. Nozaki, T. Fukano, T. Motohiro, K. Jimbo, and H. Katagiri, *Analysis of lattice site occupancy in kesterite structure of Cu_2ZnSnS_4 films using synchrotron radiation x-ray diffraction*, Journal of Applied Physics **110** (2011), no. 7, p. 074511.

[38] I. D. Olekseyuk, I. V. Dudchak, and L. V. Piskach, *Phase equilibria in the Cu_2S–ZnS–SnS_2 system*, Journal of Alloys and Compounds **368** (2004), no. 1, pp. 135–143.

[39] D. Berg, *Kesterite Equilibrium Reaction and the Discrimination of Secondary Phases from Cu_2ZnSnS_4*, Doctoral thesis, University of Luxembourg, Luxembourg City, Luxembourg, 2012.

[40] H. Katagiri, K. Jimbo, M. Tahara, H. Araki, and K. Oishi, *The Influence of the Composition Ratio on CZTS-based Thin Film Solar Cells*, MRS Online Proc. Libr. Arch. **1165** (2009/ed).

[41] H. Katagiri and K. Jimbo, *Development of rare metal-free CZTS-based thin film solar cells*, 37th IEEE Photovoltaic Specialists Conference, 2011, pp. 003516–003521.

[42] D. Mamedov, M. Klopov, and S. Z. Karazhanov, *Influence of Cu_2S, SnS and $Cu_2ZnSnSe_4$ on optical properties of Cu_2ZnSnS_4*, Mater. Lett. **202** (2017), pp. 70–72.

[43] B. G. Mendis, M. C. J. Goodman, J. D. Major, A. A. Taylor, K. Durose, and D. P. Halliday, *The role of secondary phase precipitation on grain boundary electrical activity in Cu_2ZnSnS_4 (CZTS) photovoltaic absorber layer material*, Journal of Applied Physics **112** (2012), no. 12, p. 124508.

[44] P. Sarker, M. M. Al-Jassim, and M. N. Huda, *Theoretical limits on the stability of single-phase kesterite-Cu_2ZnSnS_4*, Journal of Applied Physics **117** (2015), no. 3, p. 035702.

[45] M. C. Johnson, *The synthesis and characterization of thin film copper zinc tin sulfide for solar cell applications*, Doctoral thesis, University of Minnesota, US-MN, 2014.

[46] T. Prabhakar and N. Jampana, *Effect of sodium diffusion on the structural and electrical properties of Cu_2ZnSnS_4 thin films*, Sol. Energy Mater. Sol. Cells **95** (2011), no. 3, pp. 1001–1004.

[47] A. Nagaoka, H. Miyake, T. Taniyama, K. Kakimoto, Y. Nose, M. A. Scarpulla, and K. Yoshino, *Effects of sodium on electrical properties in Cu_2ZnSnS_4 single crystal*, Appl. Phys. Lett. **104** (2014), no. 15, p. 152101.

[48] T. Gershon, B. Shin, N. Bojarczuk, M. Hopstaken, D. B. Mitzi, and S. Guha, *The Role of Sodium as a Surfactant and Suppressor of Non-Radiative Recombination at Internal Surfaces in Cu_2ZnSnS_4*, Adv. Energy Mater. **5** (2015), no. 2, p. 1400849.

[49] M. Johnson, S. V. Baryshev, E. Thimsen, M. Manno, X. Zhang, I. V. Veryovkin, C. Leighton, and E. S. Aydil, *Alkali-metal-enhanced grain growth in Cu_2ZnSnS_4 thin films*, Energy Environ. Sci. **7** (2014), no. 6, pp. 1931–1938.

[50] C. M. Sutter-Fella, J. A. Stueckelberger, H. Hagendorfer, F. La Mattina, L. Kranz, S. Nishiwaki, A. R. Uhl, Y. E. Romanyuk, and A. N. Tiwari, *Sodium Assisted Sintering of Chalcogenides and Its Application to Solution Processed $Cu_2ZnSn(S,Se)_4$ Thin Film Solar Cells*, Chem. Mat. **26** (2014), no. 3, pp. 1420–1425.

[51] W. Xiao, J. N. Wang, X. S. Zhao, J. W. Wang, G. J. Huang, L. Cheng, L. J. Jiang, and L. G. Wang, *Intrinsic defects and Na doping in Cu_2ZnSnS_4: A density-functional theory study*, Solar Energy **116** (2015), pp. 125–132.

[52] S. Tajima, R. Asahi, D. Isheim, D. N. Seidman, T. Itoh, and K. Ohishi, *Sodium distribution in solar-grade Cu_2ZnSnS_4 layers using atom-probe tomographic technique*, Jpn. J. Appl. Phys. **54** (2015), no. 11, p. 112302.

[53] O. P. Singh, K. S. Gour, R. Parmar, and V. N. Singh, *Sodium induced grain growth, defect passivation and enhancement in the photovoltaic properties of Cu_2ZnSnS_4 thin film solar cell*, Mater. Chem. Phys. **177** (2016), pp. 293–298.

[54] K.-J. Yang, J.-H. Sim, D.-H. Son, D.-H. Kim, and J.-K. Kang, *Two different effects of Na on Cu_2ZnSnS_4 thin-film solar cells*, Current Applied Physics **15** (2015), no. 11, pp. 1512–1515.

[55] Q. Wen, Y. Li, J. Yan, and C. Wang, *Crystal size-controlled growth of Cu_2ZnSnS_4 films by optimizing the Na doping concentration*, Materials Letters **140** (2015), pp. 16–19.

[56] G. P. Smestad, *Optoelectronics of solar cells*, SPIE Press monograph (PM115),

SPIE Press, Bellingham, US-WA, 2002.

[57] C. Malerba, F. Biccari, C. L. Azanza Ricardo, M. Valentini, R. Chierchia, M. Müller, A. Santoni, E. Esposito, P. Mangiapane, P. Scardi, and A. Mittiga, *CZTS stoichiometry effects on the band gap energy*, Journal of Alloys and Compounds **582** (2014), pp. 528–534.

[58] G. Rey, A. Redinger, J. Sendler, T. P. Weiss, M. Thevenin, M. Guennou, B. El Adib, and S. Siebentritt, *The band gap of $Cu_2ZnSnSe_4$: Effect of order-disorder*, Appl. Phys. Lett. **105** (2014), no. 11, p. 112106.

[59] J. Paier, R. Asahi, A. Nagoya, and G. Kresse, *Cu_2ZnSnS_4 as a potential photovoltaic material: A hybrid Hartree-Fock density functional theory study*, Phys. Rev. B **79** (2009), no. 11, p. 115126.

[60] J. P. Leitão, N. M. Santos, P. A. Fernandes, P. M. P. Salomé, A. F. da Cunha, J. C. González, G. M. Ribeiro, and F. M. Matinaga, *Photoluminescence and electrical study of fluctuating potentials in Cu_2ZnSnS_4-based thin films*, Phys. Rev. B **84** (2011), no. 2, p. 024120.

[61] D. P. Halliday, R. Claridge, M. C. J. Goodman, B. G. Mendis, K. Durose, and J. D. Major, *Luminescence of Cu_2ZnSnS_4 polycrystals described by the fluctuating potential model*, Journal of Applied Physics **113** (2013), no. 22, p. 223503.

[62] T. Gokmen, O. Atici, T. K. Todorov, and D. B. Mitzi, *Band tailing and efficiency limitation in kesterite solar cells*, Appl. Phys. Lett. **103** (2013), no. 10, p. 103506.

[63] T. J. Huang, X. Yin, G. Qi, and H. Gong, *CZTS-based materials and interfaces and their effects on the performance of thin film solar cells*, Phys. Status Solidi RRL **8** (2014), no. 9, pp. 735–762.

[64] G. Rey, G. Larramona, S. Bourdais, C. Chone, B. Delatouche, A. Jacob, G. Dennler, and S. Siebentritt, *On the origin of band-tails in kesterite*, Sol. Energy Mater. Sol. Cells **179** (2018), pp. 142–151.

[65] M. Lang, T. Renz, A. Opolka, C. Zimmermann, C. Kraemmer, M. Neuwirth, H. Kalt, and M. Hetterich, *Impact of the degree of Cu-Zn order in $Cu_2ZnSn(S,Se)_4$ solar cell absorbers on defect states and band tails*, Appl. Phys. Lett. **113** (2018), no. 3, p. 033901.

[66] S. Adachi, *Earth-Abundant Materials for Solar Cells: Cu_2-II-IV-VI_4 Semiconductors*, John Wiley & Sons, Chichester, UK, 2015.

[67] J. I. Pankove, *Optical Processes in Semiconductors*, Dover Publications, New York, US, 1975.

[68] V. Kosyak, A. V. Postnikov, J. Scragg, M. A. Scarpulla, and C. Platzer-Björkman, *Calculation of point defect concentration in Cu_2ZnSnS_4: Insights into the high-temperature equilibrium and quenching*, Journal of Applied Physics **122** (2017), no. 3, p. 035707.

[69] J. B. Li, V. Chawla, and B. M. Clemens, *Investigating the Role of Grain Boundaries in CZTS and CZTSSe Thin Film Solar Cells with Scanning Probe Microscopy*, Adv. Mater. **24** (2012), no. 6, pp. 720–723.

[70] G. Y. Kim, A. R. Jeong, J. R. Kim, W. Jo, D.-H. Son, D.-H. Kim, and J.-K.

Kang, *Surface potential on grain boundaries and intragrains of highly efficient $Cu_2ZnSn(S,Se)_4$ thin-films grown by two-step sputtering process*, Sol. Energy Mater. Sol. Cells **127** (2014), pp. 129–135.

[71] A. Khare, A. W. Wills, L. M. Ammerman, D. J. Norris, and E. S. Aydil, *Size control and quantum confinement in Cu_2ZnSnS_4 nanocrystals*, ChemComm **47** (2011), no. 42, pp. 11721–11723.

[72] N. J. Carter, W.-C. Yang, C. K. Miskin, C. J. Hages, E. A. Stach, and R. Agrawal, *$Cu_2ZnSn(S,Se)_4$ solar cells from inks of heterogeneous Cu-Zn-Sn-S nanocrystals*, Sol. Energy Mater. Sol. Cells **123** (2014), pp. 189–196.

[73] H. W. Hillhouse and M. C. Beard, *Solar cells from colloidal nanocrystals: Fundamentals, materials, devices, and economics*, Current Opinion in Colloid & Interface Science **14** (2009), no. 4, pp. 245–259.

[74] C. de Mello Donegá, *Synthesis and properties of colloidal heteronanocrystals*, Chem. Soc. Rev. **40** (2011), no. 3, pp. 1512–1546.

[75] L. S. Khanzada, I. Levchuk, Y. Hou, H. Azimi, A. Osvet, R. Ahmad, M. Brandl, P. Herre, M. Distaso, R. Hock, W. Peukert, M. Batentschuk, and C. J. Brabec, *Effective Ligand Engineering of the Cu_2ZnSnS_4 Nanocrystal Surface for Increasing Hole Transport Efficiency in Perovskite Solar Cells*, Adv. Funct. Mater. **26** (2016), no. 45, pp. 8300–8306.

[76] T. J. Huang, X. Yin, C. Tang, G. Qi, and H. Gong, *Influence of Ligands on the Formation of Kesterite Thin Films for Solar Cells: A Comparative Study*, ChemSusChem **9** (2016), no. 9, pp. 1032–1041.

[77] S. M. Sze, *Physics of Semiconductor Devices*, 2 ed., John Wiley & Sons, New York, US, 1981.

[78] K. P. Stroh, *Capacitance-Voltage Measurements of a Manganite-Titanite p-n Heterojunction*, Bachelor thesis, Georg-August-Universität Göttingen, Göttingen, Germany, 2017.

[79] R. Gross and A. Marx, *Festkörperphysik*, Oldenbourg, München, DE, 2012.

[80] K. Kopitzki and P. Herzog, *Einführung in die Festkörperphysik*, 6th ed., Teubner Studienbücher Physik, Teubner, Wiesbaden, DE, 2007.

[81] W. Shockley, *The Theory of p-n Junctions in Semiconductors and p-n Junction Transistors*, Bell Syst. Tech. J. **28** (1949), no. 3, pp. 435–489.

[82] J. Li, D. B. Mitzi, and V. B. Shenoy, *Structure and Electronic Properties of Grain Boundaries in Earth-Abundant Photovoltaic Absorber $Cu_2ZnSnSe_4$*, ACS Nano **5** (2011), no. 11, pp. 8613–8619.

[83] V. T. Tiong, Y. Zhang, J. Bell, and H. Wang, *Carbon concentration dependent grain growth of Cu_2ZnSnS_4 thin films*, RSC Adv. **5** (2015), no. 26, pp. 20178–20185.

[84] S. Engberg, K. Agersted, A. Crovetto, O. Hansen, Y. M. Lam, and J. Schou, *Investigation of Cu_2ZnSnS_4 nanoparticles for thin-film solar cell applications*, Thin Solid Films **628** (2017), pp. 163–169.

[85] A. Redinger, D. M. Berg, P. J. Dale, and S. Siebentritt, *The Consequences of*

Kesterite Equilibria for Efficient Solar Cells, J. Am. Chem. Soc. **133** (2011), no. 10, pp. 3320–3323.

[86] K. Maeda, K. Tanaka, Y. Fukui, and H. Uchiki, *Influence of H_2S concentration on the properties of Cu_2ZnSnS_4 thin films and solar cells prepared by sol–gel sulfurization*, Sol. Energy Mater. Sol. Cells **95** (2011), no. 10, pp. 2855–2860.

[87] K. Maeda, K. Tanaka, Y. Nakano, Y. Fukui, and H. Uchiki, *H_2S Concentration Dependence of Properties of Cu_2ZnSnS_4 Thin Film Prepared under Nonvacuum Condition*, Jpn. J. Appl. Phys. **50** (2011), no. 5S2, p. 05FB09.

[88] B. A. Williams, M. A. Smeaton, N. D. Trejo, L. F. Francis, and E. S. Aydil, *Effect of Nanocrystal Size and Carbon on Grain Growth during Annealing of Copper Zinc Tin Sulfide Nanocrystal Coatings*, Chem. Mat. **29** (2017), no. 4, pp. 1676–1683.

[89] R. Mainz, B. C. Walker, S. S. Schmidt, O. Zander, A. Weber, H. Rodriguez-Alvarez, J. Just, M. Klaus, R. Agrawal, and T. Unold, *Real-time observation of $Cu_2ZnSn(S,Se)_4$ solar cell absorber layer formation from nanoparticle precursors*, Phys. Chem. Chem. Phys. **15** (2013), no. 41, pp. 18281–18289.

[90] F. Liu and R. Kirchheim, *Nano-scale grain growth inhibited by reducing grain boundary energy through solute segregation*, Journal of Crystal Growth **264** (2004), no. 1, pp. 385–391.

[91] F. Inam, H. Yan, T. Peijs, and M. J. Reece, *The sintering and grain growth behaviour of ceramic–carbon nanotube nanocomposites*, Composites Science and Technology **70** (2010), no. 6, pp. 947–952.

[92] B. Flynn, W. Wang, C.-H. Chang, and G. S. Herman, *Microwave assisted synthesis of Cu_2ZnSnS_4 colloidal nanoparticle inks*, Phys. Status Solidi A **209** (2012), no. 11, pp. 2186–2194.

[93] H. Azimi, Y. Hou, and C. J. Brabec, *Towards low-cost, environmentally friendly printed chalcopyrite and kesterite solar cells*, Energy Environ. Sci. **7** (2014), no. 6, pp. 1829–1849.

[94] W. Wu, Y. Cao, J. V. Caspar, Q. Guo, L. K. Johnson, I. Malajovich, H. D. Rosenfeld, and K. R. Choudhury, *Studies of the fine-grain sub-layer in the printed CZTSSe photovoltaic devices*, J. Mater. Chem. C **2** (2014), no. 19, pp. 3777–3781.

[95] Q. Guo, G. M. Ford, W.-C. Yang, C. J. Hages, H. W. Hillhouse, and R. Agrawal, *Enhancing the performance of CZTSSe solar cells with Ge alloying*, Sol. Energy Mater. Sol. Cells **105** (2012), pp. 132–136.

[96] C. M. Fella, A. R. Uhl, Y. E. Romanyuk, and A. N. Tiwari, *$Cu_2ZnSnSe_4$ absorbers processed from solution deposited metal salt precursors under different selenization conditions*, Phys. Status Solidi A **209** (2012), no. 6, pp. 1043–1048.

[97] A. Rockett, J. S. Britt, T. Gillespie, C. Marshall, M. M. Al Jassim, F. Hasoon, R. Matson, and B. Basol, *Na in selenized Cu(In,Ga)Se_2 on Na-containing and Na-free glasses: Distribution, grain structure, and device performances*, Thin Solid Films **372** (2000), no. 1, pp. 212–217.

[98] J. Malmström, S. Schleussner, and L. Stolt, *Enhanced back reflectance and quantum efficiency in Cu(In,Ga)Se_2 thin film solar cells with a ZrN back reflector*, Appl.

Phys. Lett. **85** (2004), no. 13, pp. 2634–2636.

[99] P. Chelvanathan, M. I. Hossain, J. Husna, M. Alghoul, K. Sopian, and N. Amin, *Effects of Transition Metal Dichalcogenide Molybdenum Disulfide Layer Formation in Copper–Zinc–Tin–Sulfur Solar Cells from Numerical Analysis*, Jpn. J. Appl. Phys. **51** (2012), no. 10S, p. 10NC32.

[100] D. Seo, J. Na, C. Kim, C. Jeong, and S. Lim, *Improvement of Cu_2ZnSnS_4 thin film properties by a modified sulfurization process*, Thin Solid Films **591** (2015), pp. 289–294.

[101] J. J. Scragg, J. T. Wätjen, M. Edoff, T. Ericson, T. Kubart, and C. Platzer-Björkman, *A Detrimental Reaction at the Molybdenum Back Contact in $Cu_2ZnSn(S,Se)_4$ Thin-Film Solar Cells*, J. Am. Chem. Soc. **134** (2012), no. 47, pp. 19330–19333.

[102] Y. Cao, M. S. Denny, J. V. Caspar, W. E. Farneth, Q. Guo, A. S. Ionkin, L. K. Johnson, M. Lu, I. Malajovich, D. Radu, H. D. Rosenfeld, K. R. Choudhury, and W. Wu, *High-Efficiency Solution-Processed $Cu_2ZnSn(S,Se)_4$ Thin-Film Solar Cells Prepared from Binary and Ternary Nanoparticles*, J. Am. Chem. Soc. **134** (2012), no. 38, pp. 15644–15647.

[103] F. Zhou, F. Zeng, X. Liu, F. Liu, N. Song, C. Yan, A. Pu, J. Park, K. Sun, and X. Hao, *Improvement of J_{sc} in a Cu_2ZnSnS_4 Solar Cell by Using a Thin Carbon Intermediate Layer at the Cu_2ZnSnS_4/Mo Interface*, ACS Appl. Mater. Interfaces **7** (2015), no. 41, pp. 22868–22873.

[104] C. Steinhagen, M. G. Panthani, V. Akhavan, B. Goodfellow, B. Koo, and B. A. Korgel, *Synthesis of Cu_2ZnSnS_4 Nanocrystals for Use in Low-Cost Photovoltaics*, J. Am. Chem. Soc. **131** (2009), no. 35, pp. 12554–12555.

[105] S. G. Kwon and T. Hyeon, *Formation Mechanisms of Uniform Nanocrystals via Hot-Injection and Heat-Up Methods*, Small **7** (2011), no. 19, pp. 2685–2702.

[106] S. C. Riha, B. A. Parkinson, and A. L. Prieto, *Solution-Based Synthesis and Characterization of Cu_2ZnSnS_4 Nanocrystals*, J. Am. Chem. Soc. **131** (2009), no. 34, pp. 12054–12055.

[107] N. Mirbagheri, S. Engberg, A. Crovetto, S. B. Simonsen, O. Hansen, Y. M. Lam, and J. Schou, *Synthesis of ligand-free CZTS nanoparticles via a facile hot injection route*, Nanotechnology **27** (2016), no. 18, p. 185603.

[108] R. J. Martín-Palma, *Nanotechnology: A crash course*, SPIE tutorial texts, vol. 86, SPIE, Bellingham WA, US, 2010.

[109] Y. Qu, *$Cu_2ZnSn(S,Se)_4$ Solar cells prepared from Cu_2ZnSnS_4 nanoparticle inks*, Doctoral thesis, Northumbria University, Newcastle, UK, 2015.

[110] R. E. Dinnebier and S. J. L. Billinge (eds.), *Powder Diffraction: Theory and Practice*, RSC Publishing, Cambridge, UK, 2008.

[111] W. H. Bragg and W. L. Bragg, *The reflection of X-rays by crystals*, Proc. R. Soc. Lond. A **88** (1913), no. 605, pp. 428–438.

[112] A. D. Collord and H. W. Hillhouse, *The effect of nanocrystal reaction time on $Cu_2ZnSn(S,Se)_4$ solar cells from nanocrystal inks*, Sol. Energy Mater. Sol. Cells

141 (2015), no. Supplement C, pp. 383–390.

[113] M. R. Byeon, E. H. Chung, J. P. Kim, T. E. Hong, J. S. Jin, E. D. Jeong, J. S. Bae, Y. D. Kim, S. Park, W. T. Oh, Y. S. Huh, S. J. Chang, S. B. Lee, I. H. Jung, and J. Hwang, *The effects for the deposition temperature onto the structural, compositional and optical properties of pulsed laser ablated Cu_2ZnSnS_4 thin films grown on soda lime glass substrates*, Thin Solid Films **546** (2013), pp. 387–392.

[114] A. Smekal, *Zur Quantentheorie der Dispersion*, Naturwissenschaften **11** (1923), no. 43, pp. 873–875.

[115] C. V. Raman and K. S. Krishnan, *A New Type of Secondary Radiation*, Nature **121** (1928), no. 3048, pp. 501–502.

[116] N. B. Colthup, *Introduction to Infrared and Raman Spectroscopy*, 3 ed., Academic Press, San Diego, US, 1990.

[117] S. Perkowitz, *Optical characterization of semiconductors: Infrared, raman, and photoluminescence spectroscopy*, Techniques of Physics, vol. 14, Academic Press, London, UK, 1993.

[118] M. C. Tobin, *Laser Raman Spectroscopy*, Chemical analysis, vol. 35, Wiley-Interscience, New York, US, 1971.

[119] D. Chescoe, *The operation of transmission and scanning electron microscopes*, Microscopy handbooks, vol. 20, Oxford University Press, New York, US, 1990.

[120] J. I. Goldstein, D. E. Newbury, P. Echlin, D. C. Joy, C. Fiori, and E. Lifshin, *Scanning Electron Microscopy and X-Ray Microanalysis: A Text for Biologists, Materials Scientists, and Geologists*, 1 ed., Plenum Press, New York, US, London, UK, 1981.

[121] S. J. Hill (ed.), *Inductively Coupled Plasma Spectrometry and its Applications*, 2 ed., Blackwell Publishing, Oxford, UK, 2008.

[122] J. G. Solé, *An Introduction to the Optical Spectroscopy of Inorganic Solids*, John Wiley & Sons, Chichester, UK, 2005.

[123] K. Hönes, *Photoluminescence measurements on solar cell materials: Chalcopyrites and kesterites*, Doctoral thesis, University of Luxembourg, Luxembourg City, Luxembourg, 2011.

[124] J. P. F. Jemetio, P. Zhou, and H. Kleinke, *Crystal structure, electronic structure and thermoelectric properties of $Cu_4Sn_7S_{16}$*, J. Alloys Compd. **417** (2006), no. 1-2, pp. 55–59.

[125] T. Sorgenfrei, F. Hofherr, T. Jauß, and A. Cröll, *Synthesis and single crystal growth of SnS by the Bridgman-Stockbarger technique*, Cryst. Res. Technol. **48** (2013), no. 4, pp. 193–199.

[126] A. Napolitano and E. G. Hawkins, *Viscosity of a standard soda-lime-silica glass*, J. Res. Natl. Bur. Stand. Sect. Phys. Chem. **68A** (1964), no. 5, p. 439.

[127] B. D. Cullity, *Elements of X-ray diffraction*, Addison-Wesley Metallurgy Series, Addison-Wesley Publishing Company, Reading, US-MA, 1956.

[128] K. Sugimoto, N. Suyama, K. Nakada, and A. Yamada, *Crystal growth mechanism*

of $Cu_2ZnSn(S,Se)_4$ thin films fabricated from nanoparticles, Jpn. J. Appl. Phys. **56** (2017), no. 3, p. 035502.

[129] C. Sripan, R. Ganesan, E. M. Vinod, and A. K. Viswanath, *The effect of sulfur on the phase formation of Cu_2ZnSnS_4 solar cell material*, Materials Letters **180** (2016), pp. 295–297.

[130] K. P. Stroh, I. G. Pérez Marín, Y. A. Altowairqi, M. Szablewski, and D. P. Halliday, *Thin films made of Cu_2ZnSnS_4 nanocrystal inks for solar cells*, Conference poster (HL 13.29), Joint meeting of the Condensed Matter Divisions of the European and the German Physical Society (EPS and DPG), Berlin, DE, March 2018.

[131] K. Tanaka, T. Shinji, and H. Uchiki, *Photoluminescence from Cu_2ZnSnS_4 thin films with different compositions fabricated by a sputtering-sulfurization method*, Solar Energy Materials and Solar Cells **126** (2014), pp. 143–148.

[132] M. Grossberg, J. Krustok, J. Raudoja, and T. Raadik, *The role of structural properties on deep defect states in Cu_2ZnSnS_4 studied by photoluminescence spectroscopy*, Appl. Phys. Lett. **101** (2012), no. 10, p. 102102.

[133] K. Timmo, M. Kauk-Kuusik, M. Pilvet, T. Raadik, M. Altosaar, M. Danilson, M. Grossberg, J. Raudoja, and K. Ernits, *Influence of order-disorder in Cu_2ZnSnS_4 powders on the performance of monograin layer solar cells*, Thin Solid Films **633** (2017), pp. 122–126.

[134] J. Krustok, T. Raadik, M. Grossberg, M. Kauk-Kuusik, V. Trifiletti, and S. Binetti, *Photoluminescence study of deep donor- deep acceptor pairs in Cu_2ZnSnS_4*, Mater. Sci. Semicond. Process **80** (2018), pp. 52–55.

[135] S. Campbell, Y. Qu, L. Bowen, P. Chapon, V. Barrioz, N. S. Beattie, and G. Zoppi, *Influence of OLA and FA ligands on the optical and electronic properties of $Cu_2ZnSn(S,Se)_4$ thin films and solar cells prepared from nanoparticle inks*, Solar Energy **175** (2018), pp. 101 – 109.

[136] J. K. Larsen, S.-Y. Li, J. J. S. Scragg, Y. Ren, C. Hägglund, M. D. Heinemann, S. Kretzschmar, T. Unold, and C. Platzer-Björkman, *Interference effects in photoluminescence spectra of Cu_2ZnSnS_4 and $Cu(In,Ga)Se_2$ thin films*, Journal of Applied Physics **118** (2015), no. 3, p. 035307.

[137] Y. Hamanaka, M. Tsuzuki, K. Ozawa, and T. Kuzuya, *Solution-phase Synthesis and Photoluminescence Characterization of Quaternary Cu_2ZnSnS_4 Nanocrystals*, Physics of Semiconductors (Melville), vol. 1566, Am. Inst. Physics, 2013.

[138] O. Zaberca, F. Oftinger, J. Y. Chane-Ching, L. Datas, A. Lafond, P. Puech, A. Balocchi, D. Lagarde, and X. Marie, *Surfactant-free CZTS nanoparticles as building blocks for low-cost solar cell absorbers*, Nanotechnology **23** (2012), no. 18, p. 185402.

[139] X. Wang, W.-H. Zhou, Z.-J. Zhou, Z.-L. Hou, J. Guo, and S.-X. Wu, *High-efficient dye-sensitized solar cells with all-inorganic $Cu_2ZnSnSe_4$ counter-electrode by ligand exchange*, Electrochimica Acta **104** (2013), pp. 26–32.

[140] Z.-X. Zhang, Z.-J. Zhou, B. Bai, M.-H. Liu, W.-H. Zhou, D.-X. Kou, and S.-X. Wu, *Effect of ligand exchange of Cu_2ZnSnS_4 nanocrystals on the charge transport and photovoltaic performance of nanostructured depleted bulk heterojunction solar*

cell, J Nanopart Res **17** (2015), no. 12, p. 463.

[141] X. Wang, D.-X. Kou, W.-H. Zhou, Z.-J. Zhou, S.-X. Wu, and X. Cao, *$Cu_2ZnSnSe_4$ nanocrystals capped with S_2- by ligand exchange: Utilizing energy level alignment for efficiently reducing carrier recombination*, Nanoscale Research Letters **9** (2014), no. 1, p. 262.

[142] L. Korala, M. B. Braun, J. M. Kephart, Z. Tregillus, and A. L. Prieto, *Ligand-Exchanged CZTS Nanocrystal Thin Films: Does Nanocrystal Surface Passivation Effectively Improve Photovoltaic Performance?*, Chem. Mater. **29** (2017), no. 16, pp. 6621–6629.

[143] K. Rudisch, Y. Ren, C. Platzer-Björkman, and J. Scragg, *Order-disorder transition in B-type Cu_2ZnSnS_4 and limitations of ordering through thermal treatments*, Appl. Phys. Lett. **108** (2016), no. 23, p. 231902.

[144] T. K. Todorov, J. Tang, S. Bag, O. Gunawan, T. Gokmen, Y. Zhu, and D. B. Mitzi, *Beyond 11% Efficiency: Characteristics of State-of-the-Art $Cu_2ZnSn(S,Se)_4$ Solar Cells*, Adv. Energy Mater. **3** (2013), no. 1, pp. 34–38.

[145] I. Repins, C. Beall, N. Vora, C. DeHart, D. Kuciauskas, P. Dippo, B. To, J. Mann, W.-C. Hsu, A. Goodrich, and R. Noufi, *Co-evaporated $Cu_2ZnSnSe_4$ films and devices*, Sol. Energy Mater. Sol. Cells **101** (2012), pp. 154–159.

[146] S. Ahmed, K. B. Reuter, O. Gunawan, L. Guo, L. T. Romankiw, and H. Deligianni, *A High Efficiency Electrodeposited Cu_2ZnSnS_4 Solar Cell*, Adv. Energy Mater. **2** (2012), no. 2, pp. 253–259.

[147] M. Dimitrievska, A. Fairbrother, A. Pérez-Rodríguez, E. Saucedo, and V. Izquierdo-Roca, *Raman scattering crystalline assessment of polycrystalline Cu_2ZnSnS_4 thin films for sustainable photovoltaic technologies: Phonon confinement model*, Acta Materialia **70** (2014), pp. 272–280.

[148] M. Guc, S. Levcenko, I. V. Bodnar, V. Izquierdo-Roca, X. Fontane, L. V. Volkova, E. Arushanov, and A. Pérez-Rodríguez, *Polarized Raman scattering study of kesterite type Cu_2ZnSnS_4 single crystals*, Sci. Rep. **6** (2016), p. 19414.

[149] P. Hovington, D. Drouin, and R. Gauvin, *CASINO: A new monte carlo code in C language for electron beam interaction - part I: Description of the program*, Scanning **19** (1997), no. 1, pp. 1–14.

[150] D. Drouin, A. R. Couture, D. Joly, X. Tastet, V. Aimez, and R. Gauvin, *CASINO V2.42 - A Fast and Easy-to-use Modeling Tool for Scanning Electron Microscopy and Microanalysis Users*, Scanning **29** (2007), no. 3, pp. 92–101.

[151] A. M. Munro, I. Jen-La Plante, M. S. Ng, and D. S. Ginger, *Quantitative Study of the Effects of Surface Ligand Concentration on CdSe Nanocrystal Photoluminescence*, J. Phys. Chem. C **111** (2007), no. 17, pp. 6220–6227.

[152] A. M. Munro and D. S. Ginger, *Photoluminescence Quenching of Single CdSe Nanocrystals by Ligand Adsorption*, Nano Lett. **8** (2008), no. 8, pp. 2585–2590.